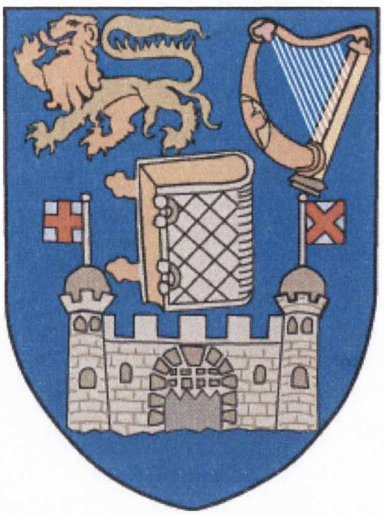

Impurities and magnetic interactions in graphene: a theoretical study

By

Stephen R. Power

A thesis submitted for the degree of
Doctor of Philosophy
School of Physics
Trinity College Dublin

2012

Declaration

I, Stephen Robert Power, hereby declare that this dissertation has not been submitted as an exercise for a degree at this or any other University.

It comprises work performed entirely by myself during the course of my Ph.D. studies at Trinity College Dublin. I was involved in a number of collaborations, and where it is appropriate my collaborators are acknowledged for their contributions.

A copy of this thesis may be lended or copied by the Trinity College Library upon request by a third party provided it spans single copies made for study purposes only, subject to normal conditions of acknowledgement.

Summary

Graphene is a two-dimensional carbon material that until its recent discovery was assumed not to exist in the free state. Graphene-related materials have been in the scientific limelight since then due to several key discoveries regarding their production and properties. There are numerous technological applications envisaged for them. Besides the huge potential for applicability, one key feature that makes graphene particularly popular is the simplicity with which many of its physical properties can be described, primarily due to the simple dispersion relation for its electrons. In this thesis a number of different topics relating to graphene systems, and in particular those doped with impurities, are investigated using a combination of analytical and numerical methods. We consider both graphene sheets and quasi-one-dimensional strips of graphene that are called 'nanoribbons'.

The electronic properties of materials can be engineered by doping, but in the case of graphene nanoribbons the introduction of two symmetry-breaking edges introduces an additional dependence on the location of an impurity across the width of the ribbon. This dependence has been noted previously in electronic transport calculations, but in this work we extend the discussion to the binding energy of the impurity and also to the magnetic moment that is formed if the impurity is magnetic. The results of simple model calculations are found to match those of more sophisticated *ab initio* calculations.

Magnetically-doped graphene systems are potential candidates for application in future spintronic devices. A key step is to understand the pairwise interactions that occur between magnetic impurities embedded in graphene

that are mediated by the graphene conduction electrons. In this thesis we examine interactions between such impurities using a Green function formalism. By developing an analytical expression for the Green function in graphene, we are able to explore the distance dependence of these interactions in a mathematically transparent fashion. We also demonstrate that *ab initio* calculations may yield spurious results if the effects of this interaction are neglected. The quick decay with separation of the interaction in graphene, reported by many authors, is often seen as a major obstacle for the spintronic application of these systems. However, in this work we report that a significant augmentation of the interaction is possible when the impurity moments are set to precess. An experimental setup to probe this dynamic form of the magnetic interaction in graphene is also suggested.

Acknowledgements

Over the last four years I have received an incalculable amount of support, assistance and encouragement from a number of sources, without which this thesis would not have been written.

Firstly, I'd like to thank Dr. Mauro Ferreira for his patient, enthusiastic and active supervision of the project. Mauro was always available to discuss any difficulty I stumbled across during my studies around his much overburdened whiteboard.

I would like to acknowledge the financial support this project received from the Irish Research Council for Science, Engineering and Technology under the EMBARK initiative and also from the School of Physics, Trinity College Dublin.

I'm grateful for the many fruitful collaborations I have had the opportunity to engage in. For their friendly, keen and lively participation in our shared projects I am indebted to Dr. Antonio Costa, Dr. Roberto Bechara Muniz, Dr. Filipe Guimarães, Dr. Pedro Venezuela, Dr. Solange Fagan, Dr. Stefan Hansel, Vivian de Menezes and Dr. Vojislav Krstic. I must give a special thanks to Filipe and Marina for their generous hospitality during my stays in Brazil. *Valeu!*

I am grateful to all my office colleagues over the years for providing such an enjoyable and productive working environment. In particular I would like to thank Drs. Andrew Wall, Claudia da Rocha, David Kirwan and Luiz Felipe Pereira - all former members of Mauro's group, for assistance during the earlier years of my studies. I would also like to thank Dr. Tom Archer for

the technical assistance that really wasn't his job, and the staff at TCHPC, who fixed anything Tom couldn't.

I am lucky to have made some excellent friends over the years, who provided marvellous company in the office, at lunch, at home in Tramore, in various apartments and houses we shared in Dublin, over drinks, on trips abroad, over a hand of bridge, up mountains, at sea, but most importantly, at tea. For the sake of brevity, and the fear of accidental omission, I can't thank them all by name. However, I would like to offer all of them my sincerest gratitude for their friendship, except Steve.[1]

On a personal note, I am especially thankful to my family for their unwavering support and belief over the years. For their continuing commitment to someone who still hasn't a real job, I thank my parents, Mike and Noeleen, and my sister, Corey. I would like to acknowledge and remember the kindnesses I received over many years from Ellen and Dick Butler and Joan and Phillip Corish. This thesis is dedicated to their memory.

Finally I'd like to thank Nuala for her love and friendship throughout. I'd say more but I promised not to embarrass her.

[1]This is a Steve-joke.

CONTENTS

List of peer-reviewed publications resulting from this work

- S. R. Power, V. M. de Menezes, S. B. Fagan, and M. S. Ferreira. Model of impurity segregation in graphene nanoribbons. *Physical Review B* **80**, 235424 (2009).
- P. Venezuela, R. B. Muniz, A. T. Costa, D. M. Edwards, S. R. Power, and M. S. Ferreira. Emergence of local magnetic moments in doped graphene-related materials. *Physical Review B* **80**, 241413 (2009).
- S. R. Power and M. S. Ferreira. Electronic structure of graphene beyond the linear dispersion regime. *Physical Review B* **83**, 155432 (2011).
- S. R. Power, V. M. de Menezes, S. B. Fagan, and M. S. Ferreira. Magnetization profile for impurities in graphene nanoribbons. *Physical Review B* **84**, 195431 (2011).
- S. R. Power, F. S. M. Guimarães, A. T. Costa, R. B. Muniz and M. S. Ferreira. Dynamic RKKY interaction in graphene. *submitted* (2011).

CHAPTER

ONE

Introduction

The historical narrative of technological evolution is inextricably entwined with the discovery and exploitation of carbon-based materials. Charcoal, an impure form of carbon obtained by burning wood in the absence of oxygen, was used by the ancient Egyptians and Sumerians for the reduction of metal ores in the manufacture of bronze [1]. The superlative physical and optical properties of diamonds have led to their use in a wide variety of fields - scientific, industrial and aesthetic. The immense chemical family of hydrocarbons, compounds made of carbon and hydrogen atoms, has long been plundered for the materials that compose the majority of man-made objects and for the energy that fuels modern life. Graphite, the most stable and common of the naturally forming carbon allotropes, is familiar to even schoolchildren as the "lead" in their pencils [2]. However, graphite has also a wealth of industrial applications, with end uses in high-temperature lubricants and fuel cells, amongst others [3]. The study of nanoscale carbon materials related to graphite has led to major advances in recent years and is predicted to beget many of the technologies of the future [4–8].

Graphite is composed of stacked layers of carbon atoms, with the atoms on each layer arranged in a hexagonal, or honeycomb, lattice. A single layer of carbon atoms arranged in this way is called *graphene*. The hexagonal lattice can also be interpreted as two intersecting triangular sublattices. A

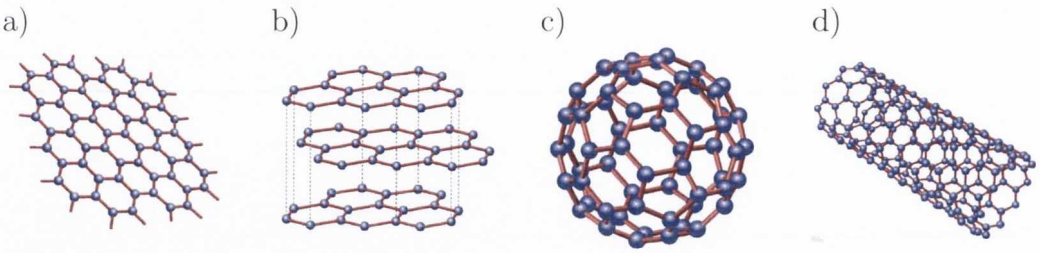

Figure 1.1: a) A single graphene sheet is the building block for a number of related materials, including b) graphite stacks, c) fullerenes and d) carbon nanotubes. Figure adapted from Ref. [9].

unit cell containing two neighbouring atoms, one from each sublattice, can by translation generate the entire graphene lattice. The individual graphene layers in a graphite stack are held together by weak van der Waals forces, which allows them to separate with relative ease. It is this process that occurs everytime a pencil is used. A single layer of graphene can be thought of as the building block for not just graphite, but for a number of other related materials as shown in Fig. 1.1. Spherical molecules of carbon atoms, called fullerenes, can be obtained from a graphene by introducing pentagons into the lattice which create curvature effects. These quasi-zero-dimensional objects were discovered in 1985 [10] and heralded in a new era of carbon-based nanoscience. Six years later, the discovery [11] (or possibly rediscovery [12, 13]) of cylindrical fullerenes, dubbed carbon nanotubes, marked another exciting breakthrough in the field. They can be thought of as sheets of graphene that have been "rolled up" along a particular direction. These quasi-one-dimensional systems displayed an unexpected array of fascinating and potentially useful physical and electronic properties [8, 14]. Apart from their extraordinary strength and stiffness [8], nanotubes also display sensitive and tunable electronic properties [8, 14, 15]. Nanotubes can be either metallic or semiconducting, depending on the direction in which they are rolled up. Importantly, metallic nanotubes are stable against the Peierls distortion [15], which usually destroys metallicity in one-dimensional systems and they have been shown experimentally to behave as ballistic conductors [16].

Despite the many successes in synthesising and investigating the proper-

ties of these graphene-based materials, graphene itself was not isolated until 2004 [17, 18]. Before this, graphene was not even predicted to exist in the free state [4, 19, 20], even though it is possible that small quantities of it are produced every time a pencil is used. We will now summarise the discovery and production of graphene samples before discussing some of the many interesting properties it possesses. The doping of graphene with impurity atoms and its potential for application in spintronics will be introduced as a means of broaching the topics investigated in this thesis. The topics of magnetic interaction and spin dynamics will be introduced to provide context and motivation for the remainder of the thesis. A quick summary of the research in the thesis is then given.

1.1 Graphene : discovery and properties

The first monolayers of graphene large enough to be studied using conventional techniques were produced in 2004 by the so-called "Scotch-tape" method [17]. This technique, also known as micromechanical cleavage, involves removing the top layer of a high-quality graphite crystal using adhesive tape and then transferring it onto a substrate. Amazingly, despite the simplicity of the procedure, extremely high quality graphene crystals can be produced, as shown in Fig. 1.2. Since then graphene samples have been produced using other methods also, for example, chemical exfoliation by dispersion in organic solvents [21, 22].

The experimental and theoretical interest in graphene has increased dramatically since its discovery. An abundance of interesting and unique physical properties have been postulated and probed. A wide range of possible applications have been suggested. Its discoverers have been acknowledged for their identification and subsequent investigations into the properties of graphene with the 2010 Nobel Prize for Physics [7,23]. Besides being the first two-dimensional atomic crystal, graphene is also the thinnest and strongest material ever obtained, with a breaking strength 200 times greater than steel [7, 24]. It is found to be an extremely effective electrical [25] and thermal [26] conductor. Graphene has extraordinary elastic properties, and can

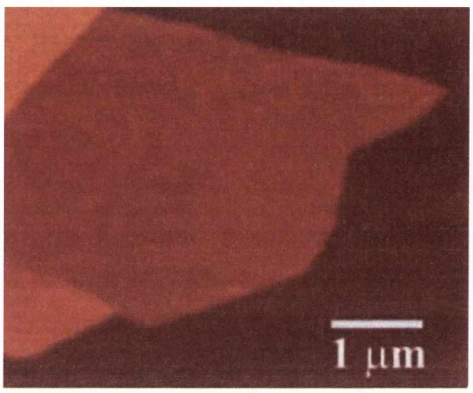

Figure 1.2: An atom force microscopy (AFM) image of graphene on a SiO_2 surface. The dark brown background is the SiO_2 surface whilst the other regions consist of graphene flakes of varying thickness. The large brown-red central region has height 0.8nm and the lighter regions are slightly thicker. This figure is taken from Ref. [17].

be stretched by more than 20%, which is more than any other crystal [24]. Furthermore, for such a thin material it is impermeable to molecules and gases [27]. However, it is perhaps the electronic properties of graphene that have garnered the most attention and have been the subject of the most studies since its discovery [6]. Despite its relatively recent discovery, much of the electronic theory of graphene had been formulated long before [28–30] and used as the starting point for calculating the electronic properties of graphite and later, carbon nanotubes [14,15]. Graphene is found to be a zero-bandgap semi-metal whose valence and conduction bands touch at two discrete points of the Brillouin zone, labelled the K points or Dirac points. In Chapter 3 we will explore this calculation in more detail, but in brief the p_z orbitals from the carbon atoms in the lattice hybridise to form π and π^* bands which cross at the K points. The electronic band structure of graphene for energies near the Fermi energy, where these bands cross, is found to be linear. This is in contrast to the more standard parabolic bands found in other materials. As a consequence of the linear bands, electrons at these energies lose their effective mass and behave more like relativistic particles than normal electrons. Their behaviour can even be described using a Dirac-like equation instead of the standard Schroedinger equation, and in fact the behaviour of these elec-

trons mimics the physics of quantum electrodynamics (QED) for massless fermions [5, 6, 18]. As such, graphene can be used to test some of the predictions of QED in a simpler laboratory environment than would be feasible for truly relativistic systems. An example of this kind of behaviour is Klein tunnelling [31], where a relativistic particle has an enhanced tunnelling probability through a potential barrier, due to a suppression of backscattering, that even approaches unity for completely massless particles. Such behaviour has been described theoretically [32] and observed experimentally [33, 34] for Dirac fermions in graphene. Another consequence of the massless nature of the electrons in graphene is that they can propagate without scattering over large distances and this has been confirmed experimentally at the micrometer scale [17]. Graphene also presents a different quantum Hall response to that of other systems. The presence of a quantised level at zero energy that is shared by electrons and holes gives rise to an anomalous sequence of "half-integer" Landau levels and hence Hall conductance plateaus [18, 35]. Due to the high Fermi velocity, the separation between the zeroth and first Landau levels is unusually large, making it possible to observe the quantum Hall effect even at room temperatures [36].

1.2 Graphene-based materials

The exploration and analysis has not just been confined to simple graphene sheets. A number of other materials related to or composed from graphene have been postulated and examined. Multilayer sheets of graphene, not thick enough to be considered "graphite" or to display its physical properties, but yet fundamentally different to monolayers have been investigated. Systems with two (graphene bilayers) or more layers of graphene are found to have a wealth of properties that depend not only on the number of layers but also on the order of their stacking [37, 38]. Apart from stacking graphene layers, new materials can be formed from a single graphene sheet by "cutting" a narrow strip from it to form a quasi-one-dimensional object called a *graphene nanoribbon*. Their dimensionality suggests a comparison with the previous mentioned carbon nanotubes. Much in the same way that the prop-

erties of nanotubes depended on the rolling direction and circumference of the tube, the properties of ribbons depend strongly on their edge geometry and width [39–44]. Experimentally, graphene nanoribbons can be produced in a number of ways, including lithography [45, 46], etching [47], bottom-up chemical methods [48] or even by "unzipping" carbon nanotubes [49] as shown schematically in Fig. 1.3. Two principle nanoribbon edge geometries, armchair and zigzag, are generally studied and are found to have radically different electronic properties. Zigzag edges in particular are unusual in that they can sustain localised edge states, which give rise to a range of properties not seen in armchair-edged ribbons or in graphene sheets [40–42]. The formation of localised states near the Fermi energy may lead to spin-polarised edge states when electron-electron interactions are taken into account. Although some signatures of these edge states have been found experimentally [50], there are concerns about their stability and any resulting magnetic properties are not predicted to be particularly robust under the introduction of edge disorder [51]. Unlike nanotubes which can be either metallic or semiconducting, nanoribbons are predicted to always be semiconducting [52] due to electron-electron interactions or edge deformations which destroy the metallicity that simple models predict. However there was still a large discrepancy between experimentally measured bandgaps [53–55] and those predicted by theory. The theory that emerged is that this discrepancy arose from the difficulty in achieving pristine edges experimentally. Extended edge defects in

Figure 1.3: "Unzipping" a carbon nanotube to form a graphene nanoribbon. This figure is adapted from Ref. [49].

the form of vacancies or other deformations were investigated by a number of authors [56–64] and a broad consensus from these studies is that the presence of edge-disorder induces Anderson-type localisation [65–67] in the ribbons, causing the suppression of conductive paths through the ribbons for certain energies.

1.3 Impurities in graphene

The edge disorder that was investigated in the studies mentioned above arises due to the difficulties in engineering atomically precise edges for the ribbons. However, the deliberate introduction of disorder into graphene systems, either in the form of vacancies or impurity atoms, is another subject that has received much attention in the literature, particularly in the fields of transport and magnetism [68–75]. This is because the doping of a material can be an effective way to tailor or tune its properties. However there is a crucial difference between the case of a graphene sheet and that of a nanoribbon. This is the existence of two symmetry-breaking edges, which are expected to make some of the physical properties of the nanoribbon dependent on the impurity position. This dependence has been noted in a number of studies which examined the conductance through a nanoribbon system when the impurity location or distribution was varied [56, 57, 70–72, 75]. Another aspect that is often overlooked is that a similar dependence should arise also in other properties of the system, for example, in the energetics of the doping process. In other words, the binding energy of a dopant should depend on its location across the width of a ribbon. Bearing in mind that impurity segregation is known to occur at symmetry-breaking interfaces between two materials due to quantum interference effects [76, 77], it should come as no surprise that the edges of a nanoribbon are capable of inducing similar segregational features in the impurity distribution. What is surprising in the case of nanoribbons is that the segregation may be controllable by external factors, which opens the possibility of manipulating the impurity distribution within a ribbon and hence engineering some of the related physical properties of the ribbon. This topic is studied in some detail in Chapter 4.

1.4 Graphene applications

1.4.1 General application

Due to the multitude of interesting physical and electronic properties that graphene has been found to exhibit, a large number of possible technological applications have been proposed [4–7]. As an immensely strong material, graphene seems ideally positioned for application as a reinforcement in high-performance composites [78]. Here its thinness is also a great advantage as it cannot cleave, thus giving it the maximum possible strength in the out-of-plane direction. Another advantage is that the strain in a graphene sample can be monitored using its Raman spectrum [79–81], which allows mechanical distortions of even a fraction of a percent to be detected. Much of the current interest in graphene focuses on its potential application in computer electronics. Promising results for graphene field effect transistors suggest that these devices may be suitable for high-frequency applications [17,82,83]. Graphene-based integrated circuits are however more troublesome. These require the conducting channel to be completely closed in the off state, which is difficult to achieve with the gapless spectrum found in graphene. However, as discussed previously, bandgaps are present in nanoribbons and indeed nanoribbon transistors with large on/off ratios have been demonstrated [54, 55, 84]. Graphene has also been suggested as a support material for transmission electron microscopy (TEM) where its thinness, strength and low atomic mass offer benefits such as rigidity and high contrast when examining biological or other samples [85, 86]. Graphene has also emerged as a viable candidate in the field of optoelectronics and graphene coatings have been suggested for use in products like solar cells and LCD displays [87–89]. However the resistivity found in graphene films with the required transparency is to date much higher than that of the industry standard, indium tin oxide (ITO). If the resistivity can be reduced sufficiently, graphene coatings could offer advantages like flexibility to such products.

1.4.2 Spintronics

Another field where graphene-based materials have been mooted for application is in the field of spintronics [90]. This field is projected to play a major role in the evolution of the electronic industry as it allows information storage, processing and communication at faster speeds and with lower energy consumption than is currently possible with conventional electronics [91–94]. The principal idea of spintronics is to exploit not only the charge of an electron, but also the spin degree of freedom associated with its intrinsic angular momentum. Currently, all the magnetic materials used for modern technology belong to either the d or f-blocks of the periodic table. Despite the wide range of diverse structures that carbon is able to form, it is not in itself magnetic. However, graphene-based spintronics may be achievable when we consider that many of its derivative materials and nanostructures display various scenarios of magnetism [90] and also that graphene has many properties that suggest its possible use as a carrier of spin information. These include weak spin-orbit and hyperfine couplings which are the main sources of relaxation and decoherence of electron spin [95–101].

Many of the proposed graphene-based spintronic devices are underpinned by the spin-polarised edge states, mentioned above, that are predicted to occur when a graphene sheet is cut to have a zigzag edge geometry. Particular focus has been paid to zigzag-edged graphene nanoribbons, with parallel zigzag edges that are predicted to display opposite spin orientations as shown in Fig. 1.4 a). Such a system may allow a possibility of tuning its spin-transport properties [39–42, 102, 103]. For example, the prospect of triggering a half-metallic[1] state using external electric fields in zigzag-edged nanoribbons has been suggested [41]. The realisation of such a device would allow efficient electronic control of spin transport, a very useful property in spintronics and something that is difficult to achieve in other materials. Despite theoretical advances in the study of nanoribbons, experimental verification of their properties has so far been inconclusive, due in part to the difficulty in patterning the edge geometries required for these effects to be observed.

[1]This means the system is metallic only for electrons of one spin orientation.

a) b)

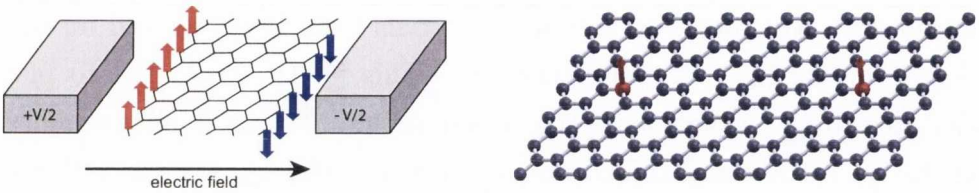

Figure 1.4: a) Schematic adapted from Ref. [90] showing the possible setup of achieving half-metallicity in a zigzag edged graphene nanoribbon using external electric fields, as suggested by Ref. [41] b) Two magnetic impurity moments embedded in a graphene sheet. Understanding the interaction between moments in such a setup is necessary if magnetically-doped graphene systems are to be used in future spintronic devices. Of particular interest in this thesis is how the range of the interaction varies if one of the moments is set to precess.

Furthermore, the spin-polarised edge state for zigzag edges is predicted to be highly dependent on the edge geometry and not particularly robust under the introduction of edge disorder [51]. These factors present major obstacles in the path of utilising the intrinsic magnetic edge states of graphene in experimentally realisable devices. In Chapter 4 we consider the features of nanoribbons doped with magnetic impurities. The position dependence of the resulting magnetic moments is considered in a similar fashion to the energetics previously mentioned. However, we also find that the magnetic properties of such systems are robust under the introduction of edge disorder and argue that magnetically doped nanoribbons may provide an alternative route to applications previously envisaged for nanoribbons with intrinsic magnetic ordering.

Another possibility that has been proposed for graphene-based spintronics is the exploitation of defect-driven magnetic moments that arise in graphene [73, 74]. Magnetic moments have been predicted to form around vacancies and other defects in the graphene lattice and the possibility of engineering a ferromagnetic state in graphene from such moments has been suggested. However, such a claim would seem to be restricted by the implications of the

Lieb theorem [104], which states that any such magnetic moments arise from a disparity between the two sublattices of graphene. Large-scale, randomised disorder would tend to minimise such a disparity and prevent the formation of a ferromagnetic state. However, recent experimental evidence suggests the possibly of engineering such a state through partial hydrogenation [105]. The existence of such a state may then be accessible through magnetoresistance measurements [106].

A third possibility for incorporating graphene in spintronic devices, and one that we shall focus on in this work, is through the doping of graphene with magnetic impurity atoms, as shown in Fig. 1.4 b). We have already touched on this topic above for the case of nanoribbons. This approach takes advantage of the indirect exchange coupling [107–110], often referred to as the Ruderman-Kittel-Kasuya-Yosida (RKKY) interaction [111–115], between magnetic impurities in a graphene system which is mediated by the conduction electrons of the graphene host. A long-ranged interaction of this type allows impurity moments on graphene to feel each other's presence and respond to magnetic perturbations or excitations at other impurity sites. The usual manifestation of this interaction is through the lowering of the total energy of the system when the moments adopt certain favourable alignments. In this way the interaction can dictate any magnetic ordering that arises between the moments. Studies in carbon nanotubes have found the presence of a long-ranged interaction whose amplitude decays as D^{-1}, where D is the distance between the magnetic impurities [116]. Unique features arising from the peculiar electronic structure of graphene were also found that affected the sign of the interaction and its decay rate for certain impurity configurations [117–119]. Signatures of a magnetic interaction between impurities in carbon nanotubes have also been detected experimentally [120]. Whilst the studies to date of the interaction in carbon nanotubes have been promising, the outlook is less clear in the case of graphene sheets. A large number of studies [121–133] have been performed, with the consensus that the interaction decays at least as fast as D^{-3} for undoped graphene. In Chapter 5, the indirect exchange coupling in graphene is examined in detail and we examine the effects it can have in *ab initio* calculations that use periodic boundary

conditions. Regarding spintronic application, it seems that a decay rate this fast would limit the prospects for devices consisting of magnetically-doped graphene systems.

It has been suggested that the range of RKKY-like interactions can be augmented if the magnetic moments are set in motion, for example, if they are set to precess by the application of a suitable time-dependent magnetic field [134,135]. Such an interaction is driven by non-equilibrium spin currents emanating from the precessing moments. The magnitude of the interaction can be measured by a quantity called the dynamic spin susceptibility, which describes the response of the magnetism of the system to a dynamic magnetic perturbation. Investigation of this quantity in carbon nanotubes [136] has revealed a decay rate slower than that of the static coupling. Further studies of spin dynamics in graphene systems have suggested the use of these materials as spin waveguides [137], spin-pumping transistors [138] and spin current lenses [139]. These reports, together with recent experimental evidence suggesting possible long-range spin current behaviour in graphene [140], motivate a comprehensive study of the dynamic magnetic interaction in graphene within a fully quantum-mechanical framework. In Chapter 6, we examine the spin susceptibility in graphene as a dynamic analogue of the static RKKY coupling, with a particular focus on the separation dependence of the interaction. We find an augmentation of the interaction range that suggests magnetically-doped graphene systems may be suitable for spintronic application when spin dynamics is taken into account. Furthermore, by relating the dynamic interaction studied to the lifetimes of magnetic excitations, measurements of which are currently achievable using inelastic scanning tunnelling spectroscopy [141–144], we suggest how this interaction may be probed experimentally.

1.5 Thesis Layout

This thesis uses a combination of analytical and computational methods to study many of the topics discussed above. It is organised as follows:

- Chapter 2 introduces the bulk of the methods to be used throughout the thesis. In particular, the calculation and manipulation of Green functions is discussed. These quantities underpin the majority of the calculations performed. A brief introduction is also given to electron-electron interactions as accounted for using the Hubbard model and Hartree-Fock approximation. The methods discussed in this chapter are not specific to graphene and a broad overview of their general usage is given.

- The electronic band structure of graphene, calculated using the nearest-neighbour tight-binding approximation, is discussed in Chapter 3. The difficulties involved in calculating the corresponding Green function matrix elements for graphene sheets are mentioned. An original approach to performing the necessary integrals analytically using certain approximations is presented. The results of this method are shown to be in excellent agreement with numerically calculated results. Finally the recursive method used to calculate the Green functions for nanoribbon systems is demonstrated.

- Chapter 4 focuses on graphene nanoribbons, and in particular on how their physical properties depend on the location of an introduced impurity. A discussion of previous studies examining the conductance in such systems is illustrated with a simple model of our own. This is followed with an analysis of our results for how the binding energies and magnetic moments of impurities depend on their location. Comparisons are made between simple model and full *ab initio* calculations and a range of ribbon geometries and impurity configurations are considered. The possible applications of these results are discussed for both the energy and magnetic moment calculations.

- The static magnetic interaction between impurity atoms embedded in graphene is considered in Chapter 5. Different approaches to calculating the coupling are introduced and compared. The Green functions derived in Chapter 3 are applied to determine the separation depen-

dence of the interaction and this is compared with results from previous studies. By treating the interaction in a more complete fashion, we find effects that are not predicted by the standard approach and discuss some of the possible implications of these. Finally, we show the effect that the magnetic interaction can have on *ab initio* calculations using periodic boundary conditions. Failing to account for these effects can lead to the spurious suppression of magnetic moments.

- Chapter 6 extends the discussion of the magnetic interaction between impurities in graphene to the case of precessing moments. The spin susceptibility formalism is introduced and a dynamic analogue of the RKKY interaction is suggested. The distance dependence of such an interaction is examined thoroughly using analytical and numerical methods. The range of the interaction is found to increase significantly in the dynamic case. The interaction studied is related to the lifetimes of magnetic excitations in such systems, and a possible experimental setup to probe the decay of the interaction is suggested.

- The results and conclusions of the thesis are summarised in Chapter 7, where possible extensions of the work are also discussed.

CHAPTER

TWO

Mathematical methods

2.1 Introduction

This chapter will introduce the majority of the mathematical methods that will be used throughout the thesis. Most of the techniques that will be discussed are underpinned by a quantity called the *Green function* [145] and the majority of the chapter deals with calculations involving these functions. The final section of the chapter features a discussion on the Hubbard model which is used in later chapters to model systems with magnetic moments.

2.2 Green Functions

Fundamentally, Green functions are solutions to differential equations that are used to relate a response function to a source term. Within the realm of condensed matter physics, the differential equation in question is almost always the Schroedinger equation, which describes the quantum states of system of interest. The Green function acts as a correlation function that relates the response of this system to a perturbation. For this reason, they are useful in calculating the properties of disordered systems. Green functions also describe the propagation of electrons in conducting systems and are thus commonly utilised in transport calculations also. As we shall see below, the

Green function is also intrinsically linked to the density of states (DOS), a fundamental quantity used to describe the electronic structure of a system in solid state physics.

The Green function corresponding to the Schrodinger equation is defined as

$$\hat{g} = \lim_{\eta \to 0} \left[(E \pm i\eta)\hat{I} - \hat{\mathcal{H}} \right]^{-1}, \tag{2.1}$$

where $\hat{\mathcal{H}}$ is the Hamiltonian describing the system, $\hat{I}$ is the identity operator and E is the energy. η is a small, positive imaginary part added to the energy to ensure that the Green function is well defined around the eigenvalues of the Hamiltonian. The limit can be taken with + or a −, corresponding to the cases of the *retarded* and *advanced* Green functions respectively. The retarded Green function describes propagation away from the site of the perturbation, whereas the advanced Green function describes propagation towards it. In this work, the term 'Green function' will generally refer to the retarded case, however the distinction only becomes important later when we consider transport or spin dynamic calculations where both types are needed. It is important to note that at this stage the form of the Hamiltonian used to describe the system has not yet been specified. The discussion to date has been general, however the Green function operator will depend on the form of $\mathcal{H}$, which depending on the level of complexity required can be a free electron, tight-binding or more complete *ab initio* Hamiltonian. In the next chapter, we shall introduce the tight-binding Hamiltonian that is sufficient to describe the electronic properties of graphene and which will be used throughout the rest of this thesis. Consequently, the results of this chapter will be shown for Hamiltonians expressed in terms of linear combinations of atomic orbitals (LCAO).

Relation to the Density of States

The Density of States (DOS) is an important quantity in Solid State Physics. It describes the number of energy states (per energy interval) that are available to be occupied at a particular energy. One of the major advantages of working within the Green function formalism is the ease with which the DOS

can be calculated. To begin with, if $\hat{\mathcal{H}}$ has eigenvalues ϵ_a and eigenstates $|\Psi_a\rangle$ then we can write

$$\mathcal{H} = \sum_a |\Psi_a\rangle \epsilon_a \langle \Psi_a| \,. \tag{2.2}$$

Substituting this into the definition of the Green function, Eq. (2.1), yields

$$\hat{g} = \lim_{\eta \to 0} \sum_a |\Psi_a\rangle \frac{1}{E + i\eta - \epsilon_a} \langle \Psi_a| \,. \tag{2.3}$$

Assuming a LCAO-type Hamiltonian, we can describe $\mathcal{H}$ by a basis of localised orbitals $|j\rangle$, centered on site j. Projecting onto orbitals $|j\rangle$ and $|l\rangle$ gives

$$g_{jl} \equiv \langle j|\hat{g}|l\rangle = \lim_{\eta \to \infty} \sum_a \langle j|\Psi_a\rangle \frac{1}{E + i\eta - \epsilon_a} \langle \Psi_a|l\rangle \,. \tag{2.4}$$

Multiplying above and below by $(E - i\eta - \epsilon_a)$ gives

$$g_{jl} = \lim_{\eta \to 0} \sum_a \langle j|\Psi_a\rangle \frac{E - i\eta - \epsilon_a}{(E - \epsilon_a)^2 + \eta^2} \langle \Psi_a|l\rangle \,, \tag{2.5}$$

the imaginary part of which is given by

$$\mathrm{Im}(g_{jl}) = \lim_{\eta \to 0} \sum_a \langle j|\Psi_a\rangle \frac{-\eta}{(E - \epsilon_a)^2 + \eta^2} \langle \Psi_a|l\rangle \,. \tag{2.6}$$

Setting $l = j$ and availing of the definition of the Dirac Delta function

$$\delta(x) = \frac{1}{\pi} \lim_{a \to 0} \frac{a}{x^2 + a^2} \,, \tag{2.7}$$

allows us to write

$$-\frac{1}{\pi} \mathrm{Im}(g_{jj}) = \sum_a |\langle j|\Psi_a\rangle|^2 \delta(E - \epsilon_a) \,. \tag{2.8}$$

However, this is exactly the definition of the Local Density Of States (LDOS) at site j, $\rho_j(E)$. This is a very useful quantity that can be used to calculate physical quantities like the occupation number and energy changes. Summing over all sites in the system results in the total density of states. Alternatively,

this can be written as a trace over the Green function matrix:

$$\rho_{total}(E) = \sum_j \rho_j(E) = -\frac{1}{\pi}\text{Im Tr}\,(\hat{g})\,. \tag{2.9}$$

2.3 The Dyson Equation

As we have seen above, the DOS of a system under investigation is very closely linked to the Green function describing the system. However, in the derivation above we have assumed knowledge of the eigenstates of the system, $|\Psi_a\rangle$. If the system displays translational invariance then the eigenvectors can be calculated using Bloch's Theorem, as we shall demonstrate for the case of graphene in the following chapter. However when translational invariance is broken, for example by the introduction of an impurity, then the Bloch wavevectors are no longer eigenvectors of the system. It is in situations like this that the power of the Green function approach is fully revealed. The Dyson equation allows us to write the Green function of the perturbed system in terms of the Green function of the unperturbed system and the applied perturbation, without the need to calculate the eigenvectors of the perturbed system. This process allows for easy calculation of the relevant physical properties, such as the DOS, of the perturbed system.

2.3.1 Derivation

The Dyson equation can be derived quite easily from the definition of the Green function in Eq. (2.1). If $\hat{G}$ is the Green function associated with a Hamiltonian $\hat{\mathcal{H}} = \hat{\mathcal{H}}_0 + \hat{V}$, where $\hat{V}$ is a perturbation potential, then we can write it in terms of the Green function $\hat{g}$ associated with the unperturbed Hamiltonian $\hat{\mathcal{H}}_0$ as follows:

$$\begin{aligned}\hat{G} &= \left[(E+i\eta)\hat{I} - (\hat{\mathcal{H}}_0 + \hat{V})\right]^{-1} \\ &= \left[\hat{g}^{-1} - \hat{V}\right]^{-1} \\ &= \left[\hat{I} - \hat{g}\hat{V}\right]^{-1}\hat{g}\,.\end{aligned}$$

Multiplying across from the left by $\left[\hat{I} - \hat{g}\hat{V}\right]^{-1}$ results in the Dyson equation in its usual form

$$\hat{G} = \hat{g} + \hat{g}\hat{V}\hat{G}\,. \tag{2.10}$$

Another common form of the Dyson equation is in terms of the $\hat{T}$-matrix, defined as

$$\hat{T} = \hat{V}\left[\hat{I} - \hat{g}\hat{V}\right]^{-1} \tag{2.11}$$

which allows us to write

$$\hat{G} = \hat{g} + \hat{g}\hat{T}\hat{g}\,. \tag{2.12}$$

This form of the equation is often preferable as it collects all the contributions from the perturbation into one term, namely $\hat{T}$, which describes the scattering caused by the introduced perturbation.

Now that the Dyson equation has been introduced, we shall demonstrate its usefulness with a few examples. The primary use we will find for the Dyson equation is for investigating the properties of perturbed systems when those of the unperturbed system are known or can be easily calculated. Within this work this will usually consist of introducing an impurity atom into a graphene system and investigating how the properties of the system change. However, the Dyson equation can also be used to connect two larger systems and when applied recursively, can be used to build up a large system from many small parts.

2.4 Perturbations and Disorder

Within the tight-binding Hamiltonians that we will use throughout this work, the majority of the perturbations encountered will consist of changes to either the on-site energy terms or the hopping potentials connecting atomic orbitals in a lattice, or to both. Perturbations of these kinds can be used to represent substitutional or adsorbed impurities introduced into the host system, as we shall demonstrate explicitly below. The change in the on-site energy term represents the fact that the relevant energy orbital on the impurity atom will differ from that of the orbitals on the graphene host. Similarly the hopping

parameters which account for the overlap between orbitals on neighbouring sites will vary depending on whether the sites contain two carbon atoms, or one carbon and one impurity atom. We will now demonstrate how the Green functions for the cases of a single substitutional atom and a single adsorbed atom (adatom) attached to host can be calculated. In the examples below, the host system is represented by a simple linear atomic chain.

2.4.1 Substitutional Atom

The simplest type of impurity involves replacing a carbon atom in the lattice with an atom of another element. To model such an impurity we need to change the onsite energy term(s) describing the relevant orbital(s) at this lattice site, and also the hopping parameters describing the overlap between these orbitals and those on the neighbouring carbon atoms. In the simplest possible case, we can consider only a single orbital on the impurity atom and neglect changes to the hopping parameters. In this case, the perturbing potential is written

$$\hat{V} = |n\rangle \delta_n \langle n| \,, \tag{2.13}$$

where n labels the perturbation site and $\delta_n = \epsilon_n - \epsilon_0$, the difference between the onsite energies of the impurity atom and the lattice atom it replaced. For the simple case we are considering here, many of the quantities involved are simply scalars. When extending the results here to more complicated models care must be taken as these now become matrices. To calculate a general matrix element, G_{ij}, of the Green function for the perturbed system we apply the Dyson equation to the unperturbed Green function and this potential as follows

$$G_{ij} = g_{ij} + g_{in}\delta_n G_{nj} \,, \tag{2.14}$$

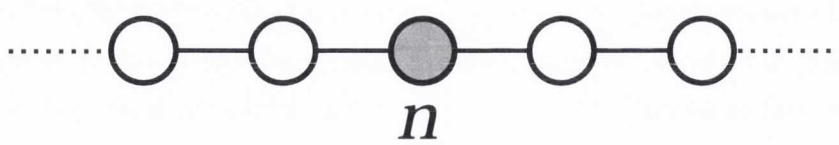

Figure 2.1: A substitutional impurity at site n is modelled by a shift in the onsite energy at this site

and then apply it again to the term G_{nj}

$$\begin{aligned} G_{nj} &= g_{nj} + g_{nn}\delta_n G_{nj} \\ &= \frac{g_{nj}}{1 - g_{nn}\delta_n} . \end{aligned}$$

Substituting this expression for G_{nj} back into (2.14) yields

$$\begin{aligned} G_{ij} &= g_{ij} + \frac{g_{in}\delta_n g_{nj}}{1 - g_{nn}\delta_n} \\ &= g_{ij} + g_{in}T_{nn}g_{nj} , \end{aligned} \tag{2.15}$$

where

$$T_{nn} = \frac{\delta_n}{1 - g_{nn}\delta_n} \tag{2.16}$$

is the $\hat{T}$-matrix element describing the scattering caused by the perturbation. For this simple perturbation it is the only non-zero term in the $\hat{T}$-matrix given by Eq. (2.11). Examining the form of G_{ij} in more detail gives an insight into the physical meaning of the expression. Recall that this term is describing electron propagation between lattice sites i and j. The final form of the expression consists of two terms, which can be thought of as the summation of propagation along two different paths. The first of these, g_{ij} obviously corresponds to direct propagation between sites i and j without any contribution from the introduced perturbation and is identical to propagation in the pristine system. The other term, $g_{in}T_{nn}g_{nj}$, corresponds to indirect propagation between i and j via the perturbation site n, where the scattering that occurs at this site introduces a factor of T_{nn}.

If we want to investigate the LDOS at the impurity site the quantity of interest to us is the diagonal element of the Green function at that site, which we find by setting $i = j = n$ in Eq. (2.15). Simplifying the resulting expression gives

$$G_{nn} = \frac{g_{nn}}{1 - g_{nn}\delta_n} .$$

However, we can also investigate properties of the system *away* from the site of the impurity. Supposing we are interested in a site $i \neq n$, we can calculate

the Green function at this site by setting $i = j \neq n$ and we find

$$G_{ii} = g_{ii} + \frac{g_{in}\delta_{nn}g_{ni}}{1 - g_{nn}\delta_n}.$$

In these derivations the importance of the *off-diagonal* matrix elements of the Green function - terms of the form g_{in} and G_{ni} - is noted. These terms act as correlation functions between the different sites of the lattice, and are used to calculate the response of a system at one point to a perturbation elsewhere. We will come across these terms repeatedly throughout this work, and they underpin many of the results in the upcoming chapters. In the next chapter we shall examine in detail the functional form of these terms in a graphene lattice in order to predict the distance dependence of interactions mediated by the conduction electrons of graphene.

2.4.2 Adsorbed Atom

In this section another type of impurity will be discussed. This is an adsorbed atom, or *adatom*, and occurs when an impurity species bonds to atoms within the host lattice, rather than replacing one, as was previously seen with substitutional impurities. For simplicity, we again consider only a single atomic orbital on the impurity atom, although a generalisation to a multi-orbital atom follows an identical procedure to that outlined below. We label the relevant orbital on the impurity atom α and assume for simplicity that it connects to a single site n on the host material. That is, the

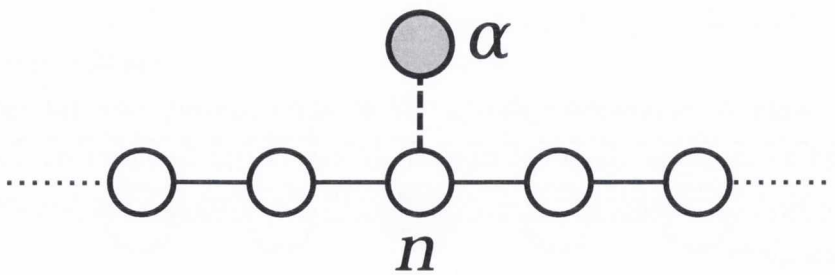

Figure 2.2: An adsorbed atom impurity is modelled using a perturbation potential to connect an orbital on the impurity atom, α, with one located at site n on the host system.

only nonzero hopping parameters between the host and the impurity atom are those connecting sites α and n. Before the impurity is introduced, we consider a pristine host material with a Green function matrix g_{ij} where i and j run over all the orbital sites of the system. We also consider the Green function relating to the impurity atom, $g_{\alpha\alpha}$, which disconnected from the rest of the system is simply a scalar. From Eq. (2.1), we find

$$g_{\alpha\alpha}(E) = \frac{1}{E + i\eta - \epsilon_\alpha}, \tag{2.17}$$

where ϵ_α is the onsite energy of the impurity.

This type of impurity is different to the substitutional case in that the Dyson equation will be used to *connect* two parts of the system which were previously separate. This is perhaps one of the simplest cases in which the Dyson equation connects two systems, but more complex cases shall be examined shortly when recursive methods are considered in Section 2.5. Here, the perturbation potential that is applied does not alter the onsite potentials at any of the lattice sites, but rather 'turns on' a connecting potential between them. This is achieved by changing the relevant off-diagonal matrix elements of the Hamiltonian from zero. For a single adatom, the perturbing potential is given by

$$\hat{V} = |n\rangle V_{n\alpha} \langle\alpha| + |\alpha\rangle V_{\alpha n} \langle n| \,. \tag{2.18}$$

Note that the two terms are complex conjugates of each other ($V_{n\alpha} = V_{\alpha n} \in \mathbb{R}$), which ensures that the Hamiltonian describing the perturbed system is hermitian. In matrix form, the disconnected Green function for the entire

system, and the perturbing potential are

$$\hat{g} = \left(\begin{array}{ccccc|c} g_{11} & \cdots & g_{1n} & \cdots & g_{1N} & 0 \\ \vdots & \ddots & \vdots & & \vdots & \vdots \\ g_{n1} & \cdots & g_{nn} & \cdots & g_{nN} & 0 \\ \vdots & & \vdots & \ddots & \vdots & \vdots \\ g_{N1} & \cdots & g_{Nn} & \cdots & g_{NN} & 0 \\ \hline 0 & \cdots & 0 & \cdots & 0 & g_{\alpha\alpha} \end{array}\right)$$

and

$$\hat{V} = \left(\begin{array}{ccccc|c} 0 & \cdots & 0 & \cdots & 0 & 0 \\ \vdots & \ddots & \vdots & & \vdots & \vdots \\ 0 & \cdots & 0 & \cdots & 0 & V_{n\alpha} \\ \vdots & & \vdots & \ddots & \vdots & \vdots \\ 0 & \cdots & 0 & \cdots & 0 & 0 \\ \hline 0 & \cdots & V_{\alpha n} & \cdots & 0 & 0 \end{array}\right) .$$

Applying the Dyson equation, we find

$$G_{ij} = g_{ij} + g_{in}V_{n\alpha}G_{\alpha j} + g_{i\alpha}V_{\alpha n}G_{nj} .$$

We note that if $i = \alpha$, the term $g_{in}V_{n\alpha}G_{\alpha j}$ vanishes since $g_{\alpha n} = 0$ for the disconnected system. Similarly, if $i \neq \alpha$ the term $g_{i\alpha}V_{\alpha n}G_{nj}$ vanishes for similar reasons. Thus for any Green function element we want to calculate we need only consider one of these terms.

The Green function between two sites on the host lattice after the impurity atom is connected, corresponding to $i, j \neq \alpha$, is given by

$$G_{ij} = g_{ij} + g_{in}V_{n\alpha}G_{\alpha j} ,$$

where using the usual approach we also find

$$G_{\alpha j} = g_{\alpha\alpha}V_{\alpha n}G_{nj} \qquad \text{and} \qquad G_{nj} = g_{nj} + g_{nn}V_{n\alpha}G_{\alpha j} ,$$

yielding

$$G_{\alpha j} = \frac{g_{\alpha\alpha}\, V_{\alpha n}\, g_{nj}}{1 - g_{\alpha\alpha}\, V_{\alpha n}\, g_{nn}\, V_{n\alpha}}$$

and

$$G_{ij} = g_{ij} + \frac{g_{in}\, V_{n\alpha}\, g_{\alpha\alpha}\, V_{\alpha n}\, g_{nj}}{1 - g_{\alpha\alpha}\, V_{\alpha n}\, g_{nn}\, V_{n\alpha}}\,. \tag{2.19}$$

The diagonal Green function corresponding to the impurity site is easily calculated and is given by

$$G_{\alpha\alpha} = \frac{g_{\alpha\alpha}}{1 - g_{\alpha\alpha}\, V_{\alpha n}\, g_{nn}\, V_{n\alpha}}\,. \tag{2.20}$$

The $\hat{T}$-matrix elements for this type of impurity are found from the definition in Eq. (2.11). The only non-zero matrix elements are those corresponding to sites n and α. The $\hat{T}$-matrix relating to these two sites is given by

$$\hat{T} = \frac{1}{1 - g_{\alpha\alpha}\, V_{\alpha n}\, g_{nn}\, V_{n\alpha}} \begin{pmatrix} V_{n\alpha} g_{\alpha\alpha} V_{\alpha n} & V_{n\alpha} \\ V_{\alpha n} & V_{\alpha n} g_{nn} V_{n\alpha} \end{pmatrix}. \tag{2.21}$$

If we are concerned with sites in the host system, and not the impurity atom itself, the only matrix element of interest is

$$T_{nn} = \frac{V_{n\alpha}\, g_{\alpha\alpha}\, V_{\alpha n}}{1 - g_{\alpha\alpha}\, V_{\alpha n}\, g_{nn}\, V_{n\alpha}}\,. \tag{2.22}$$

All Green function matrix elements within the host system can be calculated from

$$G_{ij} = g_{ij} + g_{in} T_{nn} g_{nj}\,. \tag{2.23}$$

We note the similarity between this expression and that for a substitutional impurity, given by Eq. (2.15). In fact, by comparing the $\hat{T}$ matrix elements for substitutional and adsorbed impurities in Eqs. (2.16) and (2.22), we can express the effect of an adsorbed impurity on the system as an energy dependent perturbation potential applied to the site to which the impurity adsorbs. In other words, by applying an onsite potential $\Sigma_{nn}(E)$ at site n, we take into account the effects of an adsorbed impurity at this site. This

potential, called a *self energy*, is given by

$$\Sigma_{nn}(E) = V_{n\alpha} g_{\alpha\alpha} V_{\alpha n} \,. \tag{2.24}$$

Using a self energy term to account for an external effect is a very common method in condensed matter physics. The important point is that the self energy represents the potential felt by the electrons in the host material due to the introduction of the adsorbed impurity. Unlike the substitutional impurity, the potential felt by the electrons due to an adatom is not constant, and electrons of different energy experience a different potential. This is due to the presence of the $g_{\alpha\alpha}$ term in the expression for Σ_{nn}. The energy dependence of $g_{\alpha\alpha}$ is clear from Eq. (2.17). In fact, when the energy of electrons in the host equals the onsite energy of the adsorbed impurity, the potential felt by electrons in the host diverges, while for large energies the potential becomes increasingly small and the adsorbed impurity is essentially invisible to them.

2.4.3 Multiple impurities

We shall now extend our discussion to the case of more than one impurity in a system and see how the expressions derived earlier are affected. We consider substitutional impurities of the kind described in the section 2.4.1. If we have two impurities, located at sites m and n on the lattice, then the potential describing the perturbation is given by

$$\hat{V} = |m\rangle \delta_m \langle m| + |n\rangle \delta_n \langle n| \,. \tag{2.25}$$

For an ensemble, N_i, of such impurities, we have

$$\hat{V} = \sum_{a \in N_i} |a\rangle \delta_a \langle a| \,. \tag{2.26}$$

From the Dyson equation, Eq. (2.10),

$$G_{ij} = g_{ij} + \sum_{a \in N_i} g_{ia}\delta_a G_{aj} \,. \tag{2.27}$$

Expanding the G_{aj} term as before,

$$G_{aj} = g_{aj} + \sum_{b \neq a \in N_i} g_{ab}\delta_b G_{bj}$$

and substituting the result back in gives

$$G_{ij} = g_{ij} + \sum_{a \in N_i} g_{ia}\delta_a g_{aj} + \sum_{a \in N_i} \sum_{b \neq a} g_{ia}\delta_a g_{ab}\delta_b G_{bj} \,.$$

We now must repeat this process for the term G_{bj} and so on, for each of the scatterers until we have an expression in terms of only the unperturbed propagators and then we begin the backsubstitution process. This method increases in complexity very quickly with the number of impurities considered. It soon becomes more convenient to solve this type by inverting the matrix $(\hat{I} - \hat{g}\hat{V})$ numerically and solving for $\hat{G} = \left[\hat{I} - \hat{g}\hat{V}\right]^{-1} \hat{g}$.

We can get a better understanding of the form of the Green function of a system with many scatterers by examining the $\hat{T}$-matrix describing the scattering. Recall that it is given by $\hat{T} = \hat{V}\left[\hat{I} - \hat{g}\hat{V}\right]^{-1}$. Expanding the term $\left[\hat{I} - \hat{g}\hat{V}\right]^{-1}$ as a power series we find

$$\hat{T} = \hat{V} + \hat{V}\hat{g}\hat{V} + \hat{V}\hat{g}\hat{V}\hat{g}\hat{V} + \cdots \,. \tag{2.28}$$

Rewriting in terms of single-impurity $\hat{T}$-matrices $\hat{t}_a$, where

$$\hat{t}_a = |a\rangle t_{aa} \langle a| \,,$$

where $t_{aa} = \delta_a \left[1 - g_{aa}\delta_a\right]^{-1}$, we find

$$\hat{T} = \sum_{a \in N_i} \hat{t}_a + \sum_{a \in N_i} \sum_{b \neq a} \hat{t}_a \hat{g} \hat{t}_b + \sum_{a \in N_i} \sum_{b \neq a} \sum_{c \neq b} \hat{t}_a \hat{g} \hat{t}_b \hat{g} \hat{t}_c + \cdots \,. \tag{2.29}$$

Thus, we can write the Green function G_{ij} in the form

$$G_{ij} = g_{ij} + \sum_{a \in N_i} g_{ia} t_{aa} g_{aj} + \sum_{a \in N_i} \sum_{b \neq a} g_{ia} t_{aa} g_{ab} t_{bb} g_{bj} + \\ + \sum_{a \in N_i} \sum_{b \neq a} \sum_{c \neq b} g_{ia} t_{aa} g_{ab} t_{bb} g_{bc} t_{cc} g_{cj} + \cdots . \tag{2.30}$$

By writing the expressions for the $\hat{T}$ and Green function matrix elements in terms of the single-scatterer $\hat{T}$-matrix elements, t_{aa}, we can clearly see that the effect of multiple scatterers is not merely a summation of the effects of single scatterers, but consists of higher order interference terms also, as should be expected. These higher order terms correspond to propagation pathways connecting sites i and j via a number of scattering sites. With more than one scatterer in the system, we open up the possibility of a pathway visiting the same site multiple times and thus there are now an infinite number of possible paths between the two sites. It is important to note that although we used a power series in our analysis of these expressions, the Dyson equation, as given in Eq. (2.10) and solved using matrix inversion or the exact substitution method illustrated earlier, gives the *exact* Green function of the perturbed system, and not merely an approximation to it. If it is too difficult or time-consuming to solve using these methods, we can truncate the power series given in Eq. (2.30) after a finite number of terms to give an approximation to it. If we are dealing with an infinite number of randomly located scatterers, methods such as the *Coherent Potential Approximation* [146, 147] can be used to yield a configurational average for the $\hat{T}$-matrix and hence the Green function itself.

Perhaps the most common Green function matrix element to appear in this work will be the off-diagonal matrix element between two sites containing impurities. This term plays a major role in the magnetic coupling calculations that will be discussed at length later in this work, and it is instructive to examine it now. We wish to calculate the matrix element G_{mn} when the perturbation potential for two impurities, given in Eq. (2.25) has

been applied. With two impurities, Eq. (2.27) becomes

$$G_{mn} = g_{mn} + g_{mm}V_{mm}G_{mn} + g_{mn}V_{nn}G_{nn}\,.$$

Using the substitution process, we can use the Dyson equation again to write G_{nn} in terms of G_{mn}. Substituting the resulting expression back in and reorganising terms gives

$$G_{mn} = \frac{g_{mn}}{(1 - g_{mm}\delta_m)(1 - g_{nn}\delta_n) - g_{mn}\delta_n g_{nm}\delta_m}\,. \tag{2.31}$$

The equivalent expression for the Green function between two adsorbed impurities adsorbed onto sites m and n, like those discussed in Section 2.4.2, is given by

$$G_{\alpha\beta} = \frac{g_{\alpha\alpha}\, V_{\alpha m}\, g_{mn}\, V_{n\beta}\, g_{\beta\beta}}{(1 - g_{\alpha\alpha}V_{\alpha m}g_{mm}V_{m\alpha})(1 - g_{\beta\beta}V_{\alpha n}g_{nn}V_{n\beta}) - g_{\alpha\alpha}V_{\alpha m}g_{mn}V_{n\beta}g_{\beta\beta}V_{\beta n}g_{nm}V_{m\alpha}} \tag{2.32}$$

2.5 Recursive Methods

The definition of the Green function, given in Eq. (2.1), suggests an obvious method for their calculation - namely a direct inversion of the quantity $\left[(E + i\eta)\hat{I} - \hat{\mathcal{H}}\right]$ using matrix techniques. This amounts to inverting a matrix whose dimension is the total number of orbitals considered in describing the system. As the size of the system in question increases, the matrices involved become unwieldy and alternative methods must be exploited. For periodic systems, we can introduce Bloch functions and reduce the problem to an integration in k-space. This method shall be illustrated explicitly for graphene in the next chapter. For the case of disordered systems, or other cases when the Bloch function method is not viable, recursive methods can be used.

Recursive methods involve building a system in a piecewise fashion, and updating the necessary Green function matrix elements at each stage. The

advantage of this kind of approach becomes clear when only a limited number of Green function matrix elements are required to calculate the quantity of interest. This is the case for the majority of calculations. In this case, the only Green function elements that need to be calculated or stored are those required to connect the piece of the system being added at the current iteration and those corresponding to the lattice sites of interest or required for their calculation at later iterations. This can greatly reduce the size of the matrices involved and thus increase the speed of the calculation.

Each piece, or *cell*, added to the system need not be the same, and so a recursive approach is often used when building a system in which disorder is present. However, if each cell is the same, a recursive approach can still offer advantages over Bloch function methods as more advanced techniques, like the Rubio-Sancho method outlined below, can be availed of.

2.5.1 Standard recursive approach

We consider a general case where the Green function of a system composed of N individual cells, each consisting of n_i orbital sites, is required. We assume that the Green function matrices for each of the individual components, $\hat{g}_{ii}$, are known. Note that here $\hat{g}_{ii}$ is not a single matrix element, but rather a $n_i \times n_i$ matrix containing all the Green function matrix elements describing the i^{th} unit cell disconnected from the rest of the system. For complete generality, we do not restrict the unit cells to being identical, or even to having the same number of sites. We now introduce a set of connection matrices, $\hat{V}_{i,i+1}$ and $\hat{V}_{i+1,i}$, describing the hopping parameters that are 'turned on' to connect the cells i and $i+1$. The matrix $\hat{V}_{i,i+1}$ has dimension $n_i \times n_{i+1}$, so is not necessarily square.

We begin by considering the case when the Green function of interest is that of the last cell of the fully connected system, $\hat{G}_{nn}$. This is a common scenario in transport calculations, where the *surface green function* of a lead is required. In this case, we start at the first cell, $i = 0$, and connect the cells individually until we have added the last cell. At each stage we only need to store the Green function of the last unit cell added. This is clear from the

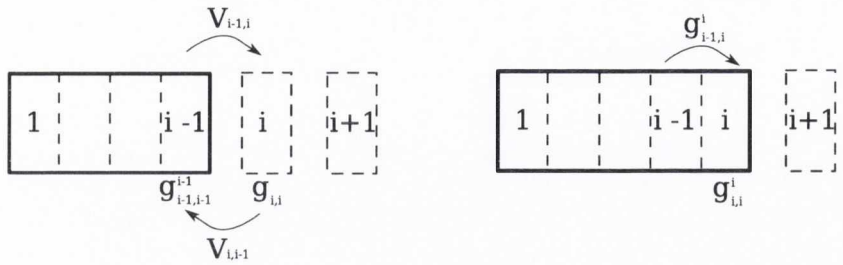

Figure 2.3: Before and after the connection of the i^{th} cell to the system.

Dyson equation used to connect any given unit cell to the system. Defining $\hat{g}^a_{ij}$ to be the Green function matrix of the system after the a^{th} cell has been added, then the Green function of cell i after it is connected is given by

$$\hat{g}^i_{ii} = \hat{g}_{ii} + \hat{g}_{ii}\,\hat{V}_{i,i-1}\,\hat{g}^i_{i-1,i}\,, \tag{2.33}$$

where all quantities are matrices, and

$$\hat{g}^i_{i-1,i} = \hat{g}^{i-1}_{i-1,i-1}\,\hat{V}_{i-1,i}\,\hat{g}^i_{ii}\,,$$

to give

$$\hat{g}^i_{ii} = \left(\hat{I} - \hat{g}_{ii}\,\hat{V}_{i,i-1}\,\hat{g}^{i-1}_{i-1,i-1}\,\hat{V}_{i-1,i}\right)^{-1}\hat{g}_{ii}\,. \tag{2.34}$$

Here we have calculated the surface Green function matrix of the system after i iterations in terms of that for $i-1$ iterations and the Green function matrix describing the i^{th} disconnected cell, as shown in Fig. 2.3. Eq. (2.34) thus defines an iterative algorithm to calculate the Green function required at the far edge of the fully connected system. We simply repeat the process for each $i = 0, \ldots, N$.

We now consider a more general case, where the Green function required is not that at the final edge of the system, but at an arbitrary cell k in the system. We find that the procedure followed is very similar to the previous case, but with a slightly more advanced algorithm to update the required Green function at each iteration. For $i \leq k$, we follow the exact same procedure as before to calculate $\hat{g}^k_{kk}$ - the surface Green function after k iterations when the cell of interest is currently at the edge. For each cell that is added

after this, $k < i \leq N$, we must update not only the Green function matrix of the edge cell, but also $\hat{g}^i_{kk}$ and any additional Green function matrices that are needed to calculate it. The edge cell is updated as before using Eq. (2.34). The matrix $\hat{g}^i_{kk}$, at each $i > k$, is found using

$$\hat{g}^i_{kk} = \hat{g}^{i-1}_{kk} + \hat{g}^{i-1}_{k,i-1} \; \hat{V}_{i-1,i} \; \hat{g}^i_{ik}. \tag{2.35}$$

Note that to update $\hat{g}^i_{kk}$ at each iteration we require $\hat{g}^{i-1}_{k,i-1}$ and $\hat{g}^i_{ik}$ - off-diagonal Green function matrices between the cell of interest and the edge cell, from the previous and current iterations respectively. We can thus define an algorithm to update all the necessary Green functions at each iteration.

$$\begin{aligned}
\hat{g}^i_{ii} &= \left(\hat{I} - \hat{g}_{ii} \hat{V}_{i,i-1} \; \hat{g}^{i-1}_{i-1,i-1} \hat{V}_{i-1,i}\right)^{-1} \hat{g}_{ii} \\
\hat{g}^i_{ik} &= \hat{g}^i_{ii} \hat{V}_{i,i-1} \hat{g}^{i-1}_{i-1,k} \\
\hat{g}^i_{kk} &= \hat{g}^{i-1}_{kk} + \hat{g}^{i-1}_{k,i-1} \hat{V}_{i-1,i} \hat{g}^i_{ik} \\
\hat{g}^i_{ki} &= \hat{g}^{i-1}_{k,i-1} \hat{V}_{i-1,i} \hat{g}^i_{ii} \; .
\end{aligned} \tag{2.36}$$

Note that in each iteration the quantities above should be calculated in the order shown, as many depend on the quantities calculated before them in the same iteration. Furthermore, although we have calculated the Green function here for a cell within the system, it is easy to adapt the procedure here to any set of sites within the system. Once the cell containing a site of interest has been added to the system we simply update the relevant Green functions on each iteration; i.e. the matrix element of interest and the off-diagonal elements linking it to the current edge cell. An analogous algorithm to Eqs. (2.36) is then followed until the system is complete.

A common use for recursive techniques is to calculate the surface Green function of a semi-infinite lead. This quantity is often required in transport calculations where a device region is connected to a semi-infinite lead at either side. Similarly, by connecting two semi-infinite leads the Green function in an infinite lead can be calculated. For this sort of calculation it is usually the case that each cell in the system is identical and we shall make this assumption here also. Thus to simplify notation, we define $\hat{g_C}$ to be the Green

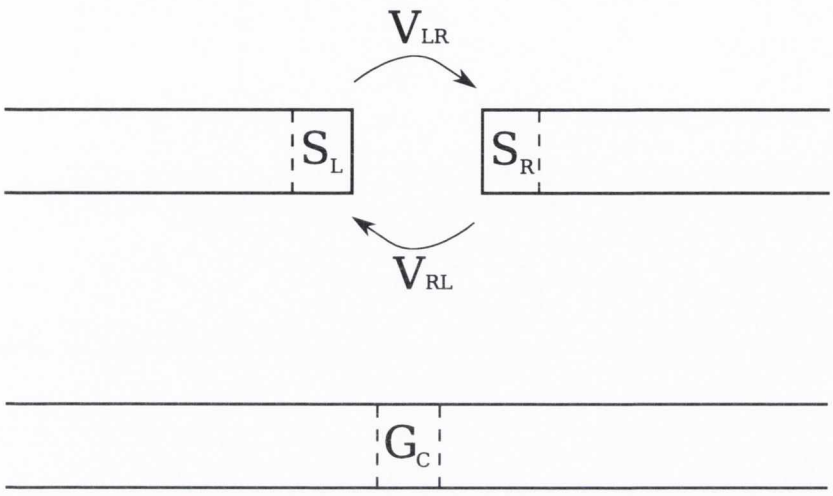

Figure 2.4: Two semi-infinite leads can be connected using the Dyson equation to calculate the Green function of an infinite system

function of an individual cell, and V_{RL} (V_{LR}) to be the hopping matrix used to connect it to the cell to the left (right). The general approach is to recursively add cells to the system until the addition of an extra cell does not change the Green function elements of the edge cell. When $|\hat{g}^N_{NN} - \hat{g}^{N-1}_{N-1,N-1}| < \epsilon$, for some suitably small ϵ, electrons in cell N do not feel the presence of the opposite edge and so g^N_{NN} acts as the surface Green function of a semi-infinite lead. Note that it is possible to build a lead by adding cells either to the left or to the right of the starting cell, and that the surface Green functions for these two cases are not necessarily equivalent. We distinguish between these two cases by introducing the notation $\hat{S}^N_{L/R}$ to denote the surface Green function of a system of N cells that has been built from the left / right. The superscript is dropped to denote the surface Green function of a semi-infinite lead. We can now rewrite the recursive algorithms for these surface Green functions as

$$\hat{S}^i_L = \left(\hat{I} - \hat{g}_C \hat{V}_{RL} \hat{S}^{i-1}_L \hat{V}_{LR}\right)^{-1} \hat{g}_C \tag{2.37}$$

$$\hat{S}^i_R = \left(\hat{I} - \hat{g}_C \hat{V}_{LR} \hat{S}^{i-1}_R \hat{V}_{RL}\right)^{-1} \hat{g}_C \ . \tag{2.38}$$

When convergence has been reached, the two leads can be joined to give the

Green function of the infinite system, as shown schematically in Fig. 2.4. The Green function matrix for a cell in the infinite system, $\hat{G}_C$, is found using the Dyson equation

$$\hat{G}_C = \left(\hat{I} - \hat{S}_L \hat{V}_{LR} \hat{S}_R \hat{V}_{RL}\right)^{-1} \hat{S}_L \,. \tag{2.39}$$

Off-diagonal Green function matrix elements between sites in different cells in an infinite lead system can be found by combining the techniques discussed above. Firstly, a semi-infinite lead from the left is constructed, with a surface Green function $\hat{S}_{L1}$. Then the required distance between the sites of interest is formed by the connection of single cells added recursively. As these cells are added, the Green function at the old edge, $L1$, and those connecting it with the new edge, are updated using Eq. (2.38). When the required number of cells are added, the surface Green function of the second site, $\hat{S}_{L2}$ is connected to a semi-infinite lead to the right, and the required Green function $\hat{G}_{L1,L2}$ is calculated by updating the relevant Green functions as before.

2.5.2 Rubio-Sancho Method

In the previous section, a simple recursive method to calculate the surface Green function of a semi-infinite lead was discussed. The efficiency of this method is of order N, where N is the number of cells that must be added to the system before the surface of the system acts as the surface of a semi-infinite lead. It should be noted that this number is dependent on the energy at which the Green function is being calculated and can increase dramatically near singularities. We will now outline an alternative method of calculating the surface Green function which has an efficiency of order 2^N. This is the so-called *Rubio-Sancho method* [148].[1]

We shall show the full form of this method below, which is written in terms of *transfer matrices*. However the fundamental concept is quite simple

[1] We note that both methods depend not only on the number of unit cells, N, added to the system but also on the number of sites considered in each unit cell, M. Both methods are of order M^2, i.e. the number of matrix elements used to describe the unit cell

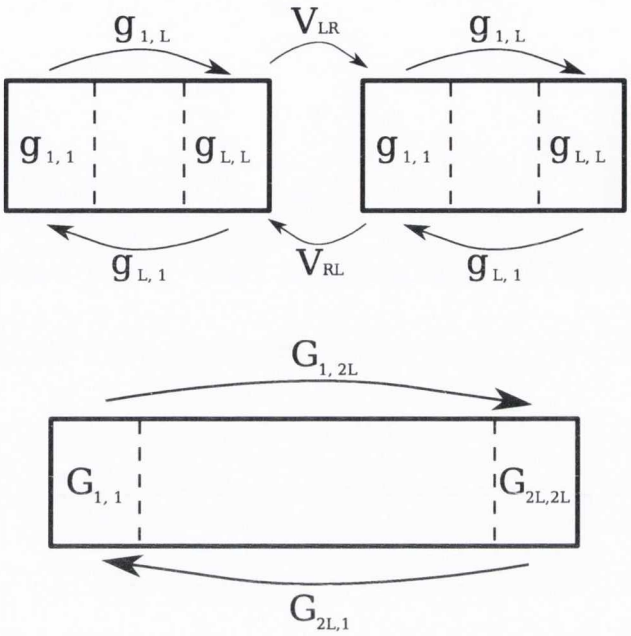

Figure 2.5: At each iteration in the Rubio-Sancho method the length of the lead approximating a semi-infinite system is doubled.

and the method is equivalent to the following. At each iteration, we update not only the Green function matrix corresponding to one edge, but to both edges and also to the off-diagonal Green functions connecting them. At the next iteration this allows us to add not just one cell to the system, but to double the length of the system as shown in Fig. 2.5. If we have a system of L connected cells $1, 2, \ldots, L$ and have calculated the Green functions $\hat{g}_{1,1}$, $\hat{g}_{L,L}$, $\hat{g}_{1,L}$ and $\hat{g}_{L,1}$ of this connected system, then the corresponding Green functions for a system twice this size can be calculated by joining the right edge of this system to the left edge of an identical system, whose cells we denote $L+1, \ldots, 2L$. The Green function for the new edge cell, $\hat{G}_{2L,2L}$ is found, after using the Dyson equation for intermediate terms $\hat{G}_{L,2L}$ and $\hat{G}_{L+1,2L}$, to be

$$\hat{G}_{2L,2L} = \hat{g}_{2L,2L} + \hat{g}_{2L,L+1}\,\hat{V}_{RL}\,\left[\hat{I} - \hat{g}_{L,L}\,\hat{V}_{LR}\,\hat{g}_{L+1,L+1}\,\hat{V}_{RL}\right]^{-1} \hat{g}_{LL}\,\hat{V}_{LR}\,\hat{g}_{L+1,2L}\,,$$

where as before $\hat{V}_{RL}$ ($\hat{V}_{LR}$) connects a cell to the neighbouring cell on the left (right). Since the system composed of cells $1, \ldots, L$ is equivalent to that composed of cells $L+1, \ldots, 2L$, we can rewrite this expression in terms of the Green functions with indices $1, \ldots, L$ as follows

$$\hat{G}_{2L,2L} = \hat{g}_{L,L} + \hat{g}_{L,1}\, \hat{V}_{RL} \left[\hat{I} - \hat{g}_{L,L}\, \hat{V}_{LR}\, \hat{g}_{1,1}\, \hat{V}_{RL}\right]^{-1} \hat{g}_{LL}\, \hat{V}_{LR}\, \hat{g}_{1,L}\,. \tag{2.40}$$

This expression updates the surface term on each iteration, and we see quite clearly that it relies on the diagonal Green function matrices for the two edge cells and the off-diagonal matrices connecting them. These must also be updated at each iteration and we can define an algorithm similar to that discussed in Eq. (2.36) to do this. However, we shall instead use an alternative algorithm to perform this calculation.

We consider a semi-infinite lead, with a surface cell labelled 0, whose surface Green function to wish to calculate. This term, $\hat{G}_{00}$ may be written in terms of the Green function of the disconnected cell $\hat{g}_{00}$ and the surface Green function, $\hat{g}_{11}$, of another semi-infinite chain that terminates at cell 1 in the usual manner

$$\hat{G}_{00} = \left[\hat{I} - \hat{g}_{00}\, \hat{V}_{LR}\, \hat{g}_{11}\, \hat{V}_{RL}\right]^{-1} \hat{g}_{00}\,, \tag{2.41}$$

and in the calculation of which we make use of the Dyson equation expression for $\hat{G}_{10}$:

$$\hat{G}_{10} = \hat{g}_{11}\, \hat{V}_{RL}\, \hat{G}_{00}\,. \tag{2.42}$$

Since all the cells in this system are equivalent, we introduce the notation $\hat{g}_C$ to refer to the Green function matrix of a disconnected cell. We also note that $\hat{G}_{00} = \hat{g}_{11}$ since both represent the surface Green function of the semi-infinite lead system. We thus rewrite Eqs (2.41 - 2.42) as

$$\hat{G}_{00} = \left[\hat{I} - \hat{g}_C\, \hat{V}_{LR}\, \hat{T}\right]^{-1} \hat{g}_{00}\,, \tag{2.43}$$

and

$$\hat{G}_{10} = \hat{T}\, \hat{G}_{00}\,, \tag{2.44}$$

where we have also introduced the *transfer matrix* $\hat{T} = \hat{G}_{00}\,\hat{V}_{RL}$. This term can also be written in a self-consistent form

$$\hat{T}^{i+1} = \left[\hat{I} - \hat{g}_C\,\hat{V}_{LR}\,\hat{T}^i\right]^{-1}\,\hat{V}_{RL}\,.$$

Solving for $\hat{T}$ in this manner and then substituting back into Eq. (2.43) is equivalent to calculating the surface Green function using the simple method discussed in the previous section.

The Rubio-Sancho method instead makes use of a different approach. First we consider an off-diagonal term, $\hat{G}_{N0}$, connecting the surface to a cell within the lead. Consider disconnecting cell N from the system, and then reconnecting it with the appropriate connection potentials. Using the Dyson equation, this scenario allows us to write the following expression

$$\begin{aligned}\hat{G}_{N0} &= \hat{g}_C\,\hat{V}_{RL}\,\hat{G}_{N-1,0} + \hat{g}_C\,\hat{V}_{LR}\,\hat{G}_{N+1,0} \\ &\equiv \hat{t}_0\,\hat{G}_{N-1,0} + \hat{s}_0\,\hat{G}_{N+1,0}\end{aligned} \tag{2.45}$$

where

$$\hat{t}_0 = \hat{g}_C\,\hat{V}_{RL} \qquad \text{and} \qquad \hat{s}_0 = \hat{g}_C\,\hat{V}_{LR}\,. \tag{2.46}$$

Eq. (2.45) allows us to rewrite an off-diagonal Green function element between the surface and a cell N within the system in terms of those between the surface and the cells neighbouring N. Applying it in turn to the terms $\hat{G}_{N-1,0}$ and $\hat{G}_{N+1,0}$, for $N \geq 2$, yields

$$\begin{aligned}\hat{G}_{N0} &= \hat{t}_0\,\left[\hat{t}_0\,\hat{G}_{N-2,0} + \hat{s}_0\,\hat{G}_{N,0}\right] + \hat{s}_0\,\left[\hat{t}_0\,\hat{G}_{N,0} + \hat{s}_0\,\hat{G}_{N+2,0}\right] \\ &\equiv \hat{t}_1\,\hat{G}_{N-2,0} + \hat{s}_1\,\hat{G}_{N+2,0}\end{aligned}$$

where

$$\hat{t}_1 = \left[\hat{I} - \hat{t}_0\hat{s}_0 - \hat{s}_0\hat{t}_0\right]^{-1}\hat{t}_0^2 \qquad \text{and} \qquad \hat{s}_1 = \left[\hat{I} - \hat{t}_0\hat{s}_0 - \hat{s}_0\hat{t}_0\right]^{-1}\hat{s}_0^2\,.$$

Repeating this process we find (for $N \geq 2^i$)

$$\hat{G}_{N0} = \hat{t}_i\,\hat{G}_{N-2^i,0} + \hat{s}_i\,\hat{G}_{N+2^i,0} \tag{2.47}$$

and

$$\begin{aligned} \hat{t}_i &= \left[\hat{I} - \hat{t}_{i-1}\hat{s}_{i-1} - \hat{s}_{i-1}\hat{t}_{i-1}\right]^{-1} \hat{t}_{i-1}^2 \\ \hat{s}_i &= \left[\hat{I} - \hat{t}_{i-1}\hat{s}_{i-1} - \hat{s}_{i-1}\hat{t}_{i-1}\right]^{-1} \hat{s}_{i-1}^2 \,. \end{aligned} \tag{2.48}$$

Letting $N = 2^i$ in Eq. (2.47) results in a sequence of equations

$$\begin{aligned} \hat{G}_{10} &= \hat{t}_0\hat{G}_{00} + \hat{s}_0\hat{G}_{20} \\ \hat{G}_{20} &= \hat{t}_1\hat{G}_{00} + \hat{s}_1\hat{G}_{40} \\ &\vdots \\ \hat{G}_{2^i0} &= \hat{t}_i\hat{G}_{00} + \hat{s}_i\hat{G}_{2^{i+1}0} \,. \end{aligned} \tag{2.49}$$

Starting at the final equation, backsubstitution yields

$$\hat{G}_{10} = \left[\hat{t}_0 + \hat{s}_0\hat{t}_1 + \hat{s}_0\hat{s}_1\hat{t}_2 + \cdots + \hat{s}_0\hat{s}_1\cdots\hat{s}_{i-1}\hat{t}_i\right]\hat{G}_{00} + \hat{s}_n\hat{G}_{2^{i+1}0} \,. \tag{2.50}$$

This process is repeated until the terms $\hat{t}_{2^{i+1}}$, $\hat{s}_{2^{i+1}}$ are satisfactorily small such that $\hat{G}_{2^{i+1}0} \sim 0$, and the first term in Eq. (2.50) gives a suitable approximation for $\hat{G}_{10}$. Comparison with Eq. (2.44) yields an expansion for $\hat{T}$,

$$\hat{T} = \hat{t}_0 + \hat{s}_0\hat{t}_1 + \hat{s}_0\hat{s}_1\hat{t}_2 + \cdots + \hat{s}_0\hat{s}_1\cdots\hat{s}_{i-1}\hat{t}_i \,, \tag{2.51}$$

that can in turn be substituted into Eq. (2.43) to obtain an expression for the surface Green function.

Equations (2.46), (2.48), (2.51) and (2.43) provide an easy-to-implement algorithm for calculating the surface Green function of a system with a significant increase in efficiency over the simple method discussed earlier. Once calculated, these surface Green functions can be used as before to calculate other quantities of interest.

2.6 The Lloyd Formula Method

In the previous few sections we have shown how Green functions can be calculated for a number of different systems using Dyson equation methods. In Section 2.4, we showed how to calculate the Green function of a system when a number of different perturbations were introduced. Now we will introduce a method to examine how the total energy of a system changes under such perturbations. The total change in energy, ΔE, is the difference between the energies of the perturbed and pristine systems, E and E_0 respectively,

$$\Delta E = E - E_0 \,. \tag{2.52}$$

Such a quantity is often of interest as it tells us if a perturbation is energetically favourable. By varying the exact nature of the perturbation, it can also be used to examine under what conditions a perturbation is most favourable. This quantity will be examined in detail later to determine preferential impurity locations and magnetic moment orientations. The most obvious approach to calculating such a quantity is a direction calculation of E and E_0. However for large systems and perturbations only involving a few orbital sites, ΔE will be very small compared to either quantity and cancellation errors may occur. The *Lloyd Formula* [149] allows for a more convenient approach, as it gives an expression for the total change in energy without requiring the total energy of either system to be calculated. Instead, the total energy is expressed in terms of the Green function of the pristine system and the perturbing potential.

The total energy difference can be expressed in terms of the change in the density of states, and hence in terms of the Green functions of the pristine

and perturbed systems, $\hat{g}$ and $\hat{G}$ respectively, using Eq. (2.9)

$$\begin{aligned}\Delta E &= \int_{-\infty}^{E_F} \mathrm{d}E\; E\; (\rho(E) - \rho_0(E)) \\ &= -\frac{1}{\pi}\,\mathrm{Im}\sum_j \int_{-\infty}^{E_F} \mathrm{d}E\; E\,(G_{jj}(E) - g_{jj}(E)) \\ &\equiv -\frac{1}{\pi}\,\mathrm{Im}\sum_j \int_{-\infty}^{E_F} \mathrm{d}E\; E\,\Delta G(E)\,.\end{aligned} \tag{2.53}$$

From the $\hat{T}$-matrix form of the Dyson equation, Eq. (2.12), the term $\Delta G = G_{jj} - g_{jj}$ can be written

$$\begin{aligned}\Delta G &= \sum_{j,m,n} g_{jn}\, T_{nm}\, g_{mj} \\ &= \sum_{m,n} \left(\sum_j g_{mj}\, g_{jn}\right) T_{nm} \\ &= \sum_{m,n} \left(\hat{g}^2\right)_{mn} T_{nm}\,,\end{aligned}$$

since the orbitals indexed by j form a complete set. Furthermore, from the definition of the operator $\hat{g}$ in Eq. (2.1) we find

$$\hat{g}^2 = \left(E\hat{I} - \hat{\mathcal{H}}\right)^{-2} = -\frac{\mathrm{d}}{\mathrm{d}E}\,\hat{g}\,.$$

Using this result, defining $[g'_{ab}] \equiv \frac{\mathrm{d}}{\mathrm{d}E}\,[g_{ab}]$ and rewriting $\hat{T} = \hat{V}\left(\hat{I} - \hat{g}\hat{V}\right)^{-1}$, we find that

$$\Delta G = -\mathrm{Tr}\left[\hat{g}'\hat{V}\left(\hat{I} - \hat{g}\hat{V}\right)^{-1}\right].$$

Assuming that the perturbation potential $\hat{V}$ is energy-independent, then $\frac{\mathrm{d}}{\mathrm{d}E}\left(\hat{I} - \hat{g}\,\hat{V}\right) = -\hat{g}'\hat{V}$, and

$$\begin{aligned}\Delta G &= \mathrm{Tr}\left[\left(\hat{I} - \hat{g}\,\hat{V}\right)'\left(\hat{I} - \hat{g}\,\hat{V}\right)^{-1}\right] \\ &= \frac{\mathrm{d}}{\mathrm{d}E}\,\mathrm{Tr}\ln\left(\hat{I} - \hat{g}\,\hat{V}\right),\end{aligned} \tag{2.54}$$

where we have used the identity $\mathrm{Tr}(\ln\hat{A})' = \mathrm{Tr}[\hat{A}'\hat{A}]$. The change in the density of states, $\Delta\rho(E)$, is then given by

$$\begin{aligned}\Delta\rho(E) &= -\frac{1}{\pi}\,\mathrm{Im}\,\Delta G \\ &= -\frac{1}{\pi}\,\mathrm{Im}\,\frac{\mathrm{d}}{\mathrm{d}E}\,\mathrm{Tr}\ln\left(\hat{I}-\hat{g}\,\hat{V}\right).\end{aligned} \tag{2.55}$$

Using the identity $\mathrm{Tr}\,\ln\hat{A} = \ln\det\hat{A}$, we arrive at the canonical form of the Lloyd formula

$$\Delta\rho(E) = -\frac{1}{\pi}\,\mathrm{Im}\,\frac{\mathrm{d}}{\mathrm{d}E}\,\ln\left(\det(\hat{I}-\hat{g}(E)\hat{V})\right). \tag{2.56}$$

An expression of this form for the change in the density of states is very convenient. The order of the matrix whose determinant must be taken is simply the number of orbital sites perturbed by $\hat{V}$. Furthermore, the energy derivative simplifies the calculation of many properties which involve an integration of the density of states over energy as the Fundamental Theorem of Calculus can be applied. For example, the change in the occupation number, ΔN, is given by

$$\begin{aligned}\Delta N(E_F) &= \int_{-\infty}^{E_F}\mathrm{d}E\,\Delta\rho(E) \\ &= -\frac{1}{\pi}\,\mathrm{Im}\,\ln\left(\det(\hat{I}-\hat{g}(E)\hat{V})\right)\Big|_{E_F}.\end{aligned} \tag{2.57}$$

Finally, we calculate the total change in the energy of the system when a perturbation is introduced. From Eqs. (2.53) and (2.54), we get

$$\Delta E\,(E_F) = -\frac{1}{\pi}\,\mathrm{Im}\int_{-\infty}^{E_F}\mathrm{d}E\,E\,\frac{\mathrm{d}}{\mathrm{d}E}\,\ln\left(\det(\hat{I}-\hat{g}(E)\hat{V})\right).$$

Integrating by parts yields

$$\Delta E\,(E_F) = E_F\,\Delta N(E_F) + \frac{1}{\pi}\,\mathrm{Im}\int_{-\infty}^{E_F}\mathrm{d}E\,E\,\ln\left(\det(\hat{I}-\hat{g}(E)\hat{V})\right).$$

We note that the total charge should not change as a result of connecting two systems, and so the first term above vanishes. It should be noted that the condition $\Delta N(E_F) = 0$ is not automatically satisfied, and can be viewed as a constraint to find a suitable parameterisation. Alternatively, it may be necessary to allow a small unphysical change in the Fermi energy to account for it [150–152]. Thus, the final expression for the change in the energy of a system when a perturbation $\hat{V}$ is introduced is given by

$$\Delta E\,(E_F) = \frac{1}{\pi}\,\mathrm{Im}\int_{-\infty}^{E_F} \mathrm{d}E\,\ln\left(\det(\hat{I} - \hat{g}(E)\hat{V})\right). \tag{2.58}$$

This form of the Lloyd formula will be used repeatedly throughout this thesis. In the next section, the details of how the sort of integral contained within this expression can be calculated are discussed.

2.7 Integrating over Green functions

In many of the calculations in this thesis, an integral over energy of a function containing Green functions is required. This scenario arises in expressions resulting from the use of the Lloyd formula, Eq. (2.58), but also in other cases. A simple example is the calculation of the occupation of an orbital. The Lloyd formula was used earlier to calculate the *total change* in this quantity over all orbitals, but in some calculations it is necessary to calculate the occupation at a single site. It is given by an integral over the LDOS at this site as follows

$$n_i = \int_{-\infty}^{E_F} \mathrm{d}E\,\rho_i(E) = -\frac{1}{\pi}\lim_{\eta\to 0}\,\mathrm{Im}\left[\int_{-\infty}^{E_F} \mathrm{d}E\,G_{ii}(E+i\eta)\right]. \tag{2.59}$$

Performing this integration as shown along the real energy axis can present a number of difficulties. Firstly, low dimensional systems can exhibit *Van Hove singularities* at certain energies. The inclusion of a non-zero imaginary energy component, η, in the Green function definition prevents these from lying on the axis of integration, but they can still present problems for a numerical integration in the form of sharp, narrow peaks in the integrand.

Another concern is that the DOS of perturbed systems often contain sharp peaks, corresponding to bound states, outside the energy band of the bulk system. This can lead to difficulty in the selection of a suitable lower bound for the integral in Eq. (2.59).

These difficulties can be overcome by observing that the retarded Green function is analytic in the Upper Half Energy Plane, that is, the function $G(z)$ where z is a point in the complex energy plane $z = E + iy$, has no singularities for $y > 0$. We also note that the function $G(z)$ is much smoother, and more easily integrable, along the imaginary than the real axis. Consider the integration contour, C, in the complex energy plane shown in Fig. 2.6. By Cauchy's theorem [153], the integral of $G(z)$ around this contour is zero, since C encloses no singular points. The contour C can be split into three component parts

- r - A line parallel to the real axis, from $E_F - R$ to E_F, with constant imaginary part η,

- i - A line parallel to the imaginary axis, from $i\eta$ to iR, with constant real part E_F,

- c - An arc of radius R connecting the top of i with the end of r.

Note that the integral we require in Eq. (2.59) corresponds to the $R \to \infty$ limit of I_r, the integral along r. Now

$$\begin{aligned} I_C &= I_r + I_i + I_c = 0 \\ \implies I_r &= -I_i - I_c \,. \end{aligned} \tag{2.60}$$

In the limit $R \to \infty$ and $G(z) \sim \frac{1}{z}$. Thus the integrand vanishes along the

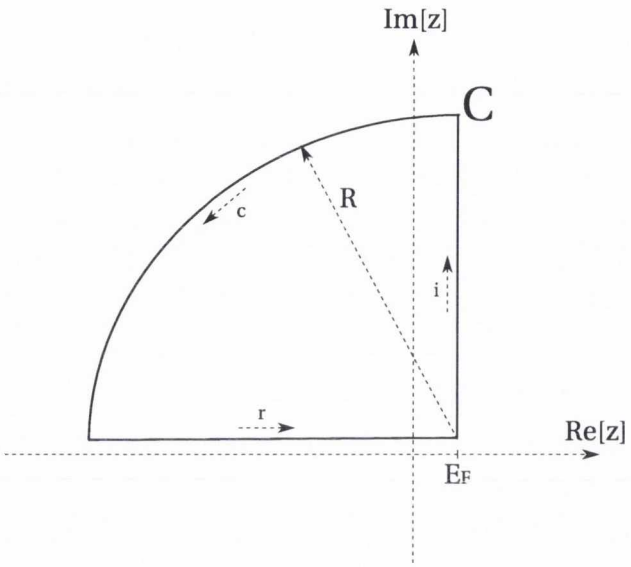

Figure 2.6: The integration contour C and its three component parts r, i and c.

arc c. However, the integral over the arc is not necessarily zero:

$$\begin{aligned}\lim_{R\to\infty} I_c &= \lim_{R\to\infty} \int_c \mathrm{d}z\, \frac{1}{z} \\ &= \lim_{R\to\infty} \int_{\frac{\pi}{2}}^{\pi} (iRe^{i\theta}\mathrm{d}\theta)\, \frac{1}{Re^{i\theta}} \\ &= \int_{\frac{\pi}{2}}^{\pi} \mathrm{d}\theta\, i \\ &= \frac{i\pi}{2}\,.\end{aligned} \tag{2.61}$$

Thus the contribution to the integrand from I_c is not zero. However, if the integrand vanishes as $\sim \frac{1}{R^2}$ or faster in the limit $R \to \infty$, then the contribution over the arc *does* vanish. This scenario occurs if the integrand contains a product of Green functions, rather than the single Green function

in the integrand here. From Eqs. (2.59) and (2.60), we can now write

$$\begin{aligned} n_i &= -\frac{1}{\pi}\,\mathrm{Im}\left[-i\lim_{\eta\to 0}\int_{\eta}^{\infty}\mathrm{d}y\; G_{ii}(E_F+iy) \;-\; \frac{i\pi}{2}\right] \\ &= \frac{1}{2}+\frac{1}{\pi}\lim_{\eta\to 0}\int_{\eta}^{\infty}\mathrm{d}y\;\mathrm{Re}\left[G_{ii}(E_F+iy)\right] \\ &= \frac{1}{2}+\lim_{\eta\to 0}\frac{1+\eta}{\pi}\int_0^1\mathrm{d}t\;\frac{1}{t^2}\,\mathrm{Re}\left[G_{ii}(E_F+i(\frac{1+\eta-t}{t}))\right]\,, \end{aligned} \tag{2.62}$$

where in the last of the above equations we have made the variable substitution $y=\frac{1+\eta-t}{t}$ to make the limits of the integration more manageable. The integration over the real axis in Eq. (2.59) has been replaced by one over the imaginary axis, where the function is in general far smoother and easier to integrate.

A similar method can be used for more complicated integrands. The aim in general is to write a real axis integration in terms of one over the imaginary axis, whilst taking care to account for any contributions arising from the third part of the contour. As discussed above, when the integrand involves a product of Green functions these contributions vanish. We shall now briefly consider another case where these contributions do not necessarily vanish - the Lloyd formula integral (2.58) describing the total change in energy of a system when a perturbation $\hat{V}$ is applied. The integral we need to solve here is of the form

$$\int_{-\infty}^{E_F}\mathrm{d}E\;\ln\;\det(\hat{I}-\hat{g}(E)\;\hat{V})\,.$$

Once again we use the contour shown in Fig 2.6 and can write $I_r=-I_i-I_c$. We will focus now on the contribution from I_c. Using the identity $\mathrm{Tr}\,\ln\hat{A}=\ln\det\hat{A}$, we can write

$$\begin{aligned} I_c &= \int_c \mathrm{d}z\;\ln\;\det\;(\hat{I}-\hat{g}(z)\;\hat{V}) \\ &= \int_c \mathrm{d}z\;\mathrm{Tr}\;\ln\;(\hat{I}-\hat{g}(z)\;\hat{V}) \\ &= \int_c \mathrm{d}z\;\mathrm{Tr}\;\ln\;(\hat{I}-\frac{\hat{I}}{z}\;\hat{V}) \qquad\qquad \text{as } R\to\infty\,. \end{aligned}$$

For large R, the ln term in the integral becomes

$$\ln\left(\hat{I} - \frac{\hat{I}}{z}\,\hat{V}\right) \sim -\frac{\hat{V}}{z}\,.$$

So, the integral becomes

$$\begin{aligned} I_c &= \int_{\frac{\pi}{2}}^{\pi} \mathrm{d}\theta\ \mathrm{Tr}\, iRe^{i\theta} \left(-\frac{\hat{V}}{R}e^{-i\theta}\right) \\ &= \int_{\frac{\pi}{2}}^{\pi} \mathrm{d}\theta\ \mathrm{Tr}\left[-i\hat{V}\right] \\ &= -\frac{i\pi\ \mathrm{Tr}\,\hat{V}}{2}\,. \end{aligned}$$

We see that there will only be a contribution from this term when the trace of the perturbation potential is nonzero, corresponding to perturbations where the onsite energy of sites are changed. Substitutional impurities, as discussed in Section 2.4.1, are an example of such a perturbation.

2.8 Electron - electron interactions

In the next chapter we will introduce a single-body, tight-binding type Hamiltonian to describe the electronic structure of graphene. While such a model is sufficient for many of the calculations within this work, it does not take into account electron-electron interactions which are needed to describe magnetic materials. To account for these interactions it is necessary to include an additional many body term to the Hamiltonian. In this section, we will detail the general method to include such a term using the Hubbard Model approach, and also how the resulting Hamiltonian can be simplified using a self-consistent procedure within the Mean Field Approximation (MFA) [154].

2.8.1 Hubbard Model

In this section we shall move from the *bra-ket* notation to that of the creation and annihilation operators of the second quantisation. Consider a simple

tight-binding Hamiltonian of the form

$$\mathcal{H}_{TB} = \sum_{i,j} |i\rangle \, \gamma_{ij} \, \langle j| \tag{2.63}$$

where i and j index orbital sites on the lattice, and $\gamma_{ij} = 0$ except for $i = j$, when it corresponds to onsite energy terms and for neighbouring i's and j's when it takes the value of the hopping integral between them. This Hamiltonian can be rewritten, incorporating the spin degree of freedom σ, using creation ($\hat{c}^{\dagger}_{i\sigma}$) and annihilation ($\hat{c}_{i\sigma}$) operators which respectively create or annihilate an electron in state i with spin state σ, as

$$\mathcal{H}_{TB} = \sum_{i,j,\sigma} \gamma_{ij} \, \hat{c}^{\dagger}_{j\sigma} \, \hat{c}_{i\sigma} \, . \tag{2.64}$$

It is clear from the spin degeneracy of this Hamiltonian that it cannot lead to the formation of magnetic moments. Magnetic moments in materials result from an exchange term arising from the Coulomb repulsion between electrons. This term breaks the degeneracy between up and down spin electrons and thus potentially leads to the formation of a moment. The Coulomb interaction, in a system of N electrons, is given by

$$V_C = \sum_{i,j=1}^{N} \frac{e^2}{|\vec{r}_i - \vec{r}_j|} \tag{2.65}$$

and each term is a function of the positions of two electrons. The general form of such a term can be written in operator form as

$$V_{ab} = \frac{1}{2} \sum_{i,j,k,l} \langle \, i,j \mid \frac{e^2}{r_{ab}} \mid k,l \, \rangle \sum_{\sigma,\sigma'} \hat{c}^{\dagger}_{i\sigma} \, \hat{c}^{\dagger}_{j\sigma'} \, \hat{c}_{k\sigma'} \, \hat{c}_{l\sigma} \, , \tag{2.66}$$

where $\langle \, i,j \mid \frac{e^2}{r_{ab}} \mid k,l \, \rangle$ is the expectation value of the Coulomb term, which is given by

$$\langle \, i,j \mid \frac{e^2}{r_{ab}} \mid k,l \, \rangle = \int \mathrm{d}\vec{r}_a \int \mathrm{d}\vec{r}_b \; \psi^*_i(\vec{r}_a) \, \psi^*_j(\vec{r}_b) \, \frac{e^2}{r_{ab}} \, \psi_k(\vec{r}_b) \, \psi_l(\vec{r}_a) \, , \tag{2.67}$$

where ψ_i is the localised wavefunction centred around site i. In the Hubbard model, it is assumed that screening restricts the interaction to one site and only the term corresponding to $i = j = k = l$ need be considered. This term corresponds to the Coulomb repulsion between electrons sharing the same orbital, which by the Pauli exclusion principle imposes the constraint $\sigma \neq \sigma'$. The Hubbard Hamiltonian can thus be written as

$$\mathcal{H}_{Hub} = \frac{U}{2} \sum_{i,\sigma} \hat{n}_{i\sigma}\, \hat{n}_{i\bar{\sigma}} \tag{2.68}$$

where U is the diagonal Coulomb integral and the *number operator* $\hat{n}_{i\sigma} = \hat{c}^{\dagger}_{i\sigma}\hat{c}_{i\sigma}$ gives the occupation of the state at site i with spin σ. In addition to exploring magnetic properties of materials, the Hubbard model in this form can be used to investigate a group of materials known as *Mott Hubbard insulators*. These are materials that are predicted to be conducting by models not including electron-electron interactions. However, a competition between the electron repulsion term and the hopping integral term can lead to a transition from conductor to insulator as the distances and angles between neighbouring atoms are varied, for example by heating. This is because the hopping integral is strongly dependent on these variables, whereas the purely onsite electron repulsion is not. The Hubbard Hamiltonian given in Eq. (2.68) is still a many-body Hamiltonian and we cannot yet avail of the methods discussed earlier in the Chapter. In the next section, a method to treat this interaction as a single particle effect will be explored.

2.8.2 Hartree Fock approximation

Combining the Hubbard and tight-binding components into a single Hamiltonian, we get

$$\mathcal{H} = \sum_{i,j,\sigma} \gamma_{ij}\, \hat{c}^{\dagger}_{j\sigma}\, \hat{c}_{i\sigma} + \frac{U}{2} \sum_{i,\sigma} \hat{n}_{i\sigma}\, \hat{n}_{i\bar{\sigma}}\,. \tag{2.69}$$

Within this work, we shall always consider the Hubbard term within the Hartree-Fock Approximation (HFA). This is a mean field approximation and

amounts to making the substitution

$$\hat{n}_{i\sigma} = \langle n_{i\sigma} \rangle + (\hat{n}_{i\sigma} - \langle n_{i\sigma} \rangle) ,$$

which is trivially true, and neglecting any terms of order $(\hat{n} - \langle n \rangle)^2$. Here $\langle n_{i\sigma} \rangle$ is the expectation value of the occupation number. We can now write

$$\hat{n}_{i\sigma}\, \hat{n}_{i\bar{\sigma}} \;\approx\; \hat{n}_{i\sigma} \langle n_{i\bar{\sigma}} \rangle + \hat{n}_{i\bar{\sigma}} \langle n_{i\sigma} \rangle - \langle n_{i\sigma} \rangle \langle n_{i\bar{\sigma}} \rangle ,$$

noting that we have written the many-body term from the Hamiltonian as a sum of single particle terms. The final term above applies spin-independent shift to the band centre of the magnetic atoms.

Defining the average occupation at site i

$$n_i = \langle n_{i\uparrow} \rangle + \langle n_{i\downarrow} \rangle \tag{2.70}$$

and the (dimensionless) magnetic moment at site i

$$m_i = \langle n_{i\uparrow} \rangle - \langle n_{i\downarrow} \rangle \tag{2.71}$$

allows us to rewrite the interaction term in the Hamiltonian as

$$\sum_i \left(\frac{U}{2} \left(n_i \; \mp m_i \right) - \; U \, \langle n_{i\sigma} \rangle \langle n_{i\bar{\sigma}} \rangle \right) \hat{n}_{i\sigma} , \tag{2.72}$$

where the choice of sign in the the first term is $-$ for $\sigma = \uparrow$ and $+$ for $\sigma = \downarrow$.

Within the Hartree-Fock approximation, the electron-electron interaction is accounted for by the inclusion of an on-site potential applied at the site of the magnetic moment. Furthermore, we observe that this potential can be divided into two components by separating the spin dependent and independent contributions. The spin-independent contribution, δ, gives the *bandcentre shift* for the magnetic site

$$\delta_i = U \left(\frac{n_i}{2} - \langle n_{i\sigma} \rangle \langle n_{i\bar{\sigma}} \rangle \right) . \tag{2.73}$$

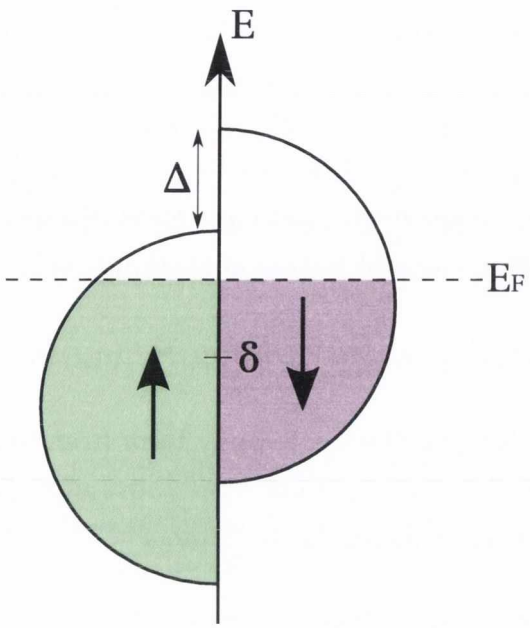

Figure 2.7: Schematic densities of states of up and down spin bands. The bandcentre, δ, and exchange splitting, Δ, can be calculated within the Hartree-Fock approximation using a self consistent procedure.

The spin-dependent contribution meanwhile consists of half the exchange splitting, Δ, between the up- and down-spin bands, where

$$\Delta_i = U\, m_i\,. \tag{2.74}$$

These two contributions are illustrated schematically in Fig. 2.7. The splitting, Δ, between the bands leads to a greater occupation of up (majority) spin electrons and hence to the formation of a magnetic moment. The local onsite potential applied at magnetic sites to account for the electron-electron interactions can be written in terms of the bandcentre shift and splitting as

$$V_{ii}^{\sigma} = \delta \mp \frac{\Delta}{2}\,, \tag{2.75}$$

with once more the choice of sign determined by the spin orientation.

2.8.3 Self consistent procedure

The Hartree-Fock approximation above allows us to calculate the Green function of a system containing magnetic moments by applying a spin dependent perturbation at the magnetic sites using the Dyson equation. We note that since the potential to be applied is spin dependent, the Green function describing the electrons of the system is no longer spin degenerate. The perturbation is written above in terms of Δ and δ - the splitting and bandcentre of the magnetic orbitals. Within a simple model, arbitrary values of these parameters can be used to ascertain the behaviour of a system with a magnetic impurity. However, in many cases it is necessary to parameterise the magnetic moment more carefully, particularly if we want to investigate how the moment itself changes under different conditions. Within the study of graphene, electron-electron interactions generally need to be accounted for in two cases. The first of these is to investigate the formation of magnetic moments in graphene in the presence of edges or vacancies. In this case the moment arises due to the formation of localised states induced by the particular geometry of the system, and the carbon atoms in the graphene themselves obtain magnetic moments. The other case is when the graphene system is doped with objects which already possess a magnetic moment themselves, for example *d*-band transition metals. This is the scenario that will be encountered frequently in this work. In both these cases, rather than arbitrarily selecting values of the bandcentre and splitting, we can calculate them using a self-consistent procedure that assumes knowledge of the occupation, n_i, of the relevant orbitals. For undoped graphene systems the p_z orbital is half-full, corresponding to $n_i = 1$, where each orbital can hold at most two electrons - one of each spin orientation. For transition metal atoms, the relevant band occupation can be found by comparison with *ab initio* calculations or can be varied over a range of values to examine the effects of different magnetic dopants on the system. In both cases, the following procedure is implemented to calculate V_{ii}^{σ} :

1. Initial guesses for the magnetic moments, $\vec{m}^0$, and bandcentres, $\vec{\delta}^0$, are taken and used to calculate the onsite potentials.

2. The occupation of the up and down spin bands, $\vec{n}_\uparrow$ and $\vec{n}_\downarrow$, are obtained by integrating the densities of states, calculated by applying the onsite potentials to the Green function.

3. New estimates for the bandcentres, $\vec{\delta}^1$, are found by adjusting them until the constraint $n_i = n_{i\uparrow}(\vec{\delta}^1) + n_{i\downarrow}(\vec{\delta}^1)$ is satisfied at each site.

4. New estimates for the magnetic moments are calculated at each site from $m_i^1 = n_{i\uparrow}(\vec{\delta}^1) - n_{i\downarrow}(\vec{\delta}^1)$.

5. Steps 1 to 4 are repeated until convergence.

In this way we can calculate the bandcentre and the moment (and hence the band splitting) associated with each magnetic site. These are used to calculate the spin-dependent potential, V^σ, and Green function, G^σ, from which the required properties of the system can be calculated using the methods described earlier in this Chapter.

2.9 Summary of chapter

This chapter has introduced us to the concept of Green functions and briefly discussed how they may be calculated and manipulated for use in condensed matter physics calculations. The discussion to date has been very general and not restricted to a particular material or Hamiltonian. The simple examples used to illustrate the various methods can be straightforwardly extended to more complex systems.

The Green function was defined and its relationship to the density of states (DOS) shown in section 2.1. The advantages of the Green function formalism for describing perturbed and disordered systems were highlighted by the use of the Dyson equation to connect the Green functions of perturbed and unperturbed systems in section 2.3, before specific examples of its use for simple cases were examined in section 2.4. Methods for calculating the Green function for a large system in a piecewise, or recursive, fashion were detailed in section 2.5. A description of the Lloyd formula method for calculating the change in various properties of the system when a perturbation is applied, and

details on performing integrals involving the Green function, completed our introduction to Green function methods in sections 2.6 and 2.7 respectively.

Finally, a brief introduction to the Hubbard model and its treatment within the mean-field approximation was given in section 2.8. The steps of a self-consistent procedure to include magnetic moments within the formalism developed earlier in the chapter were described.

In the next chapter, the focus will shift away from the general approach taken to date and towards graphene and related materials. The electronic structure of graphene will be calculated, and various methods of calculating its Green functions discussed. The recursive methods introduced in this chapter will be demonstrated for the specific case of graphene nanoribbons.

CHAPTER

THREE

Electronic structure and Green functions of Graphene

3.1 Introduction

In this chapter we calculate the electronic band structure of graphene within the nearest neighbour tight binding (NNTB) approximation and show how it can be used to calculate the corresponding Green function - a quantity discussed at length in the previous chapter. The band structure of graphene is compared to that of related materials, namely carbon nanotubes (CNTs) and graphene nanoribbons (GNRs). The Green function calculation for graphene can be tackled in a number of ways. Despite the simplicity of the tight-binding description of the graphene band structure, the corresponding Green functions are often calculated numerically or by availing of a linear approximation. In this chapter we attempt to simplify the calculation by showing how to derive it in a mathematically transparent form. We demonstrate that by moving to reciprocal space, the calculation becomes a two dimensional integration, the first of which can be performed completely analytically. For special cases, we propose a method to tackle the second integration using the Stationary Phase approximation (SPA). This approach takes advantage of the highly oscillatory nature of the integrand and yields an excellent approximation to the true Green function across almost the entire energy band. The resultant analytical results offer mathematical transparency when calcu-

lating physical properties that can be expressed in terms of Green functions. In particular the distance dependence of the Green function clearly emerges from our derivation. Finally, the recursive methods introduced in the previous chapter are illustrated in the case of GNRs.

3.2 Electronic structure of graphene

Graphene consists of a planar sheet of carbon atoms arranged in a hexagonal, or honeycomb lattice, as depicted in Fig. 3.1. This atomic arrangement is particularly stable due to the strength of the σ bonds formed between sp^2 hybridised orbitals on neighbouring carbon atoms. Three hybridised orbitals are formed per carbon atom from the $2s$ together with the $2p_x$ and $2p_y$ orbitals and each of these hybridised orbitals bonds with another on one of the three neighbouring carbon atoms. These bonding orbitals are each occupied by two electrons, one of each spin orientation, leaving one electron per carbon atom remaining in the $2p_z$ orbital. These orbitals stick out of the plane and form π bonds with other p_z orbitals on neighbouring lattice sites. This leads to the energy bands near the Fermi energy which control the electronic properties of graphene, and which we shall study using the tight-binding approximation. For most purposes it is sufficient to neglect the other energy bands, which are far enough away from the Fermi energy to not play a major role in our calculations.

3.2.1 Tight binding approach

Throughout this work, we shall employ a *nearest-neighbour tight-binding* (NNTB) approximation to describe the electronic band structure of graphene. As discussed above, the electronic properties of graphene are predominantly determined by the p_z orbitals. In fact, by restricting the Hamiltonian describing the system to these orbitals and the electron hopping probabilities to those between orbitals at neighbouring sites, an excellent approximation to the band structure of graphene is recovered. This is the essence of the

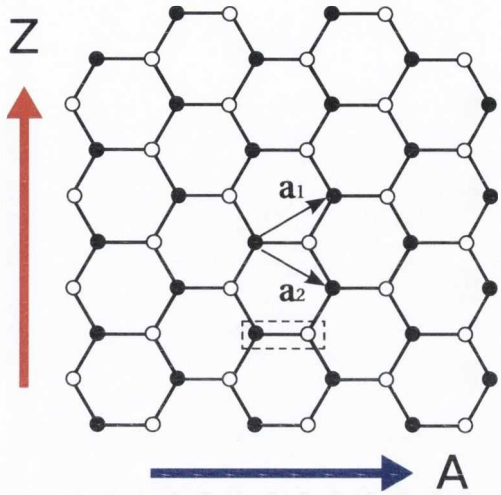

$$\mathbf{a}_1 = a(\tfrac{\sqrt{3}}{2}\hat{\mathbf{x}} + \tfrac{1}{2}\hat{\mathbf{y}})$$

$$\mathbf{a}_2 = a(\tfrac{\sqrt{3}}{2}\hat{\mathbf{x}} - \tfrac{1}{2}\hat{\mathbf{y}})$$

Figure 3.1: A section of the honeycomb graphene lattice with sites from the two intersecting triangular sublattices represented by filled or hollow symbols at the lattice sites. The dashed rectangle encloses a unit cell containing one site from each sublattice. The primitive lattice vectors $\mathbf{a}_1$ and $\mathbf{a}_2$ are also shown. The large, coloured arrows highlight the important armchair (A) and zigzag (Z) directions in the lattice.

NNTB model, where the Hamiltonian describing the system is of the form

$$\mathcal{H} = \sum_i |i\rangle \, \epsilon_i \, \langle i| + \sum_{\langle i,j \rangle} |j\rangle \, \gamma_{ij} \, \langle j| \,, \tag{3.1}$$

where $|i\rangle$ represents an atomic orbital centred at lattice site i, ϵ_i is the *onsite energy* at that site, γ_{ij} is the *hopping integral* between the orbitals centred at sites i and j and the sum is restricted to sites which are nearest neighbours.

The band structure is then found by finding the eigenvalue solutions of the Schroedinger equation. This is generally a matrix equation where the matrices involved have a dimension equal to the number of orbitals used to describe the system. This approach suffices for small molecules, but for larger, extended systems a different method must be used. Usually this involves taking advantage of periodicity within the system. If the full system can be generated by the translation of a finite cell under a set of vectors, then we can express the problem in a more easily solveable form. First, we

define a Bloch function, $|\mathbf{k}\rangle$, composed of atomic orbitals with coefficients $\phi^{\mathbf{k}}$

$$|\mathbf{k}\rangle = \frac{1}{\sqrt{N}} \sum_j e^{i\,\mathbf{k}\cdot\mathbf{R}_j}\, \phi^{\mathbf{k}}\, |j\rangle\,, \tag{3.2}$$

where $\mathbf{R}_j$ is the position vector of lattice site j. The next step is to substitute this expression into the Schroedinger equation

$$\begin{aligned} \mathcal{H}\,|\mathbf{k}\rangle &= \epsilon(\mathbf{k})\,|\mathbf{k}\rangle \\ \Rightarrow \epsilon(\mathbf{k}) \sum_j \phi^{\mathbf{k}}\, e^{i\,\mathbf{k}\cdot\mathbf{R}_j}\, |j\rangle &= \sum_j \phi^{\mathbf{k}}\, e^{i\,\mathbf{k}\cdot\mathbf{R}_j}\, \mathcal{H}\,|j\rangle\,, \end{aligned}$$

and then to project onto $\langle l|$ to get the so-called *secular* equation

$$\epsilon(\mathbf{k}) \sum_j \phi^{\mathbf{k}}\, e^{i\,\mathbf{k}\cdot\mathbf{R}_j}\, \langle l|j\rangle = \sum_j \phi^{\mathbf{k}}\, e^{i\,\mathbf{k}\cdot\mathbf{R}_j}\, \langle l|\mathcal{H}\,|j\rangle\,. \tag{3.3}$$

If we assume that the basis set of atomic orbitals is orthogonal, then the overlap matrix elements simplify to $\langle l|j\rangle = \delta_{l,j}$ and we find

$$\epsilon(\mathbf{k})\,\phi^{\mathbf{k}} = \sum_j \phi^{\mathbf{k}}\, e^{i\,\mathbf{k}\cdot(\mathbf{R}_j - \mathbf{R}_l)}\, \langle l|\mathcal{H}\,|j\rangle\,, \tag{3.4}$$

which can usually be solved quite easily for eigenvalues $\epsilon(\mathbf{k})$ and eigenstates $|\mathbf{k}\rangle$ using standard matrix methods.

3.2.2 Band structure of graphene

A cursory glance at the structure of graphene makes clear that it is a periodic system. Furthermore, although commonly regarded as a hexagonal, or honeycomb, lattice of carbon atom sites, it can also be regarded as two intersecting triangular sublattices of sites, represented schematically in Fig. 3.1 by filled or hollow circles. It is this *bipartite* nature of graphene that leads to many of its intriguing properties. The unit cell which constructs the entire lattice by translation consists of two neighbouring sites, one from each of the sublattices. We choose the primitive lattice vectors $\mathbf{a}_1$ and $\mathbf{a}_2$. Any unit cell in the graphene lattice can be located by a linear combination

of these vectors with integer coefficients, $\mathbf{r} = m\mathbf{a}_1 + n\mathbf{a}_2$. The orbital basis set used to calculate the electronic structure is denoted by $|\mathbf{r}, n\rangle$, where $\mathbf{r}$ gives the location of the unit cell and $n = 1, 2$, for filled and hollow sites respectively, denotes the site within the unit cell that the orbital is centred around. Switching to reciprocal space, we define the basis set of Bloch waves

$$|\mathbf{k}, n\rangle = \frac{1}{\sqrt{N}} \sum_{\mathbf{r}} e^{i\mathbf{k}\cdot\mathbf{r}} |\mathbf{r}, n\rangle . \tag{3.5}$$

Each atom on the lattice has three nearest neighbours, and the hopping integral for nearest neighbours in graphene is known to be $\gamma_{ij} \equiv -t \approx -2.7eV$ [155]. The magnitude of this quantity, t, will be used as a unit of energy throughout this work. The onsite energy, ϵ_0, is the same at each lattice site and defines the centre of the energy bands, and is set to zero in these calculations. The Hamiltonian matrix has become a 2×2 diagonal matrix under the transformation in Eq. (3.5) and is of the form

$$\mathcal{H} = \begin{pmatrix} 0 & t\,f(\mathbf{k}) \\ t\,f^*(\mathbf{k}) & 0 \end{pmatrix} , \tag{3.6}$$

where $f(\mathbf{k})$ ($f^*(\mathbf{k})$) is calculated by summing over the phase terms coming from each nearest neighbour of an atom on a filled (hollow) site. For the filled site case the relevant sites and vectors are illustrated in Fig. 3.2, and we find

$$\begin{aligned} f(\mathbf{k}) &= \sum_{i=1}^{3} e^{i\mathbf{k}\cdot\mathbf{R}_i} \\ &= e^{i\frac{k_x a}{\sqrt{3}}} + e^{i\left(\frac{-k_x a}{2\sqrt{3}} + \frac{k_y a}{2}\right)} + e^{i\left(\frac{-k_x a}{2\sqrt{3}} - \frac{k_y a}{2}\right)} \\ &= e^{i\frac{k_x a}{\sqrt{3}}} + 2\cos(\frac{k_y a}{2})\, e^{-i\frac{k_x a}{2\sqrt{3}}} . \end{aligned} \tag{3.7}$$

The eigenvalues $\epsilon(\mathbf{k})$ are found by solving

$$\begin{vmatrix} 0 - \epsilon(\mathbf{k}) & tf(\mathbf{k}) \\ tf^*(\mathbf{k}) & 0 - \epsilon(\mathbf{k}) \end{vmatrix} = 0 , \tag{3.8}$$

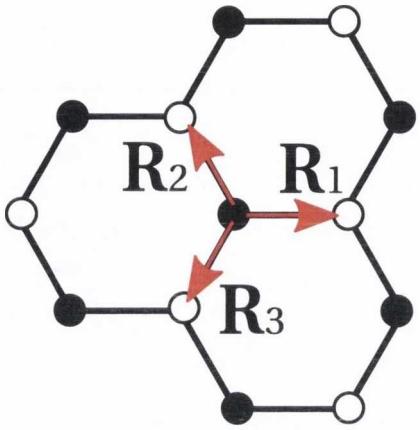

Figure 3.2: The nearest neighbours of a filled lattice site in graphene, as used in the calculation in Eq. (3.7).

which gives

$$\begin{aligned}\epsilon_{\pm}(\mathbf{k}) &= \pm t \\ &= |f(\mathbf{k})| = \pm t\sqrt{1 + 4\cos^2\left(\frac{k_y a}{2}\right) + 4\cos\left(\frac{k_y a}{2}\right)\cos\left(\frac{\sqrt{3}k_x a}{2}\right)}\end{aligned} \tag{3.9}$$

with corresponding eigenstates

$$|\mathbf{k}, \pm\rangle = \frac{1}{\sqrt{2N}} \sum_{\mathbf{r}} e^{-i\mathbf{k}\cdot\mathbf{r}} \left(|\mathbf{r}, 1\rangle \pm e^{-i\phi(\mathbf{k})}|\mathbf{r}, 2\rangle\right) , \quad \text{where } e^{-i\phi(\mathbf{k})} = \frac{f^*(\mathbf{k})}{|f(\mathbf{k})|} . \tag{3.10}$$

The energy band structure described by Eq. (3.9) is plotted in Fig. 3.3 as a function of k_x and k_y, and also along some of the important high symmetry points of the Brillouin Zone (BZ). The density of states for this system is also shown. We note that since the p_z orbitals in carbon contain one electron each, then the band is half full and the Fermi energy of the undoped system is $E_F = 0$. This is exactly the point where the two bands, called π and π^* and given by ϵ_- and ϵ_+ respectively, touch and the DOS vanishes. Graphene is thus a zero-bandgap semiconductor, or a *semi-metal*. The resultant Fermi surface consists of six discrete points, only two of which are unique, lying

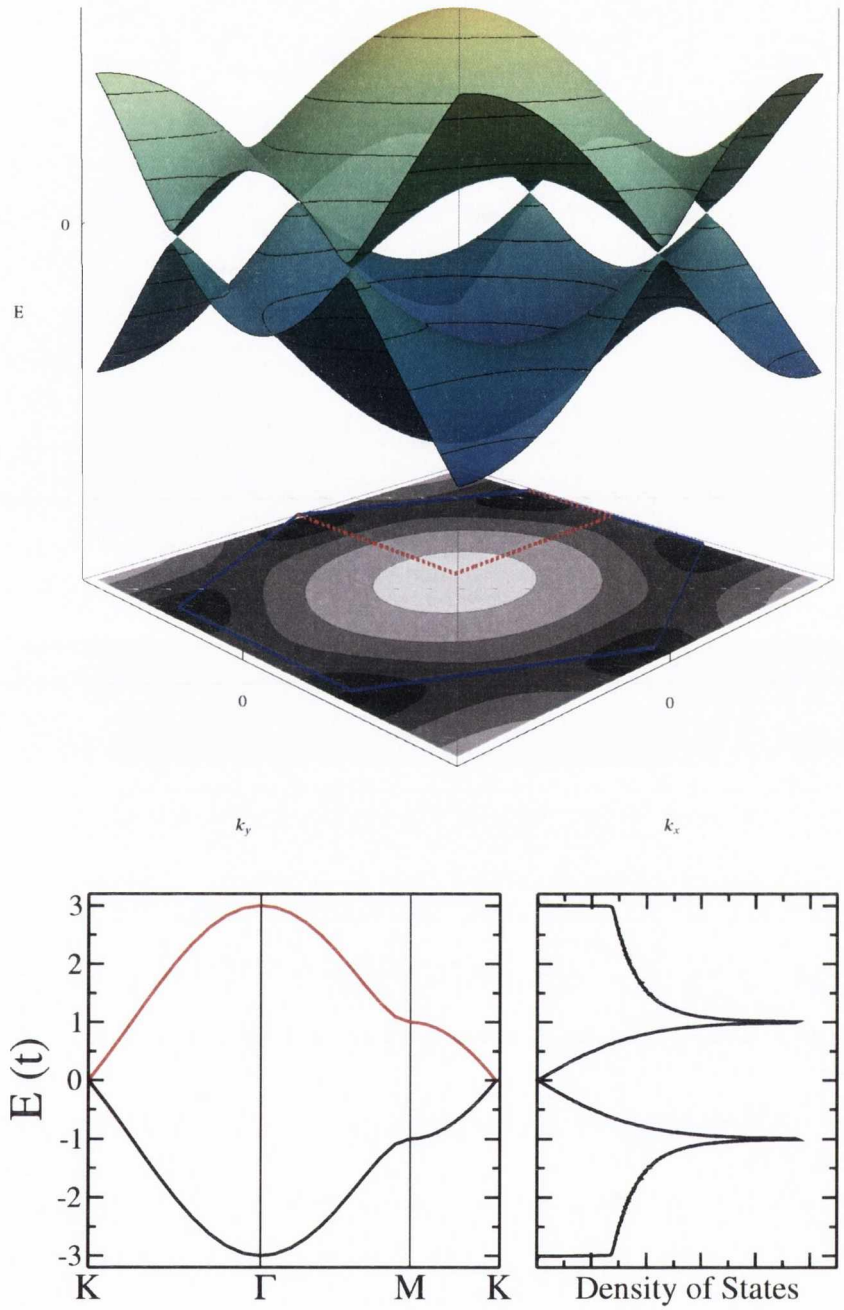

Figure 3.3: The top panel plots the nearest-neighbour tight-binding band structure of graphene as a function of k_x and k_y. The Fermi surface consists of six discrete points at $E = 0$ where the upper and lower bands touch. The first Brillouin Zone (BZ) of graphene is a hexagon described by these six points, and marked in blue on the projection below showing the constant energy surfaces of the band structure equation. The dashed red path is between the high symmetry points of the first BZ, and the bands along this path are shown by the bottom left panel. The bottom right panel shows the corresponding density of states.

at the vertices, or K points, of the first Brillouin Zone illustrated by the blue hexagon in Fig. 3.3. These are often referred to as *Dirac points*. The degeneracy of the π and π^* bands at these points is general to the one-electron description of graphene and persists even when the symmetry of the bands around $E_F = 0$ is broken. Many of the interesting properties belonging to graphene arise due to the shape of the bands near the Fermi energy. Unlike in conventional semiconductors where the bands are parabolic, the band structure of graphene is *linear* near E_F. This results in electrons or holes near the Dirac points having zero effective mass and behaving like relativistic particles which can be described using the Dirac equation from Quantum Electrodynamics (QED). Graphene can thus be investigated using standard condensed matter techniques, but can also act as a medium for exploring the methods and predictions of QED in a laboratory environment [4, 18]. This thesis will not focus on the latter methodology, but it is worth investigating briefly how graphene electrons are approximated in the linear regime and the range of energy values over which the approximation is valid.

Linear dispersion regime

The part of the graphene spectrum around $E_F = 0$ can be approximated linearly to simplify the calculation of physical properties and to allow the use of QED methodology. To do this, we expand the equation for the band structure around one of the K points. Without loss of generality, we choose that located at $\mathbf{K} = (0, \frac{4\pi}{3a})$ in reciprocal space. We now recalculate the term $f(\mathbf{k})$ as in Eq. (3.7) for a point in reciprocal space near the Dirac point, $\mathbf{k} = \mathbf{K} + \delta\mathbf{k}$, and find

$$\begin{aligned} f(\mathbf{k}) &= \sum_{i=1}^{3} e^{i\mathbf{K}\cdot\mathbf{R}_i}\, e^{i\delta\mathbf{k}\cdot\mathbf{R}_i} \\ &\approx 1 + (-\frac{1}{2} + i\,\frac{\sqrt{3}}{2})(1 + i\,\delta\mathbf{k}\cdot\mathbf{R}_2) + (-\frac{1}{2} - i\,\frac{\sqrt{3}}{2})(1 + i\,\delta\mathbf{k}\cdot\mathbf{R}_3) \\ &\approx \frac{\sqrt{3}\,a}{2}\,|\delta\mathbf{k}|\,e^{i(\frac{\pi}{2}-\theta)} \end{aligned}$$

where θ is the angle from the k_x plane. To calculate the band structure, we only need the modulus of this quantity, where the additional phase term $e^{i(\frac{\pi}{2})}$ vanishes. However this term, called the *Berry phase*, has a marked effect on other properties of graphene and in particular its Quantum Hall response [35].

Using the above approximation for $f(\mathbf{k})$, the band structure equation becomes

$$\epsilon_{\pm}\left(|\delta\mathbf{k}|\right) = \pm\frac{\sqrt{3}\,a\,t}{2}\,|\delta\mathbf{k}|\,. \tag{3.11}$$

This is most commonly written in terms of the Fermi velocity of graphene, $v_F = \frac{1}{\hbar}\frac{\mathrm{d}E}{\mathrm{d}k} \sim 10^6\,\mathrm{m\,s^{-1}}$, as

$$\epsilon_{\pm}\left(|\delta\mathbf{k}|\right) = \pm\hbar\,v_F\,|\delta\mathbf{k}|\,. \tag{3.12}$$

In Fig. 3.4 we compare the linear approximation of the band structure with that calculated previously. It is seen to be a very good approximation in the region surrounding $E = 0$, but loses accuracy quickly outside this regime. The approximation returns the correct band structure (to within 1%) for a region covering less than 5% of the bandwidth. However, since it is inaccurate over large parts of the band, difficulties arise when it is necessary to calculate quantities involving energies outside the linear dispersion regime or when an integral over energy is required. Later in this chapter we will introduce a technique that removes these shortcomings when calculating the Green function matrix elements of graphene.

3.2.3 Quasi-one-dimensional graphene systems

The electronic band structure of graphene, given in Eq. (3.9), had been calculated long before [28–30] the experimental discovery of graphene in 2004 [17]. It was used initially as a starting point to calculate the electronic properties of graphite, which consists of multiple stacked layers of graphene weakly connected by a van der Waals interaction. More recently it has been used to calculate those of Carbon Nanotubes (CNTs) - quasi one-dimensional materials consisted of rolled up graphene sheets [8,14]. It is also the starting

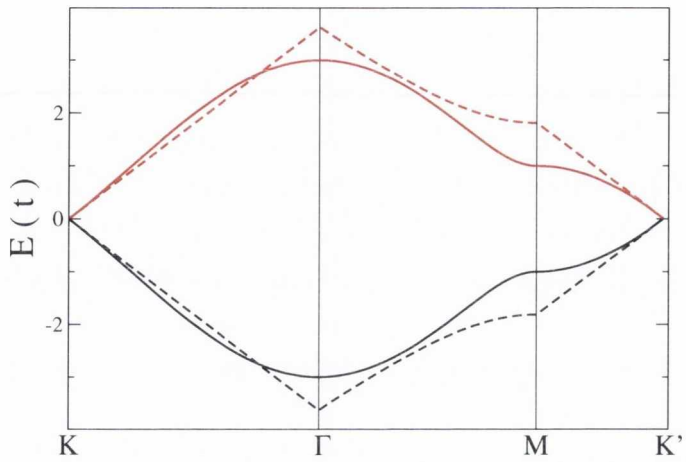

Figure 3.4: Band structure of graphene along the important high symmetry points calculated using the full tight-binding (solid) and linear approximation (dashed) methods.

point for investigating another one-dimensional allotrope of carbon - narrow strips of graphene called graphene nanoribbons (GNRs) [39]. We will now show how the electronic structure of CNTs emerges from that of graphene with periodic boundary conditions applied, and how difficulties arise when a similar approach, with hard edge boundary conditions, is attempted for GNRs.

Carbon Nanotubes

Carbon nanotubes are characterised by their circumferential, or *chiral*, vector which determines their diameter and the direction in which they are rolled. This vector is given in terms of the primitive lattice vectors of graphene as $\mathbf{R}_{ch} = m\,\mathbf{a}_1 + n\,\mathbf{a}_2$ and nanotubes are generally labelled according to this vector using the notation (m, n). Nanotubes of the form $(m, -m)$ and (m, m) have corresponding chiral vectors in the special zigzag and armchair directions respectively. These are called achiral nanotubes, and we shall examine their band structure here.

The band structure of these systems can be found by applying *periodic boundary conditions* to the graphene electronic wavevectors in Eq. (3.10). To

ensure the continuity of the electron wavefunction we enforce the constraint

$$\begin{aligned} & |\mathbf{k}, \pm\rangle(\mathbf{r}) = |\mathbf{k}, \pm\rangle(\mathbf{r} + \mathbf{R}_{ch}) \\ \Longrightarrow \; & e^{i\,\mathbf{k}\cdot\mathbf{R}_{ch}} = 1 \\ \Longrightarrow \; & \mathbf{k}\cdot\mathbf{R}_{ch} = 2\pi\alpha \qquad \text{where } \alpha = 0, 1, 2, \cdots . \end{aligned} \tag{3.13}$$

For zigzag chiral vectors this constraint becomes $k_y = \frac{2\pi\alpha}{ma}$ and for armchair chiral vectors, $k_x = \frac{2\pi\alpha}{\sqrt{3}ma}$. Thus rolling up a sheet of graphene into a nanotube has the effect of quantising the k-space vector component in the circumferential direction. There are now only m allowed values of this vector component, corresponding to the cases $\alpha = 0, 1, \cdots, m-1$. Replacing k_y (k_x) with the above quantised versions in the equation for the graphene band structure gives the required band structure for an armchair (zigzag) nanotube. Although graphene is a zero bandgap semiconductor, nanotubes can be either metallic or semiconducting depending on their rolling vector. This is determined by the quantisation conditions given above, which correspond to lines of allowed $\mathbf{k}$ values. If one of these lines passes through one of the discrete points forming the graphene Fermi surface, then the corresponding nanotube is metallic. It is easy to show that this occurs for nanotubes whose indices obey the constraint $(m - n) \bmod 3 = 0$. Therefore one third of nanotubes are metallic, including all nanotubes with an armchair chiral vector. The band structures of sample armchair and zigzag nanotubes are shown in Fig 3.5 a) and b).

Graphene Nanoribbons

An analogous approach to that taken for nanotubes is not as satisfactory for the case of nanoribbons. Such an approach, outlined in detail in Ref. [43], essentially consists of replacing the periodic boundary conditions used above for nanotubes with 'hard wall' boundary conditions $|\mathbf{k}, \pm\rangle(\mathbf{r_{edge}}) = 0$ so that the wavefunction goes to zero beyond the edge of the nanoribbon.

Taking this approach for zigzag nanoribbons (ZGNRs) breaks the sublattice symmetry since one edge of the ribbon consists solely of black sites and the other of white sites. The net effect of this is that a quantisation condition

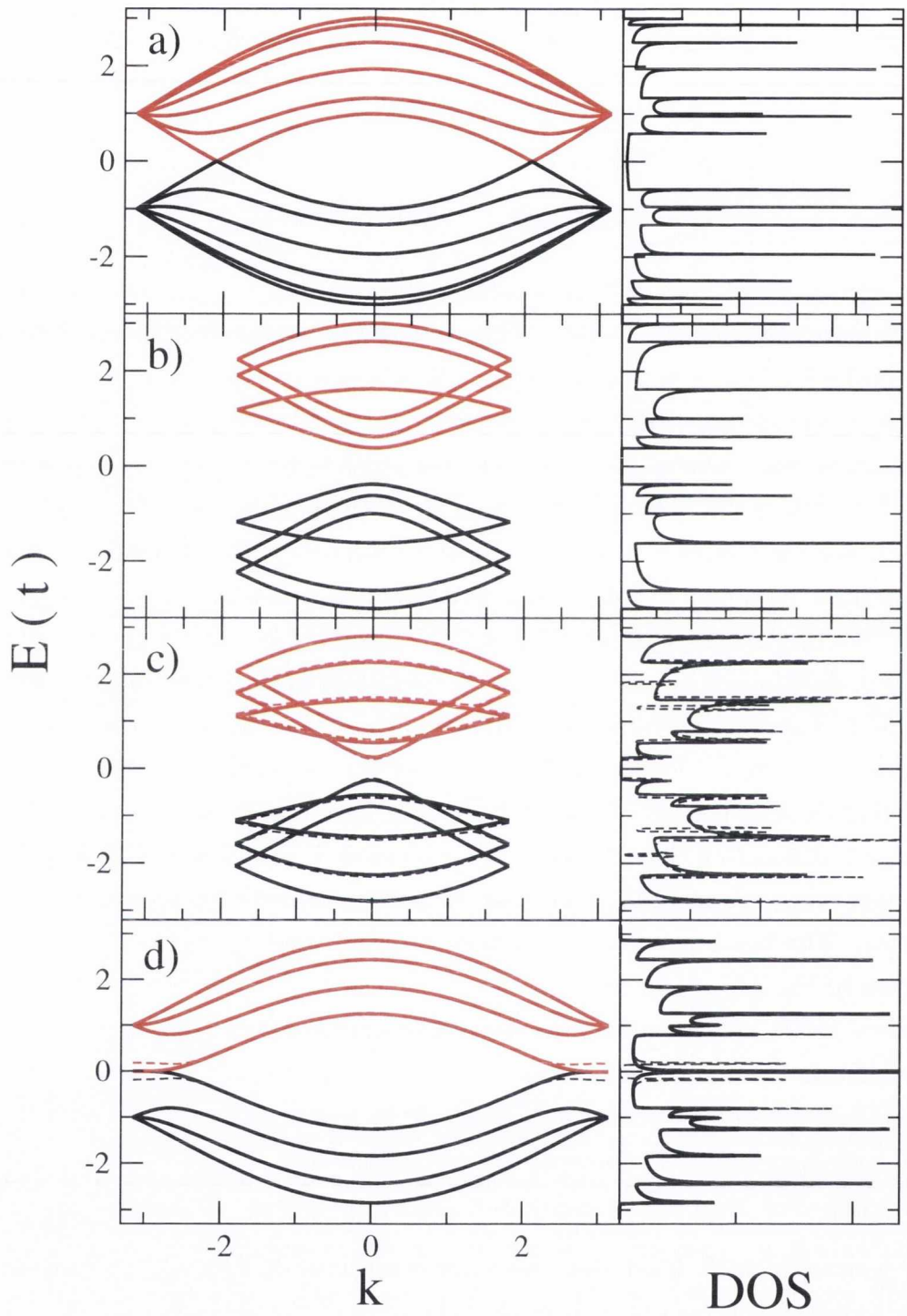

Figure 3.5: Band structure and density of states of a selection of quasi-one-dimensional graphene structures: a) $(5,-5)$ ZCNT, b) $(5,5)$ ACNT, c) 6-AGNR and d) 4-ZGNR. The dashed lines in the nanoribbon plots correspond to corrections to the simple tight-binding model to account for edge deformations in AGNRs and electron-electron effects in ZGNRs.

similar to that in Eq. 3.13 does not yield all the states of the system. The remaining state can be found from the solution of a transcendental equation which yields a complex value for the quantised wavevector [43,44]. This corresponds to the well-known states localised at the edge of the ribbon which contribute a large peak to the density of states at the Fermi energy. Indeed, when electron-electron interactions are included, as described in Chapter 2, spin polarised edges are found which decay towards the ribbon centre, with the ground state of the system having the two edges with opposite polarisation [40]. Alternatively, the band structure can be calculated numerically with or without electron-electron interactions by considering a unit cell containing lattice sites across the width of the ribbon. Then the standard Bloch function method can be applied by taking advantage of translational symmetry along the length of the ribbon. The band structure of a ZGNR is shown in Fig 3.5 d). The solid curves refer to a calculation neglecting electron-electron interactions whilst the dashed curves reveal the changes to the band structure when a Hubbard term $U = 1.33t$ is introduced. This value corresponds closely to results from experiment [156] and from *ab initio* calculations [157].

For armchair edged ribbons (AGNRs), an application of hard wall boundary conditions is more successful and reproduces the expected band structure for the tight-binding model. We note that the imposition of such boundary conditions in this case does not break the sublattice symmetry. However, the simple tight-binding description of armchair nanoribbons does not agree with the results of more sophisticated calculations, which suggest that a small deformation at the edge of the ribbon needs to be taken into account [52]. This can be included in the tight-binding calculations by changing the hopping parameter at the edge of the ribbon to $t_{edge} = 1.12t$. The unaltered tight-binding band structure finds that one third of AGNRs are metallic. However the alteration opens up a small band gap in these cases with the result that all AGNRs are found to be semiconducting, in agreement with Density Functional Theory predictions. In a similar manner to the zigzag case, the AGNR band structure can be calculated numerically with a larger unit cell. The band structure for a 6-AGNR without (solid) and with (dashed) the edge correction is shown in Fig 3.5 c).

For both of the principal nanoribbon geometries, we have seen that complications arise which prevent the calculation of their band structures using the application of simple boundary conditions to that of a graphene sheet. Since our principle requirement for calculating energy bands is to use them to calculate Green functions using Eq. 2.1, it may be more convenient to consider an alternative method to calculate the Green functions of such systems. We have considered such methods in Section 2.5 and in Section 3.4 we will illustrate how recursive methods can be used to calculate the Green functions of nanoribbons directly, without the need to calculate their band structure as an interim step.

3.3 Graphene green functions

Recall from the previous chapter that the matrix elements of the pristine Green function are given by an expression of the form

$$g_{jl} = \sum_a \langle j|\Psi_a\rangle \frac{1}{E-\epsilon_a} \langle \Psi_a|l\rangle \,. \tag{3.14}$$

where ϵ_a (Ψ_a) denotes the eigenvalues (eigenvectors) of the system, $|j\rangle$ is the orbital wavevector located at site j and the sum is taken over all the eigenstates of system.

For graphene, we have derived the eigensystem in terms of Bloch functions in reciprocal space, so the corresponding Green function expression consists of an integral over the first Brillouin Zone in place of the sum over discrete eigenstates above. The first BZ of graphene consists of a hexagon with vertices corresponding to the discrete Fermi surface of graphene, as shown in Fig. 3.6 a). For convenience, we can instead integrate over a rectangular area consisting of segments drawn from multiple neighbouring Brillouin zones whose area equals that of the hexagonal BZ. By translating the various segments outside the hexagon back into it, we can see that these rectangular BZs are equivalent. A few possibilities for the limits of integration are shown in Fig. 3.6 a) and b).

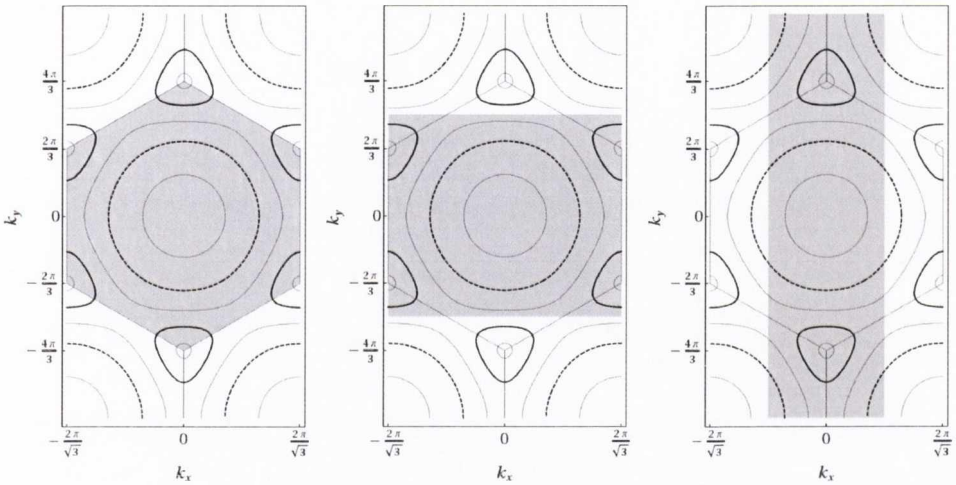

a) b) c)

Figure 3.6: The shaded areas highlight three different choices of Brillouin Zones that can be used when performing the integrations in this chapter. The contours represent constant energy surfaces of the graphene band structure.

The Green function expression becomes

$$\begin{aligned} g_{jl}^{n_j,n_l} &= \langle \mathbf{r}_j, n_j \,|\, \hat{g}(E) \,|\, \mathbf{r}_l, n_l \rangle \\ &= \frac{a}{2\pi} \frac{a\sqrt{3}}{4\pi} \int \mathrm{d}k_y \int \mathrm{d}k_x \, \frac{N(E)\, e^{i\mathbf{k}\cdot(\mathbf{r_l}-\mathbf{r_j})}}{E^2 - t^2\,|f(\mathbf{k})|^2} \,, \end{aligned} \tag{3.15}$$

where

$$N(E) = \begin{cases} E & \text{if} \quad n_j = n_l \\ tf(\mathbf{k}) & n_j = 1, n_l = 2 \\ tf^*(\mathbf{k}) & n_j = 2, n_l = 1 \,. \end{cases}$$

This integration can be approached in a number of ways. The most obvious is a two-dimensional numerical integration - however this can be prohibitively expensive if the Green function is required for many site indices or energy values. As we shall now demonstrate, one of the two integrals in this expression can be solved analytically, which reduces the numerical computation required to a one-dimensional integral. Furthermore, we shall show that for certain cases, the second integration can be approximated and solved with a

great deal of accuracy for the majority of energy values across the bandwidth.

3.3.1 First Integral

To simplify the resultant expressions, we rewrite the integral in terms of dimensionless wavevectors

$$k_A = \frac{ak_x}{2} \quad , \quad k_Z = \frac{\sqrt{3}ak_y}{2} \tag{3.16}$$

where the subscripts refer to the armchair and zigzag directions of these vectors, so that Eq. (3.15) becomes

$$g_{jl}^{n_j,n_l} = \frac{1}{2\pi^2}\int_{-\pi/2}^{\pi/2} \mathrm{d}k_Z \int_{-\pi}^{\pi} \mathrm{d}k_A \, \frac{N(E)e^{i(k_Z(m-n)+k_A(m+n))}}{E^2 - t^2(1+4\cos^2(k_Z)+4\cos(k_Z)\cos(k_A))} \, , \tag{3.17}$$

where we have rewritten the separation vector in terms of the lattice vectors,

$$\mathbf{r_l} - \mathbf{r_j} = m\,\mathbf{a}_1 + n\,\mathbf{a}_2 \, .$$

We now have a choice of which variable, k_Z or k_A to integrate over first. This choice is not important if we wish to perform the remaining integral numerically, but later we shall see that for other methods, or for calculating the Green functions of nanotubes analytically, the choice of first integration variable is important. With this in mind, we now illustrate how the first integral can be performed in both cases.

Armchair direction

Choosing to integrate over k_A first, we choose the Brillouin zone in Fig 3.6 b) and the integral that needs to be solved is

$$I_A = \int_{-\pi}^{\pi} \mathrm{d}k_A \, \frac{N(E)\; e^{i(k_Z(m-n)+k_A(m+n))}}{E^2 - t^2(1+4\cos^2(k_Z)+4\cos(k_Z)\cos(k_A))} \, . \tag{3.18}$$

This will be solved by transposing the problem to the complex plane and using the methods of contour integration, specifically the *residue theorem*

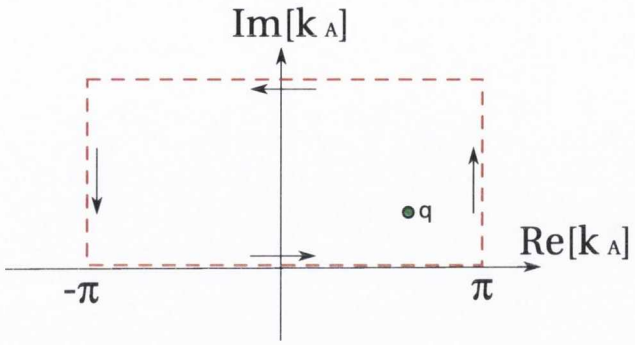

Figure 3.7: Integration contour in the complex k_A plane containing a pole q. The contour is closed in the upper half plane for $m + n \geq 0$.

[116, 153] . For $m + n \geq 0$, we consider the contour in the complex k_A plane shown in Fig 3.7. In the upper half plane, where $\mathrm{Im}(k_A) > 0$, the integrand vanishes as $\mathrm{Im}(k_A) \to \infty$, so that no contribution arises from the top section of the contour. Furthermore, we note that the net contribution from the left and right contours is also zero due to the integrands periodicity. Thus the integration we require is equivalent to the integral over the entire contour, which in turn reduces to a sum of the residues at the poles of the integrand. The poles, q, correspond to the zeroes of the denominator, and are given by

$$\cos(q) = \frac{\frac{E^2}{t^2} - 1 - 4\cos^2(k_Z)}{4\cos(k_Z)}. \tag{3.19}$$

Note that this equation does not define the pole uniquely as there are two possible solutions arising from a choice of sign when the inverse cosine is taken. The sign of the pole must be selected carefully to ensure that it lies within the integration contour, i.e., that $\mathrm{Im}(q) > 0$. The residue of a function of the form $f(z) = \frac{g(z)}{h(z)}$ at a pole z_0 is given by $\mathrm{Res}(f(z)) = \frac{g(z_0)}{h'(z_0)}$, where $h'(z) = \frac{\mathrm{d}h}{\mathrm{d}z}$. Thus the integral becomes

$$I_A = 2\pi i \left(\frac{N(E)\, e^{i(k_Z(m-n)+q(m+n))}}{4\, t^2\, \cos(k_Z)\sin(q)} \right) \tag{3.20}$$

and the Green function can be written

$$g_{jl}^{n_j,n_l} = \frac{i}{4\pi t^2} \int_{-\frac{\pi}{2}}^{\frac{\pi}{2}} \mathrm{d}k_Z \frac{N(E)\, e^{i(k_Z(m-n)+q(m+n))}}{\cos(k_Z)\sin(q)} . \tag{3.21}$$

Zigzag direction

To perform the k_Z integration first, we follow a similar approach to the previous case, but using the Brillouin zone shown in Fig 3.6 c). We again move to the complex plane and make use of the residue theorem, and consider a similar contour in the complex k_Z plane when $m-n \geq 0$. Again the solution reduces to a sum of the residues of poles, which are given this time by

$$\cos(q) = -\frac{1}{2}\left(\cos(k_A) \pm \sqrt{\frac{E^2}{t^2} - \sin^2(k_A)}\right) . \tag{3.22}$$

This time there are two poles inside the contour, arising from the choice of sign inside the brackets. Each of these poles must also have its overall sign chosen carefully as before to ensure it lies within the contour. The residues are calculated in a similar manner to before, and the required integral becomes

$$I_Z = \frac{2\pi i}{4t^2} \sum_q \frac{N(E)\, e^{i(q(m-n)+k_A(m+n))}}{\sin(2q) + \sin(q)\cos(k_A)} . \tag{3.23}$$

Thus the expression for the Green function in this case becomes

$$g_{jl}^{n_j,n_l} = \frac{i}{4\pi t^2} \sum_q \int_{-\pi}^{\pi} \mathrm{d}k_A \frac{N(E)\, e^{i(q(m-n)+k_A(m+n))}}{\sin(2q) + \sin(q)\cos(k_A)} . \tag{3.24}$$

Analytic expressions for nanotubes

As we have seen in section 3.2.3, the electronic band structure of achiral carbon nanotubes can be accurately found by imposing periodic boundary conditions on that of a graphene sheet. This has the effect of restricting the values that can be taken by electron wavevectors in either the armchair or zigzag direction. This allows us to replace one of the integrals in Eq. (3.15) with a sum over these allowed values. The remaining integral can then be

solved using the contour integration methods discussed above. A detailed account of this method for nanotubes can be found in Ref [116].

3.3.2 Second Integral

We have shown how the first integral in the calculation of the Green function can be performed in both the armchair and zigzag directions. We have also seen how the full analytical Green functions for certain one dimensional graphene systems follow from these calculations since one of the k-space integrals can be replaced with a sum over the finite k values imposed by quantisation. The remaining integral for two-dimensional graphene is not easily solveable in its current form, however it can be solved numerically with a lot less effort than the two-dimensional integral we started with. We shall now examine the remaining integral, and in particular the form of its integrand, to see if there are any cases when we can make approximations to solve it using analytical methods.

Fig. 3.8 plots the integrand (as a function of the integration variable) that appears in Eqs. (3.21) and (3.24) for a number of different cases. We note that the integrand corresponding to the off-diagonal Green function between two distant sites is either zero, or oscillates rapidly around zero over much of the integration range. This behaviour is easily understood from the exponential terms in the integrands which for large values of separation oscillate rapidly. This oscillatory behaviour is the key to performing the remaining integrals for large separations, as the contributions from the oscillatory sections of the integrand do not contribute significantly to the integral.

3.3.3 Stationary phase approximation

Consider a function of the form

$$I(x) = \int \mathrm{d}y \; f(y) \; e^{i\,\phi(y)\,x} \,. \tag{3.25}$$

For large, positive values of x, the exponential term will oscillate with a varying phase, $\phi(y)$ for large sections of the integrand. These oscillatory sections,

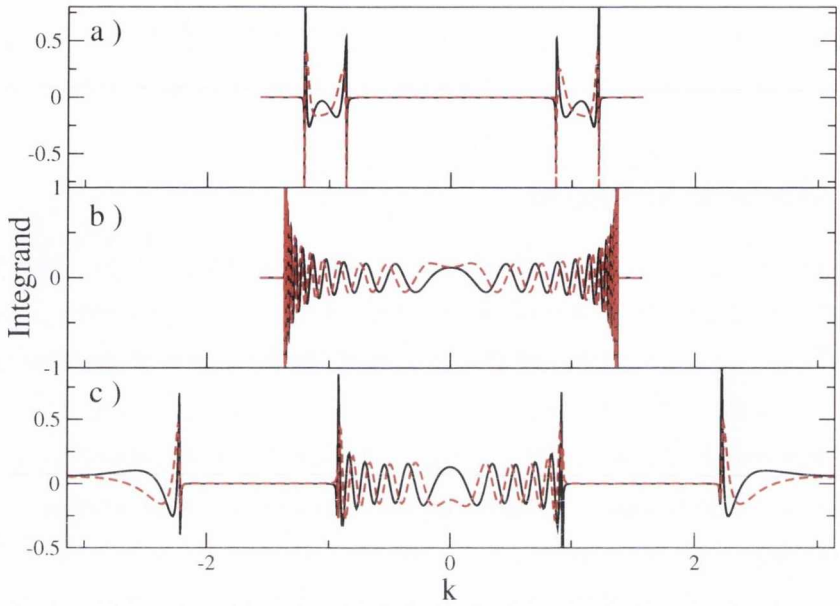

Figure 3.8: The integrand of the remaining integral for a) separation of $20\sqrt{3}a$ in the armchair direction for $E = 0.3|t|$, b) separation of $30\sqrt{3}a$ in the armchair direction for $E = 1.4|t|$, c) separation of $40a$ in the zigzag direction for $E = 0.8|t|$.

having different phase, will largely cancel each other out when an integration over y is performed. The only regions that will contribute significantly to the integral are those whose contributions add together coherently. These correspond to values of y near where the phase is stationary. The main idea of the Stationary Phase Approximation (SPA) [158] is to replace the integrand in Eq. (3.25) with a Taylor expansion around its stationary points, y^0 - the values of y for which the phase term is stationary and which are given by

$$\left.\frac{\mathrm{d}\phi}{\mathrm{d}y}\right|_{y^0} = 0\,. \tag{3.26}$$

The phase term becomes

$$\phi(y) \approx \sum_{y^0} \left[\phi(y_0) + \frac{1}{2}\left.\frac{\mathrm{d}^2\phi}{\mathrm{d}y^2}\right|_{y^0} (y - y^0)^2 + \cdots\right], \tag{3.27}$$

where the first order expansion term (not shown) is zero by the definition of the stationary points. Assuming that the function $f(y)$ is slowly varying about y_0, then each stationary point y^0 has a corresponding contribution given by

$$\begin{aligned} I_{y^0}(x) &= \int \mathrm{d}y\; f(y_0)\; e^{i\left[\phi(y_0)\,x + \frac{1}{2}\,\phi''(y^0)\,(y-y^0)^2\,x\right]} \\ &= f(y_0)\; e^{i\,\phi(y_0)\,x} \int \mathrm{d}y\; e^{i\,\frac{1}{2}\,\phi''(y^0)\,(y-y^0)^2\,x} \\ &= f(y_0)\; e^{i\,\phi(y_0)\,x} \sqrt{\frac{2\,i\,\pi}{\phi''(y^0)\,x}}\,, \end{aligned} \tag{3.28}$$

where the final integral has been performed using the well known Gaussian integral identity.

In the next two sections, we will apply this method to the integrals that appear in the expressions for the graphene Green functions. We note that the phase term in these expressions depends on the direction of the separation vector between the two sites. We shall calculate in detail the Green function between sites on the same graphene sublattice separated by vectors in the armchair and zigzag directions, and then briefly describe how the method can be generalised to other directions and cases. The two cases we discuss are the most frequently investigated in graphene lattices, and an analytic expression for the Green function in these directions will be extremely useful in calculating distance-dependent properties in graphene, as we shall see later.

Armchair Direction

The first case we shall examine is the Green function between two sites on the same sublattice separated by a vector in the *armchair direction*, corresponding to $m = n$ and shown schematically in Fig. 3.1. In this case we shall use the Green function expression calculated by first integrating over

k_A, given by Eq. (3.21), which now becomes

$$g_{jl}(E) = \frac{iE}{4\pi t^2} \int_{-\frac{\pi}{2}}^{\frac{\pi}{2}} \mathrm{d}k_Z \, \frac{e^{i\,q\,(m+n)}}{\cos(k_Z)\,\sin(q)} \,. \tag{3.29}$$

Note that the choices of separation and contour integration directions have led to a simple functional form for the phase term. Here it is simply the pole of the contour integral, given by Eq. (3.19). A plot of the pole as a function of k_Z at a certain energy is equivalent to the constant energy plot of the band structure of graphene at that energy, which provides a useful visualisation of the stationary points, k_Z^0. These points are found from Eq. (3.19) using the condition $\left.\frac{\mathrm{d}q}{\mathrm{d}k_Z}\right|_{k_Z^0} = 0$, which gives the following solutions

$$k_Z^0 = 0 \;,\; \pm\cos^{-1}\left(\frac{\sqrt{t^2 - E^2}}{2t}\right) \,. \tag{3.30}$$

We note that although both solutions are valid throughout the entire energy spectrum, there are regions in the spectrum where one or the other gives rise to complex values for the pole q. With these evanescent solutions, the integrand in Eq. (3.29) tends to vanish for any sizeable value of separation $m + n$. Consequently, we need only consider stationary solutions that yield real-valued solutions for q. For separations in the armchair direction this allows the energy spectrum to be divided into two distinct regimes

$$k_Z^0 = \begin{cases} \pm\cos^{-1}\left(\frac{\sqrt{t^2-E^2}}{2t}\right) & \text{if } |E| < |t| \\ 0 & \text{if } |E| > |t| \end{cases} \,. \tag{3.31}$$

Only for energy values near to $E = \pm t$ must we consider contributions from both stationary points. We can understand these regimes by examining the constant energy surfaces in reciprocal space, shown in Fig. 3.9a). The shaded area is the Brillouin Zone that we are integrating over in this case. Constant energy plots are shown for a number of different energies. At E=0, the surface is simply six discrete points. As the energy is increased, these points become roughly circular in shape and then triangular. A topologi-

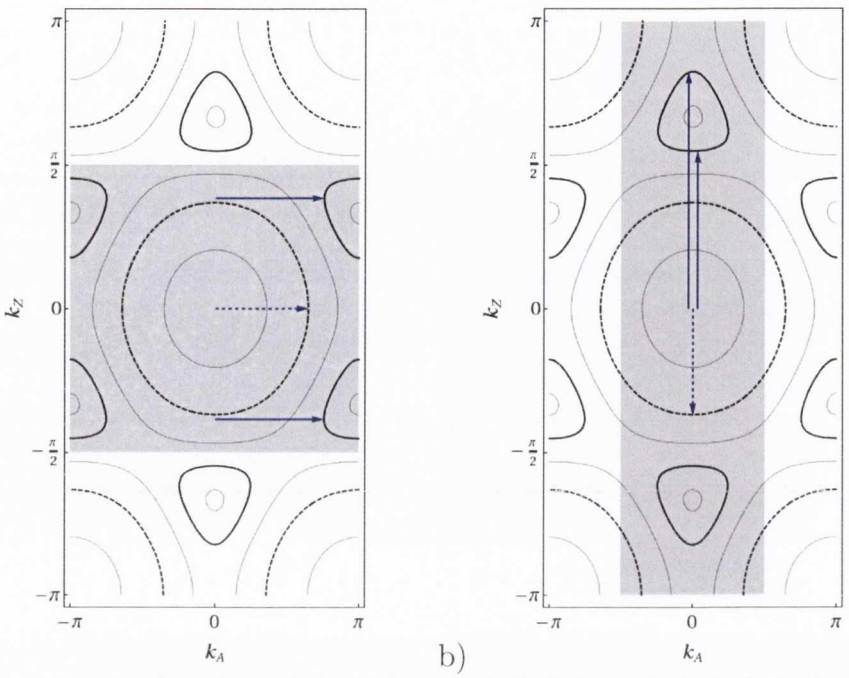

Figure 3.9: Constant energy plots, Brillouin zones (shaded areas) and stationary points for calculations in the a) armchair and b) zigzag direction. The thicker lines correspond to the energies $0.7t$ and $1.8t$ and the corresponding stationary wave vectors for these energies are highlighted with arrows.

cal change occurs at $E = t$, when the six shapes merge to form a single, large, hexagonal contour which shrinks and becomes roughly circular again as the energy increases further. Stationary values of the phase here correspond to flat regions of contour parallel to the y-axis. For $E < |t|$, there is one stationary point on each of the contours enclosing a Dirac point, whose corresponding value of k_Z^0 is energy dependent. Although there are four such points inside the chosen Brillouin Zone, only two obey the necessary sign convention for a pole of the contour integral and the contribution from each of these is easily shown to be identical. These stationary points and corresponding energy contours, are shown using solid, bold arrows and curves, for $E = 0.7|t|$ in the energy contour plot. For $E > |t|$, there is only one stationary solution for the pole, which is fixed at $k_Z^0 = 0$. This point corresponds to the top of the central contour formed for this energy range and again its sign must be chosen to ensure the stationary value for the pole lies within

the first integration contour. This type of stationary point and contour are illustrated for $E = 1.8|t|$ using dashed arrows and curves in Fig 3.9a).

Now that we have identified the relevant stationary points, we proceed with the SPA approach outlined above. The wavevector q, when expanded in a Taylor series around a stationary point k_Z^0 has no linear component and is approximated, up to second order, by

$$q\,(k_Z) \approx \mathcal{Q}(E) \;+\; \mathcal{W}(E)\;(k_Z - k_Z^0)^2\,, \tag{3.32}$$

where

$$\mathcal{Q}(E) = \begin{cases} \pm\,\cos^{-1}\left(-\sqrt{1-\frac{E^2}{t^2}}\,\right) & \text{if } |E| < |t| \\ \pm\,\cos^{-1}\left(\frac{E^2-5t^2}{4t^2}\,\right) & \text{if } |E| > |t| \end{cases} \tag{3.33}$$

and

$$\mathcal{W}(E) = \begin{cases} \pm\,\frac{E^2+3t^2}{2E\sqrt{t^2-E^2}} & \text{if } |E| < |t| \\ \pm\,\frac{E^2+3t^2}{2\sqrt{(t^2-E^2)(E^2-9t^2)}} & \text{if } |E| > |t| \end{cases}\,. \tag{3.34}$$

The sign of $\mathcal{Q}(E)$ must be chosen as before to ensure that it lies within the integration contour. In addition to this, the correct sign of $\mathcal{W}(E)$ must be determined by its correspondence to the curvature of q at the stationary point.

Substituting the expression q, Eq. (3.32), into the integral in Eq. (3.29) yields a much-simplified expression for the Green function

$$\begin{aligned} g_{jl}(E) &= \frac{iE}{4\pi t^2} \sum_{k_Z^0} \frac{e^{i\mathcal{Q}(E)\,(m+n)}}{\cos(k_Z^0)\sin(\mathcal{Q}(E))} \int_{-\frac{\pi}{2}}^{\frac{\pi}{2}} \mathrm{d}k_Z\; e^{i\,\mathcal{W}(E)\,(k_Z-k_Z^0)^2\,(m+n)} \\ &= \frac{iE}{4\pi t^2} \sum_{k_Z^0} \sqrt{\frac{i\pi}{\mathcal{W}(E)(m+n)}}\; \frac{e^{i\mathcal{Q}(E)\,(m+n)}}{\cos(k_Z^0)\sin(\mathcal{Q}(E))}\,, \end{aligned} \tag{3.35}$$

where the number of stationary points, k_Z^0 to be summed over is determined by the energy regime discussed above. By using the definitions of $\mathcal{Q}(E)$ and $\mathcal{W}(E)$ above we can rewrite a more complete analytic expression for the

Green function in the two distinct energy regimes. For $E > 0$, we find

$$g_{jl}(E) = \sqrt{\frac{2}{i\pi}} \frac{1}{\sqrt{m+n}} \frac{1}{\sqrt{(E^2+3t^2)\sqrt{t^2-E^2}}} \times \times \begin{cases} -i\sqrt{E}\, e^{i\mathcal{Q}(E)\,(m+n)} & \text{if } |E| < |t| \\ \frac{E}{(E^2-9t^2)^{\frac{1}{4}}}\, e^{i\mathcal{Q}(E)\,(m+n)} & \text{if } |E| > |t| \end{cases} . \tag{3.36}$$

Panels (a) and (b) of Fig. 3.10 compare the real and imaginary parts of the Green function for the case of $m+n = 10$, calculated using both the analytical expressions derived above and a numerical evaluation of the integral. We note that at this separation there is an excellent agreement between the two methods over the entire band. The contributions from the individual stationary points are illustrated in panels (c) and (d) to verify the splitting of the band into two energy regimes and we can clearly see that one of the stationary points dominates in each of these regions. To test how good an approximation Eq. (3.35) is, we plot, as a function of separation, the fraction of the bandwidth $\mathcal{F}_{1\%}$ for which the relative error between the numerical and analytical evaluations is less than 1% in Fig 3.11. The armchair direction corresponds to the plot with circular points and we see that even for small separations ($\approx 10a$), the energy range for which the Green functions are very accurately described exceeds 90% of the bandwidth. In other words, there is only a very narrow energy range for which the disagreement exceeds 1%, and this range decreases rapidly as the separation is increased.

Zigzag Direction

We now turn our attention to the case of separation vectors along the zigzag direction, for which the procedure followed is almost identical to that for the armchair direction. From Eq. (3.24), the Green function integral we need to solve is

$$g_{jl} = \frac{iE}{4\pi t^2} \sum_q \int_{-\pi}^{\pi} \mathrm{d}k_A \, \frac{e^{iq(m-n)}}{\sin(2q) + \sin(q)\cos(k_A)} . \tag{3.37}$$

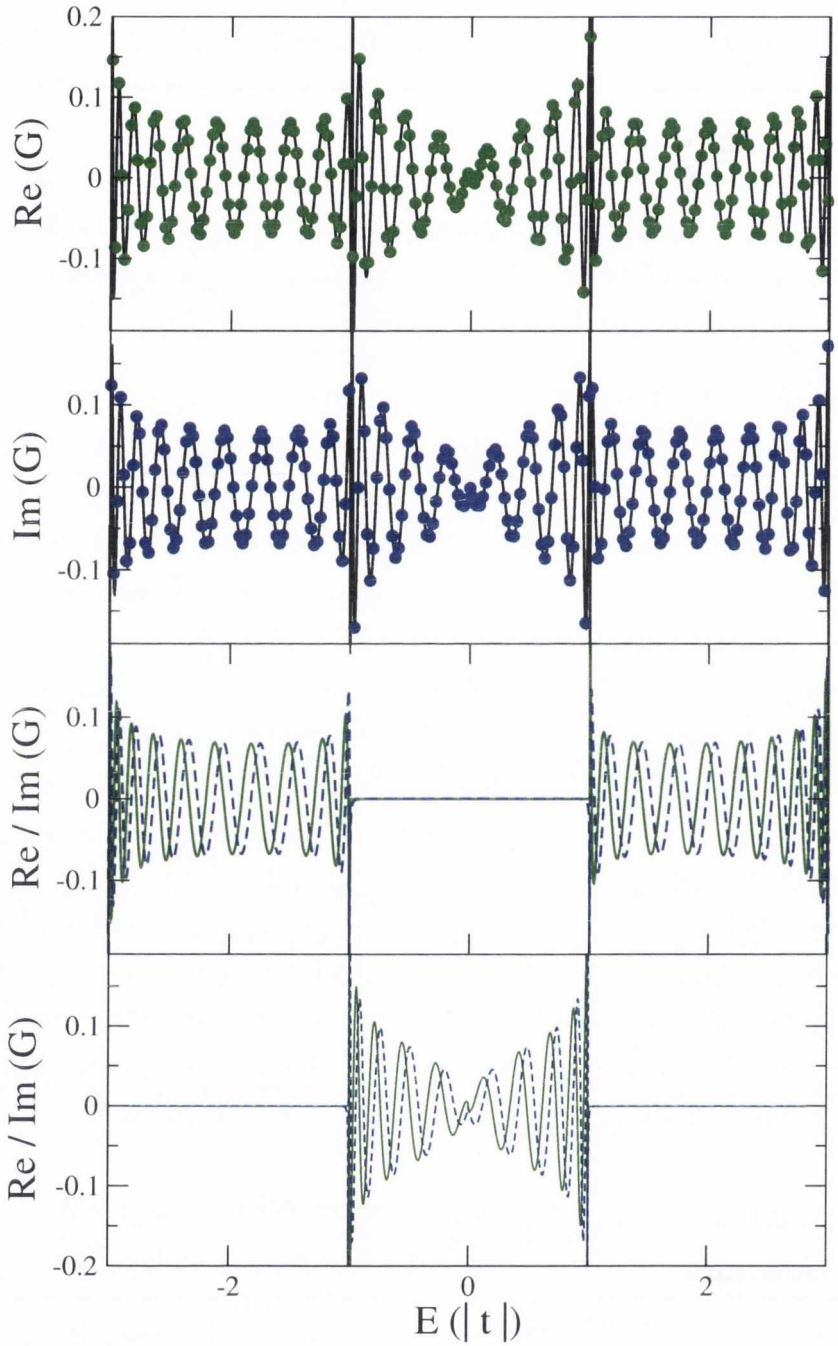

Figure 3.10: a) Real and b) imaginary parts of the Green function between two sites separated by $m + n = 20$ in the armchair direction calculated using the SPA method (solid lines) and numerical integration (symbols). The bottom two panels show the contributions to the real (green) and imaginary (blue) SPA Green function arising from the two different stationary points. It is clear that the energy band can be divided between them as discussed in the text.

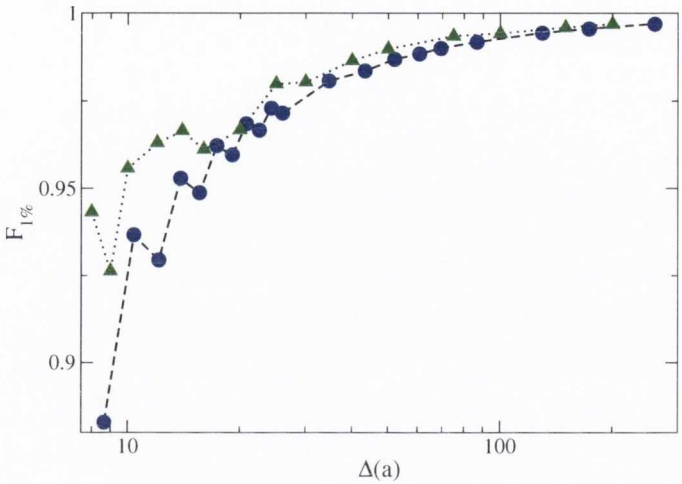

Figure 3.11: Percent of the band with less than 1% difference between the numerical and SPA Green functions in the armchair (circle) and zigzag (triangle) directions

In this equation the phase term is the pole arising from the contour integration over k_Z and the stationary points are the values of k_A where this is stationary. Recall that the contour integral in this case has two poles and the contributions from these must be summed to give the total result. The stationary points, k_A^0, for each pole are found from the condition $\frac{\mathrm{d}q}{\mathrm{d}k_A}\Big|_{k_A^0} = 0$ which gives only one stationary point inside the Brillouin Zone,

$$k_A^0 = 0\,. \tag{3.38}$$

Unlike the stationary points calculated for the armchair direction, the zigzag direction stationary points are independent of energy. This fact is evident when the constant energy plots shown in Fig 3.9 are examined from the perspective of stationary values of k_A. The separation of the energy band into two separate regions is not necessary in this case as the stationary points for both regions occur for the same value of k_A. The wavevector q is now Taylor expanded as before and we find expressions for $\mathcal{Q}(E)$ and $\mathcal{W}(E)$ analogous to Eqs. (3.33) and (3.34), except now we have to account for two poles rather

than one. This gives

$$\begin{aligned} \mathcal{Q}^{+} &= \pm \cos^{-1}\left(\frac{-t-E}{2t}\right) \\ \mathcal{Q}^{-} &= \pm \cos^{-1}\left(\frac{-t+E}{2t}\right) \end{aligned} \tag{3.39}$$

and

$$\begin{aligned} \mathcal{W}^{+} &= \pm\frac{t}{2E}\,\frac{t+E}{\sqrt{(3t+E)(t-E)}} \\ \mathcal{W}^{-} &= \pm\frac{t}{2E}\,\frac{t-E}{\sqrt{(3t-E)(t+E)}} \end{aligned}, \tag{3.40}$$

where the superscript sign in the expressions for $\mathcal{Q}$ and $\mathcal{W}$ refer to the sign choice in the pole definition, Eq. (3.22). Using these expressions the integral again reduces to a Gaussian integral whose solution gives

$$g_{jl}(E) = \frac{iE}{4\pi t^2}\sum_{\alpha=\pm}\sqrt{\frac{i\pi}{\mathcal{W}^{\alpha}(m-n)}}\,\frac{e^{i\,\mathcal{Q}^{\alpha}(E)(m-n)}}{\sin(2\mathcal{Q}^{\alpha}(E))+\sin(\mathcal{Q}^{\alpha}(E))\cos(k_A^0)}\,. \tag{3.41}$$

Using Eqs 3.39 and 3.40 we can once more write a more complete analytic expression for the Green function. For $E > 0$, this becomes

$$\begin{aligned} g_{jl}(E) = \sqrt{\frac{1}{2i\pi(m-n)}}\Bigg(&\sqrt{\frac{E}{|t|(t+E)}}\,\frac{e^{i\mathcal{Q}^{+}(E)(m-n)}}{((3t+E)(t-E))^{\frac{1}{4}}} \\ &+\sqrt{\frac{E}{|t|(t-E)}}\,\frac{e^{i\mathcal{Q}^{-}(E)(m-n)}}{((3t-E)(t+E))^{\frac{1}{4}}}\Bigg)\,. \end{aligned} \tag{3.42}$$

Fig. 3.12 compares the Green function calculated analytically with that from a numerical calculation for a separation of $m-n = 20$ and again we note an excellent agreement across the band. The plot with triangular symbols in Fig. 3.11 shows the discrepancy between the numerical and analytical results as a function of distance. As in the armchair direction case, we find that beyond a couple of lattice spacings there is only a very narrow energy

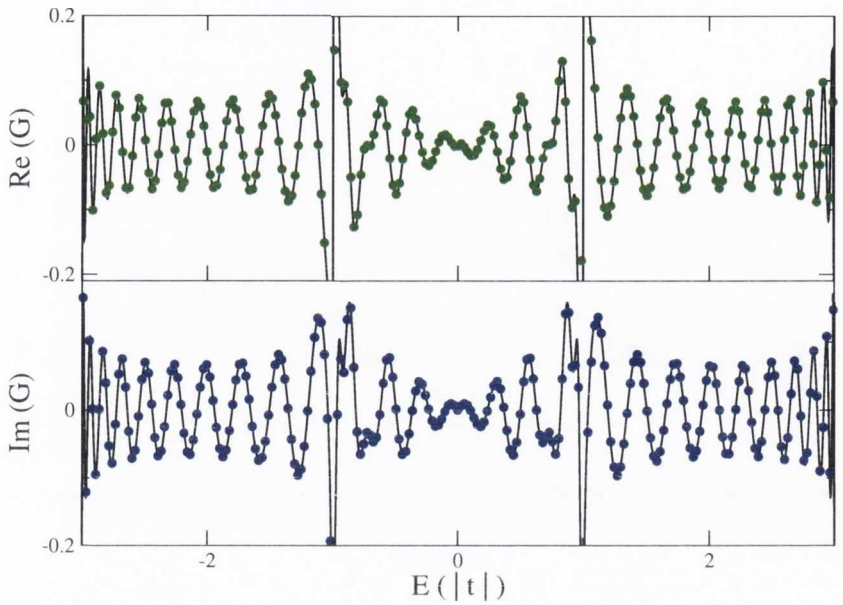

Figure 3.12: a) Real and b) imaginary parts of the Green function between two sites separated by $m - n = 20$ in the zigzag direction calculated using the SPA method (solid lines) and numerical integration (symbols).

range in which the disagreement exceeds 1%.

Other directions

Having presented the derivation of the Green function for the separation vector along the armchair and zigzag directions, it is straightforward to generalise it to other cases. For arbitrary directions, although the procedure is similar, we shall see that the identification of the poles or stationary solutions may result from high order polynomial equations that are not always analytically solvable.

In the armchair (zigzag) case, the expression for the stationary point is given by an easily solvable expression of the form $dq/dk = 0$. This expression arises from the decision to take the contour integral along the k-space direction parallel to the separation vector, which results in a phase term equal to the pole of the contour integral. Since the expressions for the poles in the armchair and zigzag directions, Eqs.(3.19) and (3.22) respectively, are easily found from Eq. (3.9) , the calculation of all the necessary quantities

is quite straightforward. To extend this approach to an arbitrary separation vector, we must first rewrite Eq. (3.9) in terms of k-space vectors $k_{\parallel}$ and $k_{\perp}$ which are parallel and perpendicular respectively to the required separation vector. Following this, we must perform the contour integral over $k_{\parallel}$ to get an expression for the Green function analogous to Eqs. (3.21) and (3.24). However, the expression for the poles of this contour integral will depend strongly on the separation vector chosen and will usually result from a high order polynomial equation that may need to be solved numerically. It is important to note that this equation will only depend on the direction, and not the length, of the separation vector, so that once the Green function for a particular direction has been constructed it is valid for any required distance across the graphene lattice in that direction.

A similar methodology holds for the case of Green functions between sites on the different sublattices of graphene. In this case Eq. 3.15 must be altered slightly to read

$$g_{jl}^{1,2} = \frac{a}{2\pi}\frac{a\sqrt{3}}{4\pi}\int \mathrm{d}k_y \int \mathrm{d}k_x \frac{t\, f(\vec{k})\, e^{i\mathbf{k}\cdot(\mathbf{r_l}-\mathbf{r_j})}}{E^2 - t^2\,|f(\mathbf{k})|^2}\,, \tag{3.43}$$

The integral can now be split into two parts with different phase terms coming from the two components of $f(\vec{k})$. These can then be solved individually using the approach described above to give the required Green function.

3.3.4 Application of SPA Green functions

The usefulness of having an analytical expression for the real space Green function, valid throughout the entire electronic energy band, becomes obvious when physical properties of graphene involving energy scales outside the linear dispersion region are investigated. This is particularly advantageous when such properties carry size or position dependence because in this case Eq. (3.35) for the armchair direction, or Eq. (3.41) for the zigzag direction, can be more concisely expressed in the form

$$\mathcal{G}_{\Delta}(E) = \frac{\mathcal{A}(E)\, e^{i\mathcal{Q}(E)\Delta}}{\sqrt{\Delta}}\,, \tag{3.44}$$

where Δ represents the separation between sites, so that the E- and Δ-dependences are clearly distinguished. Furthermore, even in the case when the functional form of the coefficient $\mathcal{A}(E)$ is not particularly simple, the expressions in Eqs. (3.35) and (3.41) can be used to expand the Green function in a polynomial series, which is undoubtedly far simpler and more treatable than the original expression in Eq. 3.15. The ability to clearly isolate the distance dependence in the Green function clearly allows a more transparent treatment of some of the more eagerly investigated properties of graphene.

This approach will be shown more clearly in later chapters when our formalism is used to investigate the interaction between magnetic moments in graphene. This type of interaction is perfectly suited for investigation using our approach since it is mediated by the conduction electrons of the graphene host. We will consider the case of static moments (Chapter 5) and precessing moments (Chapter 6) using this formalism. However, there are many other interesting physical properties that can be explored. A topic that lends itself to our approach is the effect of disorder [68] and in particular, the effect of an impurity, on the properties of graphene. Friedel oscillations, occurring in the local density of states as a function of distance from an introduced impurity, have been studied within the linear dispersion regime using a Green function formalism [159]. Although the local density of states is associated with the diagonal term of the Green function, the distance dependence of the oscillations will be determined solely by the off-diagonal term calculated here. Similarly, the signatures of magnetic adatoms in graphene when probed by scanning tunnelling spectroscopy have also been investigated using a theoretical approach [160]. This method again avails of Green function methods within the linear dispersion regime. We anticipate that the SPA approach may allow for an extension of such studies to energies beyond the linear dispersion regime.

3.4 Recursive Methods

In Section 3.2.3, we outlined reasons why the fully analytic approach to calculating Green functions can run into difficulties when applied to the case of graphene nanoribbons. Either the formation of edge states in zigzag ribbons or the edge hopping-parameter variation needed to return the correct properties of armchair edged ribbons render the application of hard-edge boundary conditions to the band structure of a graphene sheet inappropriate. Instead, we demonstrate here how the recursive methods introduced in the previous chapter provide an alternative method to calculate Green functions in these systems. The method involves first calculating the Green function matrix for one unit cell of the nanoribbon in question and then using this with left and right hopping matrices in the simple recursive or Rubio-Sancho methods outlined previously.

3.4.1 AGNRs

For armchair-edged GNRs the repeated unit cell consists of two linear chains connected at every second atom, as shown schematically for an 6-AGNR in Fig 3.13. In Section 3.2.3, we used this unit cell to calculate the Hamiltonian and electronic band structure of AGNRs. In the simplest tight-binding approach every hopping element is equal to that in a graphene sheet and a third of all AGNRs are found to be metallic. As discussed earlier, this does not agree with *ab initio* results that predict all AGNRs to be semiconducting [52]. The discrepancy can be explained by a contraction of the π bond at the edge of the ribbon. The relevant bonds are shown in red in Fig 3.13. The contraction of these bonds leads to a 12% increase in the value of the corresponding hopping parameter. When this is taken into account, the tight-binding results once more agree with those from more detailed calculations and the band structure shown in Fig. 3.5 is found.

To calculate the Greens function for this system, we must construct the Green function for a disconnected unit cell of the system, $\hat{g}_{00}$. This is found by inverting the matrix $E\hat{I} - \hat{\mathcal{H}}_{00}$, where the Hamiltonian matrix for the unit

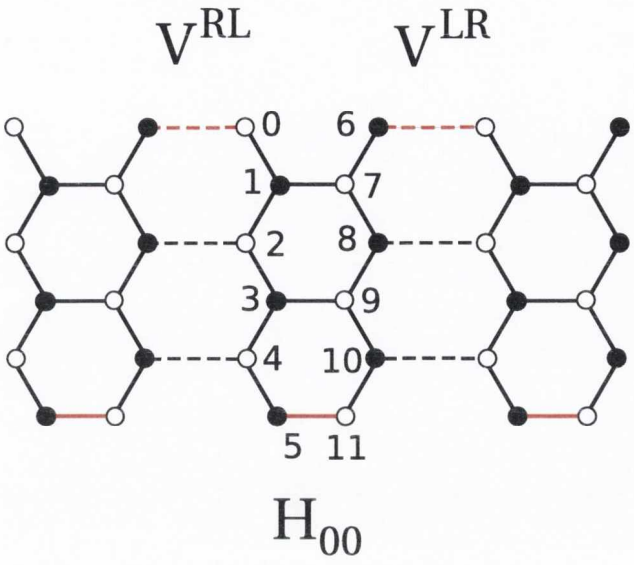

Figure 3.13: Unit cell and connection matrices (dashed lines) for a 6-AGNR. The red lines correspond to contracted bonds in the unit cell and connection matrices.

cell (for the example case of a 6-AGNR) is given by

$$\mathcal{H}_{00} = \begin{pmatrix} \epsilon_0 & t & 0 & 0 & 0 & 0 & 0 & 0 & 0 & 0 & 0 & 0 \\ t & \epsilon_0 & t & 0 & 0 & 0 & 0 & t & 0 & 0 & 0 & 0 \\ 0 & t & \epsilon_0 & t & 0 & 0 & 0 & 0 & 0 & 0 & 0 & 0 \\ 0 & 0 & t & \epsilon_0 & t & 0 & 0 & 0 & 0 & t & 0 & 0 \\ 0 & 0 & 0 & t & \epsilon_0 & t & 0 & 0 & 0 & 0 & 0 & 0 \\ 0 & 0 & 0 & 0 & t & \epsilon_0 & 0 & 0 & 0 & 0 & 0 & 1.12t \\ 0 & 0 & 0 & 0 & 0 & 0 & \epsilon_0 & t & 0 & 0 & 0 & 0 \\ 0 & t & 0 & 0 & 0 & 0 & t & \epsilon_0 & t & 0 & 0 & 0 \\ 0 & 0 & 0 & 0 & 0 & 0 & 0 & t & \epsilon_0 & t & 0 & 0 \\ 0 & 0 & 0 & t & 0 & 0 & 0 & 0 & t & \epsilon_0 & t & 0 \\ 0 & 0 & 0 & 0 & 0 & 0 & 0 & 0 & 0 & t & \epsilon_0 & t \\ 0 & 0 & 0 & 0 & 0 & 1.12t & 0 & 0 & 0 & 0 & t & \epsilon_0 \end{pmatrix},$$

where we set $\epsilon_0 = 0$ and use $t = -2.7eV$ as our energy unit. To calculate Green functions of the system using recursive methods we also need the connection matrices V^{LR} and V^{RL} containing hopping parameters between a

unit cell and its neighbours to the right and left respectively. These matrices are quite sparse and for the 6-AGNR considered here the only non-zero matrix elements are

$$\begin{aligned} V^{LR}_{6,0} &= 1.12t & V^{RL}_{0,6} &= 1.12t \\ V^{LR}_{8,2} &= t & V^{RL}_{2,8} &= t \\ V^{LR}_{10,4} &= t & V^{RL}_{4,10} &= t \end{aligned} \quad ,$$

where the matrix indices correspond to the atoms as labelled in Fig 3.13. Having constructed these matrices, we can now use them in the algorithms discussed in Chapter 2. Fig 3.14 shows the surface Green function as a function of energy for 6-AGNRS with 1, 16 and 256 cells compared to that for a semi-infinite system calculated using the Rubio-Sancho method. The inset plot for the semi-infinite case shows the number of iterations needed for convergence of the algorithm as a function of energy. The bottom panel shows the Green function of an infinite ribbon constructed by joining together two semi-infinite ribbon leads.

3.4.2 ZGNRs

To calculate the Green functions of zigzag edged ribbons using recursive techniques we follow a similar approach to that outlined above for AGNRs. The repeated unit cell in this case is a single atomic chain shown schematically for a 4-ZGNR in Fig 3.15. The Green function matrix for the disconnected unit cell is again found from $\hat{g}_{00} = (E\hat{I} - \hat{\mathcal{H}}_{00})^{-1}$, where

$$\mathcal{H}_{00} = \begin{pmatrix} \epsilon_0 & t & 0 & 0 & 0 & 0 & 0 & 0 \\ t & \epsilon_1 & t & 0 & 0 & 0 & 0 & 0 \\ 0 & t & \epsilon_2 & t & 0 & 0 & 0 & 0 \\ 0 & 0 & t & \epsilon_3 & t & 0 & 0 & 0 \\ 0 & 0 & 0 & t & \epsilon_4 & t & 0 & 0 \\ 0 & 0 & 0 & 0 & t & \epsilon_5 & t & 0 \\ 0 & 0 & 0 & 0 & 0 & t & \epsilon_6 & t \\ 0 & 0 & 0 & 0 & 0 & 0 & t & \epsilon_7 \end{pmatrix}$$

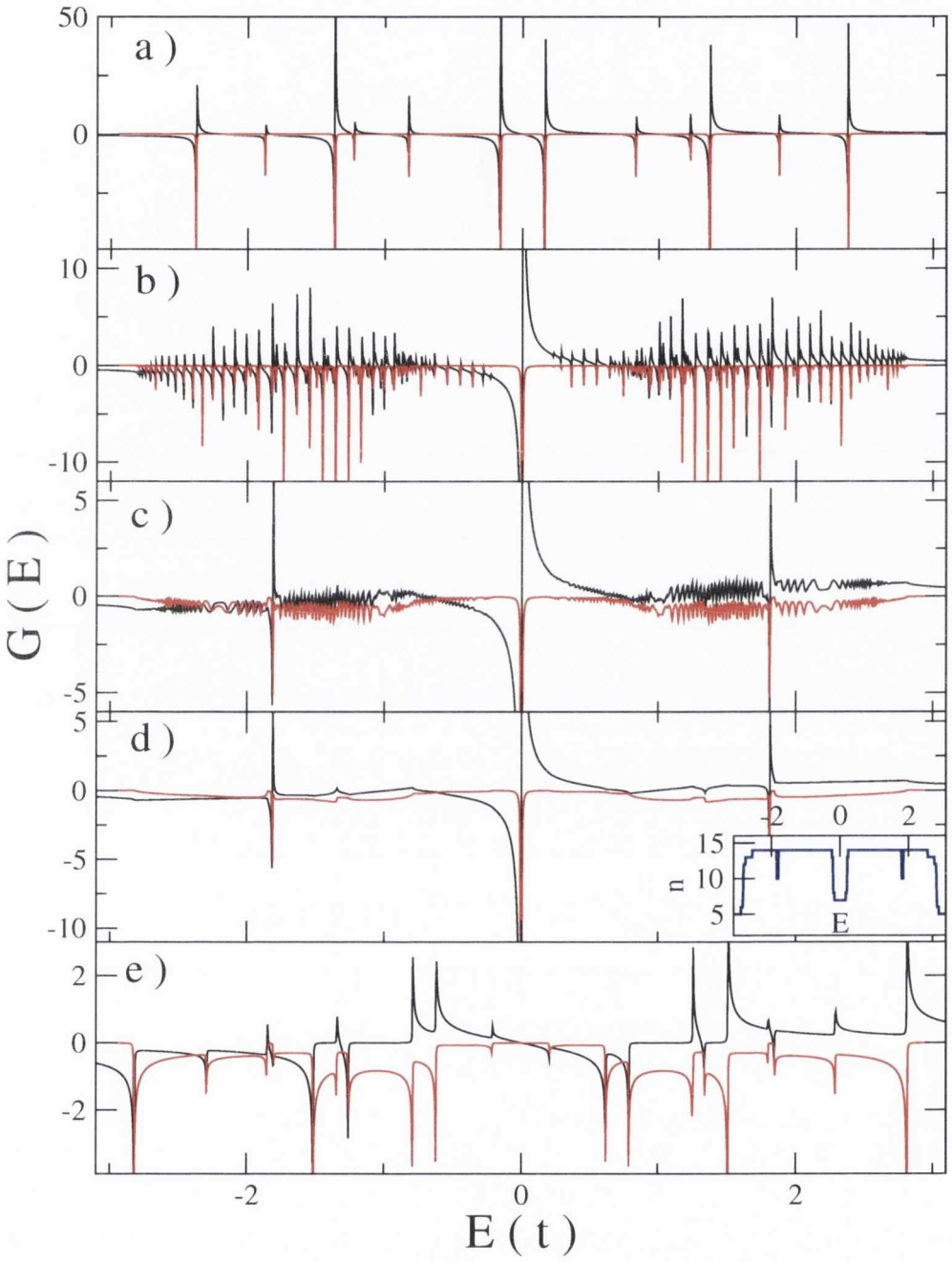

Figure 3.14: Real (black) and imaginary (red) components of the surface Green function for 6-AGNRs with lengths of a) 1, b) 16 and c) 256 unit cell(s). Panels d) and e) show the semi-infinite and infinite ribbon Green functions calculated within the Rubio-Sancho scheme. The inset shows the number of steps, n, in the Rubio-Sancho scheme needed to achieve convergence.

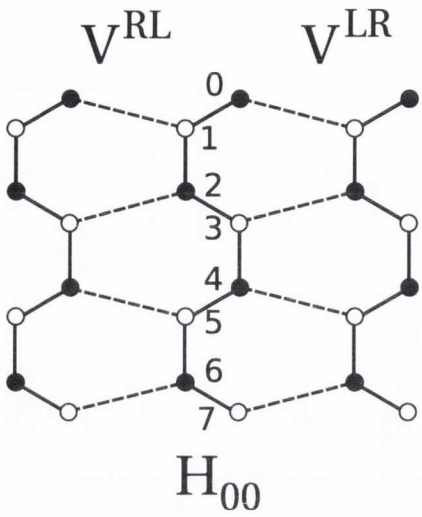

Figure 3.15: Unit cell and connection matrices (dashed lines) for a 4-ZGNR.

and the matrices connecting the unit cell to its neighbours on the right and left are given by

$$V^{LR} = \begin{pmatrix} 0 & t & 0 & 0 & 0 & 0 & 0 & 0 \\ 0 & 0 & 0 & 0 & 0 & 0 & 0 & 0 \\ 0 & 0 & 0 & 0 & 0 & 0 & 0 & 0 \\ 0 & 0 & t & 0 & 0 & 0 & 0 & 0 \\ 0 & 0 & 0 & 0 & 0 & t & 0 & 0 \\ 0 & 0 & 0 & 0 & 0 & 0 & 0 & 0 \\ 0 & 0 & 0 & 0 & 0 & 0 & 0 & 0 \\ 0 & 0 & 0 & 0 & 0 & 0 & t & 0 \end{pmatrix} \qquad \text{and} \qquad V^{RL} = V^{LR\,\dagger}.$$

When dealing with a non magnetic zigzag ribbon with $U = 0$ we set $\epsilon_i = 0$. However, if we want to construct the Green functions of a magnetic ribbon, the degeneracy is broken between the Green functions for up-spin and down-spin electrons and the onsite potentials are calculated using the self-consistent procedure described in Section 2.8. We can now use these matrices in the recursive Green function algorithms to calculate the necessary quantities. Fig 3.16 shows the resulting Green function at edge (a) and central (b) sites in an infinite nonmagnetic 4-ZGNR. The insets show the number of unit

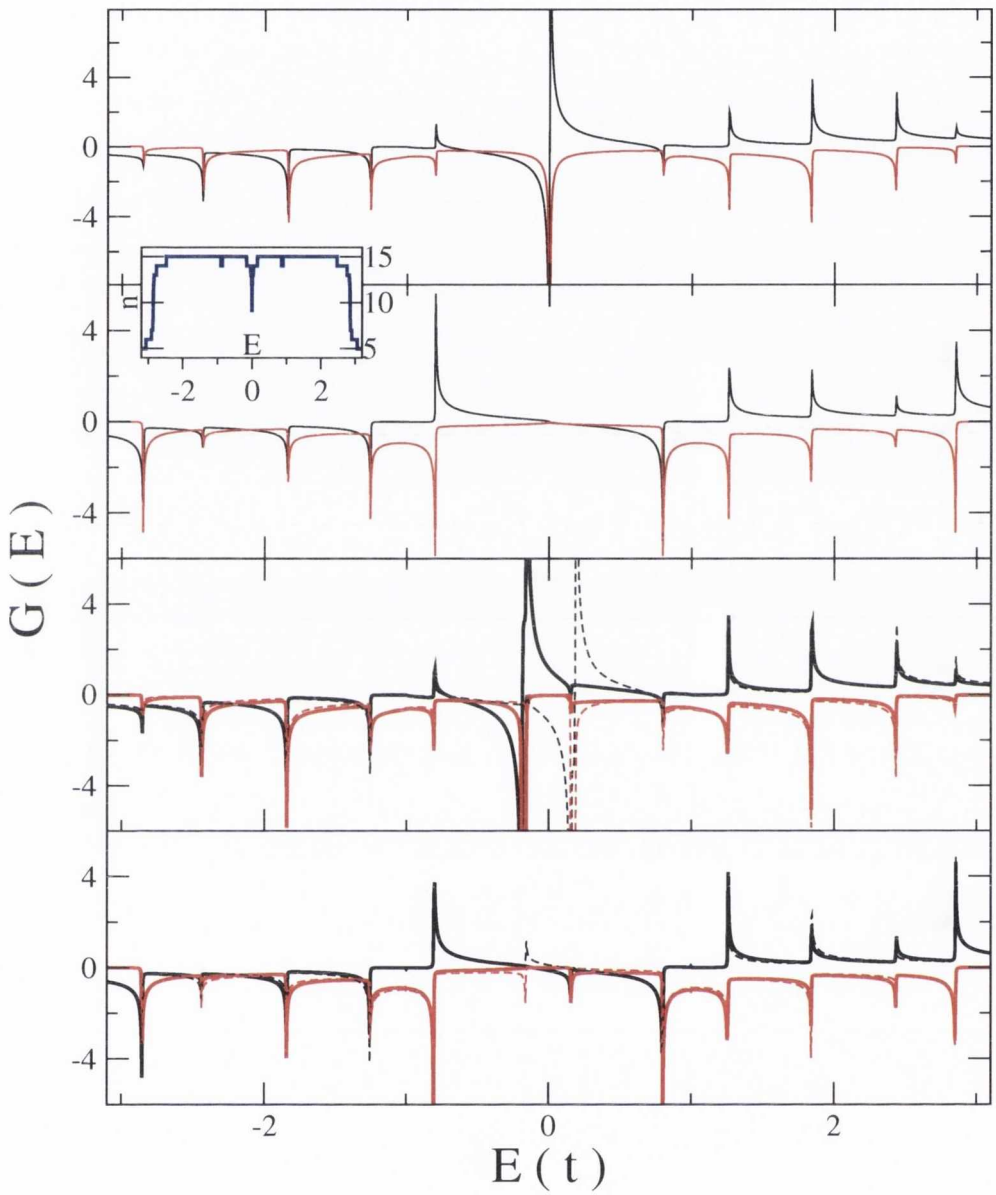

Figure 3.16: Green function matrix elements calculated at the edge (a) and central (b) sites in an infinite nonmagnetic 4-ZGNR, where the inset shows the number of steps in the Rubio-Sancho scheme needed to achieve convergence. The bottom panels show the Green functions for both majority (bold) and minority (dashed) spin electrons at the edge (c) and centre (d) of a magnetic ribbon.

cells required for convergence of the semi-infinite Green function used in its construction. A large peak in the imaginary part of the Green function for the edge site is noted corresponding to a large density of states at the Fermi energy arising from the localised band formation. This feature is not present in the Green function for the central site. The bottom panels show the Green functions for both majority (bold) and minority (dashed) spin electrons[1] taken at edge (c) and central (d) sites for a magnetic ribbon with $U = 1.33t$, corresponding to the band structure shown in Fig. 3.5. We note that the edge peak previously present at the Fermi energy has split into two parts - a majority-spin peak below the Fermi energy and a minority-spin above it, in agreement with the results of *ab initio* calculations.

3.5 Summary of Chapter

In this chapter we shifted our attention from the general description of Green functions given in Chapter 2 to a specific discussion of their calculation in the case of graphene and related materials. In section 3.2 the electronic structure of graphene was calculated within the nearest-neighbour tight-binding approximation which will be used throughout this thesis. The resulting band structure was analysed and a brief discussion of the popular linear approximation often used for small Fermi energies was given. The band structures of one-dimensional graphene systems, namely nanotubes and nanoribbons, were presented and their calculation related to that of graphene sheets.

Section 3.3 focused on calculating the Green function matrix elements for graphene sheets. The calculation was first of all reduced to a one dimensional integral using contour integration, allowing for much more efficient numerical calculation. Furthermore, we showed that in certain cases the remaining integral could be approximated analytically with great accuracy using the Stationary Phase Approximation. A detailed description of this calculation for the two principal high-symmetry directions in graphene and an outline

[1]The terms 'majority' and 'minority' spin are used here loosely, as the imbalance is localised to the edge. If, say, the spin-up is the majority-spin orientation at one edge it will be the minority-spin orientation at the opposite edge.

of its implementation in more general cases was given. The existence of an analytical expression for the Green function allows for the behaviour of many physical properties which can be calculated in terms of Green functions to be explored in a mathematically transparent fashion. It underpins many of the analytical calculations performed in Chapters 5 and 6 and has a wide range of applicability.

Finally, the recursive methods introduced in the previous chapter were demonstrated explicitly for the case of graphene nanoribbons in section 3.4. The unit cells and overlap matrices needed for such calculations were shown and it was demonstrated that these methods can be used to easily account for edge-distortions or electron-electron interactions that render other methods of calculation more difficult.

In the following chapters, the Green functions calculated here will be used repeatedly. In Chapter 4 the dependence of a range of nanoribbon properties on the location of an impurity will be investigated using recursive methods. In the following chapters, our attention will shift to the interaction between magnetic moments embedded into graphene sheets. Our understanding of such interactions is assisted by a complementary approach using both numerical and analytic calculation of the graphene Green functions.

The derivation of the Green function for graphene using the Stationary Phase Approximation presented in this chapter was published as part of "Electronic structure of graphene beyond the linear dispersion regime" (Phys. Rev. B 83, 155432).

CHAPTER

FOUR

Position dependent properties in Graphene Nanoribbons

4.1 Introduction

In this chapter we will focus our attention on some of the physical properties of graphene nanoribbons (GNRs). These one-dimensional strips of graphene have received much attention in the literature since the discovery of graphene and applications for these materials in the fields of nanoelectronics and spintronics, amongst others, have been postulated. The electronic structure and Green functions for these materials were calculated in Chapter 3, where the characterisation of GNRs in terms of their width and edge geometry was also introduced. We will focus on the two principal edge geometries, namely those corresponding to the armchair and zigzag directions. The ribbon width is denoted by the number of dimer pairs (for AGNRs) or zigzag chains (for ZGNRs) across the ribbon width. Schematic examples are shown in Fig 4.1.

Since doping with impurity species is an effective way of tailoring the electronic properties of a material, much investigation of graphene and related materials with introduced impurities has taken place [69, 161, 162]. A crucial difference between GNRs and the bulk case or carbon nanotubes is the existence of two symmetry-breaking edges. Introducing edges into a graphene sheet breaks the equivalency of the sites on the lattice which are now charac-

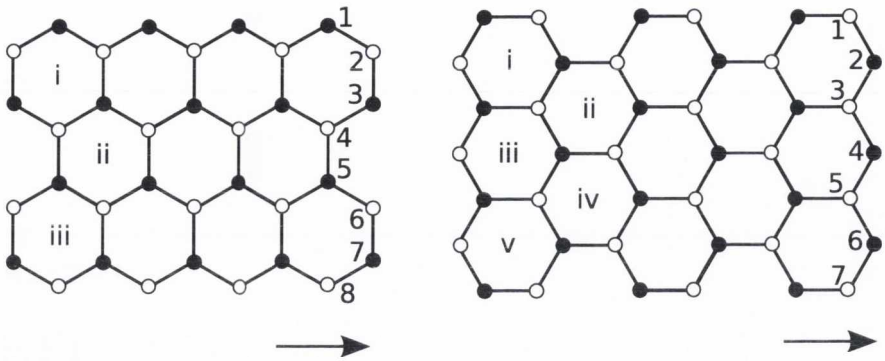

Figure 4.1: Schematic representation of a 4-ZGNR (left) and 7-AGNR (right), with the two graphene sublattices represented by filled and hollow symbols. The possible sites for substitutional (centre-adsorbed) impurities are labelled with Arabic (Roman) numerals. The arrows refer to the periodicity direction.

terised by their distance from either edge of the ribbon. We thus expect that the physical properties of a GNR with an impurity becomes dependent on the position of that impurity across the width of the ribbon. Indeed previous studies have investigated how the electronic conductance of GNRs depends on the location of impurities [57, 70, 71]. The principal findings of these studies will be discussed and illustrated with a simple model of our own in Section 4.2.

In addition to the conductance of the GNR, this distance dependence also arises in the energetics of the doping process. In other words, the binding energy of a dopant depends on its position across the ribbon. In Section 4.3 we introduce a simple model based on the Lloyd formula to investigate this dependence and compare our results to those obtained from a full *ab initio* calculation. Furthermore we investigate how the impurity segregation introduced by the position dependence of the binding energy can be controlled by external factors, in this case a gate voltage applied to the system. This opens the road to manipulating the impurity distribution within a ribbon which we argue might be a possible route to engineering some of the physical properties of GNRs.

Finally, in Section 4.4 we switch our attention to the case of magnetic dopants. This study is motivated by the potential for graphene-based spin-

tronic devices. GNRs have been at the forefront of research in this area, primarily due to the existence of spin polarised edge states in ZGNRs [40, 41]. However, these states are predicted to be highly dependent on the edge geometry of the ribbon and not particularly robust under the introduction of edge disorder [51]. Another possibility for incorporating graphene in spintronic devices lies in the doping of GNRs with magnetic impurity atoms. Similarly to the conductance and binding energy, the magnetic moment of such an impurity should also depend on the impurity position. Using the self-consistent model introduced in Chapter 2, we show how the magnetic moment for various impurity configurations varies across the ribbon width. Once more a comparison is made with *ab initio* calculations to verify the qualitative features of our findings. The robustness of the magnetic moments introduced is then illustrated by examining the effect of an introduced edge defect on the magnetic moment profile.

The work presented in this chapter illustrates the importance of position dependent effects in three areas of nanoribbon research. It also highlights how these effects can be exploited to the advantage of future graphene based devices. The additional degree of freedom afforded by the introduction of edges into a graphene lattice thus opens up new opportunities for engineering the physical properties of disordered graphene-based systems.

4.2 Transport

In this section we examine the effects of impurity position on the electronic transport properties of a ribbon system. The Caroli formalism for calculating conductance is briefly introduced and used to calculate the conductance of a sample of pristine ribbons. Following this the effect of a single impurity at various locations across the width of ribbons with armchair and zigzag geometry is investigated. Finally, we move from a single impurity to discuss extended disorder in the form of a disordered length of ribbon with a certain concentration of impurities. The effects of ribbon type and also of the impurity type and distribution are discussed.

4.2.1 Caroli Formalism

To calculate the electronic conductance, Γ, through a system we make use of the Caroli formalism. An expression for the conductance can be derived in terms of Green functions as

$$\Gamma(E_F) = \frac{4e^2}{h} \mathrm{Tr}\left(\tilde{G}_{ii}(E_F)\, V_{ij}\, \tilde{G}_{jj}(E_F)\, V_{ji} - V_{ij}\, \tilde{G}_{ji}(E_F)\, V_{ij}\, \tilde{G}_{ji}(E_F)\right), \tag{4.1}$$

where $\tilde{G}_{ij} = \frac{1}{2i}\left(G^R_{ij} - G^A_{ij}\right)$ and G^R (G^A) is the retarded (advanced) Green function [163]. Here we have used i and j to denote two adjacent layers of the system, the choice of which is arbitrary. Equivalent expressions for the conductance can be derived using the Kubo or Landauer-Buttiker formalisms [164].

When calculating conductances of systems consisting of semi-infinite left- and right-hand side leads and a finite central device region, as illustrated schematically in Fig 4.2, the approach taken is as follows

- the left- and right-hand side leads are built recursively using the methods of Chapter 2 to yield the surface Green functions g_{LL} and g_{RR}
- the central device region is added layer by layer to the left hand side lead to give a new surface Green function, g_{DD}
- the two sides of the system are connected using the Dyson equation, yielding the connected Green function $\hat{G}$
- the conductance is evaluated using Eq. (4.1) where we set $i = D$ and

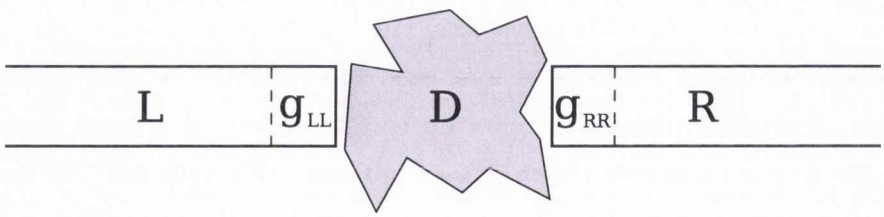

Figure 4.2: The left lead (L), central device (D) and right lead (R) sections of a system used in typical conductance calculations. using the Caroli Formula method.

$$j = R.$$

Using this algorithm we can calculate conductances for a wide variety of nanoribbon systems. Fig 4.3 shows the conductance as a function of Fermi energy through pristine armchair and zigzag nanoribbons. For pristine ribbons, we are in the ballistic transport regime and each additional subband contributes an additional quantum of conductance ($\frac{e^2}{h}$). This is clear from the density of states (shaded plot) in the background of each of these graphs. We shall now use this formalism to calculate the conductances of nanoribbons with impurities.

4.2.2 Single Impurity

The doping of nanoribbons is expected to allow much modification of their characteristics. It is predicted that the introduction of various elements, functional groups or vacancies into a ribbon system will lead to a wide array of possible properties, including but not limited to semiconducting with wide range of possible band gaps, metallic, ferromagnetic, antiferromagnetic, half-metallic and half-semiconducting [165]. The numerous possibilities for fine-tuning such properties suggest a wide range of possible applications for these materials. One of the properties that is of particular interest is how the transport through a nanoribbon is affected by the introduction of impurities. A large number of works have focused on various facets of this topic [56–64, 70–72,75,165]. Unlike carbon nanotubes, a similar material whose properties when doped have long been studied [8], nanoribbons have an extra degree of freedom when it comes to doping as the possible sites across the ribbon width where impurities may form are not equivalent. In this section we shall examine how the conductance of armchair- and zigzag-edged ribbons depends on the location of a single impurity before considering the effects of extended edge or bulk type impurity distributions in the next section.

The position dependence of transport properties for doped materials has been the subject of a few recent works. Usually this consists of an *ab initio* study of a ribbon with a specific impurity species considered at different locations across it [70–72]. Some work has also been performed on the effect

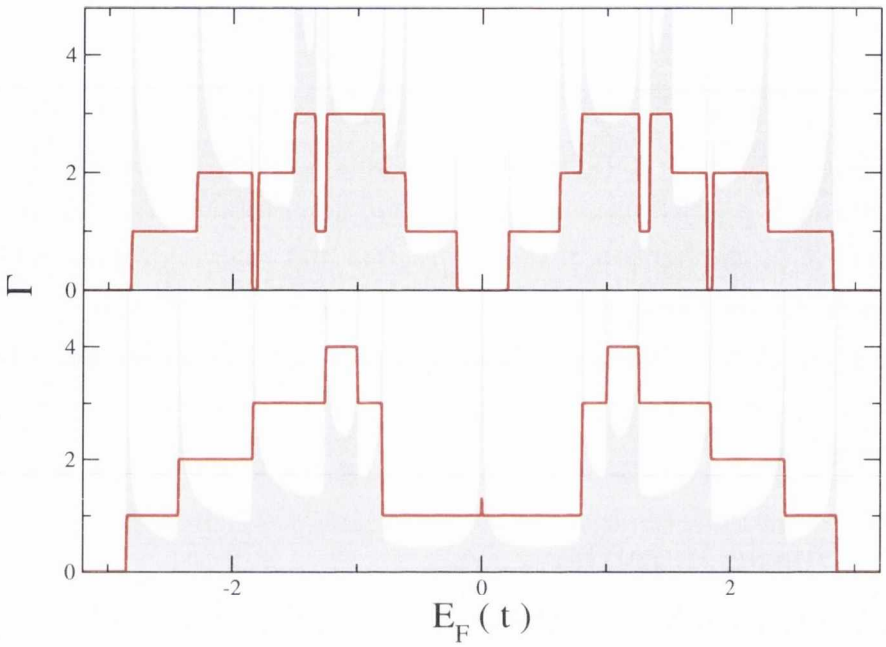

Figure 4.3: Conductance, $\Gamma(E_F)$, through a pristine 6-AGNR (top) and 4-ZGNR (bottom) shown by red, solid line. The density of states for each ribbon is shown by the grey shaded area in each plot.

of vacancy defects on the conductance through ribbons. A tight-binding study reports that vacancies near the centre of a wide ZGNR have a more detrimental effect on the conductance than those near the edge [75]. However, much of the study of vacancy defects has focused on edge vacancies due to the importance of extended edge disorder that we shall discuss in the next section. Li and Lu [56] begin a comprehensive study of edge disorder in GNRs with a demonstration of the effects of two impurity types on the conductance of both armchair and zigzag-edged GNRs. The impurity types considered are vacancies and *weak scatterers* which can represent local lattice distortions, or adsorbed or substitutional impurities. Both types of impurities are accounted for in a tight-binding description of the ribbons by a change in the onsite potential, ϵ_i at the impurity site. For a vacancy defect this quantity is set to infinity and for a weak scatterer a small value ($\leq 2eV$) is chosen. We shall now consider impurities of these types to examine the position dependence of the conductance. Fig 4.4 shows the conductance for Fermi energies in

the region around $E_F = 0$ through a 11-AGNR (top panels) and 6-ZGNR (bottom panels) for three different impurity locations between the edge and centre of the ribbon, as shown in the schematics. Both vacancy (left panels) and weak scatterers (with $\epsilon_i = 0.7t$, right panels) are considered.

For both defect and both ribbon types, the results for edge impurities (the red dashed curves) agree with those of Li and Lu [56], with the exception that we have included the edge correction required for AGNRs [52], so that our pristine AGNR is semiconducting and not metallic. For vacancies in AGNRs (top, left) we observe that edge positions (red, green) have the largest effect on the conductance in the region around $E_F = 0$ with a wide dip in the conductance throughout the first plateau. In contrast, a vacancy at the ribbon centre (blue, dash-dotted) has only a mild broadening effect on the bandgap. For ZGNRs, a different picture emerges. In all cases the vacancy induces dips in the conductance in the region of the first plateau. However, for edge vacancies these are quite narrow and towards the band edge. However, as the vacancy moves towards the ribbon centre these dips become broader and migrate towards $E_F = 0$. This is the general trend noted in Ref. [75] for the position dependence of vacancy defects in ZGNRs. A single weak scatterer (right panels) has, in general, a very small effect on the conductance of either ribbon. The only exception is the case of an edge scatterer in ZGNRs. Li and Lu account for this by considering the group velocity of electrons near $E_F = 0$ in graphene. As the bands are partially flat in this region, as we have seen in Chapter 3, the group velocity of these electrons is close to zero and so even a very weak scatterer can produce a quasi-localised state near the Fermi energy causing a dip in conductance. Another consideration is the localisation of the edge states at $E_F = 0$, which makes them particularly susceptible to scattering by a weak edge defect. As the strength of the scatterer is increased, the conductance dip broadens and shifts away from $E_F = 0$. As it is increased further it splits into two dips at either side of $E_F = 0$ which in the limiting case of a vacancy defect are located at the band edges, as seen in the red curve of the bottom left panel.

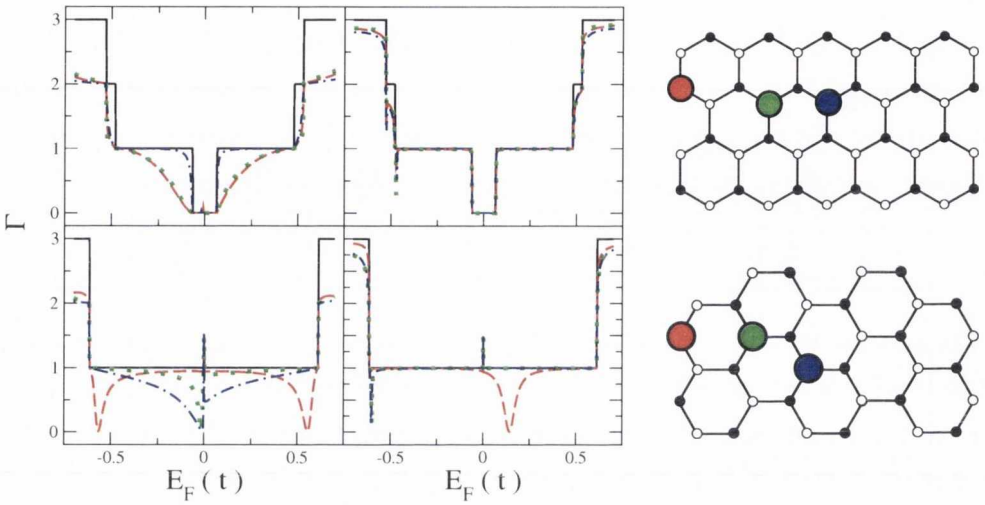

Figure 4.4: The conductance through an 11-AGNR (top panels) and a 6-ZGNR (bottom panels) for the pristine case (solid, black lines) or with a single vacancy (left) or weak scatterer (right) located at one of three different locations between the edge (red) and centre (blue) of the ribbon, as shown by the schematic diagrams for each case.

4.2.3 Extended disorder

Much of the investigation into extended disorder in GNRs has focused on edge defects and vacancies [56–64]. This work was principally motivated by the discrepancy between the band gaps of GNRs estimated by experiment [53–55] and those predicted theoretically for pristine ribbons using either tight-binding models (Refs [39, 40, 52], and Chapter 3) or *ab initio* methods. A broad consensus from the study of edge-disordered GNRs is that the presence of edge-disorder induces Anderson-type localisation [65–67] in the ribbons, causing enhancement of the density of states at the ribbon edges and a blocking of conductive paths through the ribbons. The conductance of a ribbon with a finite length, L, of disorder is expected to decay exponentially due to this localisation, so that

$$\Gamma = \Gamma_0 \, e^{-\frac{L}{L_0}} , \tag{4.2}$$

where Γ_0 is the pristine conductance and L_0 is the *localisation length* which is found to increase with ribbon width [56–58]. For both ribbon geometries, the introduction of edge vacancies leads to conductance suppression and the opening of a bandgap around the Fermi energy.[1] However the gap is less pronounced for ZGNRs [57] - a finding easily reconciled with the single vacancy results in Fig 4.4. Vacancies at the ribbon edge were shown here to have a more severe effect in the case of AGNRs. An extended ensemble of weak edge scatterers was found however to have a different effect [56] - a gap opening was reported for ZGNRs but the effects of localisation were found to be significantly weaker for the armchair case where no bandgap was found due to a very long localisation length. Again this is in agreement with what can be predicted from the single weak-scatterer conductances in Fig. 4.4.

In their study, Mucciolo et al [57] supplement the standard discussion by considering also the effects of an extended bulk disorder on the conductance of the ribbon. In this case the impurities are uniformly distributed across the ribbon and not localised to the edge as before. They note some important contrasts between the signatures of edge and bulk disorder. Firstly, moderate bulk disorder is found to have a lesser effect on AGNRs, where the current carrying states are concentrated near the ribbon edge. This is again consistent with the single-impurity findings in Fig. 4.4, where impurities towards the centre of the ribbon were shown to have a minimal effect on the ribbon conductance around $E_F = 0$. The opposite situtation is reported in ZGNRs where bulk disorder significantly suppresses the conductance. The findings for bulk disorder are roughly the opposite to those reported for edge vacancies. Furthermore, this study finds contrasting signatures for edge and bulk disorders in the shape of the conductance plateaux. Weak edge disorder is found to lower the conductance steps without changing the energies at which they occur. However bulk disorder has the effect of smearing the plateaux without shifting their conductance values.

In summary, the conductances of ribbon systems with edge- and bulk-type disorders are found to display quite different behaviour. The conductance features are found to depend strongly not only on the ribbon geometry, but

[1] The studies cited here use metallic nanoribbons in their models.

on the nature and distribution of the disorder. The degree to which the conductance depends on the impurity distribution suggests that selective doping of nanoribbons may be an effective method to tailor their electronic transport for specific device applications.

4.3 Impurity segregation

In the previous section we examined how the conductance of a GNR was effected by the introduction of an impurity into the system and noted that the position of the impurity across the width of the GNR played an important role in determining the characteristics of the electronic transport through the system. One crucial aspect that seems to be often overlooked however is that the dependence noted for the conductance also arises in the energetics of the doping process. As a result, by examining how the binding energy for an impurity varies across the ribbon width we can identify energetically favourable locations for impurities, leading to a degree of spatial segregation in the impurity concentration. Bearing in mind that impurity segregation is known to occur at symmetry-breaking interfaces between two materials due to quantum interference effects [76, 77], it should come as no surprise that the proximity of the two edges of a GNR is capable of inducing similar segregational features in the impurity distribution. What is surprising in the case of GNRs is that the segregation may be easily controllable by external factors, which may in turn allow some manipulation of the impurity distribution within a ribbon. This suggests a possible route to engineering some of the physical properties of GNRs which depend on the impurity distribution, including the conductance, as illustrated in Section 4.2.

4.3.1 Impurity Types

To account for the position dependence of the binding energy we must first define the geometry of the host ribbon and the types of impurities considered. We consider GNRs of infinite length and finite width with either the zigzag or armchair edge geometries. We consider three different types of impurity

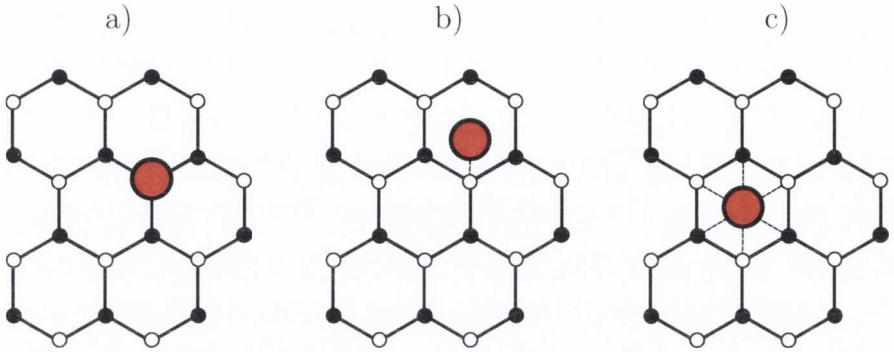

Figure 4.5: The three types of impurity configuration considered: a) substitutional atom, b) top-adsorbed atom and c) centre-adsorbed atom

atom, shown schematically in Fig. 4.5. The first of these is a *substitutional* atom impurity, where a single carbon atom from the graphene lattice is replaced with an atom of a different species. We also consider *top-adsorbed* impurities, where the impurity atom adsorbs to an atom from the lattice instead of replacing it. Finally we consider the *centre-adsorbed* type impurity, where the impurity atom sits at the centre of a hexagon and connects to each of the surrounding six carbon atoms. In Chapter 2, we demonstrated how the Green functions of systems with substitutional and top-adsorbed impurities could be calculated in terms of the pristine system Green functions and the perturbation potentials describing the impurities. The case of centre-adsorbed impurities follows an identical procedure to that for top-adsorbed atoms except that the connecting potential describes connections to six lattice sites instead of just one.

Tight-binding parameterisation

Throughout this thesis we are studying a range of phenomena involving impurities in graphene. However, in most of these cases, the important features of the interaction emerge from the electronic properties of graphene and not from the particular properties of the chosen impurity. For this reason, we choose an arbitrary set of tight-binding parameters to use with the formulas in Chapter 2 for calculating the necessary perturbed Green functions. The parameters in question are the onsite energy of the impurity, ϵ, and

the impurity-carbon hopping term t'. Throughout this work we write these terms in units of the carbon-carbon hopping t. For substitutional impurities we generally set $\epsilon = t$ and $t' = t$. However, in this and the next chapter we examine some of the effects of changing t' on the properties of magnetic impurities in graphene. For adsorbed impurities, the default parameters used are $\epsilon = 0$ and $t' = t$. However, we note that in both cases when we consider magnetic impurities the onsite energy terms are calculated self-consistently within the mean field approximation discussed in Chapter 2. We note that the qualitative features discussed later in this work are quite general, and in most cases the location or separation dependences we are interested in do not vary strongly as the impurity species is changed. If a more quantitative analysis is required, the tight-binding parameters for a particular atomic species hybridising with graphene can be calculated. This is usually done by a comparison with a full Density Functional Theory calculation, where the relevant tight-binding parameters are varied so that agreement is reached between either the bandstructure [166, 167], total energy results [151, 152, 168] or magnetic moments [118] of both calculations. Table 4.3.1 shows a range of values calculated for different impurity species in both graphene and nanotube (NT) systems where the parameterisation is expected to be similar. We note that the parameters we have chosen, although arbitrary, do not differ significantly from those calculated for a range of impurity types. This suggests that our results should not be altered to a large extent if a full parameterisation is performed.

Impurity species	Type	$\epsilon(t)$	$t'(t)$	Reference
B	substitutional	-0.56	0.54	[169]
Ni	substitutional (NT)	-1.82	0.23	[118]
Mn	substitutional (NT)	-1.17	0.36	[118]
H	top-adsorbed	-0.04	2.22	[170]
In	centre-adsorbed	0.67	0.74	[171]
Mn	centre-adsorbed (NT)	-0.79	0.61	[118]

Table 4.1: Tight-binding parameters for a range of impurity species. Results marked with 'NT' are based on a nanotube-impurity system.

4.3.2 Segregation energy function β

The quantity of interest is the difference between the total energies of two distinct configurations: one in which the GNR and impurity are connected and another in which they are far apart. This can be summarised by evaluating the total-energy variation due to the perturbation applied to the system when an impurity is introduced. We can write the total energy of a system as the electronic structure contribution added to a repulsive energy term [172] in which the latter has been given a formal correspondence with modern Density Functional Theory (DFT) [173]. This latter contribution, not expected to carry a major position dependence, should play only a minor role in the segregation features. Therefore, the bandstructure contribution to the total-energy variation becomes the most relevant quantity to be calculated. Recall that in Chapter 2, we illustrated how the Lloyd formula could be used to calculate the total energy difference without the need to calculate the Green functions of the perturbed system. From Eq. 2.58, we have

$$\Delta E = \frac{1}{\pi} \mathrm{Im} \int_{-\infty}^{E_F} \mathrm{d}E \, \ln \det(\hat{I} - \hat{g}\hat{V}) \,, \tag{4.3}$$

where $\hat{V}$ is the perturbation potential describing the considered impurity, $\hat{g}$ is the Green function associated with the unperturbed system and E_F is the Fermi energy. The segregation is now studied by selecting the type of impurity and its position within the GNR, calculating the relevant matrix elements of $\hat{g}$ and finally evaluating the integral in Eq. (4.3). This integral is performed in the complex plane using the methods described in Section 2.7. To simplify the comparison between the various cases and with *ab initio* calculations we introduce a renormalised energy scale. The segregation energy function (SEF) is defined as

$$\beta = \frac{\Delta E - \Delta E_c}{|\Delta E_c|} \,, \tag{4.4}$$

where ΔE_c is the electronic contribution to the total-energy variation evaluated at the centre of the GNR and which is taken as a reference energy.

This dimensionless quantity describes the percentage deviation of the energy variation with respect to its value at the central position.

We consider first the case of substitutional impurities in a 6-ZGNR. The square symbols in Fig. 4.6 represent the values of β for all positions across the width of a 6-ZGNR with substitutional impurities and points to a scenario in which they prefer to occupy the edges of a GNR with an energy variation that is predicted to be 30% lower than at the centre. This preference for edge sites is also true for adatoms, as we shall see shortly, and is also reported by other studies [56, 70–72, 174]. What is remarkable in our results is the way in which β varies when the impurity position moves to the central region of the GNR. Rather than simply vanishing, it does so in a non-monotonic fashion pointing to the existence of a few local minima separating the lowest value at the edges from the central zero.

To test whether such a non-monotonicity in the position dependence of the binding energy could be an artifact of our simple model, DFT calculations were performed in which a similar 6-ZGNR was substitutionally doped with Ti atoms located at different positions across the ribbon[2]. The results of these calculations are shown by the circular symbols in Fig. 4.6 and display similar behaviour for β as those from our simple model, shown by square symbols, including excellent agreement at the ribbon edges. The existence of local minima was also reproduced at the same locations, albeit with slightly different values for β. Such an excellent agreement with DFT results reassures us that our simple model contains the essential ingredients to describe the effect of impurity segregation in GNRs. With this model we can consider ribbons of all sizes and geometries as well as include an arbitrary number of impurities, if necessary.

[2]These calculations were carried out using the SIESTA [175] code with a 98-atom supercell. Double zeta basis set plus polarisation functions were employed and the exchange-correlation function was adjusted using the generalised gradient approximation according to the parameterisation proposed by Perdew, Burke and Ernzenhof [176]. To represent the charge density, a cutoff of 170 Ry for the grid integration in real space was used. The interactions between the ionic cores and the valence electrons were described with norm-conserving Troullier-Martins pseudopotentials [177]. The structural optimisations were performed with the conjugate gradient approximation [175] until the residual forces were smaller than 0.05 eV/Å.

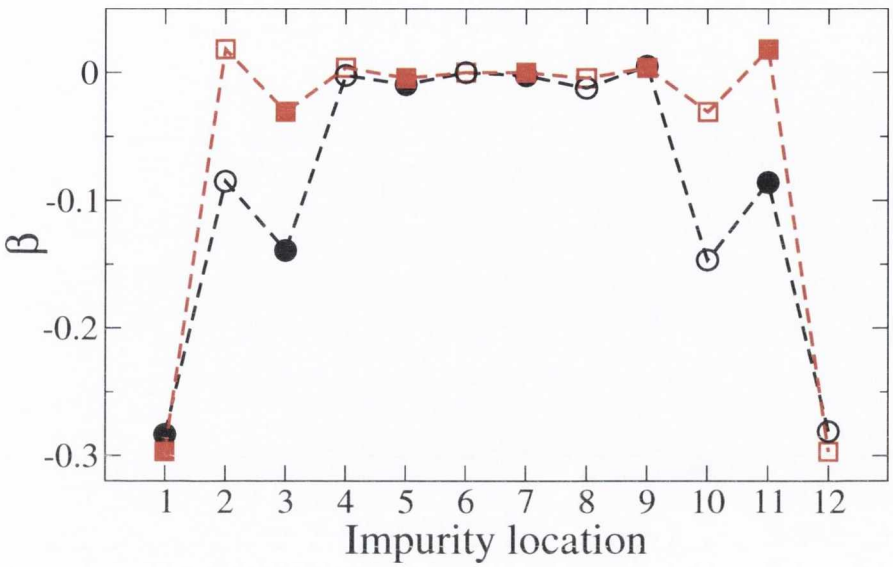

Figure 4.6: Segregation function β for substitutional impurities on different locations of a 6-ZGNR. Red squares indicate the results for the model calculations; black circles those for DFT calculations for Ti atoms. Hollow and filled symbols indicate which sub-lattice contains the substitutional replacement. Lines are guide to the eyes only.

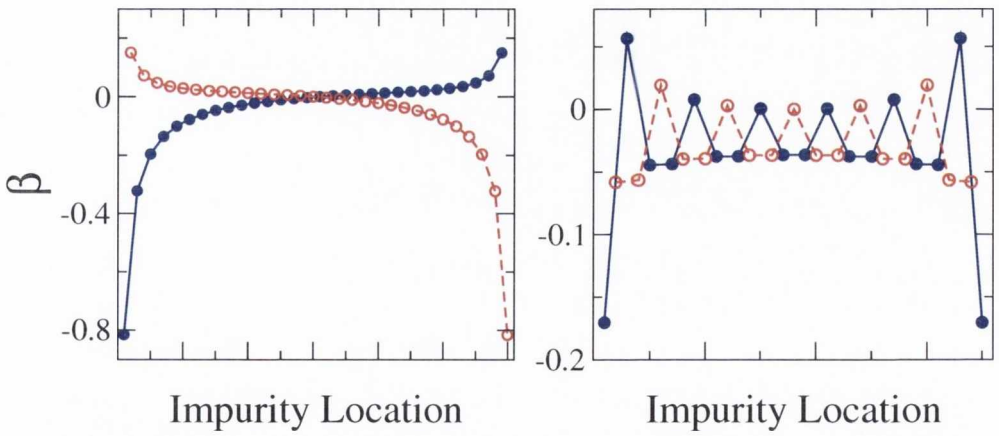

Figure 4.7: Segregation function β for top-adsorbed atoms on a 30-ZGNR (left) and 35-AGNR (right). The filled (blue) and unfilled (red) circles represent adsorption sites from the two distinct sublattices. The solid and dashed lines connect sites within a given sublattice.

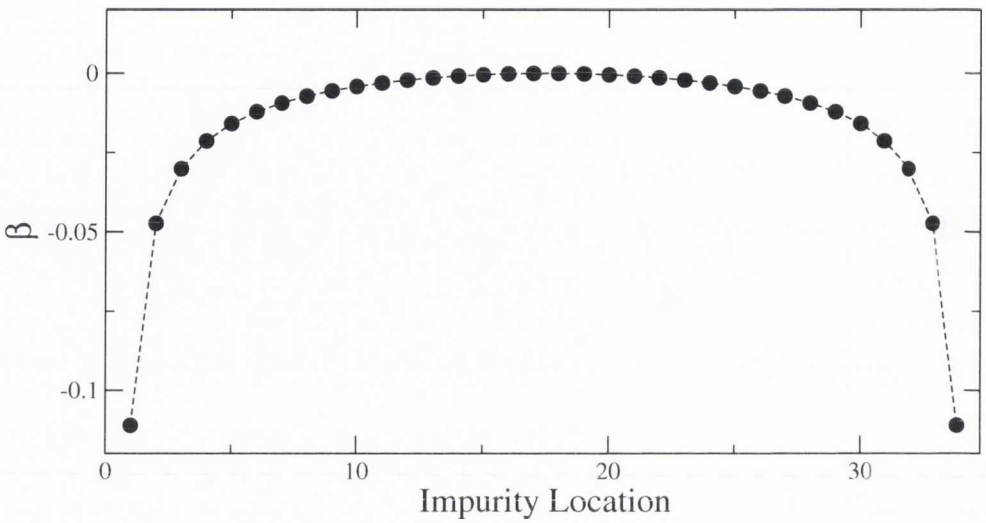

Figure 4.8: Segregation function β for centre-adsorbed atoms on a 35-ZGNR. The sublattice dependence present for top-adsorbed or substitutional impurities has been averaged out. The dashed line is a guide to eye.

A point worth raising is that the location of substitutional impurities usually follows the existence of defects and vacancies, often induced by ionic irradiation [178–180]. In this scenario, impurities will occupy the sites surrounding the defects, which means that edge-induced impurity segregation will play a minor role in the doping process. However, for adsorbed atoms the situation is very different. In this case the impurities will adsorb at the most energetically convenient sites. Thus the position dependence of the binding energy is a key factor in determining where the impurities will be adsorbed. As previously anticipated, there is very little qualitative difference in our model between the substitutional and adsorbed cases, which suggests similar non-monotonic variations in the segregation function across the ribbon. This is shown in Fig. 4.7 where the SEF for adsorbed impurities in a 30-ZGNR (35-AGNR) is displayed on the left (right) panel. Filled (blue) and hollow (red) symbols indicate above which sub-lattice the impurities are located. The left panel shows that the segregation function for ZGNR alternates between positive and negative depending on which sub-lattice the impurity is above, similar to the case for substitutional impurities. There is a clear distinction between the filled and hollow points, in the sense that on the left half

of the ribbon the former are energetically more favourable as adsorption sites for the impurities, whereas the latter becomes preferable on the right half of the GNR. A solid (dashed) line linking the values of β for hollow (filled) sites is also shown. Both lines intersect at the centre of the GNR, where $\beta = 0$, confirming that the preferential location for impurities changes from one sublattice to another precisely at this location. The sublattice dependence in the segregational features can be understood by examining the geometry of ZGNRs. Introducing zigzag edges breaks the symmetry between the sublattices across the ribbon width with the opposing edges composed entirely of atoms from opposite sublattices. This is clearly seen in the schematic ZGNR shown in Fig 4.1. Although similar non-monotonicities in the SEF are also found for AGNR, shown on the right panels of Fig. 4.7, in this case there is no obvious distinction between the two sub-lattices in regard to the most energetically favourable position. A cursory inspection of AGNR geometry reveals that armchair edges do not break the symmetry between the two sublattices. For both edge geometries we find that the impurities are found to attach much more readily to edge atoms than to central atoms. The edge value of $|\beta|$ is much larger in the zigzag case, which can be reconciled with the existence of localised edge states at the (half-filling) Fermi energy in these ribbons [39]. In Fig. 4.8 we show a similar plot, but for the case of centre-adsorbed impurities. The sublattice dependent non-monotonicity disappears in this case, as the adatoms connect to carbon atoms from both sublattices and the effect is averaged out. However, a marked preference for edge sites with a decay towards the centre is still present.

As in the case of substitutional impurities, we performed DFT calculations for adsorbed Ti atoms on a 6-ZGNR. It was found that on each side of the ribbon one of the sublattices was dominant. When an adatom was released above a site belonging to this sublattice it would remain there. However, adatoms released over sites from the other sublattice tended to migrate either to sites above the dominant sublattice or to more complex intermediary sites. The other sublattice was found to assume the dominant role on the opposite side of the ribbon. The migration behaviour described makes it difficult to make a direct comparison with the simple model SEF, as we did

for the substitutional case. However, the existence of this type of behaviour confirms qualitatively the results of our simple model, which predicts sites from a single sublattice to be favoured on either side of the ribbon, as seen in the top left panel of Fig 4.7. Once again, the agreement between the results based on our simple model and those obtained by DFT calculations are encouraging and suggest that this model can be used to shed some light in situations where *ab-initio* calculations are unable to do so.

4.3.3 Control through gating and applications

The ease with which the Fermi level, E_F, of graphene-based structures can be manipulated with external gate voltages [4] adds an extra ingredient to the study of impurity segregation in GNR. Fig. 4.9 plots the SEF for adsorbed impurities of the 30-ZGNR (35-AGNR) considered earlier in Fig. 4.7 for two distinct cases. For clarity, Fig. 4.9 focuses on the central regions of the ribbons. The top panels show the ungated case considered earlier, where for each sublattice we observe a monotonic increase in the SEF from the dominant edge of the ribbon to the opposite edge. The bottom panels of Fig. 4.9 shows the SEF for both ribbons when the Fermi energy is shifted away from half-filling by a mere 3% of the graphene bandwidth. The solid and dashed lines used to distinguish between the two different sub-lattices are clearly modified as E_F is changed and an oscillatory feature is introduced. Whereas the AGNR remains without any clear favourites for the most energetically preferred locations, there is a striking effect on the ZGNR. In this case the two lines intersect not one but five times indicating that the energetically favourable location for the adsorption of impurities changes periodically between the two sub-lattices forming a striped pattern across the ribbon width. This oscillatory feature is also present for the centre-adsorbed configuration, but once more without a sublattice dependence.

It is important to note the general nature of the model for the SEF we have constructed and used in this work. We have made no assumptions about the atomic species used as the impurity. Although it is possible to fit our tight-binding parameters to DFT calculations, this is not necessary to

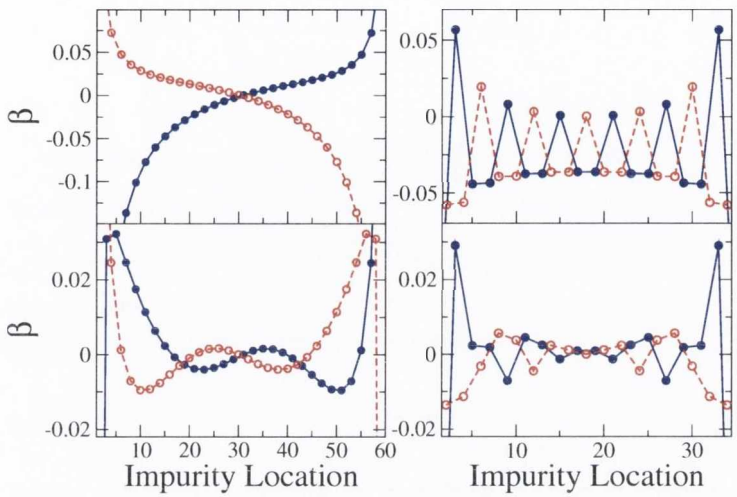

Figure 4.9: Segregation function β for adsorbed atoms on a 30-ZGNR (left panels) and 35-AGNR (right panels) for $E_F = 0.0t$ (top panels) and $E_F = 0.2t$ (bottom panels). The filled (blue) and unfilled (red) circles represent adsorption sites from the two distinct sublattices. The solid and dashed lines connect sites within a given sublattice. Here we have focused on the central region of both ribbons, but the edge sites are the most favourable adsorption sites.

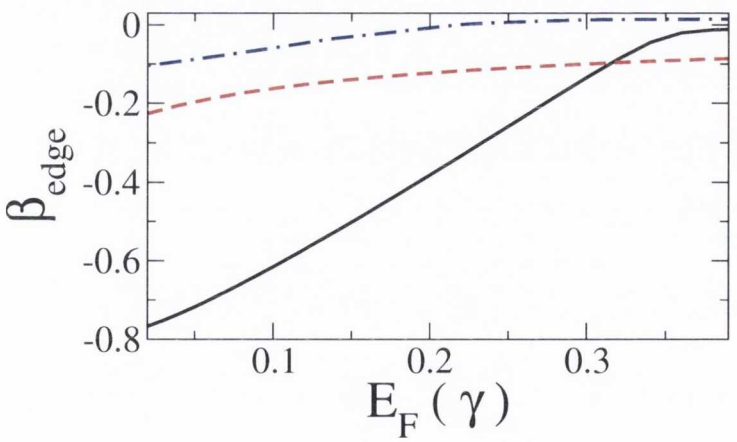

Figure 4.10: The segregation function at the edge of a ribbon, β_{edge}, reveals how favourable the edge adsorption site of a ribbon is relative to the central site. When $E_F = 0$, the edge site is far more favourable for both a 10-ZGNR (black, solid line) and 11-AGNR (red, dashed line). However by shifting E_F, the edge and central sites become more equally favourable, particularly in ZGNRs. Also shown is the case of a centre-adsorbed atom on a 30-ZGNR (blue, dot-dashed line), where a similar trend is noted.

recover the qualitative features of the results shown above. Indeed, our results for substitutional atoms with arbitrary tight-binding parameters match the results of a full *ab initio* calculation for Ti atoms to a high degree of accuracy (Fig 4.6). This suggests that the non-monotonic behaviour of β displayed in the above results is independent of the impurity species chosen, and depends only on underlying graphene lattice and how the impurity is embedded into it. This is evident from the form of Eq. (4.3), where the position dependence arises solely in the Green function matrix element of the host ribbon. Therefore similar behaviour can be expected if the impurities considered possess a magnetic moment. Recent works have established that a long range magnetic coupling can exist between magnetic atoms embedded in graphene-related materials [116–118, 136]. In the next chapter we shall examine some of the properties of this coupling in graphene. It is found that certain magnetic dopants adsorbed onto sites within the same sublattice prefer to align ferromagnetically, whereas those on opposite sublattices prefer an antiferromagnetic alignment [73, 119, 123, 124, 181]. Thus, if in a given region of a ribbon a majority of the magnetic dopants adsorb onto one of the sublattices, it follows that these dopants may prefer to align ferromagnetically, resulting in a net magnetic moment in this region. Similarly, a net magnetic moment with opposite sign should form in regions where the other sublattice is preferential. By controlling the Fermi energy, it may therefore be possible to manipulate the width of magnetic domains across the ribbon. In this manner, it may be possible to engineer doped GNRs with magnetic properties determined by the application of an electric field during the impurity adsorption phase.

In the previous section we demonstrated how the transport properties of a graphene nanoribbon have been shown to be dependent on the position of an impurity. A comparison [57] between the effects of edge and bulk disorders in GNRs reveals a marked difference between these two cases. For example, mild edge disorder produces only a small effect in the conductance of ZGNRs, whereas bulk disorder can lead to a more dramatic suppression of the conductance, with roughly the opposite effect observed for AGNRs. The difference between edge and bulk disorder suggests that controlling the

impurity distribution across a ribbon may be a viable method of engineering its transport properties. Fig. 4.10 shows β_{edge}, the value of β at the edge of a ribbon, as a function of E_F for a 10-ZGNR and 11-AGNR, and also for a centre adsorbed atom on a 30-ZGNR. When this quantity approaches zero, the edge and central sites are equally favourable. We see from Fig. 4.10 that as E_F is increased from half-filling, for ZGNRs at least, the preference for adsorption at edge sites is decreased continually until edge and central sites are almost equivalent. This suggests it may be possible to engineer ribbons with the transport properties associated with edge disorder, bulk disorder or any intermediate position on the continuum between these two. This presents itself as a possible method for fine-tuning the resistance properties of a ribbon device.

4.4 Magnetic moment profile

In the previous section we noted the generality of the model used to calculate the segregation energy function describing the variation in binding energy of an impurity placed at different locations across a GNR. This suggested the behaviour noted was independent of the atomic species chosen and should also be found if a magnetic impurity is chosen. However in the case of magnetic impurity atoms, the position dependence noted should arise not only in the binding energy, but in the magnetic moment itself, as the impurity location is varied.

A position dependence in the magnetic moments arising in pristine ZGNRs due to localised edge states has previously been noted and motivates much of the research being performed investigating magnetism in graphene [39–42]. This feature can be found within the mean-field Hubbard model described in Chapter 2 by the inclusion of a non-zero Coulomb repulsion term U at each lattice site. For a wide range of U values, the ground state consists of large moments on the edge sites, where moments along one side of the ribbon align parallel to each other and anti-parallel to those on the opposite edge. The moments are found to decay non-monotonically towards the centre of the ribbon, as shown in Fig. 4.11. The pattern formed here is again

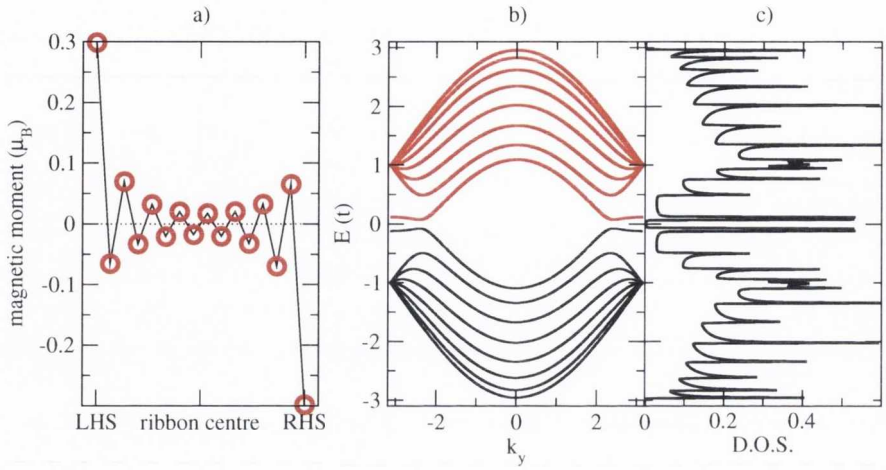

Figure 4.11: a) The magnetic moment profile across a pristine magnetic 8-ZGNR calculated with the self-consistent method with $U = 1.33t$. b)The bandstructure and c) density of states of the same system.

a sublattice effect - moments on opposite sublattices are found to prefer an anti-parallel alignment. In fact, by focusing on a single sublattice we note a monotonic change in the value of the magnetic moment over the width of the ribbon. Another interesting feature that arises in the electronic properties of the ribbon, when the band structure is calculated in this model, is that a bandgap opens up, causing a splitting of the peak in the density of states at the Fermi energy. In contrast, if all the moments on the ribbon are forced to align parallel this band gap does not open. Several magnetoresistance devices exploiting this feature have been suggested [41, 102, 103]. However, despite theoretical advances in the study of GNRs, experimental validation of their properties has so far been inconclusive, due to the difficulty in patterning the edge geometries required for these effects to be observed. Furthermore, the spin-polarised edge states in ZGNRs are predicted to be highly dependent on the edge geometry and not particularly robust under the introduction of edge disorder in the form of vacancy defects or impurity atoms [51]. These factors present major obstacles in the path of utilising the intrinsic magnetic edge states of graphene in experimentally realisable devices.

In this section, we will focus firstly on the position dependence of the magnetic moments of substitutional and centre-adsorbed atoms on zigzag and

armchair GNRs and examine the features of the moment profiles calculated. Following this we will examine the robustness of these features when an edge disorder in the form of a vacancy defect is introduced. We find that the edge vacancy only has a significant effect on moments located on neighbouring sites and that the moment profile quickly returns to that of the pristine ribbon as we move away from the defect. This suggests that the moments arising through the doping of graphene ribbons with magnetic impurity atoms may be a viable alternative to those formed intrinsically when devising graphene-based spintronic devices.

4.4.1 Moment profiles

The magnetic moment on an impurity in graphene is calculated using a combination of the methods discussed previously. The Green function at the impurity site is found from the recursively calculated Green function of the pristine ribbon using the Dyson equation and the perturbation potential associated with the particular impurity type. This is then used in the self consistent procedure for the Hartree Fock approximation to the Hubbard model described in Chapter 2. The magnetic impurities are described by a five-fold degenerate d band with occupation n_d to represent a typical transition-metal magnetic atom. The hopping parameter between the carbon atom and the magnetic impurity atom will depend on the impurity atom chosen and can be calculated in a number of ways. While a smaller value of this parameter will in general amplify the value of the magnetic moment returned, it does not have a significant qualitative effect on the moment profile across the width of the ribbon and is taken within this study to be equal to the carbon-carbon hopping parameter γ_{CC}. The moment profiles calculated using this model are compared to those calculated from a full *ab initio* approach with Mn impurities.[3]

We present results for two magnetic impurity configurations - firstly the case of a substitutional atom and then for a centre-adsorbed impurity, shown

[3]These *ab initio* calculations were performed similarly to those outlined in the previous section, but this time taking spin polarisation into account. An 84-atom supercell was used for the 8-ZGNR and an 88-atom supercell for the 11-AGNR case.

earlier in panels a) and c) of Fig. 4.5. The impurity is moved across the finite width of the ribbon and the self-consistent value for m is calculated at each site. To enable a simpler comparison with the *ab initio* results the quantity of interest is the fluctuation of the magnitude of the moment relative to its value at the centre of the ribbon, m_c. This is given by $\frac{\Delta m}{m_c} = \frac{m-m_c}{m_c}$, a quantity analogous to the SEF in the previous section. By examining the relative fluctuations we can directly compare the results of the simple parameter tight-binding model with full *ab initio* calculations. This is especially convenient considering that the mean-field approximation is sometimes found to overestimate the value of the magnetic moment [182].

Substitutional atoms

Fig 4.12 shows the magnetic moment fluctuation as function of impurity location for substitutional impurities across the width of a 6-ZGNR and a 11-ANGR. For the case of zigzag ribbons, we first note an excellent qualitative match between the simple model and the full DFT calculation, from which we infer that the underlying mechanism for the variation in the magnetic moments across the ribbon width is the electronic structure of the nanoribbon. The position dependence arises from quantum interference effects caused by the boundary conditions imposed on the electronic structure of graphene in the form of the edges of the nanoribbons. Furthermore, we note that the parameters γ_{CM}, n_d and U which characterise the magnetic species in our simple model can be altered to achieve a better numerical fit, but do not affect the qualitative form of this plot. The pattern observed is a jagged, sawtooth style curve, characteristic of properties measured across the width of zigzag ribbons and a similar feature was seen in the previous section for the binding energies of impurities. [183] This feature is a sublattice effect which arises from the degeneracy breaking that occurs between the two sublattices of graphene when a zigzag edge is formed. The sublattices are represented schematically in Fig. 4.1 by black or white circles. Each edge of the ribbon is occupied by sites entirely from one of the sublattices, and that sublattice is "dominant" on that half of the ribbon. For the case

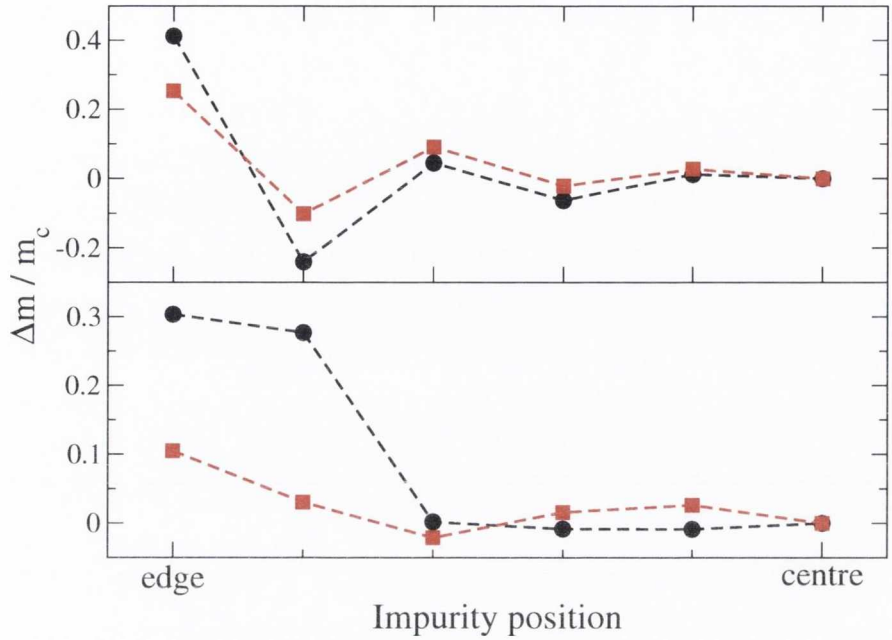

Figure 4.12: The magnetic moment profile across a 6-ZGNR (top panel) and 11-AGNR (bottom panel) for a substitutional impurity, calculated using the self-consistent Hubbard model discussed in the text (red squares) and also a full DFT treatment with Mn atoms (black circles).

of impurity magnetic moments on zigzag ribbons, this effect manifests itself in creating larger moments on impurities located on the dominant sublattice on either side of the ribbon. In other words, impurity atoms on a black site on the side of the ribbon with black edge sites will have larger moments than their neighbouring white sites. Focusing on a single sublattice, we find that the trend across the ribbon width is for the largest moment to arise on the dominant edge site for that sublattice, to decrease as the impurity is moved towards the centre of the ribbon and to reach its minimum value at the sites neighbouring the opposite edge. We note that all the features discussed here arise in both the simple model and the DFT results, confirming that this is not simply an artifact of our simple model.

The corresponding plots for the armchair case do not agree with each other as convincingly. The tight-binding model is found to underestimate the value of the edge moment found by the DFT calculation. This is because

the tight-binding calculation does not take into account the distortions in the honeycomb lattice that arise when a substitutional impurity is introduced near the edge of an AGNR. The relaxed structures for the two impurity sites nearest the ribbon edge are found to be considerably perturbed compared to the pristine ribbon and also to the relaxed structures corresponding to the other impurity sites. The shape of the tight-binding plot for AGNRs is also found to be more dependent on the parameterisation of the impurity than in the zigzag case. This issue will be explored further in the case of centre-adsorbed impurities. This suggests that the moment profile across AGNRs is not as robust as that observed in the ZGNR case, and will vary somewhat according to the magnetic species chosen. However, both tight-binding and DFT models find that the edge impurity sites lead to larger magnetic moments than the central ones. Fig. 4.12 also reveals that the sublattice effect noted in zigzag-edged ribbons is absent in the case of armchair edges. This is explained from a cursory inspection of Fig. 4.1 where it is obvious that the degeneracy between black and white lattice sites is unbroken by the imposition of armchair edges. The value of the magnetic moment approaches m_c much quicker for AGNRs, and only minor deviations from it are observed away from the edges of the ribbon, whereas in ZGNRS significant deviations are still present deeper into the ribbon.

The dramatic increase observed in the magnetic moment in impurities near the edge of zigzag ribbons is consistent with the presence of a localised edge state at the Fermi energy. This state results in a large peak in the density of states at the Fermi energy. Such a peak provides favourable conditions for moment formation under the Stoner Criterion [184], and indeed if an intrinsic electron-electron interaction is considered in an undoped ZGNR, will lead to the formation of the spin polarised edges as discussed previously.

Centre-adsorbed atoms

Fig. 4.13 shows the magnetic moment fluctuation for a centre-adsorbed impurity at various sites across a GNR, calculated again using both the simple model and a full DFT approach (black circles). Within the simple model

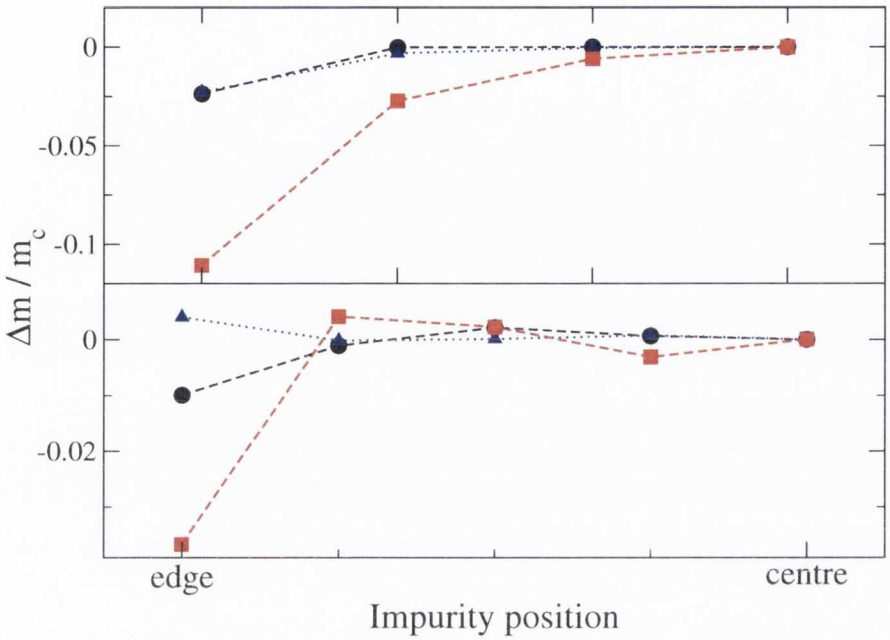

Figure 4.13: The magnetic moment profile across a 8-ZGNR (top panel) and 11-AGNR (bottom panel) for a centre-adsorbed impurity impurity. The black circles show the results from a full DFT treatment with Mn atoms, whereas the red squares and blue triangles show the results from the self-consistent Hubbard model with $\gamma_{CM} = \gamma_{CC}$ and $0.7\gamma_{CC}$ respectively. We note this parameter does not affect the qualitative features of the moment profile across the ZGNR, but alters that across the AGNR significantly.

approach we consider two values of γ_{CM}, the hopping parameter between the impurity atom and surrounding lattice sites. The values considered are $\gamma_{CM} = \gamma_{CC}$ (red squares) and $\gamma_{CM} = 0.7\gamma_{CC}$ (blue triangles). For the case of ZGNRs (top panel), we note the impressive qualitative match between the models. Furthermore we note that the change in hopping parameter does not effect the qualitative shape of the plot, but can be used to yield a better fit. We also note that, unlike the substitutional impurity considered earlier, the sublattice effect is no longer present. This is because the impurity is no longer strongly associated with a particular sublattice, but instead binds to three carbon atoms from each, which has the effect of averaging out any sublattice dependent effects. The general trend of a monotonic increase in the magnetic moment of the Mn impurity is noted as it is moved

towards the centre of the ribbon. This is in stark contrast to the result for substitutional impurities, where the largest moment is observed at the edge and, for the dominant sublattice, the moment decreases as the impurity is moved towards the centre of the ribbon. The discrepancy can be explained by the fact that the centre-adsorbed Mn impurity induces fluctuations in the magnetic moments on nearby sites in the graphene lattice. Edge atoms are particularly susceptible to magnetic moments due to the localised state discussed before, and thus have larger induced deviations in their moments than the others. Consequently, centre-adsorbed impurities atoms at the edge of a ZGNR tend to induce large moment deviations on the edge sites, resulting in a smaller moment on the impurity atom itself. This is verified by examining the spin-density plots from the DFT calculation for the case of centre-adsorbed impurities near the edge of a ZGNR. Fig 4.14 shows the spin-density plots corresponding to an impurity on the edge hexagon (left) and next-to-edge hexagon (right). It is clear that the centre-adsorbed impurity nearest the edge introduces a much larger disturbance to the values of the magnetic moments on surrounding sites than the more centrally located impurity. In fact the magnetic edge states are seen to be essentially unperturbed by the latter. In contrast to these DFT calculations, the simple model does not account for the intrinsic magnetic edge states on ZGNRs. However a similar moment profile is recovered as the magnetic impurity atom induces moments, rather than fluctuations of existing moments, on the surrounding lattice sites and these are found to be significantly larger for the case of the centre-adsorbed impurity nearest the ribbon edge.

However, in zigzag ribbons there is an additional type of adsorption site which consists of an impurity atom bound to two edge sites and the site between them. This configuration, which we shall label "edge-adsorbed" (EA), is illustrated schematically in Fig. 4.15. It can be viewed as an impurity atom connecting to half a hexagon of the graphene lattice. As this site only occurs at the edge, we cannot study the position dependence of it. However, DFT calculations reveal that a larger moment arises here than for the centre-adsorbed atom located nearest the ribbon edge and furthermore that the edge-adsorbed configuration is also more energetically favourable than

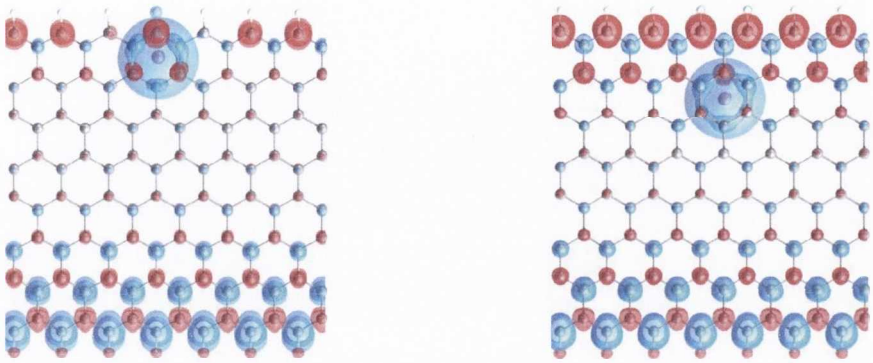

Figure 4.14: Spin density plots showing up (blue) and down (red) spin densities near a centre adsorbed impurity on the edge hexagon (left) and next-to-edge hexagon (right) on a 8-ZGNR. The isosurface used was 0.001 e/Bohr^3.

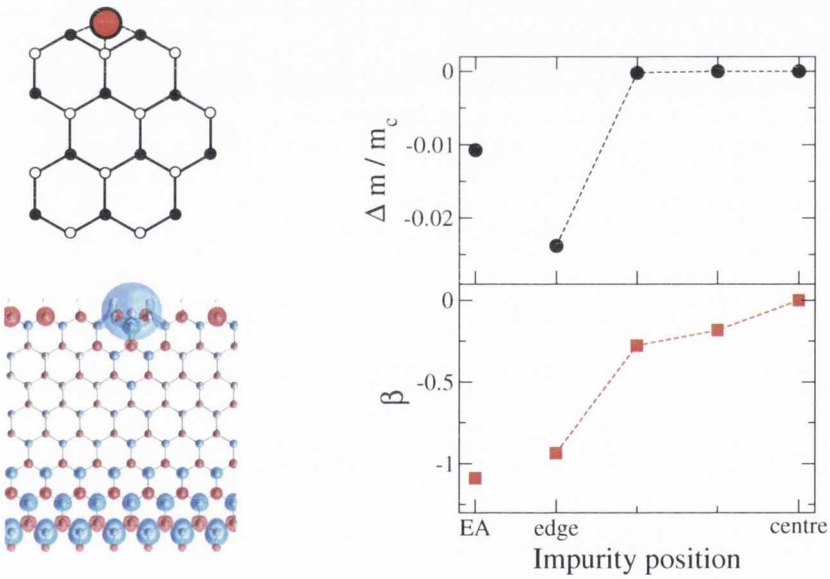

Figure 4.15: The edge adsorbed impurity discussed in the text, shown schematically in the top left panel. The spin density plot for this configuration on a 8-ZGNR is shown in the bottom left panel. The right hand side panels show the moment fluctuation (top) and segregation energy function (bottom) for this configuration calculated using the DFT approach, compared to those for the centre-adsorbed locations across the width of a 8-ZGNR.

any of centre-adsorbed sites. This is clear from the right-hand side panels of Fig. 4.15. The upper panel shows the moment fluctuation for the EA case compared with those of the centre adsorbed locations across a 8-ZGNR. The bottom panel plots the segregation energy function, $\beta = \frac{E_B - E_B^c}{|E_B^c|}$, for the same cases. This quantity, introduced in the previous section, plots the relative deviation of the binding energy of an impurity on a GNR, E_B, around its value at the centre of the ribbon, E_B^c. The edge-adsorbed case is found to be the most energetically favourable. A spin density plot for this type of impurity is shown in the bottom left panel of Fig. 4.15 and reveals that this impurity configuration has a less dramatic effect on the moments of nearby edge sites than the centre-adsorbed case on the edge hexagon, consistent with larger moment found for the EA configuration.

In the results for adsorbed Mn impurities on an AGNR in the bottom panel of Fig. 4.13 we notice that for the DFT result, and the simple model calculation with $\gamma_{CM} = \gamma_{CC}$ the edge hexagonal site has a smaller moment on it than the other sites. However the deviation in the value of the edge moment, and indeed of the moment at any site, from m_c is far smaller than in the ZGNR case. The moment profile in this case is essentially flat, with only minor deviations from m_c across the width of the ribbon. Examining the case of $\gamma_{CM} = 0.7\gamma_{CC}$ reveals that the shape of the profile across the ribbon is less robust than the zigzag case as the edge moment here is found to be slightly larger than m_c. Of the cases examined, the effect is weakest here and does not appear to be very robust. Thus the position dependence of magnetic impurities is smallest for adsorbed impurities on AGNRs and cannot be deemed a significant effect.

4.4.2 Effect of edge disorder

In this section the robustness of the features discussed in the previous section will be examined in the presence of edge vacancy defects. This is an important point to consider when comparing impurity-driven magnetic moments in GNRs to those arising intrinsically due the edge states, which have been shown to be particularly vulnerable to edge disorder. [51] For each of the

cases discussed in the previous section we examine the effect of a single edge vacancy on the magnitude of a nearby moment, calculated with the mean-field Hubbard model approach. The distance between the magnetic impurity and the edge vacancy is varied to examine the range of this effect.

Fig. 4.16 shows the effect of an edge vacancy on the magnetic moments of substitutional impurities in a 6-ZGNR (left) and an 11-AGNR (right). To show the range of the effect we plot the relative change in the moment when an edge vacancy is introduced as a function of distance between the edge vacancy and the unit cell containing the magnetic impurity atom. Note that in this case we are plotting the fluctuation of each moment relative to its value at its current position in a system without edge defects, not relative to its value at the centre of the ribbon as was shown previously. This plot is shown for a number of possible sites for the magnetic impurity across the width of the ribbon, namely the edge atom on the same side as the vacancy, the site next to the edge, a site at the centre of the ribbon and a site at the opposite edge, as shown schematically in the upper panels.

For the ZGNR, the first point to note is that the only sites that show a considerable change in their moments are the first two cases. The edge site has a slight reduction in the value of its moment, whereas the site next to the edge and belonging to the opposite sublattice to the edge has a significant increase in magnetic moment. However, the first point in this curve corresponds to a site neighbouring the edge vacancy. Excluding this, the largest deviation in magnetic moment does not exceed 5%. However, for all positions, the moment reverts very quickly back to its value without the vacancy when it is moved further away down the ribbon. This suggests that a single edge vacancy will have very little effect on the moments of magnetic impurities located more than a lattice spacing or two away. The AGNR case is quite similar. Moving away from the vacancy the deviations in the moments again become very small. It is clear that significant deviations in the moments of substitutional impurities are not seen outside the immediate vicinity of the edge vacancy in either ribbon geometry. Similar results are shown for the adsorbed cases in Fig. 4.17. The effect here is even smaller than for the substitutional case, with fluctuations of less than 2% at distances greater than

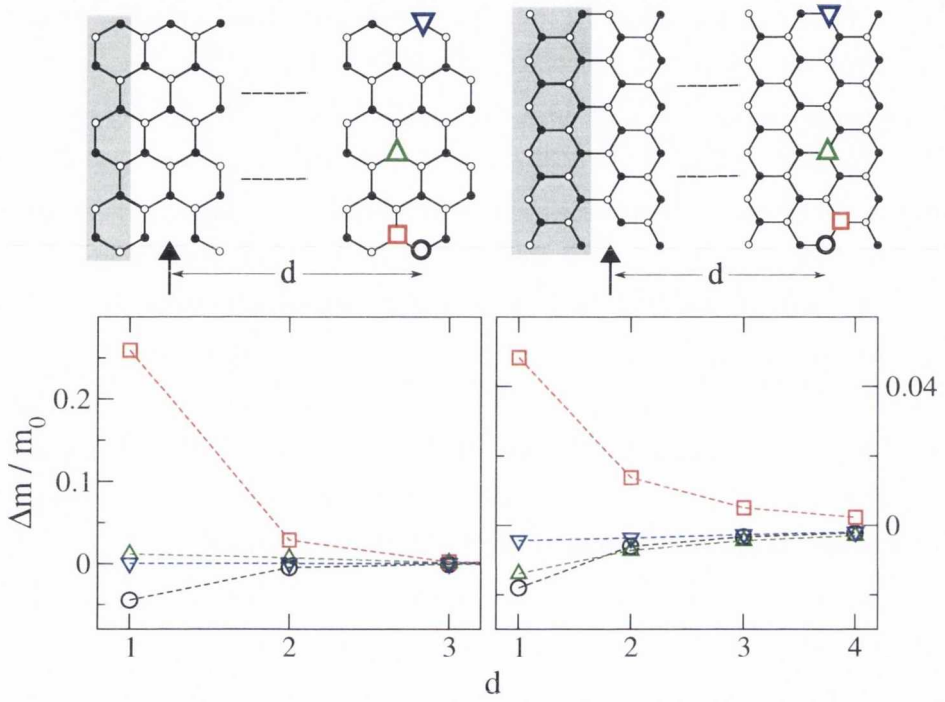

Figure 4.16: The top panels show schematically the edge vacancy and the possible sites for magnetic impurities across the width of the ribbons, a 6-ZGNR (left) and 11-AGNR (right) . For each ribbon we consider sites at the edge (black, circle), next to the edge (red, square), centre (green, triangle) and opposite edge (blue, inverted triangle) of the ribbon. The plots underneath show the fluctuation in the magnetic moment at each site under the introduction of an edge vacancy, relative to the moment the impurity would have in the absence of the edge vacancy. This is plotted as a function of the distance between the edge vacancy and the unit cell containing the magnetic impurity, given in number of unit cells. The shaded area in each of the ribbon schematics contains one unit cell of that ribbon.

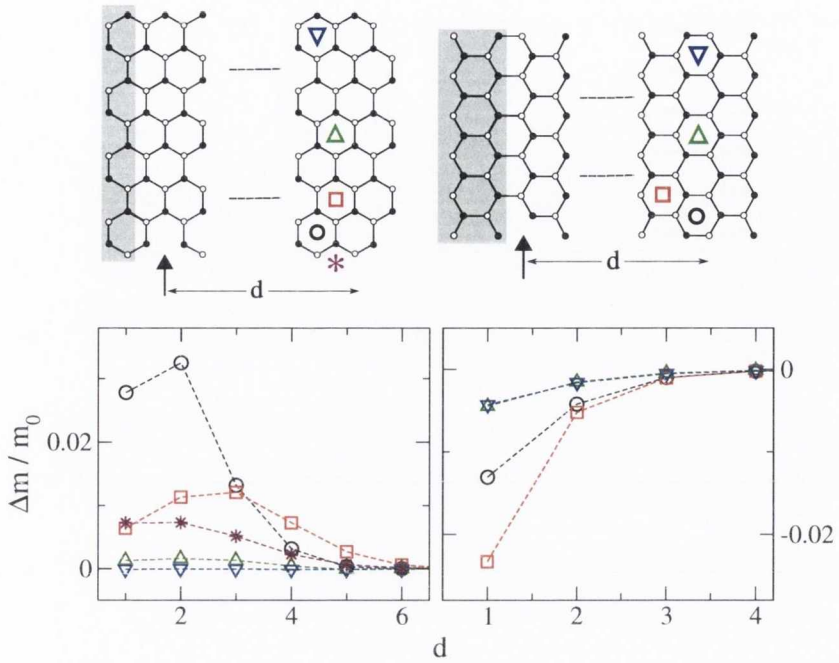

Figure 4.17: The effect of an edge vacancy on the magnetic moment of centre-adsorbed magnetic impurity atoms on an 8-ZGNR and 11-AGNR. The notation in the schematics and graphs is the same as for Fig. 4.16. For the zigzag case, the result for an edge-adsorbed impurity (star, purple) is also shown.

two unit cells away from the edge vacancy for all impurity types considered, including the edge-adsorbed case in ZGNRs.

A single edge vacancy has been shown not to have a significant effect on the magnetic moments of transition metal impurities in a GNRs. In fact, even the introduction of an extended edge defect, consisting of a length of ribbon to either side of the magnetic impurity with a certain concentration of edge vacancies, does not considerably affect the impurity moments unless there is an edge vacancy in their immediate vicinity. We conclude that magnetic moments introduced into GNRs by transition metal doping are particularly stable and robust in the presence of edge disorder. In particular, the striking moment profiles seen for magnetic impurities in ZGNRs will not be significantly perturbed by the introduction of a reasonably strong extended edge disorder. This point is illustrated quite clearly in Fig. 4.18 for the case of substitutional impurities on a 6-ZGNR, the same case considered in the up-

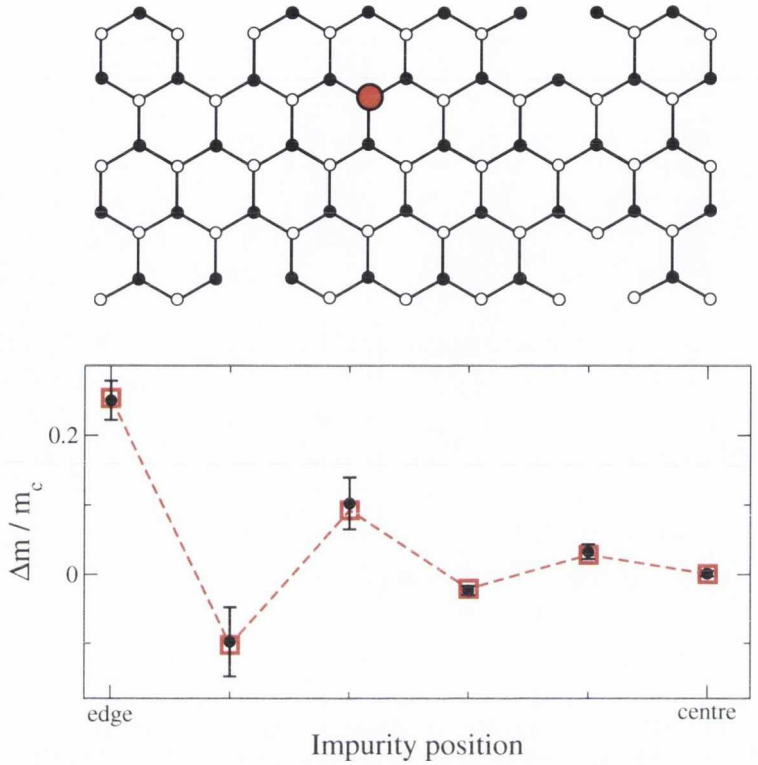

Figure 4.18: Schematic showing region of 6-ZGNR with a magnetic impurity and edge disorder consisting of atoms removed randomly from the edge zigzag chain of the ribbon (top panel) and the the resulting moment fluctuations (bottom panel). The red squares indicate the position dependent moment fluctuations in a ribbon without edge disorder, whilst the black squares correspond to the average fluctuations taken over fifty edge-disorder configurations, with the standard deviation shown by the error bars.

per panel of Fig. 4.12. The moment profile for the pristine case is shown as calculated with the mean-field Hubbard approach (red squares). Also shown is the moment profile for a system with a disordered region with a length of 100 unit cells to either side of the magnetic impurity (black circles). Within this disordered region, carbon atoms from the edge zigzag chain at either edge of the ribbon are removed with a probability of 10%. This plot shows the result of an average over 50 such configurations, with the error bars on each point indicating the standard deviation. The moment profile is seen to not vary significantly from that of pristine case, demonstrating clearly the

robustness of the moment profile.

4.5 Summary of Chapter

In this chapter we used the Green function methods introduced in previous chapters to examine some position dependent features in graphene nanoribbons doped with impurity atoms. We first considered the effect of impurity location on the electronic transport through a ribbon and demonstrated how such calculations can be performed with the Caroli formula. The results and trends of previous studies of such systems were discussed - in particular the presence of a qualitative difference between the transport through ribbons with uniform disorder or disorder localised principally at the ribbon edge.

Next we examined how the binding energy of such impurities depends on their location and how the resulting behaviour may result in a degree of spatial segregation in the impurity distribution across the ribbon. In the case of ZGNRs a non-monotonic feature found was connected to the sublattices of the graphene atomic structure. A simple theoretical model for calculating how the energy variation changes across a ribbon was developed and found to be in agreement with the results of DFT calculations. We postulated that control of the adsorbed impurity segregation within a ribbon is possible by adjusting the Fermi energy. We thus argued that, due to the sublattice dependence of magnetic interactions and the defect position dependence of transport within graphene, the magnetic profile and electronic properties of a GNR may be engineered by exploiting this control of the impurity segregation.

Finally, we considered the case of magnetic impurity atoms and considered how the impurity magnetic moment depended on the impurity position. For ZGNRs we found an excellent agreement between the simple self-consistent Hubbard model and a more complete *ab initio* treatment. Furthermore the qualitative features of the resulting moment profile remained constant for different parameterisations describing the magnetic impurity, suggesting that they hold for a wide range of magnetic species. For substitutional impurities, a nonmonotonic behaviour connected to the sublattices

of the graphene atomic structure was identified. For this type of impurity, a larger moment was found on impurities located on the edge site of a ZGNR. For impurities adsorbed onto the centre of a hexagon of the graphene lattice, a monotonic increase of the moment magnitude as the impurity was moved towards the centre of the ribbon was found. However an additional impurity type, consisting of an impurity atom connecting to three edge atoms at a zigzag edge was found to have a larger moment than one connected to the edge hexagon. It was also noted to be more energetically favourable. For armchair-edged nanoribbons, the moment profile features were noted to be less robust than for the zigzag case. However the fluctuations of the moment value around that at the ribbon centre were also found to be smaller. For both edge geometries and impurity configurations, we showed that an edge vacancy did not have a significant effect on the moment of a magnetic impurity located more than one or two lattice spacings away. Furthermore, we demonstrated that the distinctive moment profile for substitutional impurities on a zigzag-edged ribbon was robust in the presence of an extended edge disorder. In light of these findings, we argue that magnetically-doped nanoribbons may provide a route to applications previously envisaged for nanoribbons with intrinsic magnetic ordering, which is less stable in the presence of experimentally imposed constraints such as imperfect edge geometry.

The work presented in this Chapter was performed in collaboration with V. M. de Menezes (Departamento de Física, Universidade Federal de Santa Maria, Brazil) and S. B. Fagan (Área de Ciências Tecnológicas, Centro Universitário Franciscano, Brazil) who contributed the Density Functional Theory results presented throughout this chapter. The work presented in Section 4.3 was published as "Model of impurity segregation in graphene nanoribbons" (Phys. Rev. B 80, 235424). The work in Section 4.4 has published as "Magnetization profile for impurities in graphene nanoribbons" (Phys. Rev. B 84, 195431).

CHAPTER

FIVE

Static magnetic interaction in graphene

5.1 Introduction

In this chapter we begin our study of the interaction between magnetic moments in graphene. In the previous chapter we introduced single magnetic impurities into a graphene system and examined how geometry considerations affected the magnitude of the moment formed. We now consider more than one magnetic object embedded into a graphene system and investigate how the interaction between them depends on their separation. The coupling between two moments in such a system determines the relative orientation of their magnetic moments and thus the magnetic ordering in a system with many such magnetic objects. An understanding of the coupling between magnetic moments is an essential step in the effort to exploit graphene for spintronic applications as it underpins magnetic properties including the magnetic ordering and magnetoresistance of a magnetically-doped graphene device. This interaction, called the Indirect exchange coupling (IEC), between dilute magnetic moments within a conducting non-magnetic material is mediated by the conduction electrons of the host material [107–110]. It is often calculated using the Ruderman-Kittel-Kasuya-Yosida (RKKY) approx-

imation and indeed the interaction itself often takes this moniker[1] [111–115]. We will first introduce the approach used to calculate the IEC using the Lloyd formula and then relate this to the more commonly known RKKY approach. Previous findings for the interaction in graphene and related materials will be discussed, before the basic results of the RKKY approach in graphene are demonstrated using the Green function expressions calculated in Chapter 3. We shall then demonstrate how a more complete description of the interaction leads to findings not predicted by the RKKY approach and discuss some of the possible implications of these.

Finally, motivated by recent studies [181, 185] reporting the formation of localised magnetic moments in doped graphene, we investigate the energetic cost of spin polarising impurities embedded in graphene. We consider the effect that the interaction may have on calculations that make use of periodic boundary conditions to calculate the properties of graphene systems with magnetic impurities. This constraint is very common in Density Functional Theory calculations. Furthermore we find that neglecting the effect of the interaction between magnetic atoms in neighbouring unit cells can lead to the spurious suppression of the magnetic moment on these atoms. A strategy to avoid such issues is outlined. The existence of a criterion to determine whether or not a magnetic moment is likely to arise within graphene will be instrumental in helping to predict the ideal materials for future carbon-based spintronic applications.

5.2 Indirect exchange coupling

The indirect exchange coupling between two magnetic objects is distinct from the direct exchange coupling between the objects in that it is mediated solely by the conduction electrons of the host material into which the magnetic objects are embedded. The direct exchange, in contrast, depends on an overlap

[1]Throughout this chapter "RKKY" refers to the approximation to the interaction and "IEC" to the interaction itself. The meaning of "RKKY" elsewhere in the thesis is context dependent and will in general refer to a conduction-electron mediated interaction between magnetic objects.

of the electron orbitals and decays very abruptly. Initially investigated in multilayer systems, the oscillatory indirect coupling between magnetic layers as a function of their separation led to the discovery of the Giant Magnetoresistance Effect (GMR), which is now exploited in most modern memory devices [186, 187]. The IEC is defined as the energy difference between the parallel and antiparallel alignments of the magnetic moments on the objects, as shown schematically in Fig. 5.1 for a simple linear chain system. In this section we show how this quantity can be calculated using the Lloyd formula method discussed in Chapter 2, allowing us to calculate the IEC in terms of the Green functions of the system and the spin-dependent potentials arising from the description of the magnetic objects using the mean-field Hubbard model.

5.2.1 Lloyd Formula / Quantum well method

The spin-dependent potentials required to describe the magnetic objects are an integral part of the Quantum Well model of the IEC first proposed by Edwards et al [109, 110]. In this model, the introduction of spin-dependent potentials means that the electrons in the system are subject to a different potential in the magnetic regions than elsewhere as is evident in Fig. 5.1. The presence of these potential wells (or barriers) quantises[2] the allowed electron energies in the system. Furthermore, changing the separation between the wells by moving the magnetic objects shifts the allowed energies relative to the Fermi energy of the system giving rise to an oscillatory coupling. The coupling can be calculated by summing over all the levels below the Fermi energy and taking the difference between the cases with spin potentials corresponding to moments aligned parallel or anti-parallel. In this manner, the calculation of the indirect exchange coupling reduces to the calculation of an energy difference between two distinct configurations. We recall from Chapter 2 that such a calculation can be simplified using the Lloyd formula, which allows the calculation of the energy difference directly without the

[2]The allowed electron energies are quantised in one-dimensional or multilayer systems. In higher dimensions the allowed energies are modified by the wells, but are not strictly quantised.

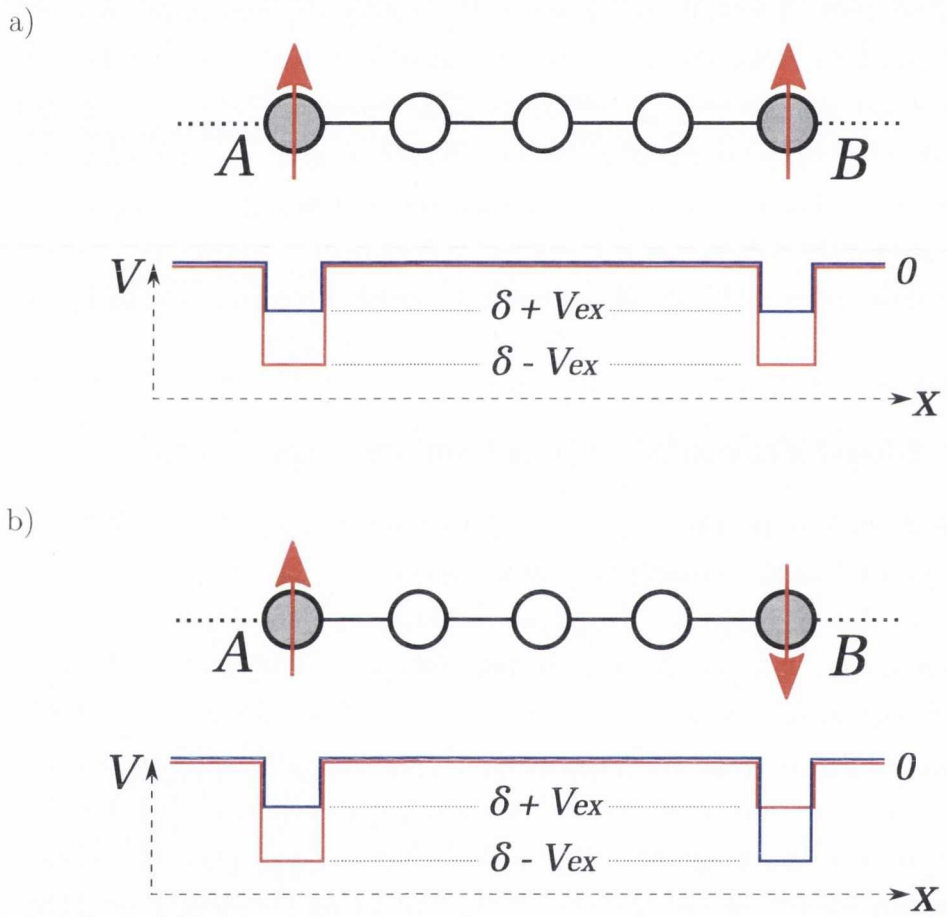

Figure 5.1: Schematic representation of the spin-split potentials at the magnetic sites for the parallel (a) and antiparallel (b) alignments of the magnetic moments. The red (blue) curves show the potential experienced by up-spin (down-spin) electrons as a function of position. For simplicity the host medium is represented by a one-dimensional linear chain.

need to calculate the total energy of either configuration.

The Lloyd formula expression to calculate the total change in the energy of a system is given by Eq (2.58) as

$$\Delta E\,(E_F) = \frac{1}{\pi}\,\mathrm{Im}\int \mathrm{d}E\; f(E)\;\ln\Big(\det(\hat{I} - \hat{g}(E)\hat{V})\Big)\;, \tag{5.1}$$

where $\hat{g}$ is the Green function describing the unperturbed system, $\hat{V}$ is the applied perturbation potential and $f(E)$ is the Fermi function. To calculate an expression for the IEC, we consider the following case. The unperturbed system consists of two moments embedded in a host material at sites A and B, which are aligned parallel along the z-direction so that the angle between them, $\theta = 0$. This setup is shown schematically in the top panel of Fig. 5.1. The Green function matrix for such a system can be calculated easily from the pristine Green functions of the host and the Dyson equation to add the magnetic objects to the system with spin dependent onsite potentials determined by the bandcentre (δ) and exchange splitting ($V_{ex} = \frac{\Delta}{2} = \frac{Um}{2}$) from the mean-field Hubbard model. We now introduce a spin perturbation which rotates the magnetic moment at B by an angle θ with respect to that at A. This perturbation is given by

$$\begin{aligned} V(\theta) &= -V_{ex}\,\left[(\cos\theta - 1)\,\hat{\sigma}_z + \sin\theta\,\hat{\sigma}_x\right] \\ &= -V_{ex}\begin{bmatrix} \cos\theta - 1 & \sin\theta \\ \sin\theta & 1 - \cos\theta \end{bmatrix}, \end{aligned} \tag{5.2}$$

where $V_{ex} = \frac{Um}{2}$ is the exchange splitting and $\hat{\sigma}_z$ and $\hat{\sigma}_x$ are the relevant Pauli matrices. Since the magnetic moments break the spin degeneracy of the electrons, the Green function of the moment to be rotated, g_{BB}, must be written in terms of its up- and down-spin components. In the initial collinear configuration there is no mixing between the spin bands and g_{BB} is diagonal

in spin space. Focusing on the determinant in Eq. (5.1) we can write

$$\begin{aligned}
&\det\left[\hat{I} - \hat{g}_{BB}(E)\,\hat{V(\theta)}\right] \\
&\quad = \left|\begin{pmatrix} 1 & 0 \\ 0 & 1 \end{pmatrix} + V_{ex}\begin{pmatrix} g^{\uparrow}_{BB} & 0 \\ 0 & g^{\downarrow}_{BB} \end{pmatrix}\begin{pmatrix} \cos\theta - 1 & \sin\theta \\ \sin\theta & 1 - \cos\theta \end{pmatrix}\right| \\
&\quad = 1 + V_{ex}\,(g^{\uparrow}_{BB} - g^{\downarrow}_{BB})\,(\cos\theta - 1) \; + 2\,V_{ex}^2 g^{\uparrow}_{BB} g^{\downarrow}_{BB}\,(\cos\theta - 1)\,.
\end{aligned} \tag{5.3}$$

Using the Dyson equation, we find

$$g^{\downarrow}_{BB} = g^{\uparrow}_{BB} + 2\,V_{ex}\,(g^{\uparrow}_{BA}\,g^{\downarrow}_{AB} + g^{\uparrow}_{BB}\,g^{\downarrow}_{BB})$$

so that

$$\det\left[\hat{I} - \hat{g}_{BB}(E)\,\hat{V(\theta)}\right] = 1 - 2V_{ex}^2\; g^{\uparrow}_{BA}\; g^{\downarrow}_{AB}\;(\cos\theta - 1)\,. \tag{5.4}$$

Taking $\theta = \pi$, corresponding to an antiparallel alignment of the moments we find, for zero temperature, that

$$J_{BA} = -\Delta E(\theta = \pi) = -\frac{1}{\pi}\,\mathrm{Im}\int_{-\infty}^{E_F} \mathrm{d}E\;\ln\left(1 + 4\;V_{ex}^2\;g^{\uparrow}_{BA}(E)\;g^{\downarrow}_{AB}(E)\right)\,, \tag{5.5}$$

where we have chosen the sign convention that a negative value of the coupling, J, corresponds to a preferential parallel alignment of the moments and a positive value to a preferential antiparallel alignment. When performing the integral in Eq. (5.5) numerically we employ the methods outlined in Chapter 2 to rewrite the integral over the imaginary axis where the integrand tends to be smoother and easier to integrate. With an imaginary axis integration, the expression for the coupling becomes

$$J_{BA} = \frac{1}{\pi}\int_{\eta}^{\infty} \mathrm{d}y\;\ln\left|1 + 4\;V_{ex}^2\;g^{\uparrow}_{BA}(E_F + iy)\;g^{\downarrow}_{AB}(E_F + iy)\right|\,. \tag{5.6}$$

We note that in these expressions the distance dependence is entirely contained within the product of off-diagonal Greens function elements for the up-spin or down-spin cases. Using the Dyson equation these can be writ-

ten in terms of the Green functions of the pristine host system and the potentials used to describe the magnetic impurities. The exact functional form of this expression will depend on the nature of the connection between the impurity and the host, as we have seen in Section 2.4. Ultimately the only distance-dependent term entering into the expression is the off-diagonal Green function of the host system and the behaviour of this term will dictate the behaviour of the interaction as the separation between the moments is varied.

5.2.2 RKKY approximation

An alternative approach to account for the coupling between magnetic objects embedded in a metallic host avails of the Ruderman-Kittel-Kasuya-Yosida formalism, initially developed to describe the coupling mechanism of nuclear magnetic moments [111], then expanded to describe a wider range of indirect coupling phenomena [112, 113] and generalised to provide a model capable of reproducing experimental observations [114, 115]. This treats the coupling as a consequence of the spin polarisation of the conduction electrons of the host by the magnetic objects. Under this approach, the coupling is written as an effective direct coupling, $J_{BA}\,\mathbf{s}_B \cdot \mathbf{s}_A$, between the two moments, where the coupling strength is given by

$$J_{BA} = -\left(\frac{\lambda^2 \hbar^2}{4}\right) \chi_{BA}\,. \tag{5.7}$$

where λ is an adjustable parameter representing the magnitude of the coupling between localised spins and conduction electrons and χ is the static magnetic susceptibility which relates the response of the host magnetisation to a static magnetic field.

Expanding the logarithm in Eq. (5.5) to second order in $\cos\theta$ and then to first order in V_{ex} gives

$$J_{BA}^{RKKY} = -2\,V_{ex}^2\,\chi_{BA}^0\,, \tag{5.8}$$

where

$$\chi^0_{BA} = -\frac{2}{\pi} \int \mathrm{d}E \; f(E) \, \mathrm{Im}\left[g_{BA}(E) \, g_{AB}(E) \right] \tag{5.9}$$

is the non-interacting static-susceptibility calculated without any exchange splitting. Note that it is written in terms of the pristine, spin-independent Green functions. This is essentially the RKKY result which is obtained in the limit of small exchange splitting. Thus the RKKY approach can be considered a second-order perturbational approximation to the IEC and provides a good description at large separations when the coupling is quite small [188–190]. An important contrast between the Lloyd formula approach to the Quantum Well model and the RKKY approach is the choice of Green function used. The former approach avails of the spin dependent Green functions in the ferromagnetic configuration, $g^{\uparrow}_{BA}$ and $g^{\downarrow}_{AB}$ whereas the latter approach generally uses their pristine, spin-independent counterparts. An intermediate approach can be taken by using the spin-dependent Green functions with an RKKY-like expansion of the logarithm in the IEC expression.

5.3 Magnetic interaction in graphene

Many of the initial investigations into RKKY-like interactions were based on magnetic multilayer devices, with both quantum well and RKKY studies finding a separation dependence of $1/D^2$, where D is the separation between the magnetic layers. However, this decay rate was further predicted to depend on the dimensionality of the system and in one-dimensional metals was predicted to be as slow as $1/D$, which would give rise to a particularly long-ranged decay. With the discovery of Carbon Nanotubes (CNTs), the possibility of 1-D metals became realistic and the study of magnetic interactions in graphene-based systems began in earnest. Of particular interest was the study of magnetic interactions in magnetically doped CNTs, particularly as many transition metal atoms were already used as catalyst particles during the growth of CNTs [191].

Studies of the IEC in CNTs revealed an unusual range of features not seen in other materials and arising from the unique electronic structure of

the underlying graphene lattice. In undoped nanotubes, the oscillatory feature seen in other systems was not present [116]. This feature arises from the peculiar Fermi surface of graphene, consisting of six discrete points, as discussed in Chapter 3. It can be shown that the wavevectors defining the period with which the coupling oscillates are necessarily commensurate with the hexagonal lattice. In other words, the oscillations are perfectly commensurate with the underlying structure and are not seen due to aliasing. It was also found that the sign of the coupling was intrinsically linked to the sublattices composing the graphene atomic structure. The sign of the coupling between sites on the same sublattice was predicted to be the opposite of that between sites on opposite sublattices. In general, the coupling between sites on the same sublattice was predicted to be ferromagnetic and on different sublattices antiferromagnetic. However, depending on the atomic species chosen the opposite could be found [119]. The decay rate of $1/D$ predicted for 1-D metals by the Quantum Well theory was found for substitutional and top-adsorbed magnetic impurities in CNTs. However, further work demonstrated that the coupling decay rate depended crucially on the specific nature of the impurity and how it bonded to the host nanotube [117]. In particular, centre-adsorbed impurities were found to have a decay rate of $1/D^5$, a far more rapid decay than predicted. This feature was shown to arise by reproducing a symmetry in the graphene lattice causing lower order terms to vanish.

The experimental discovery of two-dimensional graphene prompted similar studies of the IEC in this material [121–133]. Much of this study was performed using the RKKY approach and availing of the linear dispersion regime to simplify calculations. When the linear dispersion approximation is used, a cut-off function is required to prevent the result diverging due to high energy contributions. There has been some debate about the effect of the cutoff function chosen on the resultant interaction calculated [123, 124, 127]. Other approaches to circumvent this problem involve numerical calculations [127,128] which can lack the transparency of an analytical solution. The non-oscillatory behaviour found for nanotubes again arises in graphene sheets. However, the rate at which the coupling decays displays unusual behaviour. The $1/D^2$

dependence predicted for 2-D systems is not found in undoped graphene and instead a faster decay rate of $1/D^3$ is reported. However when the system is doped away from $E_F = 0$ the expected decay rate is recovered. This discrepancy is due to the pecularity of the graphene electronic structure at $E_F = 0$ where the density of states vanishes. The RKKY approximation also finds a strong sublattice effect in the sign of the coupling for the undoped case. Impurities situated on the same sublattice are predicted to have a ferromagnetic alignment, whereas those on opposite sublattices have an antiferromagnetic alignment. A similar effect to that noted earlier for centre-adsorbed impurities in CNTs [117] is also noted in graphene sheets [129]. In this case, the coupling decays not as $1/D^3$, but as $1/D^7$. The use of either the linear-dispersion approximation or of brute-force numerical methods to calculate the coupling arises from the difficulty in calculating the Green functions of graphene, or of 2D materials generally, using analytical methods. Although a full analytical expression for the Green function, similar to that for nanotubes, is not available for graphene, we demonstrated in Chapter 3 that an excellent approximation to it can be realised using the stationary phase approximation (SPA). In the next section we will avail of the expressions calculated earlier to derive the principal features of the magnetic interaction in graphene.

5.3.1 RKKY calculation with SPA

We have seen that the exchange energy, J, within the RKKY approximation can be expressed in terms of the Green functions of the pristine host system via the static susceptibility, allowing us to write

$$J_{BA}(E_F) \sim \mathrm{Im} \int \mathrm{d}E \; f(E) \; V_{ex}^2 \; \mathcal{G}_{BA}^2(E) \tag{5.10}$$

for two moments occupying like-sites in the graphene lattice separated by a distance D, where $f(E)$ is the Fermi function. Recall from Eq. (3.44) that

we can write the off-diagonal Green function element as

$$\mathcal{G}_{BA}(E) = \frac{\mathcal{A}(E)\, e^{i\mathcal{Q}(E)D}}{\sqrt{D}},$$

so that

$$J_{BA} \sim \frac{V_{ex}^2}{D}\ \mathrm{Im} \int \mathrm{d}E\ \frac{\mathcal{B}(E) e^{2i\,\mathcal{Q}(E)\,D}}{1 + e^{\beta(E-E_F)}}\ , \tag{5.11}$$

where $\mathcal{B}(E) = \mathcal{A}^2(E)$, $\beta = \frac{1}{k_B T}$, T being the temperature and k_B the Boltzmann constant. The integral in Eq (5.11) can be solved by replacing it with a contour integral in the energy upper-half plane. In this case the poles are given by the zeroes of the denominator of the Fermi function, namely the Matsubara frequencies, $E_p = E_F + i(2p+1)\pi k_B T$ where p is an integer labelling the poles.

$$\begin{aligned} J_{BA} &\sim \frac{V_{ex}^2}{D}\ \mathrm{Im}\ 2\pi i\ \mathrm{Res} \sum_p \left[\frac{\mathcal{B}(E) e^{2i\,\mathcal{Q}(E)\,D}}{1 + e^{\beta(E-E_F)}}\right]\Bigg|_{E=E_p} \\ &\sim \frac{V_{ex}^2\, k_B\, T}{D}\ \mathrm{Im} \sum_p \left[i\,\mathcal{B}(E_p)\, e^{2i\,\mathcal{Q}(E_p)\,D}\right] \end{aligned}$$

We now write the coefficient $\mathcal{B}(E)$ as a Taylor series, and the wavevector $\mathcal{Q}(E)$ as a first order expansion, around the Fermi energy so that

$$\begin{aligned} \mathcal{B}(E) &= \sum_l \frac{1}{l!}\, \mathcal{B}^{(l)}\, (E - E_F)^l \\ \mathcal{Q}(E) &= \mathcal{Q}^{(0)} + \mathcal{Q}^{(1)}\, (E - E_F) \end{aligned} \tag{5.12}$$

using the notation $\mathcal{B}^{(l)}$ ($\mathcal{Q}^{(l)}$) to denote the lth derivative of $\mathcal{B}$ ($\mathcal{Q}$) evaluated at the Fermi energy. The expression for the coupling now becomes

$$\begin{aligned} J_{BA} &\sim \frac{V_{ex}^2\, k_B\, T}{D}\ \mathrm{Im} \sum_l \frac{i}{l!}\, \mathcal{B}^{(l)}\, e^{2i\,\mathcal{Q}^{(0)}\,D} \sum_p e^{2i\,\mathcal{Q}^{(1)}\,(E_p - E_F)\,D}\, (E_p - E_F)^l \\ &\sim \frac{V_{ex}^2\, k_B\, T}{D}\ \mathrm{Im} \sum_l \frac{i}{l!}\, \mathcal{B}^{(l)}\, e^{2i\,\mathcal{Q}^{(0)}\,D}\, \frac{1}{(2\,i\,\mathcal{Q}^{(1)})^l}\, \frac{\mathrm{d}^l}{\mathrm{d}D^l} \left\{\sum_p e^{2\,i\,\mathcal{Q}^{(1)}(E_p - E_F)D}\right\}, \end{aligned}$$

where

$$\begin{aligned}\sum_p e^{2\,i\,\mathcal{Q}^{(1)}(E_p-E_F)D} &= \sum_p e^{-2\,\mathcal{Q}^{(1)}(2p+1)\,\pi\,k_B\,T\,D} \\ &= e^{-2\,\mathcal{Q}^{(1)}\,\pi\,k_B\,T\,D}\sum_p \left(e^{-4\,\mathcal{Q}^{(1)}\,\pi\,k_B\,T\,D}\right)^p \\ &= \frac{e^{-2\,\mathcal{Q}^{(1)}\,\pi\,k_B\,T\,D}}{1-e^{-4\,\mathcal{Q}^{(1)}\,\pi\,k_B\,T\,D}} \\ &= \frac{1}{2\,\sinh\left(2\,\mathcal{Q}^{(1)}\,\pi\,k_B\,T\,D\right)}\,,\end{aligned}$$

so that

$$J_{BA} \sim \frac{V_{ex}^2}{D}\,\mathrm{Im}\sum_l \frac{i}{l!}\,\mathcal{B}^{(l)}\,e^{\,2i\,\mathcal{Q}^{(0)}D}\,\frac{1}{(2\,i\,\mathcal{Q}^{(1)})^l}\,\frac{\mathrm{d}^l}{\mathrm{d}D^l}\left\{\frac{k_B\,T}{2\,\sinh\left(2\,\mathcal{Q}^{(1)}\,\pi k_B T D\right)}\right\}\,,$$

which in the low temperature limit, $T \to 0$, becomes

$$\begin{aligned}J_{BA} &\sim \frac{V_{ex}^2}{D}\,\mathrm{Im}\sum_l \frac{i}{l!}\,\mathcal{B}^{(l)}\,e^{\,2i\,\mathcal{Q}^{(0)}D}\,\frac{1}{(2\,i\,\mathcal{Q}^{(1)})^l}\,\frac{\mathrm{d}^l}{\mathrm{d}D^l}\left\{\frac{1}{4\,\mathcal{Q}^{(1)}\,\pi D}\right\} \\ &\sim V_{ex}^2\,e^{\,2i\,\mathcal{Q}^{(0)}D}\,\mathrm{Im}\sum_l \frac{(-1)^l\,\mathcal{B}^{(l)}}{(2\mathcal{Q}^{(1)})^{l+1}\,D^{l+2}}\end{aligned} \tag{5.13}$$

In this form the oscillation period and decay rate of the interaction at different Fermi energies can be easily extracted. The decay rate in the asymptotic limit [117] is determined by the leading term in Eq (5.13), namely $l = 0$, suggesting that, in general, $J \sim D^{-2}$. The oscillation period is determined by the term $e^{\,2i\,\mathcal{Q}^{(0)}D}$, i.e. by the Fermi wavevector. However, as we have stated previously, the RKKY coupling in graphene at $E_F = 0$ is found to be non-oscillatory[3] and decay as $J \sim D^{-3}$. This result can be reconciled with our expression by considering the analytic form of the expressions for $\mathcal{B}^{(0)}$ and $\mathcal{Q}^{(0)}$. We will focus on those for separations in the armchair direction, but a similar analysis holds for separations in the zigzag or other directions. Using the results for the Green functions calculated within the SPA from

[3]By 'non-oscillatory" here we mean that coupling has no *sign-changing* oscillations as a function of D.

Eqs. (3.34) and (3.33), we find for separations in the armchair direction that for $|E_F| < |t|$,

$$\mathcal{B}^{(0)}(E) = -\frac{2}{i\pi}\frac{E}{(E^2+3t^2)\sqrt{t^2-E^2}}$$

and

$$\mathcal{Q}^{(0)}(E) = \pm\cos\left(\frac{-\sqrt{t^2-E^2}}{t}\right).$$

In the limit $E \to 0$, $\mathcal{B}^{(0)}$ vanishes and $\mathcal{Q}^{(0)} \to \pi$ as can be seen from Fig 3.9 in Chapter 3. The vanishing of $\mathcal{B}^{(0)}$ at $E_F = 0$ means that the decay rate of the coupling is now determined by the first surviving term, $l = 1$, in Eq. (5.13) resulting in a decay rate of $J \sim D^{-3}$, as reported elsewhere [123,124,127,128]. It is also clear that since D can only take integer values, the term $e^{2i\,\mathcal{Q}^{(0)}D} = 1$ at $E_F = 0$. Thus the oscillation period of the coupling is commensurate with the graphene lattice spacings and the oscillations are masked. When $E_F \neq 0$, the leading term does not vanish, and the oscillation period is no longer commensurate with the lattice spacing, leading to the observed oscillatory interaction [124] that decays as $J \sim D^{-2}$. Note that these conclusions are reached for values of E_F regardless of whether or not they lie within the linear dispersion regime. The correct decay rate and oscillatory behaviour for the RKKY interaction in graphene have emerged naturally and in a mathematically transparent fashion from the SPA Green function formalism, without the need to resort to the linear response approximation or a cut-off function.

In Fig. 5.2 we plot the interaction calculated numerically for both the undoped (top panel) and doped (bottom panel) cases for separations in the armchair direction. The calculations were performed with a half-filled d-band for the magnetic atom and keeping the hopping parameters equal to those of graphene. Such a configuration yields only a splitting, and not a bandcentre shift, when treated within the self-consistent Hubbard model and so a close agreement is expected between the Lloyd formula equation (5.5) and the RKKY approximation (5.8) of the interaction. The black (red) curves show the results for substitutional atoms on the same (different) sublattice(s). The predicted $\frac{1}{D^3}$ and $\frac{1}{D^2}$ decay rates for the undoped and doped cases respectively are clear from the log-log plots in the insets. For the undoped case we also

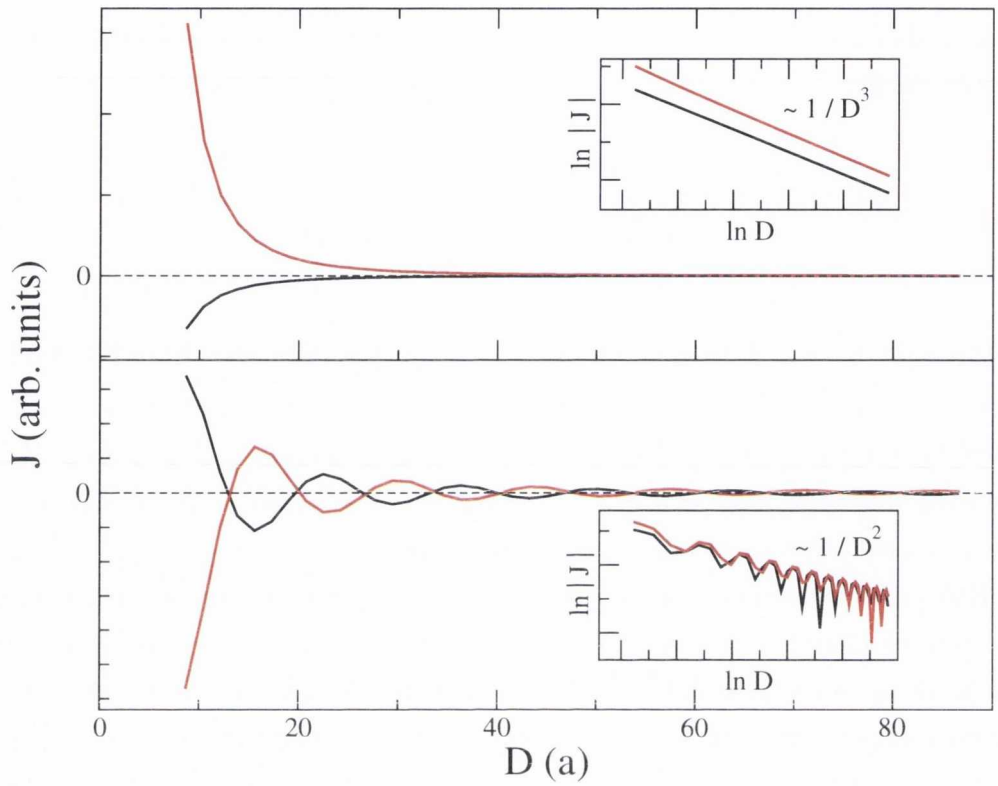

Figure 5.2: The magnetic coupling between two substitutional impurities as a function of their separation in the armchair direction for both the undoped ($E_F = 0.0$, top) and doped ($E_F = 0.2t$, bottom) cases. The black (red) curves correspond to impurities on the same (different) sublattices. The rate of decays are clear from the slope of the log-log plots shown in the insets.

note that the sign of the coupling does not change as a function of distance, but that the sign of the coupling is determined by whether the sites reside on the same or opposite sublattices. We note that a ferromagnetic alignment is energetically favourable for moments on the same sublattice, with an antiferromagnetic alignment favourable for the case of different sublattices. This result has been frequently reported in studies examining the RKKY interaction in graphene using a variety of approaches, as discussed earlier. From the analytic discussion above we note that, in the undoped case, any sign changing oscillations in the interaction as a function of distance are ruled out by a commensurability effect. Thus the sign of the interaction depends solely on the energy-dependent coefficient $\mathcal{B}^{(1)}$, which is independent of distance.

5.4 Beyond the RKKY approximation

In the previous section, the decay rates and oscillatory behaviour of the Indirect Exchange Coupling were investigated. A number of approximations were made in order to calculate these properties analytically. These included the use of the RKKY approximation instead of the full IEC integral. Another approximation was the use of the Stationary Phase Green functions for the pristine system rather than numerically calculated Green functions incorporating the perturbation potentials describing the magnetic atoms. In this section we shall expand the description of the interaction to include these potentials. The effect of the magnetic moment parameterisation on the interaction will be investigated and we demonstrate how the nature of the coupling depends on the impurity species and its connection to the graphene lattice.

5.4.1 Effect of impurity parameterisation

As we have noted above, the RKKY approximation to the IEC does not account properly for the local spin dependent potentials describing the magnetic moments. In fact, the parameterisation of the magnetic impurity is generally neglected through the usage of the pristine Green functions. In this section we consider the effect of three parameters that can be used to characterise the magnetic impurities. In addition to the magnetic moment (m) and band-centre shift (δ) that emerge from the self-consistent mean-field calculations, we also consider the hopping potential between the lattice carbon sites and the impurity site (t') which should differ from the carbon-carbon hopping. This approach is similar to the Anderson model describing localised magnetic impurity states in metals [192]. These parameters will vary between the different magnetic species that can be chosen as the embedded impurities. In Fig 5.3 we plot the coupling between like sites, calculated using the full integral and numerical Green functions for substitutional impurities, as a function of separation along the armchair direction for three different parameter sets (m, δ, t'). The first of these $(0.6, 0.0, t)$ closely replicates the results of the RKKY approach as it considers only a

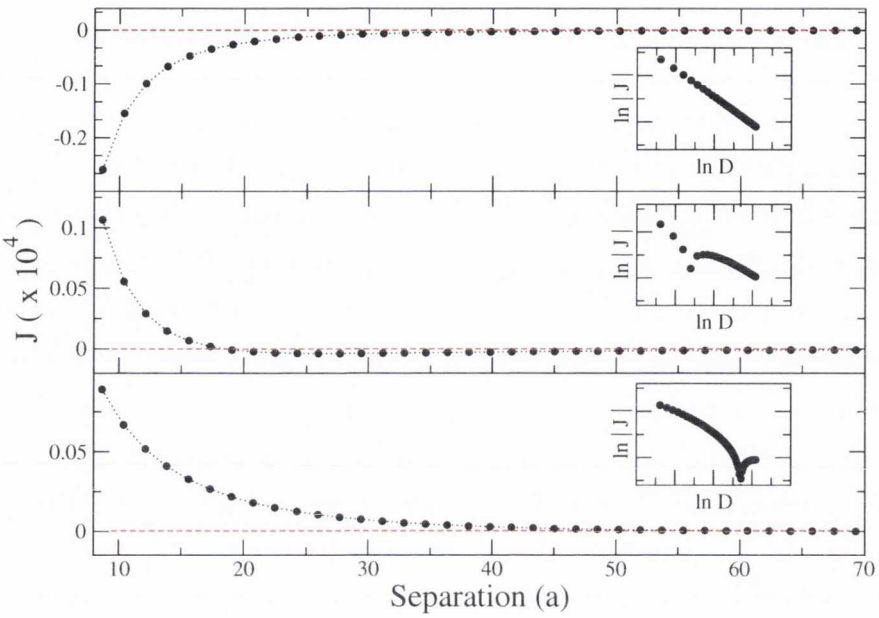

Figure 5.3: The magnetic coupling between two magnetic sites on the same sublattice as a function of their separation, D, along the armchair direction for three different impurity parameterisations: a) ($m = 0.6$, $\delta = 0.0$, $t' = t$), b) ($m = 0.6$, $\delta = 5.0t$, $t' = 0.8t$) and c) ($m = 0.6$, $\delta = 8.0t$, $t' = 0.6t$). The insets show log-log plots where a sign change in the coupling is evident from a dip feature.

band-splitting, has no band-centre shift and uses the carbon-carbon hopping value. The middle and bottom plots use the parameters $(0.6, 5.0, 0.8t)$ and $(0.6, 8.0, 0.6t)$ respectively. In these plots we see the formation of an unusual feature not predicted by the RKKY approximation. For quite a large range of distances we note a preferential *antiferromagnetic* alignment between the moments before the sign flips and the standard ferromagnetic coupling with a $1/D^3$ decay is recovered. A similar sign-changing behaviour has been reported in nanotubes [119] and also by *ab initio* calculations attempting to probe the interaction in graphene [193]. It is worth examining further how this feature depends on the parameterisation of the magnetic moments. In Fig 5.4 we present a number of phase diagrams showing the sign and strength of the coupling for different values of these parameters. Each diagram represents an area of (m, δ) phase space with ferromagnetic (antiferromagnetic)

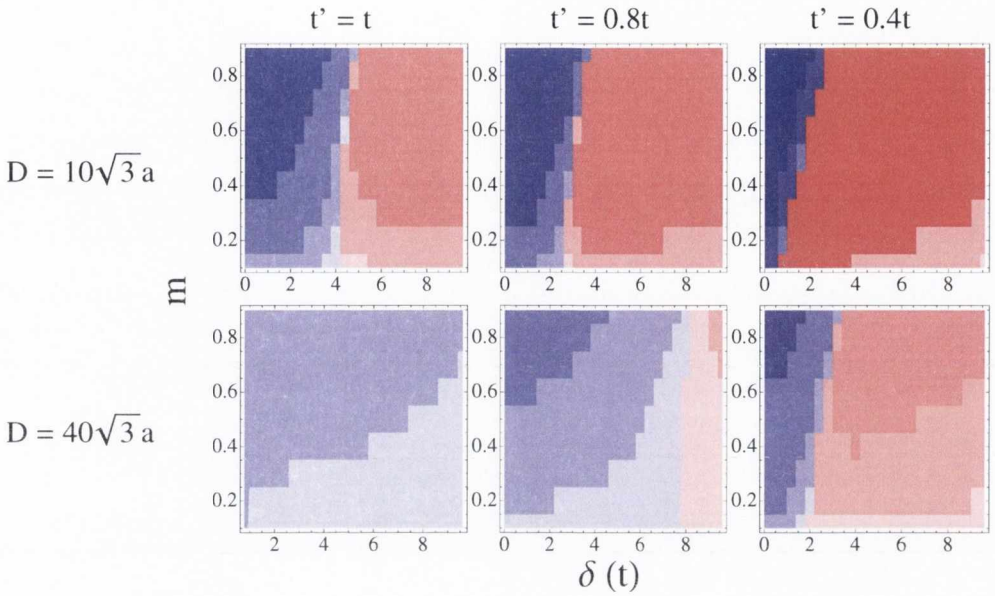

Figure 5.4: (m, δ) phase-space diagrams for separations of $10\sqrt{a}$ (top row) and $40\sqrt{a}$ (bottom row) for three different values of the impurity-carbon hopping parameter t'. The sign of the coupling is indicated by the colour (blue for FM and red for AFM) and the strength of the coupling by the degree of shading.

couplings given by a blue (red) shading that is darker for larger magnitude couplings. The diagrams on the top row correspond to a separation of $10\sqrt{a}$ between the magnetic moments and from left to right show the cases of $t' = 1.0t, 0.8t, 0.4t$. The bottom panels show the same cases for a larger separation of $40\sqrt{a}$. By examining the border between the blue and red regions in these plots we can infer under what circumstances the sign-change behaviour described above occurs. In all cases the border position varies only weakly with the magnetic moment (m) or hence the band-splitting (Δ). A stronger dependence is found on the band-centre shift (δ) and we find that, in general, an anti-ferromagnetic alignment is found above a critical value of δ. The band-centre shift is found using the recursive mean-field approach and is strongly dependent on the occupation of the magnetic orbital. For a bipar-

tite lattice like graphene a substitutional impurity with a half-filled orbital gives zero band-centre shift when $t' = t$. As we move away from half-filling a larger band-centre shift is required to return the correct band occupation. For smaller values of t' we note that the border between the blue and red regions shifts towards the left, meaning that smaller band-centre shifts will lead to an AFM alignment. Increasing the distance between the impurities reduces the phase-space area corresponding to an AFM alignment by shifting the border to the right and requiring larger band-centre shifts. This finding agrees with the plots in the distance-dependent plots in Fig. 5.3 for fixed parameters which show that in the asymptotic limit the coupling changes sign and returns the FM alignment predicted by the RKKY approximation. However, as in the bottom panel of Fig. 5.3, the magnitude of the coupling has essentially decayed to zero before the sign change occurs so the only significant coupling between two such impurities is antiferromagnetic. We have seen that, depending on the moment parameterisation, a strong antiparallel alignment between two substitutional magnetic impurities in graphene may persist to considerable separations. This result contradicts the predictions of the RKKY theory and we demonstrate in the next section that such a coupling can lead to unforeseen difficulties in calculations involving periodic boundary conditions.

5.5 Emergence of magnetic moments on impurity atoms in graphene

We now turn our attention to the energy cost required to spin polarise isolated impurities embedded in graphene. We will see that this topic is very closely related to the interaction between magnetic moments discussed in the previous sections. By applying a criterion for the formation of local magnetic moments in metals to graphene we are able to predict the existence of magnetic moments in cases that are in clear contrast to previously reported Density Functional Theory (DFT) results. These calculations often consider single impurities added to a unit cell with periodic boundary con-

ditions, under the assumption that the cells are sufficiently large and that impurities are not able to interact with their neighbouring counterparts. By generalising the criterion to periodically repeated impurities, we find that the energy balance involved in such calculations contains unavoidable contributions from long-ranged pairwise magnetic interactions between the impurities. This raises the question of whether representing independent particles by single impurity unit cells is a valid assumption in the case of magnetic dopants in graphene-based materials. We show that these problems can be circumvented if more than one impurity per unit cell is considered, in which case the DFT results agree perfectly well with the criterion-based predictions for the onset of localised magnetic moments in graphene.

5.5.1 Unexpected DFT findings

The assumption of representing independent particles by single impurity unit cells is frequently made in the case of magnetic objects in graphene-related materials. A recent study has comprehensively investigated the magnetic properties of a range of transition-metal atoms embedded in a graphene sheet [185] indicating complex magnetic behaviour as one moves across the periodic table. A remarkable finding in this survey is the absence of a magnetic moment when one Fe atom substitutionally replaces a single carbon atom in the graphene sheet. Of all the transition metal atoms, it is particularly surprising that an iconic magnetic element like Fe seems unable to develop a magnetic moment when immersed in graphene. Another study reports an unexpected dependence of the magnetic moment formed on the dimension of the unit cell considered [181]. Because the aforementioned DFT assumption of independent unit cells is used in the referred survey as well as in other studies of magnetic dopants in carbon-based structures [174, 194–196], it is instructive to ask whether the intrinsic long-ranged interaction that arises between magnetic moments in low-dimensional metals might be responsible for interfering with some of the results recently reported. If so, this interference may cause a spurious suppression of magnetic moments where they should actually exist.

5.5.2 Magnetic moment formation in graphene

Lieb's theorem [104] is often quoted to explain the magnetic properties of graphene. It shows that a net magnetisation arises when there is an imbalance between the two sub-lattices composing the bipartite lattice of graphene. While this is a perfectly sound explanation for graphene flakes and ribbons, as well as for graphene sheets containing vacancies [197], it is not directly applicable to substitutionally doped impurities since Lieb's theorem assumes a homogeneous electron-electron interaction throughout the system. In particular, the considerably narrower d-band associated with transition-metal impurities makes the electronic interaction highly non-homogeneous, and another explanation for the origin of magnetic moments in doped graphene-related materials is required. The formation of a single local moment in a non-magnetic system has been generally addressed by several authors, and a criterion for its existence has been previously derived in different contexts [192, 198], including a recent work considering the specific case of graphene as the non-magnetic host [199]. Here we develop an alternative derivation of this criterion, and generalise it to a pair of impurities in order to clarify the role played by the long range interaction between magnetic moments in low-dimensional systems. Furthermore, we show how this may affect first-principles calculations which artificially assume, for computational purposes only, that the system is translationally invariant. Although our focus is on doped graphene sheets, our conclusions result essentially from the hexagonal symmetry of the underlying lattice and are valid to graphene ribbons and flakes as well as nanotubes.

Single magnetic impurity in graphene

We start by considering a single transition metal atom embedded in a non-magnetic host, which in our case is a pristine hexagonal lattice, as shown in Fig. 5.5. The electronic structure of the system is described by a Hubbard-like Hamiltonian with the assumption that the on-site interaction only occurs between electrons occupying the d orbitals of the transition metal impurity. For simplicity we shall assume that the onsite effective exchange integrals

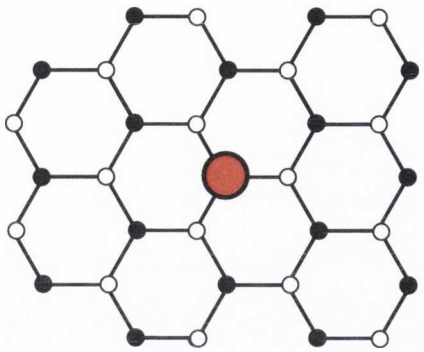

Figure 5.5: A single substitutional transition-metal atom embedded in a graphene host.

U are the same for all the d orbitals. To derive a local moment criterion we examine the stability of the non-magnetic state when a small exchange splitting, Δ, is activated. The energy cost involved in the formation of a local magnetic moment at the impurity site, $\Delta\mathcal{E}_1$, consists of two components. The first of these, ΔU, is the reduction of the effective electron-electron interaction due to the appearance of a local spin imbalance at the impurity site. This is given by

$$\Delta U = U(\Delta N^{\uparrow})\,(\Delta N^{\downarrow})\,, \tag{5.14}$$

where ΔN^{σ} is the change in the occupation number of electrons with spin σ on the impurity orbital. Assuming $\Delta N^{\uparrow} + \Delta N^{\downarrow} = 0$ and using the Lloyd formula expression for the change in occupation under the introduction of a perturbation potential given in Eq. (2.57), we find

$$\begin{aligned} \Delta U &= -U(\Delta N^{\uparrow})^2 \\ &= -U\left(\mathrm{Tr}\int \mathrm{d}E\,\Delta\rho_0^{\uparrow}\right)^2 \\ &= -U\left(-\frac{1}{\pi}\,\mathrm{Im}\,\mathrm{Tr}\int \mathrm{d}E\,\frac{g_{00}^2(E)\,\lambda^{\uparrow}}{1-g_{00}(E)\lambda^{\uparrow}}\right)^2 \end{aligned} \tag{5.15}$$

where $g_{00}(E)$ is the Green function for an electron with energy E at the impurity site, $\lambda^{\uparrow} = -\frac{\Delta}{2}$ is the perturbation potential for $\uparrow$-spin electrons due to the magnetic moment at the impurity site and the trace operator is over

the orbital degrees of freedom which in this case can be limited to the five d-orbitals.

The second contribution, ΔK, to $\Delta\mathcal{E}_1$ accounts for the change in the electronic kinetic energy of both $\uparrow$- and $\downarrow$-spin electrons due to the presence of the moment,

$$\begin{aligned}\Delta K &= \Delta K^{\uparrow} + \Delta K^{\downarrow} \\ &= \frac{1}{\pi}\sum_{\sigma} \mathrm{Im\ Tr} \int \mathrm{d}E\ \ln\left(1 - g_{00}(E)\lambda^{\sigma}\right) \\ &= \frac{1}{\pi}\mathrm{Im\ \ Tr} \int \mathrm{d}E\ \ln\left(1 - g_{00}^{2}(E)\lambda^{\uparrow\,2}\right).\end{aligned} \tag{5.16}$$

The energy cost involved in the formation of a local magnetic moment at the impurity site is thus given by

$$\begin{aligned}\Delta\mathcal{E}_1 = -U\left(-\frac{1}{\pi}\ \mathrm{Im\ Tr} \int \mathrm{d}E\ \frac{g_{00}^{2}(E)\,\lambda^{\uparrow}}{1 - g_{00}(E)\lambda^{\uparrow}}\right)^{2} \\ + \frac{1}{\pi}\int \mathrm{d}E\ \mathrm{Im}\ \ln\left(1 - g_{00}^{2}(E)\lambda^{\uparrow\,2}\right).\end{aligned} \tag{5.17}$$

The sign of $\Delta\mathcal{E}_1$ determines whether or not the non-magnetic state is unstable to a local magnetic moment formation. To derive a criterion for such an instability it is sufficient to expand Eq.(5.17) in powers of Δ to lowest order, which simplifies to

$$\Delta\mathcal{E}_1 = \left\{-U\,\ell^{2}(E_F) + \ell(E_F)\right\}\,(\Delta/2)^{2}, \tag{5.18}$$

where

$$\ell(E_F) = \frac{1}{\pi}\int_{-\infty}^{E_F} dE\,\mathrm{Im\,Tr}\left[g_{00}(E)\right]^{2} \tag{5.19}$$

is the local susceptibility. The formation of a local magnetic moment at the impurity is then energetically favourable when $\Delta\mathcal{E}_1 < 0$, *i.e.*, when

$$\ell(E_F) > \frac{1}{U}\,. \tag{5.20}$$

This inequality sets the condition for the spontaneous formation of a sin-

gle localised magnetic moment in a non-magnetic host. Written in terms of single-particle Green functions, it is model-independent and can be evaluated once the Hamiltonian is fully specified. The same criterion has been previously derived in other circumstances [198], but here we have obtained it by total energy balance considerations because it provides an easier way to analyse the effect of more impurities.

Multiple impurities

Let us now imagine that a second transition-metal impurity is added to the system at site m, as illustrated in Fig. 5.6. Similar steps to those outlined in Eqs. (5.14) - (5.17) above can be followed to derive the following expression for the energy cost involved in the formation of local magnetic moments at the two sites

$$\begin{aligned} \Delta\mathcal{E}_2 &= 2\,\Delta\mathcal{E}_1 + \frac{\Delta^2}{4\pi}\int_{-\infty}^{E_F} dE\,\mathrm{Im}\,\ln\left(1 - \frac{g_{0,m}(E)\,g_{m,0}(E)}{(1-g_{00}\frac{\Delta}{2})^2}\right) \\ &= 2\,\Delta\mathcal{E}_1 + \mathcal{J}_{0,m}\ . \end{aligned} \tag{5.21}$$

The energy cost $\Delta\mathcal{E}_2$ is not simply twice as large as $\Delta\mathcal{E}_1$ due to the interference between the two impurities. This is evident in the second term of Eq.(5.21), which contains Green function propagators between sites 0 and m. Most remarkably, the interference term, $\mathcal{J}_{0,m}$, which arises naturally when we calculate the energy cost for the formation of two separate magnetic moments

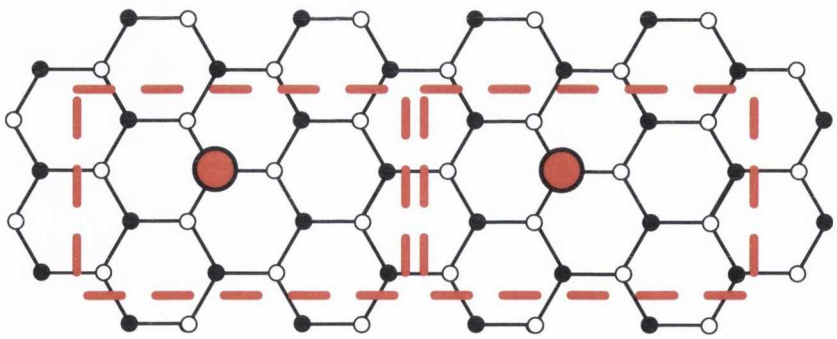

Figure 5.6: Two substitutional transition-metal atoms embedded in a graphene host in neighbouring unit cells.

can be identified with the Indirect Exchange Coupling between magnetic impurities, which is given in Eq. 5.5. Bearing in mind that this coupling is negative (positive) when the magnetic moments are parallel (antiparallel) and that it can decay slowly with impurity separation in low dimensional systems, this additional interference term may have striking consequences to the criterion presented above.

Consider for instance a hypothetical impurity that meets the inequality of Eq.(5.20), that is, an impurity that possesses a magnetic moment when immersed in the graphene lattice. Suppose that we add a second impurity of the same type to the system with the imposed constraint that both moments must be parallel to each other. The energy cost that was negative for a single impurity may become positive if the IEC favours an antiparallel alignment between the magnetic moments, as demonstrated in Section 5.4. In this case, $\Delta\mathcal{E}_2$ may become positive even though $\Delta\mathcal{E}_1 < 0$. If this occurs, the two magnetic impurities whose moments are forced to remain parallel may adopt an altogether non-magnetic configuration rather than the most favourable antiparallel alignment. This is a clear indication that the artificial imposition of parallel alignment may introduce spurious effects as far as the determination of the true ground state configuration is concerned.

DFT-based calculations that consider a single magnetic impurity per periodically repeated unit cell implicitly impose that their magnetic moments, should they exist, must be mutually parallel. Because of the periodic boundary conditions, the energy cost (per impurity) $\Delta\mathcal{E}_N/N$ for inducing the spin splitting of N equally spaced impurities becomes

$$\frac{\Delta\mathcal{E}_N}{N} = \Delta\mathcal{E}_1 + \frac{1}{N}\sum_{j}^{N} \mathcal{J}_{0,jm} \,. \tag{5.22}$$

In this case the correction to the single-impurity contribution $\Delta\mathcal{E}_1$, which once again is assumed to be negative, is a sum of terms proportional to the pairwise magnetic interactions that may be positive and sufficiently large to reverse the sign of $\Delta\mathcal{E}_N/N$. One could argue that the magnetic interaction, being traditionally oscillatory as a function of separation, will alternate

between negative and positive terms in the sum that appears in Eq.(5.22), which will then average out and never be able to reverse the sign imposed by $\Delta\mathcal{E}_1$. While this may be true in general, we have seen throughout this chapter that for graphene-based materials the underlying hexagonal atomic structure introduces a peculiar feature in the RKKY-like coupling that will seldom vanish the sum in the second term of Eq.(5.22). The magnetic coupling between impurities embedded in graphene-related materials tends not to exhibit sign-changing oscillations as the separation between the impurities is increased. Therefore, if the magnetic coupling between two sites favours the anti-parallel alignment between moments, the summation in Eq.(5.22) may be positive, and may converge to a sufficiently large value capable of overturning the satisfied criterion for single impurities. In the case of one-dimensional graphene systems, the consequences of neglecting the coupling between moments in neighbouring cells can be even more severe. Since the coupling magnitude tends to decay rather slowly as $1/D$ [116], the second term in Eq.(5.22) may diverge if the coupling is antiferromagnetic, leading to a guaranteed suppression of the magnetic moment.

5.5.3 DFT results for Fe and Mn

A striking implication of this mathematical analysis is that spurious nonmagnetic solutions may be obtained if existing magnetic moments are artificially constrained to adopt a parallel alignment when they would spontaneously prefer to be antiparallel. This raises the question whether the reported absence of magnetic moments for Fe in graphene could be one such case [185]. If so, this would be a convincing indication of the inadequacy of the assumption of independent unit cells that is commonly used in DFT-calculations dealing with magnetic dopants in graphene. A simple way of testing if the moment suppression is the result of the artificial constraint imposed by the periodic boundary conditions of the DFT scheme is to include more than one magnetic impurity per unit cell and allow them to adopt both parallel

and anti-parallel alignments. In what follows we present DFT results[4] for calculations comprising two impurities per unit cell and compare those with the results for a single impurity. The calculations were made using periodic boundary conditions and supercells comprising 4x4 and 7x7 graphene primitive cells. In these cases, one carbon atom of the graphene lattice was substituted by a single Fe atom impurity. The distance between an impurity and its image in the adjacent unit cell is 9.98 and 17.47 Å for the 4x4 and 7x7 supercells, respectively. Unsurprisingly, the results are very similar to those previously reported [185]. We find that, when relaxed, the metal impurities are displaced outwards from the graphene surface by 1.14 Å and that no magnetic moment is observed.

The results are completely different, however, when two impurities per unit cell are considered. To maintain the same impurity separation as before, the unit cells are duplicated along one direction (4x8 and 7x14 primitive cells). With two Fe impurities per unit cell, we have the freedom to start these calculations with magnetic moments in the anti-parallel configuration. Such an antiferromagnetic alignment between the Fe moments is stable and energetically favourable, by 0.03 eV, when compared to the non-magnetic solution, which can be obtained by relaxing the spin-polarisation. Remarkably, the substitutional Fe impurity has a magnetic moment that is as large as 0.99 μ_B. The energetics of the system in the configuration in which the Fe moments are parallel is also calculated. In this case the total energy is considerably higher than the antiferromagnetic configuration.

Table I shows the total energy values obtained for Fe as well as Mn impurities in the ferromagnetic (FM), spin-unpolarised (SU) and antiferromagnetic (AF) configurations. For Fe, the total energies in descending order are (FM, SU, AF). Because the AF configuration is impossible to obtain with the single-impurity unit cell, the system adopts the next possible configuration, which shows no spin polarisation. Alternatively, one can understand this in terms of Eq.(5.22), which means that the magnetic-coupling correction that

[4]Our DFT-calculations have been been made with the generalised gradient approximation [176] for the exchange-correlation term. Troullier-Martins pseudo-potentials [177] and double-zeta polarisation atomic orbitals [175] have been used.

arises due to the periodic boundary conditions is able to revert the sign imposed by $\Delta\mathcal{E}_1$ leading to a suppression of the existing Fe magnetic moments. The suppression of the magnetic moment is a spurious feature that results from the artificial imposition of a ferromagnetic alignment when the system naturally prefers to adopt a different alignment.

	Fe	Mn
FM	0.14	0.04
SU	0.03	1.80

Table 5.1: Total energies, in eV, of the FM and SU configurations, for Fe and Mn impurities in graphene. All quantities are expressed relatively to the total energy of the AF configuration, which is the most energetically favourable for both impurities.

Also shown in Table I are the values for Mn impurities, for which the total energies in descending order are (SU, FM, AF). Another interesting result, not considered in Ref. [185], is that the AF is the most energetically favourable configuration. Once again, this is easily understood by the single-impurity unit cell constraint that is unable to account for the AF alignment of the magnetic moments. In this case, the next possible configuration is the FM alignment, which again explains the results of Ref. [185]. In terms of Eq.(5.22), the magnetic-coupling correction for Mn impurities is not sufficient to overturn the sign determined by $\Delta\mathcal{E}_1$, which means that $\Delta\mathcal{E}_N/N$ is still negative, justifying the splitting of the spin-polarised bands into a FM configuration.

The results discussed above illustrate the potential problems that may arise when dealing with magnetic impurities in graphene-based structures through the standard DFT scheme of single-impurity unit cells. Furthermore, it is a clear indication of the relevance of the coupling between magnetic impurities in graphene-related materials. When this coupling is positive and sufficiently large to reverse the sign imposed by $\Delta\mathcal{E}_1$, the artificial constraints imposed by the periodic boundary conditions spuriously suppresses the magnetic moment that would spontaneously exist in isolation. In DFT calculations of doped graphene-related materials, it is therefore of paramount

importance to consider more than a single impurity per unit cell and study the energetics of all possible configurations, namely, FM, SU and AF.

5.5.4 Strategy to avoid moment suppression

Finally, regarding the condition for the formation of a localised magnetic moment expressed by the inequality of Eq.(5.20), we can test its predictive power by applying it to the cases considered above. Written in terms of single-particle Green functions, the susceptibility $\ell(E_F)$ can be further simplified in the case of small spin-splittings ($\Delta \ll 1$) to $\ell(E_F) \approx \rho_0(E_F)$, where $\rho_0(E_F)$ is the spin-unpolarised local density of states (LDOS) at the impurity site evaluated at the Fermi level E_F. The value of $U \approx 1$eV, being primarily an atomic property, is fairly constant for all transition metal elements [200]. Therefore, we can use the LDOS obtained from the SU calculations and test whether the inequality of Eq.(5.20) is satisfied. Reassuringly, $U\rho_0(E_F) > 1$ for both Fe and Mn, indicating that both elements favour the formation of a magnetic moment when embedded within graphene. Further tests were carried out with Ni impurities. In this case, the low value found for $\rho_0(E_F)$ does not meet our criterion, suggesting that Ni atoms within graphene will not develop a magnetic moment. In fact, this is what is found for DFT calculations with two Ni impurities per unit cell, which also agrees with previously reported results [181,185]. Such a good agreement with the predictions based on Eq.(5.20) indicates that SU calculations, which are considerably less time consuming than spin-polarised ones, can be carried out first to test whether a localised magnetic moment is likely to arise. If so, further spin-polarised calculations are required in which all possible configurations must be considered.

5.6 Summary of Chapter

In this chapter we introduced the concept of an indirect magnetic coupling between magnetic impurities embedded in a host system. Such a coupling has previously been investigated in a range of systems and has been tech-

nologically exploited in magnetic memory devices. A general approach, the so-called Quantum Well method, to calculating such a quantity was formulated in Section 5.2.1 using a combination of the methods previously outlined in Chapter 2. This approach was compared to the more commonly known RKKY method, which was shown to be a second-order perturbative approximation to the coupling.

In Section 5.3 the discussion shifted to the specific case of the magnetic interaction between moments in a graphene system. We reported on the progress to date in this field and summarised the methods and results of numerous studies on the topic. The difficulties with performing a fully analytic treatment of the interaction were observed. Using the Stationary Phase Green functions introduced in Chapter 3 we were able to calculate the principal features of the interaction in graphene within the RKKY approximation for a wide range of energies. This method avoids the potential pitfalls of a 'cutoff function' that is required by previous studies attempting an analytic solution of the interaction using the linear-dispersion approximation for the electronic band-structure of graphene. The distance-dependent properties of the interaction, namely the decay rate and oscillation period, were found to emerge in a mathematically transparent fashion from our results and agree with both our own numerical calculations and the expected results from the literature.

Following this, we used numerical methods in Section 5.4 to probe the magnetic interaction beyond the standard RKKY model. By varying the parameterisation of the magnetic impurities considered, we demonstrated a range of features that may occur by selecting a different magnetic species as our impurity. We found that a preferential anti-ferromagnetic alignment may persist to large separations between magnetic moments located on the same sublattice. Such a finding is in direct contradiction to the predictions of the RKKY theory reported throughout the literature, which state that the coupling between such impurities is always ferromagnetic. Thus a richer range of magnetic coupling features is present in graphene than had been previously anticipated.

Finally, we showed in Section 5.5 that the magnetic coupling discussed

to date may play a significant role in explaining some unusual *ab initio* results occurring in the literature. These include the unexpected absence of a magnetic moment on an Fe atom embedded in a graphene sheet [185]. We demonstrated that the use of single-impurity-doped unit cells in DFT calculations is highly inappropriate to describe magnetically doped graphene and that it may lead to fundamentally erroneous results as a consequence of the magnetic interaction between impurities in neighbouring unit cells. Such an interaction makes the hypothesis of independent unit cells in such systems invalid. A mathematically transparent criterion for the formation of magnetic moments in graphene is developed and tested in a number of cases. The existence of a simple criterion that can tell whether or not a magnetic moment will arise when impurities are introduced to graphene-related materials is a valuable tool to predict which of these structures may be useful for spintronic applications.

The treatment of the RKKY interaction using Stationary Phase Green functions, presented in Section 5.3, was published as part of "Electronic structure of graphene beyond the linear dispersion regime" (Phys. Rev. B 83, 155432). The work in Section 5.5 was published as "Emergence of local magnetic moments in doped graphene-related materials" (Phys. Rev. B 80R, 241413). The Density Functional Theory calculations in this section were performed by Dr. Pedro Venezuela (Instituto de Física, Universidade Federal Fluminense, Brazil).

CHAPTER

SIX

Dynamic magnetic interaction in graphene

6.1 Introduction

In the previous chapter we examined many facets of the indirect exchange coupling in graphene systems. The underlying motivation for such studies is the potential for magnetically-doped graphene systems to play a significant role in future spintronic technologies. The incorporation of these systems into potential devices is dependent on a long ranged interaction between the magnetic dopants to facilitate magnetic ordering or the transfer of information between different parts of the device. A long-ranged interaction has been predicted in Carbon Nanotubes [116–119] and signatures of such an interaction have been detected experimentally [120]. However, progress to date in graphene sheets has been hampered by the faster decay rates which arise from the peculiar electronic structure of graphene and which were examined in the previous chapter. Such rapid decay rates present an obstacle to the experimental verification of the interaction and to its technological application.

In this chapter we investigate the possibility of augmenting the range of the interaction by setting the magnetic moments to precess. The notion of a "dynamic RKKY" has been proposed by Šimánek and Heinrich [134] who generalised the concept of electron-mediated interaction between magnetic

moments to the case when these moments are no longer in static equilibrium. Further semi-classical investigation reveals the emergence of a long-ranged dynamic interaction in the case of ferromagnetic films separated by non-magnetic metal spacers [135]. Such an interaction is driven by non-equilibrium spin currents emanating from the precessing moments. The magnitude of the interaction can be measured by a quantity called the dynamic spin susceptibility, which describes the response of the magnetism of the system to a dynamic magnetic perturbation. In the next section we shall demonstrate how a full quantum mechanical description of this quantity can be derived.

A long spin-relaxation length and relatively weak spin-orbit coupling [95–98] make graphene an ideal candidate for the study of long ranged spin dynamic effects. Investigation of the dynamic susceptibility in carbon nanotubes [136] has revealed an augmentation of the decay rate beyond that of the static coupling. Further studies of spin dynamics in graphene systems have suggested the use of these materials as spin waveguides [137], spin-pumping transistors [138] and spin current lenses [139]. However to date there has not been a comprehensive study of the dynamic coupling between magnetic objects embedded in graphene sheets or how this is mediated by spin currents - a topical subject due to recent experimental reports of unusual spin current behaviour in graphene [140]. In this chapter we investigate the dynamic coupling in depth using the dynamic susceptibility formalism developed in the next section. Using the stationary phase approximation for the graphene Green functions, we demonstrate analytically how a long-ranged interaction arises and how the decay rate for the static case is recovered as the precession frequency is set to zero. We find a transition from the very fast decay predicted for the static coupling to a much longer ranged decay. We determine how this behaviour is manifested in the spin current emanating from a single precessing moment in graphene. Furthermore, we suggest a possible experiment to probe the dynamic RKKY interaction in graphene systems using the sensitive technique of inelastic scanning tunnelling spectroscopy (ISTS) [144] and model the signatures of the interaction that may be detected.

6.2 Dynamic susceptibility

In this section we introduce the methods used to calculate the dynamic susceptibility and show how the calculations required can be performed in terms of the single-particle Green function operators describing the system and with which we are well acquainted from previous chapters.

6.2.1 Magnetic Hamiltonian and time-dependent response

To describe the electronic structure of the system we use a Hubbard-like Hamiltonian of the form

$$\mathcal{H} = \sum_{i,j,\sigma} \gamma_{ij}\, \hat{c}^{\dagger}_{i\sigma}\, \hat{c}_{j\sigma} + \sum_{a,\sigma} \left(\epsilon_a\, \hat{n}_{a\sigma} + \frac{U_a}{2}\, \hat{n}_{a\sigma}\, \hat{n}_{a\bar{\sigma}} \right) + g\mu_B H_0 \sum_a \hat{S}^z_a\,, \qquad (6.1)$$

where the first term contains the relevant hopping terms included to describe the electronic band structure of the host system and the magnetic object. For our purposes it is sufficient to use the nearest-neighbour tight-binding model for graphene outlined in Chapter 3 to describe the host system. The magnetic objects we consider will consist of simple substitutional or adsorbed magnetic impurity atoms, whose description we have encountered previously in section 2.4. The sum over a in the second term is over the number of magnetic objects in the system, where ϵ_a is the atomic energy level of the magnetic site and U_a represents the effective onsite interaction between two electrons on the magnetic site and which is neglected elsewhere as before. The final term represents a local Zeeman interaction which defines the $\hat{z}$-axis as the equilibrium direction of the magnetisation. The value of the Zeeman field is arbitrarily chosen so that a free electron precessing in it would have an energy of $0.01t$, where t once more is the magnitude of the carbon-carbon hopping.

We now consider the introduction of a small harmonic, oscillatory mag-

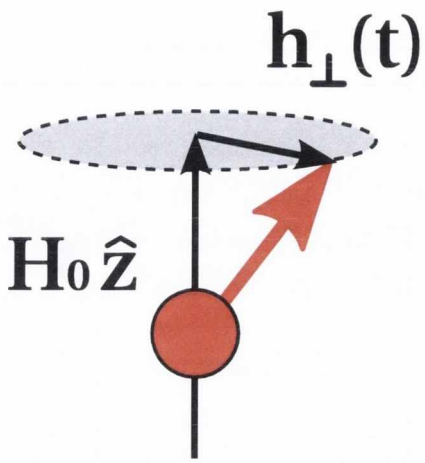

Figure 6.1: A small transverse field, $\mathbf{h}_\perp(t)$, is introduced which drives a precession of the magnetic moment around the equilibrium ($\hat{\mathbf{z}}$) direction defined by a static field $H_0\hat{\mathbf{z}}$.

netic field, $\mathbf{h}_\perp$, shown schematically in Fig. 6.1, of the form

$$\mathbf{h}_\perp = h_0 \, [\cos(\omega\, t)\, \hat{\mathbf{x}} \; - \; \sin(\omega\, t)\, \hat{\mathbf{y}}\,] \; , \tag{6.2}$$

that drives a precession with frequency ω at one of the magnetic sites, $a = 0$. The interaction between the magnetic field described by Eq. (6.2) and the spin at site 0, $\mathbf{S}_0$, is accounted for by a Hamiltonian term

$$\begin{aligned} g\,\mu_B\,\mathbf{h}_\perp \cdot \mathbf{S}_0 &= g\,\mu_B\,h_0 \, [\cos(\omega\, t)\; S_0^x \; - \; \sin(\omega\, t)\; S_0^y\,] \\ &= \frac{g\,\mu_B\,h_0}{2} \; \left[e^{i\,\omega\, t}\; S_0^+ \; + \; e^{-i\,\omega\, t}\; S_0^-\,\right] \; , \end{aligned} \tag{6.3}$$

where we have used the relation $S^\pm = S^x \pm i S^y$ and S_i^+ (S_i^-) is the spin raising (lowering) operator at site i.

Using linear response theory, the response of the spin component associated with site i of the system to the applied field can be calculated[1]. This is

[1]The limits of integration for the following derivations have been omitted for clarity. All integrals are on the interval $[-\infty, \infty]$ unless otherwise noted.

given by Refs [201, 202]

$$\delta\langle S_i^+(t)\rangle = \frac{g\,\mu_B\,h_0}{2}\int \mathrm{d}t' \left[e^{i\omega t'}\chi_{i0}^{++}(t-t') + e^{-i\omega t'}\chi_{i0}^{+-}(t-t')\right] \tag{6.4}$$

where the susceptibility terms χ_{i0}^{++} and χ_{i0}^{+-} are given by

$$\begin{aligned} \chi_{i0}^{++}(t) &= -\frac{i}{\hbar}\,\Theta(t)\langle[S_i^+(t), S_0^+(0)]\rangle \qquad \text{and} \\ \chi_{i0}^{+-}(t) &= -\frac{i}{\hbar}\,\Theta(t)\langle[S_i^+(t), S_0^-(0)]\rangle \end{aligned} \tag{6.5}$$

and the square brackets denote a commutator, the angle brackets represent the thermodynamical average reducing to the ground-state expectation value at zero temperature, and $\Theta(t)$ is the step function given by

$$\Theta(t) = \begin{cases} 0 & \text{if } t < 0 \\ 1 & \text{if } t > 0 \end{cases} . \tag{6.6}$$

Since the Hamiltonian is invariant to spin rotations around the $\hat{z}$-axis the spin component S_z is conserved. Thus terms of the form $\langle[S_i^+(t), S_0^+(0)]\rangle$ vanish and the susceptibility term χ_{i0}^{++} is zero. Now Eq. (6.4) becomes

$$\delta\langle S_i^+(t)\rangle = \frac{g\,\mu_B\,h_0}{2}\int \mathrm{d}t'\, e^{-i\omega t'}\chi_{i0}^{+-}(t-t')\,. \tag{6.7}$$

The term $\chi_{i0}^{+-}(t)$ is the time-dependent *transverse spin susceptibility* in real space. The Fourier transform of this quantity

$$\chi_{i0}^{+-}(\omega) = \int \mathrm{d}t'\, e^{i\omega t'}\,\chi_{i0}^{+-}(t') \tag{6.8}$$

is the frequency-dependent transverse spin susceptibility which tells us the response of the system to excitations of a given frequency. We can relate the

time-dependent spin disturbance at site i to this term as follows

$$\begin{aligned}\delta\langle S_i^+(t)\rangle &= \frac{g\,\mu_B\,h_0}{2}\,e^{-i\,\omega\,t}\int \mathrm{d}t'\;e^{i\,\omega\,(t-t')}\;\chi_{i0}^{+-}(t-t') \\ &= \frac{g\,\mu_B\,h_0}{2}\;\chi_{i0}^{+-}(\omega)\;e^{-i\,\omega\,t}\,.\end{aligned} \tag{6.9}$$

It is clear that the frequency-dependent susceptibility contains a lot of information about the response of the system to the applied magnetic field. From it we can extract information about the spin excitations in the system. These can be classified as single-particle spin-flip (Stoner) excitations or as collective modes (spin waves). In the next section we demonstrate how this quantity can be calculated within the random phase approximation.

6.2.2 Calculating $\chi_{ij}^{+-}(\omega)$

We begin by defining a generalised time-dependent susceptibility similar to $\chi_{ij}^{+-}(t)$ and given by

$$\chi_{ijkl}^{+-}(t) = -\frac{i}{\hbar}\,\Theta\,(t)\,\langle[S_{ij}^+(t), S_{kl}^-(0)]\rangle\,. \tag{6.10}$$

Clearly the element of interest to us is $\chi_{iijj}^{+-}(t) = \chi_{ij}^{+-}(t)$. Extending the standard definition of spin raising and lowering operators in terms of creation and annihilation operators we write

$$\begin{aligned}S_{ij}^+(t) &= \hat{c}_{i\uparrow}^\dagger(t)\,\hat{c}_{j\downarrow}(t) \qquad \text{and} \\ S_{kl}^-(0) &= \hat{c}_{k\downarrow}^\dagger(0)\,\hat{c}_{l\uparrow}(0)\,.\end{aligned} \tag{6.11}$$

$\chi_{ijkl}^{+-}(t)$ obeys the equation of motion given by

$$\begin{aligned}i\hbar\,\frac{\mathrm{d}\chi_{ijkl}^{+-}(t)}{\mathrm{d}t} &= \frac{\mathrm{d}}{\mathrm{d}t}\left\{\Theta\,(t)\,\langle[S_{ij}^+(t), S_{kl}^-(0)]\rangle\right\} \\ &= \frac{\mathrm{d}\Theta\,(t)}{\mathrm{d}t}\,\langle[S_{ij}^+(t), S_{kl}^-(0)]\rangle \;+\; \Theta\,(t)\,\langle[\,\frac{\mathrm{d}S_{ij}^+(t)}{\mathrm{d}t}\,,\,S_{kl}^-(0)\,]\rangle \\ &= \delta(t)\,\langle[S_{ij}^+(t), S_{kl}^-(0)]\rangle - \frac{i}{\hbar}\,\Theta\,(t)\,\langle[\,[S_{ij}^+(t), \hat{\mathcal{H}}]\,,\,S_{kl}^-(0)\,]\rangle\end{aligned} \tag{6.12}$$

where $\hat{\mathcal{H}}$ is the Hubbard-type Hamiltonian given by Eq. (6.1) and $\delta(t)$ is the Dirac delta function. We now examine the two terms on the right hand side of the final expression for the equation of motion individually. For the first of these, we can write

$$\begin{aligned} \delta(t)\,\langle[S_{ij}^{+}(t), S_{kl}^{-}(0)]\rangle &= \delta(t)\,\langle[S_{ij}^{+}(0), S_{kl}^{-}(0)]\rangle \\ &= \delta(t)\,\langle \hat{c}_{i\uparrow}^{\dagger}\,\hat{c}_{l\uparrow}\,\delta_{jk} \;+\; \hat{c}_{k\downarrow}^{\dagger}\,\hat{c}_{j\downarrow}\,\delta_{il}\rangle\,. \end{aligned} \tag{6.13}$$

Using the Hamiltonian from Eq. (6.1) allows us to write the commutator in the second term as

$$[S_{ij}^{+}, \hat{\mathcal{H}}] = \sum_{n}\Big(\gamma_{jn}\,\hat{c}_{i\uparrow}^{\dagger}\,\hat{c}_{n\downarrow} - \gamma_{ni}\,\hat{c}_{n\uparrow}^{\dagger}\,\hat{c}_{j\downarrow}\Big) + \Big(U_j\,\hat{c}_{j\uparrow}^{\dagger}\,\hat{c}_{j\uparrow}\,\hat{c}_{i\uparrow}^{\dagger}\,\hat{c}_{j\downarrow} - U_i\,\hat{c}_{i\uparrow}^{\dagger}\,\hat{c}_{j\downarrow}\,\hat{c}_{i\downarrow}^{\dagger}\,\hat{c}_{i\downarrow}\Big)\,. \tag{6.14}$$

The equation of motion for $\chi_{ijkl}^{+-}(t)$ now becomes

$$\begin{aligned} i\hbar\,\frac{\mathrm{d}\chi_{ijkl}^{+-}(t)}{\mathrm{d}t} &= \delta(t)\,\langle \hat{c}_{i\uparrow}^{\dagger}\,\hat{c}_{l\uparrow}\,\delta_{jk} \;-\; \hat{c}_{k\downarrow}^{\dagger}\,\hat{c}_{j\downarrow}\,\delta_{il}\rangle \\ &\quad - \frac{i}{\hbar}\,\Theta\,(t)\,\sum_{n}\langle[\gamma_{jn}\,\hat{c}_{i\uparrow}^{\dagger}(t)\,\hat{c}_{n\downarrow}(t) - \gamma_{ni}\,\hat{c}_{n\uparrow}^{\dagger}(t)\,\hat{c}_{j\downarrow}(t), S_{kl}^{-}(0)]\rangle \\ &\quad + \frac{i}{\hbar}\,\Theta\,(t)\,\Big\langle[\,\Big(U_j\,\hat{c}_{j\uparrow}^{\dagger}(t)\,\hat{c}_{j\uparrow}(t)\,\hat{c}_{i\uparrow}^{\dagger}(t)\,\hat{c}_{j\downarrow}(t) \\ &\qquad\qquad - U_i\,\hat{c}_{i\uparrow}^{\dagger}(t)\,\hat{c}_{j\downarrow}(t)\,\hat{c}_{i\downarrow}^{\dagger}(t)\,\hat{c}_{i\downarrow}(t)\Big)\;,\; S_{kl}^{-}(0)]\Big\rangle\,. \end{aligned} \tag{6.15}$$

From the definition of the time-dependent susceptibility $\chi_{ijkl}^{+-}(t)$ in Eq.(6.10), terms like $-\frac{i}{\hbar}\,\Theta\,(t)\,\langle[\gamma_{jn}\,\hat{c}_{i\uparrow}^{\dagger}(t)\,\hat{c}_{n\downarrow}(t), S_{kl}^{-}(0)]\rangle$ in Eq. (6.15) above can be written as time-dependent susceptibilities $\chi_{inkl}^{+-}(t)$. The appearance of higher-order terms in the expression above leads to an infinite chain of coupled equations for $\chi_{ijkl}^{+-}(t)$ that in general are not possible to solve.

To decouple these equations we make use of the *Random Phase Approximation* (RPA). This approximation limits the theory developed so far to low temperature as it neglects magnon-magnon interactions, as well as certain magnon-electron interactions and electron-electron interactions [203–207].

The decoupling scheme introduced by the RPA consists of replacing

$$\hat{c}_i^\dagger\,\hat{c}_j\,\hat{c}_k^\dagger\,\hat{c}_l \;\approx\; \langle\hat{c}_i^\dagger\,\hat{c}_j\,\rangle\hat{c}_k^\dagger\,\hat{c}_l - \langle\hat{c}_i^\dagger\,\hat{c}_l\,\rangle\hat{c}_k^\dagger\,\hat{c}_j + \langle\hat{c}_k^\dagger\,\hat{c}_l\,\rangle\hat{c}_i^\dagger\,\hat{c}_j - \langle\hat{c}_k^\dagger\,\hat{c}_j\,\rangle\hat{c}_i^\dagger\,\hat{c}_l\,, \tag{6.16}$$

where the expectation values are evaluated in the Hartree-Fock ground state, where the dynamics of the two spin projections are treated independently. Thus expectation values of the sort $\langle\hat{c}_{i\uparrow}^\dagger\,\hat{c}_{j\downarrow}\,\rangle = 0$. From Eq. (6.15), the terms we require are

$$\begin{aligned} &\hat{c}_{j\uparrow}^\dagger\,\hat{c}_{j\uparrow}\,\hat{c}_{i\uparrow}^\dagger\,\hat{c}_{j\downarrow} \approx \langle\hat{c}_{j\uparrow}^\dagger\,\hat{c}_{j\uparrow}\,\rangle\hat{c}_{i\uparrow}^\dagger\,\hat{c}_{j\downarrow} \;-\; \langle\hat{c}_{i\uparrow}^\dagger\,\hat{c}_{j\uparrow}\,\rangle\hat{c}_{j\uparrow}^\dagger\,\hat{c}_{j\downarrow} \\ \text{and}\qquad &\hat{c}_{i\uparrow}^\dagger\,\hat{c}_{j\downarrow}\,\hat{c}_{i\downarrow}^\dagger\,\hat{c}_{i\downarrow} \approx \langle\hat{c}_{i\downarrow}^\dagger\,\hat{c}_{i\downarrow}\,\rangle\hat{c}_{i\uparrow}^\dagger\,\hat{c}_{j\downarrow} \;-\; \langle\hat{c}_{i\downarrow}^\dagger\,\hat{c}_{j\downarrow}\,\rangle\hat{c}_{i\uparrow}^\dagger\,\hat{c}_{i\downarrow}\,. \end{aligned} \tag{6.17}$$

Within the RPA the equation of motion for $\chi_{ijkl}^{+-}(t)$ becomes

$$\begin{aligned} i\hbar\,\frac{\mathrm{d}\chi_{ijkl}^{+-}(t)}{\mathrm{d}t} &= \delta(t)\,\langle\hat{c}_{i\uparrow}^\dagger\,\hat{c}_{l\uparrow}\,\delta_{jk} \;-\; \hat{c}_{k\downarrow}^\dagger\,\hat{c}_{j\downarrow}\,\delta_{il}\rangle \\ &\quad + \sum_{m,n}\,(\delta_{im}\,\gamma_{jn} - \delta_{jn}\gamma_{mi})\;\chi_{mnkl}^{+-}(t) \\ &\quad + \sum_{m,n}\,\delta_{im}\delta_{jn}\;(U_j\langle\hat{n}_{j\uparrow}\rangle - U_i\langle\hat{n}_{i\downarrow}\rangle\,)\;\chi_{mnkl}^{+-}(t) \\ &\quad + \sum_{m,n}\,\delta_{mn}\,U_m\,\Big(\delta_{im}\langle\hat{c}_{i\downarrow}^\dagger\,\hat{c}_{j\downarrow}\rangle - \delta_{jm}\langle\hat{c}_{i\uparrow}^\dagger\,\hat{c}_{j\uparrow}\rangle\Big)\;\chi_{mnkl}^{+-}(t)\,. \end{aligned} \tag{6.18}$$

To simplify proceedings we introduce the four-index matrices given by

$$\begin{aligned} D_{ijkl} &= \langle\hat{c}_{i\uparrow}^\dagger\,\hat{c}_{l\uparrow}\,\delta_{jk} \;-\; \hat{c}_{k\downarrow}^\dagger\,\hat{c}_{j\downarrow}\,\delta_{il}\rangle \\ K_{ijkl} &= \delta_{ik}\,\gamma_{jl} - \delta_{jl}\gamma_{ki} \\ J'_{ijkl} &= \delta_{ik}\delta_{jl}\;(U_j\langle\hat{n}_{j\uparrow}\rangle - U_i\langle\hat{n}_{i\downarrow}\rangle\,) \\ J_{ijkl} &= \delta_{kl}\,U_k\,\Big(\delta_{ik}\langle\hat{c}_{i\downarrow}^\dagger\,\hat{c}_{j\downarrow}\rangle - \delta_{jk}\langle\hat{c}_{i\uparrow}^\dagger\,\hat{c}_{j\uparrow}\rangle\Big) \end{aligned} \tag{6.19}$$

where the product of two such matrices is given by $(\hat{A}\hat{B})_{ijkl} = \sum_{m,n} A_{ijmn}B_{mnkl}$, so that Eq. (6.18) can be written in matricial form as

$$i\hbar\,\frac{\mathrm{d}}{\mathrm{d}t}\,\hat{\chi}^{+-}(t) = \delta(t)\,\hat{D} + \Big(\hat{K} + \hat{J}' + \hat{J}\Big)\;\hat{\chi}^{+-}(t) \tag{6.20}$$

Using the Fourier transformations

$$\begin{aligned} \hat{\chi}^{+-}(t) &= \frac{1}{2\pi}\int \mathrm{d}\omega\, e^{-i\omega t}\,\hat{\chi}^{+-}(\omega) \\ \delta(t) &= \frac{1}{2\pi}\int \mathrm{d}\omega\, e^{-i\omega t} \end{aligned} \quad , \tag{6.21}$$

we get an equation for the frequency-dependent transverse susceptibility

$$\hbar\,\omega\,\hat{\chi}^{+-}(\omega) = \hat{D} + \left(\hat{K} + \hat{J}' + \hat{J}\right)\,\hat{\chi}^{+-}(\omega)\,. \tag{6.22}$$

RPA and Hartree-Fock susceptibilities

In order to calculate $\hat{\chi}^{+-}(\omega)$ from Eq. (6.22), we will first derive an expression connecting the RPA susceptibility to the non-interacting, or Hartree-Fock (HF) susceptibility, $\chi^0(\omega)$. This is calculated within one-electron theory and so is incapable of describing collective excitations such as spin waves. However it carries useful information about single-particle excitations, such as spin-flip (Stoner) excitations. Such information is useful as the lifetime of collective excitations in the absence of other forms of dissipation, like spin-orbit coupling, is determined by their decay into single-particle excitations. We have seen in Section 2.8 that, within the Hartree-Fock approximation, we make the substitution

$$\sum_{a,\sigma}\frac{U_a}{2}\hat{n}_{a\sigma}\hat{n}_{a\bar{\sigma}} \rightarrow \sum_{a,\sigma} U_a\,\langle\hat{n}_{a\bar{\sigma}}\rangle\hat{n}_{a_\sigma}$$

in the interacting term of the Hamiltonian in Eq. (6.1). Following a similar routine to that outlined to calculate the equation of motion and resultant equations for the full Hamiltonian from Eq (6.12) onwards, we arrive at analogous expressions to Eqs. (6.20) and (6.22) for the reduced Hartree-Fock Hamiltonian:

$$i\hbar\,\frac{\mathrm{d}}{\mathrm{d}t}\,\hat{\chi}^0(t) = \delta(t)\,\hat{D} + \left(\hat{K} + \hat{J}'\right)\,\hat{\chi}^0(t) \tag{6.23}$$

and

$$\hbar\omega\,\hat{\chi}^0(\omega) = \hat{D} + \left(\hat{K} + \hat{J}'\right)\,\hat{\chi}^{+-}(\omega)\,. \tag{6.24}$$

Rearranging Eq. (6.22), we find

$$\begin{aligned}\left(\hbar\omega\,\hat{I} - \hat{K} - \hat{J}'\right)\,\hat{\chi}^{+-}(\omega) &= \hat{D} + \hat{J}\,\hat{\chi}^{+-}(\omega) \\ \implies \hat{\chi}^{+-}(\omega) &= \left(\hbar\omega\,\hat{I} - \hat{K} - \hat{J}'\right)^{-1}\,\hat{J}\,\hat{\chi}^{+-}(\omega) + \left(\hbar\omega\,\hat{I} - \hat{K} - \hat{J}'\right)^{-1} \\ \implies \hat{\chi}^{+-}(\omega) &= \left(\hbar\omega\,\hat{I} - \hat{K} - \hat{J}'\right)^{-1}\,\hat{J}\,\hat{\chi}^{+-}(\omega) + \hat{\chi}^0(\omega)\,,\end{aligned}$$

where we have performed a similar rearrangement with Eq. (6.24) to yield

$$\hat{\chi}^0(\omega) = \left(\hbar\omega\,\hat{I} - \hat{K} - \hat{J}'\right)^{-1}\,\hat{D}\,.$$

Defining a matrix $\hat{P}$ such that $\hat{D}\,\hat{P} = \hat{J}$ allows us to write

$$\hat{\chi}^{+-}(\omega) = \hat{\chi}^0(\omega) + \hat{\chi}^0(\omega)\,\hat{P}\,\hat{\chi}^{+-}(\omega)\,. \tag{6.25}$$

From the definition of $\hat{P}$ above and those of $\hat{D}$ and $\hat{J}$ in Eq (6.19) we can write

$$\begin{aligned}P_{ijkl}\langle\hat{c}^\dagger_{i\uparrow}\hat{c}_{l\uparrow}\delta_{jk} - \hat{c}^\dagger_{k\downarrow}\hat{c}_{j\downarrow}\delta_{il}\rangle &= -U_k\,\delta_{kl}\,\langle\hat{c}^\dagger_{i\uparrow}\hat{c}_{j\uparrow}\delta_{jk} - \hat{c}^\dagger_{i\downarrow}\hat{c}_{j\downarrow}\delta_{ik}\rangle \\ \implies P_{ijkl} &= -U_k\,\delta_{kl}\,\delta_{jl}\,\delta_{ik}\,.\end{aligned} \tag{6.26}$$

Using this definition of $\hat{P}$ in Eq. (6.25) yields

$$\chi^{+-}_{ijkl}(\omega) = \chi^0_{ijkl}(\omega) - \sum_m \chi^0_{ijmm}(\omega)\,U_m\,\chi^{+-}_{mmkl}(\omega)\,. \tag{6.27}$$

For the matrix elements $\chi^{+-}_{ij}(\omega) = \chi^{+-}_{iijj}(\omega)$ that we are interested in we can write

$$\chi^{+-}_{ij}(\omega) = \chi^0_{ij}(\omega) - \sum_m \chi^0_{im}(\omega)\,U_m\,\chi^{+-}_{mj}(\omega) \tag{6.28}$$

or

$$\hat{\chi}^{+-}(\omega) = \hat{\chi}^0(\omega) - \hat{\chi}^0(\omega)\,\hat{U}\,\hat{\chi}^{+-}(\omega)\,, \tag{6.29}$$

where $U_{mn} = U_m\delta_{mn}$. This leaves us with a simple matrix equation relating

the random phase approximation and Hartree-Fock susceptibilities

$$\hat{\chi}^{+-}(\omega) = \left[\hat{I} + \hat{\chi}^{0}(\omega)\,\hat{U}\right]^{-1} \hat{\chi}^{0}(\omega)\,. \tag{6.30}$$

It is worth considering the various types of excitations that can be described by this expression. For simplicity we suppose that the external magnetic field couples to the magnetic moment of the atom at site 0. Using Eq. (6.30) to examine the excitations arising from spin precessions due to this disturbance we write

$$\chi_{00}^{+-}(\omega) = \frac{\chi_{00}^{0}(\omega)}{1 + U_0\,\chi_{00}^{0}(\omega)}\,. \tag{6.31}$$

The imaginary part of $\chi_{00}^{+-}(\omega)$, which is related to the spin excitations, is given by

$$\mathrm{Im}\left(\chi_{00}^{+-}(\omega)\right) = \frac{\mathrm{Im}(\chi_{00}^{0}(\omega))}{\left[1 + U_0\mathrm{Re}(\chi_{00}^{0}(\omega))\right]^2 + \left[U_0\mathrm{Im}(\chi_{00}^{0}(\omega))\right]^2}\,. \tag{6.32}$$

Two types of excitation are represented by Eq. (6.32), corresponding to ω ranges where $\mathrm{Im}\left(\chi_{00}^{+-}(\omega)\right) \neq 0$. The first type correspond to particle excitations where the numerator does not vanish, i.e., where $\mathrm{Im}(\chi_{00}^{0}(\omega)) \neq 0$. Under the Hartree-Fock approximation electrons with opposite spin orientations are independent. Therefore these excitations, called *Stoner modes*, do not involve correlations between particles of opposite spin. Instead they correspond to spin-flip excitations around the Fermi energy.

The other type of excitation correspond to ω values where $\mathrm{Im}\left(\chi_{00}^{0}(\omega)\right) = 0$ but where the term $1 + U_0\mathrm{Re}(\chi_{00}^{0}(\omega))$ also cancels. These are excitations which explicitly involve the effective Coulomb interaction between electrons which is responsible for the correlation between the dynamics of spin-up and spin-down electrons. These are collective excitations, or spin waves.

Calculating the HF Susceptibilities

Now that we have reduced the calculation of the RPA susceptibility to Eq. (6.30), the rest of the calculation boils down to deriving an expression for the

Hartree-Fock susceptibilities χ^0_{ij} in terms of the usual single particle Green function operators we are familiar with. The definition of the generalised time-dependent susceptibility, in Eq. (6.10), can be rewritten under the Hartree-Fock approximation as

$$\begin{aligned}\chi^0_{ijkl}(t) &= -\frac{i}{\hbar}\Theta(t)\left[\langle \hat{c}^\dagger_{i\uparrow}(t)\,\hat{c}_{l\uparrow}\rangle\,\langle \hat{c}_{j\downarrow}(t)\,\hat{c}^\dagger_{k\downarrow}\rangle - \langle \hat{c}^\dagger_{k\downarrow}\,\hat{c}_{j\downarrow}(t)\rangle\,\langle \hat{c}_{l\uparrow}\,\hat{c}^\dagger_{i\uparrow}(t)\rangle\right] \\ &= -\frac{i}{\hbar}\Theta(t)\left[\langle \hat{c}^\dagger_{i\uparrow}(t)\,\hat{c}_{l\uparrow}\rangle\,\langle \{\hat{c}_{j\downarrow}(t),\hat{c}^\dagger_{k\downarrow}\}\rangle - \langle \hat{c}^\dagger_{k\downarrow}\,\hat{c}_{j\downarrow}(t)\rangle\,\langle \{\hat{c}^\dagger_{i\uparrow}(t),\hat{c}_{l\uparrow}\}\rangle\right],\end{aligned} \tag{6.33}$$

where we have used the anticommutator $\{a,b\} = ab + ba$. Using the standard definition [145] of the time-dependent single-particle retarded Green function operator

$$G^\sigma_{mn}(t) = -\frac{i}{\hbar}\Theta(t)\,\langle\{\hat{c}_{m\sigma}(t),\hat{c}^\dagger_{n\sigma}\}\rangle\,, \tag{6.34}$$

we can write

$$\chi^0_{ijkl}(t) = \langle \hat{c}^\dagger_{i\uparrow}(t)\,\hat{c}_{l\uparrow}\rangle\,G^\downarrow_{jk}(t) + \langle \hat{c}^\dagger_{k\downarrow}\,\hat{c}_{j\downarrow}(t)\rangle\,G^{\uparrow *}_{il}(t)\,. \tag{6.35}$$

Defining

$$\begin{aligned} & & J^\sigma_{il}(t) &= \langle \hat{c}_{i\sigma}(t)\,\hat{c}^\dagger_{l\sigma}\rangle \\ &\text{and} & \bar{J}^\sigma_{li}(t) &= \langle \hat{c}^\dagger_{l\sigma}\,\hat{c}_{i\sigma}(t)\rangle \end{aligned} \tag{6.36}$$

the Green function in Eq. (6.34) can be written

$$G^\sigma_{il}(t) = -\frac{i}{\hbar}\Theta(t)\,\left\{J^\sigma_{il}(t) + \bar{J}^\sigma_{li}(t)\right\}\,. \tag{6.37}$$

Using the identity

$$\Theta(t) = \lim_{\eta\to 0^+}\left(\frac{-1}{2\pi i}\right)\int \mathrm{d}\omega \frac{e^{-i\omega t}}{\omega + i\eta} \tag{6.38}$$

allows us to calculate the Fourier transforms of the quantities defined in Eq. (6.36), yielding

$$\begin{aligned} J_{il}^{\sigma}(t) &= \frac{1}{2\pi}\int \mathrm{d}\omega\, e^{-i\omega t}\, \tilde{J}_{il}^{\sigma}(\omega) \\ \text{and} \qquad \bar{J}_{li}^{\sigma}(t) &= \frac{1}{2\pi}\int \mathrm{d}\omega\, e^{-i\omega t}\, \tilde{\bar{J}}_{li}^{\sigma}(\omega)\,. \end{aligned} \tag{6.39}$$

The fluctuation-dissipation theorem, relating the absorption or dissipation of energy of a system perturbed by an external field with fluctuations (and correlations) in the unperturbed system [208], allows us to write $\tilde{\bar{J}}_{li}^{\sigma}(\omega) = e^{-\beta\hbar\omega}\, \tilde{J}_{il}^{\sigma}$ and to rewrite the retarded Green function as

$$\begin{aligned} G_{il}^{\sigma}(t) &= \frac{1}{2\pi}\int \mathrm{d}\omega\, e^{-i\omega t}\, \frac{1}{2\pi\hbar}\lim_{\eta\to 0^{+}}\int \mathrm{d}\omega_2\; \tilde{\bar{J}}_{li}^{\sigma}(\omega_2)\, \frac{e^{\beta\hbar\omega_2}+1}{\omega-\omega_2+i\eta} \\ &= \frac{1}{2\pi}\int \mathrm{d}\omega\, e^{-i\omega t}\, G_{il}^{\sigma}(\omega) \end{aligned} \tag{6.40}$$

where

$$G_{il}^{\sigma}(\omega) = \frac{1}{2\pi\hbar}\lim_{\eta\to 0^{+}}\int \mathrm{d}\omega_2\; \tilde{\bar{J}}_{li}^{\sigma}(\omega_2)\, \frac{e^{\beta\hbar\omega_2}+1}{\omega-\omega_2+i\eta}\,. \tag{6.41}$$

A similar analysis can be performed for the *advanced* Green function, $G_{il}^{-\,\sigma}$ to find expressions for the time- and frequency-dependent advanced Green functions analogous to Eqs (6.37) and (6.41):

$$G_{il}^{-\,\sigma}(t) = -\frac{i}{\hbar}\,\Theta(-t)\,\left\{J_{il}^{\sigma}(t) + \bar{J}_{li}^{\sigma}(t)\right\} \tag{6.42}$$

and

$$G_{il}^{-\,\sigma}(\omega) = \frac{1}{2\pi\hbar}\lim_{\eta\to 0^{+}}\int \mathrm{d}\omega_2\; \tilde{\bar{J}}_{li}^{\sigma}(\omega_2)\, \frac{e^{\beta\hbar\omega_2}+1}{\omega-\omega_2-i\eta}\,. \tag{6.43}$$

From Eqs (6.41) and (6.43) we find the difference between the retarded Green functions to be

$$G^{\sigma}_{il}(\omega) - G^{-\,\sigma}_{il}(\omega) = \frac{1}{2\pi\hbar}\int \mathrm{d}\omega_2\, \tilde{\tilde{J}}^{\sigma}_{li}(\omega_2)\left[e^{\beta\hbar\omega_2}+1\right] \quad \times \quad \times \quad \lim_{\eta\to 0^+}\left[\frac{1}{\omega-\omega_2+i\eta} - \frac{1}{\omega-\omega_2-i\eta}\right]. \tag{6.44}$$

Using the relation [145]

$$\lim_{\eta\to 0^+}\frac{1}{x\pm i\eta} = P(\frac{1}{x}) \mp i\pi\delta(x)$$

this becomes

$$\begin{aligned} G^{\sigma}_{il}(\omega) - G^{-\,\sigma}_{il}(\omega) &= \frac{1}{2\pi\hbar}\int \mathrm{d}\omega_2\, \tilde{\tilde{J}}^{\sigma}_{li}(\omega_2)\left[e^{\beta\hbar\omega_2}+1\right]\left[-2\pi i\delta(\omega-\omega_2)\right] \\ &= -\frac{i}{\hbar}\,\tilde{\tilde{J}}^{\sigma}_{li}(\omega)\,\left[e^{\beta\hbar\omega}+1\right], \end{aligned} \tag{6.45}$$

which, rearranged, gives

$$\begin{aligned} \tilde{\tilde{J}}^{\sigma}_{li}(\omega) &= i\hbar\frac{1}{e^{\beta\hbar\omega}+1}\,\left[G^{\sigma}_{il}(\omega) - G^{-\,\sigma}_{il}(\omega)\right] \\ &= i\hbar\, f(\omega)\,\left[G^{\sigma}_{il}(\omega) - G^{-\,\sigma}_{il}(\omega)\right], \end{aligned} \tag{6.46}$$

where $f(\omega)$ is the Fermi function. From Eqs (6.36) - (6.46) we find

$$\langle \hat{c}^{\dagger}_{i\sigma}\,\hat{c}_{l\sigma}(t)\rangle = \frac{i\hbar}{2\pi}\int e^{-i\omega t}\, f(\omega)\,\left[G^{\sigma}_{li}(\omega) - G^{-\,\sigma}_{li}(\omega)\right]. \tag{6.47}$$

Using the cyclical property

$$\langle \hat{c}^{\dagger}_{i\sigma}\,\hat{c}_{l\sigma}(t)\rangle = \langle \hat{c}^{\dagger}_{i\sigma}\, e^{i\hat{\mathcal{H}}t}\hat{c}_{l\sigma}e^{-i\hat{\mathcal{H}}t}\rangle = \langle e^{-i\hat{\mathcal{H}}t}\hat{c}^{\dagger}_{i\sigma}\, e^{i\hat{\mathcal{H}}t}\hat{c}_{l\sigma}\rangle = \langle \hat{c}^{\dagger}_{i\sigma}(-t)\,\hat{c}_{l\sigma}\rangle \tag{6.48}$$

and setting $t \to -t$ in Eq. (6.47) gives

$$\langle \hat{c}^{\dagger}_{i\sigma}(t)\,\hat{c}_{l\sigma}\rangle = \frac{i\hbar}{2\pi}\int e^{i\omega t}\, f(\omega)\,\left[G^{\sigma}_{li}(\omega) - G^{-\,\sigma}_{li}(\omega)\right]. \tag{6.49}$$

Substituting the identities in Eqs. (6.47) and (6.49) into the expression for the generalised Hartree-Fock susceptibility given by Eq. (6.35) and the Green function identity $G^{*\sigma}_{il}(t) = G^{-\,\sigma}_{li}(t)$, yields

$$\begin{aligned}\chi^0_{ijkl}(t) = \frac{i\hbar}{2\pi} \int e^{i\omega t} f(\omega) \left[G^{\uparrow}_{li}(\omega) - G^{-\,\uparrow}_{li}(\omega)\right] G^{\downarrow}_{jk}(t) \\ + \frac{i\hbar}{2\pi} \int e^{-i\omega t} f(\omega) \left[G^{\downarrow}_{jk}(\omega) - G^{-\,\downarrow}_{jk}(\omega)\right] G^{-\,\uparrow}_{jk}(-t)\,.\end{aligned} \tag{6.50}$$

Taking the Fourier transform

$$\begin{aligned}\chi^0_{ijkl}(\omega) &= \int \mathrm{d}t\, e^{i\omega t}\, \chi^0_{ijkl}(t) \\ &= \frac{i\hbar}{2\pi} \left\{ \int \mathrm{d}\omega'\, f(\omega') \left[G^{\uparrow}_{li}(\omega') - G^{-\,\uparrow}_{li}(\omega')\right] \int \mathrm{d}t\, e^{i(\omega+\omega')t}\, G^{\downarrow}_{jk}(t) \right. \\ &+ \left. \int \mathrm{d}\omega'\, f(\omega') \left[G^{\downarrow}_{jk}(\omega') - G^{-\,\downarrow}_{jk}(\omega')\right] \int \mathrm{d}t\, e^{i(\omega-\omega')t}\, G^{-\,\downarrow}_{li}(-t) \right\}\end{aligned} \tag{6.51}$$

and using the following identities

$$G^{\downarrow}_{jk}(\omega+\omega') = \int \mathrm{d}t\, e^{i(\omega+\omega')t}\, G^{\downarrow}_{jk}(t) \tag{6.52}$$

$$G^{-\,\downarrow}_{li}(\omega'-\omega) = \int \mathrm{d}t\, e^{i(\omega'-\omega)t}\, G^{-\,\uparrow}_{li}(t) \overset{t\to -t}{=} \int \mathrm{d}t\, e^{i(\omega-\omega')t}\, G^{-\,\uparrow}_{li}(-t) \tag{6.53}$$

we arrive at a final expression for the generalised Hartree-Fock susceptibility in terms of the single-particle Green functions

$$\begin{aligned}\chi^0_{ijkl}(\omega) = \frac{i\hbar}{2\pi} \int_{-\infty}^{\infty} \mathrm{d}\omega'\, f(\omega') \left\{ \left[G^{\uparrow}_{li}(\omega') - G^{-\,\uparrow}_{li}(\omega')\right] G^{\downarrow}_{jk}(\omega+\omega') \right. \\ \left. + \left[G^{\downarrow}_{jk}(\omega') - G^{-\,\downarrow}_{jk}(\omega')\right] G^{-\,\uparrow}_{li}(\omega'-\omega) \right\}\,,\end{aligned} \tag{6.54}$$

or for the two-index susceptibility

$$\begin{aligned}\chi^0_{ij}(\omega) = \frac{i\hbar}{2\pi} \int_{-\infty}^{\infty} \mathrm{d}\omega'\, f(\omega') \left\{ \left[G^{\uparrow}_{ji}(\omega') - G^{-\,\uparrow}_{ji}(\omega')\right] G^{\downarrow}_{ij}(\omega+\omega') \right. \\ \left. + \left[G^{\downarrow}_{ij}(\omega') - G^{-\,\downarrow}_{ij}(\omega')\right] G^{-\,\uparrow}_{ji}(\omega'-\omega) \right\}\,.\end{aligned} \tag{6.55}$$

Eqs (6.30) and (6.55) are the two key results from the rather lengthy derivation presented to date in this chapter. The first of these connects the interacting and non-interacting susceptibilities allowing us to calculate the properties of collective excitations arising from the precession of the magnetic moment. The second result presents a method to calculate the non-interacting susceptibility in terms of the spin-dependent single-particle Green function, a quantity whose calculation has been described at length in Chapters 2 and 3. Within the Green function formalism we can easily account for the magnetic impurities using the methods discussed in previous chapters.

Splitting the integral

The calculation of the Hartree-Fock susceptibility as presented in Eqs. (6.54) and (6.55) involves an integral over energy of a convolution of retarded and advanced Green function matrix elements. In Section 2.7, we examined how integrals involving Green functions are in general easier to perform over the imaginary axis. A similar method, outlined by Muniz and Mills [206], will be used for the integration of the Hartree-Fock susceptibility equation. This approach is slightly more complicated due to the presence of both retarded and advanced Green functions, whose poles occur on opposite sides of the real axis. To simplify the numerical integration of this equation, we split the integral into three components. The first of these is a product of the retarded Green functions, the second a product of the advanced Green functions. The remaining cross terms are then contained in the final term. Splitting the integral in such a fashion will also prove useful later in this chapter when we turn to examining the separation dependence of the dynamic magnetic interaction in graphene. To begin, we expand out the bracketed terms in Eq. (6.54) and segregate the resultant terms by the types of Green functions they

contain.

$$\chi^0_{ijkl}(\omega) = \frac{i\hbar}{2\pi}\int_{-\infty}^{\infty} \mathrm{d}\omega'\, f(\omega')\left\{G^{\uparrow}_{li}(\omega')G^{\downarrow}_{jk}(\omega+\omega') - G^{-\downarrow}_{jk}(\omega')\, G^{-\uparrow}_{li}(\omega'-\omega) + \left[G^{\downarrow}_{jk}(\omega')G^{-\uparrow}_{li}(\omega'-\omega) - G^{-\uparrow}_{li}(\omega')G^{\downarrow}_{jk}(\omega+\omega')\right]\right\}$$
$$\equiv I_1 + I_2 + I_3\,, \tag{6.56}$$

where

$$I_1 = \frac{i\hbar}{2\pi}\int_{-\infty}^{\infty} \mathrm{d}\omega'\, f(\omega')G^{\uparrow}_{li}(\omega')G^{\downarrow}_{jk}(\omega+\omega') \tag{6.57}$$

$$I_2 = -\frac{i\hbar}{2\pi}\int_{-\infty}^{\infty} \mathrm{d}\omega'\, f(\omega')G^{-\downarrow}_{jk}(\omega')\, G^{-\uparrow}_{li}(\omega'-\omega) \tag{6.58}$$

and

$$I_3 = \frac{i\hbar}{2\pi}\int_{-\infty}^{\infty} \mathrm{d}\omega'\, f(\omega')\left[G^{\downarrow}_{jk}(\omega')G^{-\uparrow}_{li}(\omega'-\omega) - G^{-\uparrow}_{li}(\omega')G^{\downarrow}_{jk}(\omega+\omega')\right]. \tag{6.59}$$

The integrand in I_1 consists of a product of two retarded Green functions. At $T = 0$ it can be rewritten over the imaginary axis using a straightforward application of the method described in Section 2.7 and availing of the contour illustrated previously in Fig 2.6. The method is identical to that followed for the integral for the static IEC in Eq. (5.6) and we find

$$I_1 = \frac{\hbar}{2\pi}\int_{\eta}^{\infty} \mathrm{d}y\, G^{\uparrow}_{li}(\omega_F + iy)G^{\downarrow}_{jk}(\omega_F+\omega+iy)\,. \tag{6.60}$$

An analogous approach can be followed for I_2, but since it contains a product of advanced Green functions the contour should be closed in the lower half plane. This gives

$$I_2 = \frac{\hbar}{2\pi}\int_{\eta}^{\infty} \mathrm{d}y\, G^{-\downarrow}_{jk}(\omega_F - iy)\, G^{-\uparrow}_{li}(\omega_F-\omega-iy)\,, \tag{6.61}$$

and using the identity $G_{il}^{-\sigma}(z) = G_{li}^{*\sigma}(z^*)$ becomes

$$I_2 = \frac{\hbar}{2\pi} \int_{\eta}^{\infty} \mathrm{d}y \left[G_{kj}^{\downarrow}(\omega_F + iy)\, G_{il}^{\uparrow}(\omega_F - \omega + iy) \right]^* . \tag{6.62}$$

The third term cannot be solved using the same procedure as it contains products of retarded and advanced Green functions, which are analytic functions of ω' in opposite halves of the complex plane. However, we can simplify the expression for I_3 given in Eq. (6.59) by making the transformation of variables $\omega' \rightarrow \omega' + \omega$ in the first term, so that

$$I_3 = \frac{i\hbar}{2\pi} \int_{-\infty}^{\infty} \mathrm{d}\omega' \, [f(\omega' + \omega) - f(\omega')] \, G_{li}^{-\uparrow}(\omega') G_{jk}^{\downarrow}(\omega + \omega') . \tag{6.63}$$

At $T = 0$ the Fermi functions have the effect of limiting the range of the integral such that

$$I_3 = -\frac{i\hbar}{2\pi} \int_{\omega_F - \omega}^{\omega_F} \mathrm{d}\omega' \, G_{li}^{-\uparrow}(\omega') G_{jk}^{\downarrow}(\omega + \omega') . \tag{6.64}$$

It is important to note that in terms of separation dependence, the functional forms of I_1 and I_2 are almost identical to that for the static coupling. However, the third term has a different form and it makes no contribution to any of the static properties of the system. This can be seen quite clearly as, when $\omega = 0$, the range of the integral vanishes and so $I_3(\omega = 0) = 0$.

6.2.3 Spin disturbance, dynamic coupling and spin current

We now demonstrate how the spin susceptibilities we have derived can be used to calculate other useful quantities in the system . The spin disturbance at a site is the amplitude of the spin precession at that site induced by the precessing moment. It is clear from Eq. (6.9) that the absolute value of the response function $|\chi_{i0}^{+-}|$, is proportional to the magnitude of the spin disturbance at site i due to the application of the oscillating field applied at site 0. The spin disturbance at i due to multiple precessing moments, either

from a larger magnetic object consisting of multiple magnetic atoms or from a distribution of magnetic atoms, is given by

$$|\delta\langle S_i^+(t)\rangle| = \frac{g\,\mu_B\,h_0}{2}\left|\sum_a \chi_{ia}^{+-}(\omega)\right| , \tag{6.65}$$

where the sum is over the sites where the oscillating field is applied. The quantity $|\chi_{ba}^{+-}(\omega)|$, where there are magnetic atoms at both sites a and b, can be viewed as a dynamic analogue of the RKKY coupling in that it represents an interaction between two magnetic objects mediated by the conduction electrons of the host medium. Whereas the static interaction corresponds to the energy difference between parallel and antiparallel alignment of the moments, the dynamic interaction represents the magnitude of the precession induced on one moment by that of another. Since we are looking at the absolute value in the dynamic case, we are not extracting any information from the sign of the quantity calculated.

A precessing moment on a magnetic object generates a spin current which carries transverse angular momentum away from the site of precession (*spin pumping*). In systems with a long spin diffusion length and a small spin-orbit coupling effect, this spin current can travel significant distances in the host medium and excite a second magnetic moment elsewhere (*spin torque*). Such a mechanism has tremendous potential for application in spintronics devices. The spin current emanating from a precessing moment can be calculated in terms of the transverse spin-susceptibility in a manner outlined in Ref [209]. The total spin current, $\hat{I}_S^+$, flowing out of a volume V containing many spins is found to be

$$\hat{I}_S^+ = \sum_{i\in V} \hat{I}_i^+ = i \sum_{i\in V}\sum_j \left[\gamma_{ji}\,\hat{S}_{ji}^+ - \gamma_{ij}\,\hat{S}_{ij}^+\right] \tag{6.66}$$

where γ_{ij} represents the tight-binding hopping parameters from the Hamiltonian in Eq. (6.1) and $\hat{S}_{ij}^+$ is the generalised spin raising operator defined in Eq. (6.11). It is apparent that that contributions to $\hat{I}_S^+$ from $j \in V$ vanish and so the sum over j can be restricted to $j \notin V$. The amplitude of the spin

current pumped out of V by the precessing moment is

$$|\langle \hat{I}_S^+ \rangle| = \sqrt{|\langle \hat{I}_S^x \rangle|^2 + |\langle \hat{I}_S^y \rangle|^2} \,. \tag{6.67}$$

Following a similar method to that outlined for $\delta\langle \hat{S}^+ \rangle(t)$ earlier we can calculate the change in the expectation value of the spin current upon application of the magnetic field $\mathbf{h}_\perp(t)$ described by Eq. (6.2). We note that in this case $\delta\langle \hat{I}_S^+ \rangle(t) = \langle \hat{I}_S^+ \rangle(t)$ since there is no net spin current flow in the unperturbed system. The spin current generated by the oscillating field is found to be

$$\langle \hat{I}_S^+ \rangle(t) = \frac{i\, g\, \mu_B\, h_0}{2} \sum_{i \in V} \sum_{j \notin V} e^{-i\omega t} \left[\gamma_{ij}\, \chi^{+-}_{ij00}(\omega) - \gamma_{ji}\, \chi^{+-}_{ji00}(\omega) \right] , \tag{6.68}$$

where $\chi^{+-}_{ij00}(\omega)$ is the generalised transverse susceptibility within the RPA. Since we are using a nearest-neighbour tight-binding model to describe the electronic structure of the host medium the sums over i and j are restricted to nearest-neighbour pairs $\langle i, j \rangle$ where $i \in V$ and $j \notin V$. In essence we are summing over the tight-binding connections crossing a surface δV which defines the edge of the volume V out of which the spin current is flowing.

6.3 Dynamic RKKY in graphene

Earlier in this chapter we introduced the quantity $|\chi^{+-}_{ba}(\omega)|$, which gives the amplitude of the precession induced on a magnetic moment at site b due to a precession of frequency ω at site a. We stated that this quantity can be viewed as a dynamic analogue of the RKKY-like coupling that occurs between two static magnetic objects embedded in a conducting host. When a (static) magnetic impurity is placed in the host, it induces a spin polarisation of the conduction electrons. This is generally oscillatory in nature, although we have seen in Chapter 5 that in undoped graphene such oscillations can be masked by a commensurability effect. When a second moment is introduced, the energetically favourable alignment between the moments depends on the local polarisation. The spin polarisation is described by the static spin susceptibility introduced in Eq. 5.9. Within the RKKY picture, the decay rate

of the magnetic coupling is completely determined by the off-diagonal static susceptibility. As such, it is sufficient to consider how the induced spin polarisation caused by a single magnetic impurity is spread in space. In moving from the static magnetic coupling to a "dynamic RKKY" we will begin with the case of a single precessing moment in a graphene sheet. Using the expressions introduced earlier in this chapter in conjunction with the analytic Green functions for graphene, we will determine the separation dependent properties of the dynamic spin susceptibility. For simplicity we will consider the magnetic impurity throughout to be a substitutional atom. This condition can be relaxed to consider more general magnetic objects without significant affecting the results obtained. The analytical work is complemented with fully numerical calculations which confirm the behaviour predicted.

6.3.1 Distance dependence of $\chi^{+-}_{m0}(\omega)$

From Eq. (6.30), the dynamic spin susceptibility element χ^{+-}_{m0}, representing the spin disturbance at an arbitrary site m by the precession of a moment at the magnetic site 0 is given by

$$\chi^{+-}_{m0} = \left(1 + \chi^{0}_{00}\, U\right)^{-1} \chi^{0}_{m0}\,. \tag{6.69}$$

The only term in this expression that contains a distance dependence is χ^{0}_{m0}. Thus as far as the distance-dependent properties of the spin susceptibility is concerned, it is sufficient to examine those of the relevant non-interacting susceptibility matrix element. We recall from Eq. (6.55) that this is written in terms of the Green function operators as

$$\begin{aligned}\chi^{0}_{m0}(\omega) = \frac{i\hbar}{2\pi} \int_{-\infty}^{\infty} \mathrm{d}\omega'\, f(\omega') \Big\{ &\left[G^{\uparrow}_{0m}(\omega') - G^{-\uparrow}_{0m}(\omega')\right] G^{\downarrow}_{m0}(\omega+\omega') \\ &+ \left[G^{\downarrow}_{m0}(\omega') - G^{-\downarrow}_{m0}(\omega')\right] G^{-\uparrow}_{0m}(\omega'-\omega) \Big\}\,.\end{aligned} \tag{6.70}$$

To simplify proceedings further we can now take a similar approach to that taken for the static RKKY interaction and replace the Green function matrix elements, G^{σ}_{ij}, that appear in this expression with their spin-independent,

pristine counterparts, g_{ij}. We note that this replacement is justified since we are concerned principally with the distance dependence of the interaction, which is underpinned by the off-diagonal Green function elements of bulk graphene. Following this, we can split the integral above into three parts as demonstrated in Eqs. (6.56) - (6.64), so that[2]

$$\chi^0_{m0}(\omega) \approx I_1(\omega) + I_2(\omega) + I_3(\omega)\,, \tag{6.71}$$

where

$$I_1(\omega) = \frac{i}{2\pi} \int_{-\infty}^{\infty} \mathrm{d}E'\, f(E') g_{0m}(E') g_{m0}(E' + \hbar\omega) \tag{6.72}$$

$$I_2(\omega) = -\frac{i}{2\pi} \int_{-\infty}^{\infty} \mathrm{d}E'\, f(E') g^{-}_{m0}(E')\, g^{-}_{0m}(E' - \hbar\omega) \tag{6.73}$$

and

$$I_3(\omega) = -\frac{i}{2\pi} \int_{E_F - \hbar\omega}^{E_F} \mathrm{d}E'\, g^{-}_{0m}(E') g_{m0}(E' + \hbar\omega)\,. \tag{6.74}$$

We note that I_1 and I_2 are of similar form and involve the convolution of two retarded or advanced Green functions, whereas I_3 involves one of each type.

We begin our analysis of the separation dependence by examining I_1. We note that its functional form is very similar to that of the static RKKY integral given by Eq. (5.9). The only difference is that now the product in the integral contains Green functions evaluated at different energy values. Following the same approach as was taken for the static case in Section 5.3.1, we write the matrix elements of the off-diagonal pristine Green function in graphene calculated using the Stationary Phase Approximation as

$$g_{m,0}(E) = g_{0,m}(E) = \frac{\mathcal{A}(E)\, e^{i\mathcal{Q}(E)D}}{\sqrt{D}}\,, \tag{6.75}$$

where D is the separation between sites 0 and m. The functional forms of $\mathcal{A}(E)$ and $\mathcal{Q}(E)$ depend on the direction of the separation. Assuming a

[2]To allow a simpler comparison with the treatment of the static coupling in the previous chapter, we have rewritten the integrals in terms of energies (E) instead of frequencies (ω).

separation in the armchair direction as before allows us to write

$$\mathcal{A}(z) = -i\sqrt{\frac{2}{i\pi}}\sqrt{\frac{z}{(z^2+3t^2)\sqrt{t^2-z^2}}} \tag{6.76}$$

and

$$\mathcal{Q}(z) = \sin^{-1}\left(\frac{z}{t}\right),$$

where z is a complex energy. Using these identities we can rewrite I_1 in a similar manner to the static coupling as

$$I_1(\omega) = \frac{i}{2\pi}\int_{-\infty}^{\infty} \mathrm{d}E' \, \frac{\mathcal{B}(E',\omega)\, e^{i\,(\mathcal{Q}(E')+\mathcal{Q}(E'+\hbar\omega))}}{D\,(1+e^{\beta(E-E_F)})}, \tag{6.77}$$

where

$$\mathcal{B}(E',\omega) = \mathcal{A}(E')\,\mathcal{A}(E'+\hbar\omega). \tag{6.78}$$

Moving to the complex plane, the integral can be solved by replacing it with a contour integral in the upper half plane, where the relevant poles are once more given by the Matsubara frequencies $E_p = E_F - i(2p+1)\pi k_B T$, where p is an integer which labels the poles. The integral then becomes a sum of the residues over these poles,

$$I_1(\omega) = -\frac{k_B T}{D}\sum_p \mathcal{B}(E_p,\omega)\, e^{i\,(\mathcal{Q}(E_p)+\mathcal{Q}(E_p+\hbar\omega))\,D}. \tag{6.79}$$

Proceeding as before we expand $\mathcal{B}(E_p,\omega)$ in a Taylor series

$$\mathcal{B}(E_p,\omega) \approx \sum_l \frac{1}{l!}\mathcal{B}^{(l)}(E_p-E_F)^l, \tag{6.80}$$

where $\mathcal{B}^{(l)}$ is the l-th order derivative of the function $\mathcal{B}(E,0)$ evaluated at E_F. Here we have assumed that the function $\mathcal{B}(E_p,\omega)$ varies only weakly with ω around $\omega = 0$. Similarly, $\mathcal{Q}(E)$ is expanded to first order around E_F and written

$$\mathcal{Q}(E) = \mathcal{Q}^{(0)} + \mathcal{Q}^{(1)}\,(E-E_F) \tag{6.81}$$

where $\mathcal{Q}^{(l)}$ is the l-th order derivative of $\mathcal{Q}$ evaluated at E_F. With these expansions, I_1 becomes

$$I_1(\omega) \approx -\frac{k_B T}{D}\, e^{i\,(2\mathcal{Q}^{(0)}+\mathcal{Q}^{(1)}\hbar\omega)D} \sum_l \frac{1}{l!}\,\mathcal{B}^{(l)} \sum_p e^{2\,i\,\mathcal{Q}^{(1)}\,(E_p-E_F)\,D}(E_p - E_F)^l \tag{6.82}$$

which can be rewritten in the low temperature limit as

$$I_1(\omega) \approx \frac{1}{2\pi}\, e^{i\,(2\mathcal{Q}^{(0)}+\mathcal{Q}^{(1)}\hbar\omega)D} \sum_l \frac{(-1)^{l+1}\, i\,\mathcal{B}^{(l)}}{(2\,i\,\mathcal{Q}^{(1)})^{l+1}\, D^{l+2}} \tag{6.83}$$

using the same steps taken for the static coupling in 5.3.1. It is clear that the separation dependence for I_1 is identical to that found for the static coupling. For $E_F \neq 0$, the leading term, $l = 0$, dictates the decay rate so that $I_1 \sim D^{-2}$. However, as before the $l = 0$ term vanishes in the undoped case so that the decay rate is determined by the first surviving term and $I_1 \sim D^{-3}$. A similar analysis can be performed with I_2 by closing the contour in the lower half plane. However, we note that the functional forms of I_1 and I_2 are identical and that therefore both will contribute to the spin susceptibility with the same separation dependence, i.e., D^{-3} for the undoped case and D^{-2} otherwise.

Moving onto I_3, we note first of all that this integral is over a finite frequency range along the real axis:

$$I_3(\omega) = -\frac{i}{2\pi} \int_{E_F-\hbar\omega}^{E_F} \mathrm{d}E'\, g_{li}^{-}(E') g_{jk}(E' + \hbar\omega)\,. \tag{6.84}$$

Furthermore, in the static case this term clearly vanishes as the lower and upper integration limits converge when $\omega = 0$. Therefore I_3 is a purely dynamic contribution to the susceptibility, whereas in the static limit it is easy to see by comparison that $I_1 + I_2$ is essentially the static susceptibility. It is therefore unsurprising that the distance dependence of $I_1 + I_2$ is the same as that found for the static case. Since the integration in Eq. (6.84) is generally performed over a small energy range we can make the following

approximations,

$$\mathcal{A}(z) \approx -i\sqrt{\frac{2}{i\pi}}\,\frac{\sqrt{z}}{\sqrt{3t^3}} \tag{6.85}$$

and

$$\mathcal{Q}(z) \approx \pm\frac{z}{t}\,. \tag{6.86}$$

Then Eq. (6.84) becomes

$$\begin{aligned} I_3(\omega) &\approx -\frac{i}{2\pi D}\int_{E_F-\hbar\omega}^{E_F} \mathrm{d}E' \left[i\sqrt{\frac{2}{-i\pi}}\,\frac{\sqrt{E'}}{\sqrt{3t^3}}\right]\left[-i\sqrt{\frac{2}{i\pi}}\,\frac{\sqrt{E'+\hbar\omega}}{\sqrt{3t^3}}\right] e^{\pm i\frac{\hbar\omega}{t}D} \\ &\approx -\frac{1}{3\pi^2 D t^3}\, e^{\pm i\frac{\hbar\omega}{t}D}\int_{E_F-\hbar\omega}^{E_F} \mathrm{d}E'\,\sqrt{-E'(E'+\hbar\omega)}\,. \end{aligned} \tag{6.87}$$

We note that the remaining integral has no D dependence. In fact, an equation of the form $y = b\sqrt{-x(x+a)}$ can be rewritten

$$\frac{x+\frac{a}{2}}{\left(\frac{a}{2}\right)^2} + \frac{y}{\left(\frac{ab}{2}\right)^2} = 1 \tag{6.88}$$

which represents an ellipse centred at $x = -\frac{a}{2}\,, y = 0$ with respective semi-axes $\frac{a}{2}$ and $\frac{ab}{2}$ and an area $\frac{\pi a^2 b}{4}$. Returning to the integral in Eq. (6.87) and noting that

$$a = \hbar\omega \qquad \text{and} \qquad b = -\frac{1}{3\pi^2 D t^3}\, e^{\pm i\frac{\hbar\omega}{t}D}$$

it is easy to see that the ellipse is confined between $E' = -\hbar\omega$ and $E' = 0$. If $E_F = 0$ then the integral in Eq. (6.87) equals half the area of the ellipse

$$I_3(\omega) \approx -\frac{\hbar^2\omega^2}{24\pi D\, t^3}\, e^{\pm i\frac{\hbar\omega}{t}D}\,. \tag{6.89}$$

In Fig. 6.2 the real (top) and imaginary (bottom) components of the I_3 integrand are plotted for a separation of $50\sqrt{3}a$ in the armchair direction for the undoped case. Each case shows the integrand calculated in three different ways. The small square symbols show the integrand calculated with numerical pristine Green functions, whereas the larger circular symbols

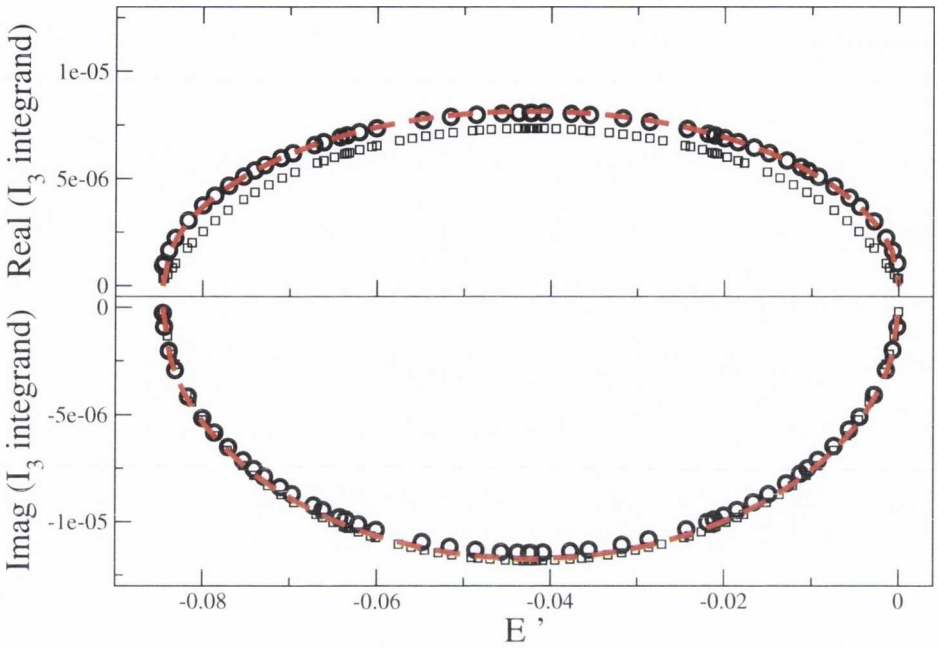

Figure 6.2: The real (top) and imaginary (bottom) parts of the I_3 integrand calculated using fully numerical pristine Green functions (large circles), the SPA Green functions (small squares) and the elliptical approximation of Eq. (6.87) (red, dashed curve). A good agreement is noted between the three calculations.

represent a calculation using the SPA Green functions. We note that the SPA overestimates the amplitude of the real part, however the overall match between the two is still good. The red, dashed line in each case represents the approximation for the integrand given by Eq. (6.87), the integral over which is given exactly by Eq. (6.89). It is clear from Fig. 6.2 that the approach taken in this section returns an excellent estimate for I_3 from which we can extract useful analytical information. The distance dependence of the I_3 term is particularly interesting. We note that this term decays as D^{-1}, presenting a much slower decay rate than was calculated for the other terms in the susceptibility. The presence of the ω^2 term in Eq. (6.89) confirms once more that this term vanishes in the static case and is a purely dynamic contribution to the susceptibility. To confirm the decay rates predicted by this analysis, Fig 6.3 plots the different contributions to the susceptibility as a function of separation for undoped graphene. These calculations are performed using

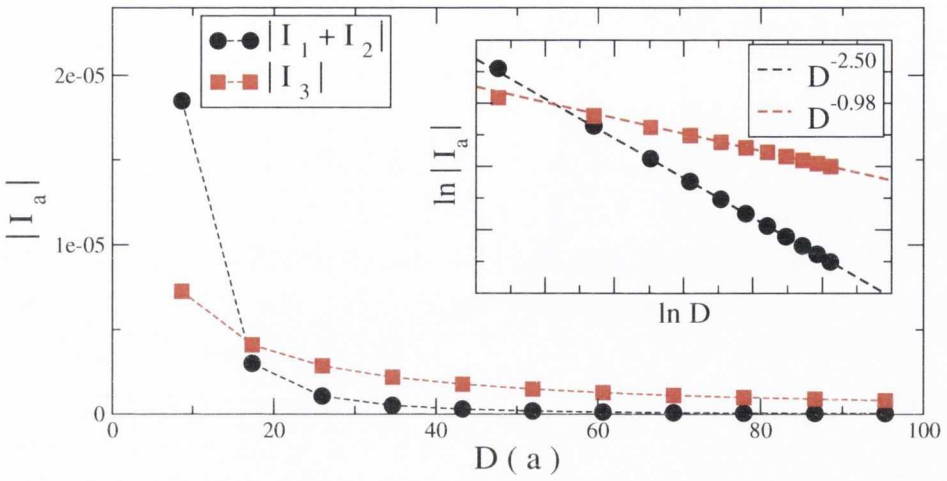

Figure 6.3: Decay rates of the different contributions to the dynamic susceptibility. The log-log plots in the inset reveal the power law exponents of $I_1 + I_2$ and I_3 to agree with those predicted in the text.

the numerically calculated pristine Green functions. The log-log plots in the inset are in good agreement with our predictions that $I_1 + I_2 \sim D^{-3}$ and $I_3 \sim D^{-1}$.

We have now fully determined the decay rates which emerge from the constituent components of the non-interacting off-diagonal susceptibility, calculated using the pristine Green functions. We have found that the components consisting of a convolution of two retarded or advanced Green functions contribute a decay rate equal to that found for the static susceptibility and indirect exchange coupling. However the final component, consisting of the convolution of retarded and advanced Green functions, contributes a slower decay rate, namely D^{-1}, which from Eq. (6.87) should hold for both the doped and undoped cases[3]. At the start of this section we predicted that the distance dependence of the interacting susceptibility, $\chi^{+-}_{m0}(\omega)$, should be entirely described by the decay rates which emerge from the non-interacting susceptibility we have examined thus far. We can now test this prediction by calculating the interacting susceptibility numerically and scrutinising how it

[3]We note that the I_3 term also adds an oscillatory component that is independent of the Fermi energy. This is generally a low frequency oscillation compared to that induced by the Fermi wavevector in terms I_1 and I_2, but traces of it may be seen in undoped results, particularly by sweeping over large separation ranges.

varies with the separation between the magnetic moment and the site we are probing. Finally, we can include a second magnetic moment at the probe site to ensure that the behaviour holds not just for the spin polarisation caused by the precessing moment, but for the full dynamic analogue of the RKKY interaction. Before showing the distance dependence, we must first fix the frequency of the excitation. If we examine the functional form of the diagonal term of the RPA susceptibility, as given for a single impurity in Eq. (6.32), we note that collective excitations should appear as peaks. The height of these peaks correspond to the amplitude of the excitation, whereas the width of the peaks are inversely proportional to the excitation lifetime. In the absence of dissipative features, such as spin-orbit effects, which are neglected in our model, the lifetimes of the excitations are generally determined by their decay into Stoner modes. For one magnetic impurity, the excitation spectrum contains a single peak at a resonance frequency corresponding to the normal mode of the system. Systems with additional magnetic moments contain peaks at frequencies corresponding to each normal mode of the system. However, as some of these peaks may occur at the same, or nearby, frequencies it may not be possible to resolve all of the peaks separately. Similar peaks occur in the off-diagonal matrix elements of the susceptibility that we examine to determine the decay rate. In Fig. 6.4, we plot the absolute value of the off-diagonal susceptibility, $|\chi^{+-}_{m0}|$, evaluated at both $\omega = 0$ and at the resonance frequency, ω_R , as a function of separation. The calculations are performed for both the undoped and doped cases. For $\omega = 0$, we note that we find the decay rates predicted before for the static susceptibility. However, in the dynamic case the decay rate converges to D^{-1} in both the doped and undoped systems, confirming the expectations of our analysis in this section. Furthermore, the exact same decay rate behaviour is noted in the insets, which correspond to calculations performed with two magnetic impurities. We can thus conclude that the dynamic RKKY interaction in graphene has a much longer range than its static counterpart.

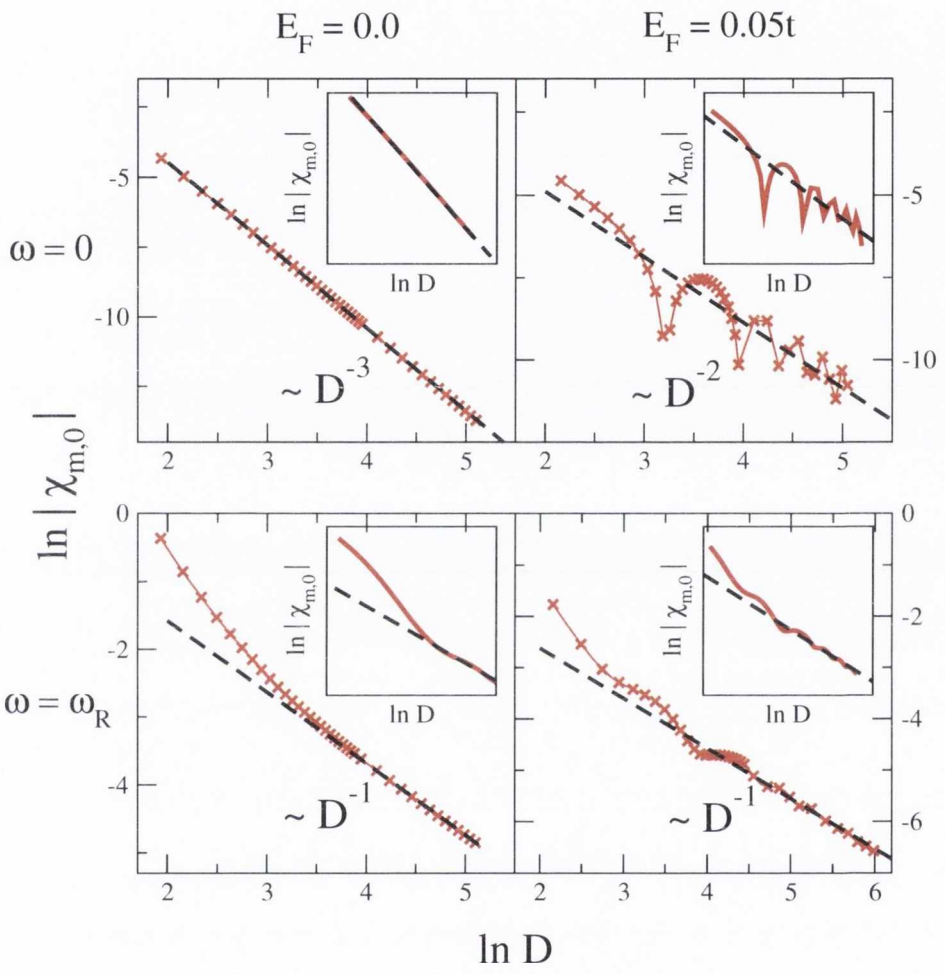

Figure 6.4: Log-log plots of the off-diagonal susceptibility as a function of separation. The main plots show the results for the static ($\omega = 0$, top panels) and dynamic ($\omega = \omega_R$, bottom panels) susceptibilities for both undoped (left) and doped (right) systems, calculated with one magnetic impurity. The red curves with 'X's are the numerical results, whereas the black, dashed lines correspond to the indicated decay rates, as predicted in the text. We note that the static susceptibility behaves as before, but the dynamic results show a convergence to a longer ranged (D^{-1}) decay rate. The exact same decay rate behaviour is shown in the insets for calculations with two magnetic impurities.

6.3.2 Spin current from a precessing moment in graphene

A related topic to the dynamic magnetic interaction considered in the previous section is that of the spin current that emanates from a precessing moment out into the graphene host. It is this current that can be thought of as mediating the interaction between multiple moments. We will now examine the spin current that flows from a single precessing moment embedded in a graphene sheet. In section 6.2.3, we showed that the spin current flowing out of a volume V could be written in terms of the spin susceptibility as

$$\langle \hat{I}_S^+ \rangle(t) = \frac{i\, g\, \mu_B\, h_0}{2} \sum_{i \in V} \sum_{j \notin V} e^{-i\omega t} \left[\gamma_{ij}\, \chi^{+-}_{ij00}(\omega) - \gamma_{ji}\, \chi^{+-}_{ji00}(\omega) \right] , \qquad (6.90)$$

where the sums over i and j amount to summing over the tight-binding connections between $i \in V$ and $j \notin V$ that cross the boundary of the volume. This is shown schematically for a small circular volume (shaded area) in the left panel of Fig. 6.5. To examine the distance dependence of the spin current, i.e., its dependence on the radius, R, of the circular volume shown in the schematic, we can look at the χ^{+-}_{ij00} terms in the above expression. Their distance dependence is entirely contained in the equivalent Hartree-Fock susceptibilities, χ^0_{ij00}, which can be written as a sum of integrals $I_1 + I_2 + I_3$ as before. The functional form of these is very similar to the corresponding terms for the χ^0_{m0} case we studied in the previous section. We should therefore expect the same decay behaviour with distance, namely that the χ^{+-}_{ij00} terms should approach a R^{-1} decay as the radius is increased. However, as the radius is increased the number of connections crossing the boundary increases also and is proportional to the circumference, and hence radius, of the volume. Therefore we should expect the overall spin current measured out of a circular volume *not* to vary strongly with the radius. This expectation is confirmed by a numerical calculation of the magnitude of the spin current, evaluated at the resonance frequency, as a function of radius as shown in the right panel of Fig. 6.5. Here we see that as the radius is increased, the spin current magnitude approaches a constant value. Such a result is consistent with the absence of dissipation terms like spin-orbit coupling in this model,

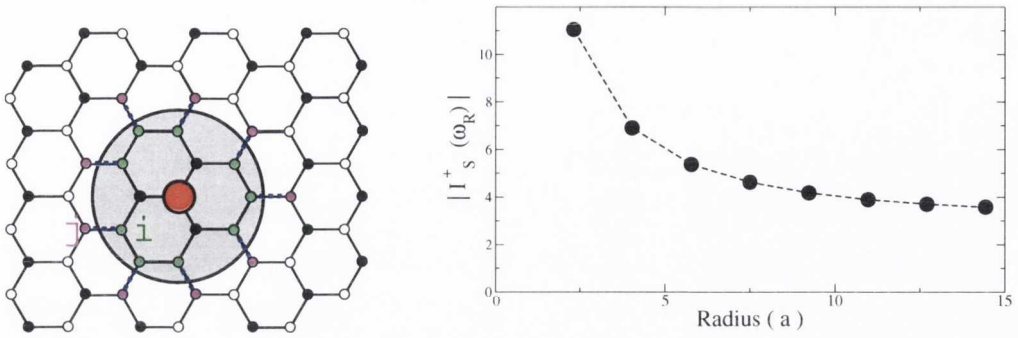

Figure 6.5: The schematic on the left shows the connections between atoms inside (green) and outside (purple) the circular volume that must be summed over when calculating the spin current. The plot on the right shows the magnitude of the spin current flowing from a circular area as a function of the radius. It is seen to approach a constant value as the radius increases.

and also with recent experimental results which suggest the propagation of spin current over a long range in graphene samples [140].

6.4 Detecting the dynamic RKKY in experiment

To date it has been very difficult to probe the RKKY interaction in graphene experimentally. It is understandable that with a decay rate as fast as D^{-3} it is difficult to probe the interaction for any reasonable separation. The presence of magnetism in disordered graphene systems may indicate the presence of an exchange coupling between magnetic moments formed around defects. Nuclear magnetic resonance experiments reveal that these defects have indeed magnetic moments, since they couple to implanted Fe atoms [210]. However, whether or not these moments couple with each other, or with the graphene lattice, to form a ferromagnetic state is a controversial subject and many of the results in this area have proved difficult to reproduce [90]. However, there has been significant progress recently in probing the spin dynamic properties of isolated magnetic impurities on the atomic scale. The method of inelastic scanning tunnelling spectroscopy (ISTS) [141–144] can be used to probe the

magnetic excitations of the system. The spin excitation spectrum of an individual atom adsorbed onto a surface is measured by positioning the tip above the relevant atom and varying the bias. Above a certain threshold voltage, electrons tunnel between the tip and the surface, registering a current. For the case considered here, tunnelling electrons are able to transfer energy to the magnetic excitations of the system. A differentiation of the standard $\frac{\mathrm{d}I}{\mathrm{d}V}$ curve from such a measurement corresponds to the density of magnetic excitations. This quantity is intrinsically connected with the diagonal term of the spin susceptibility that we have been investigating throughout this chapter.

In the previous section, we determined how the off-diagonal susceptibility, χ^{+-}_{m0}, varied as the separation between two magnetic moments was increased. We found a longer ranged decay than was predicted for the static analogue of the interaction. However it is very difficult to probe the off-diagonal element experimentally. What we can investigate instead is the diagonal matrix element of the susceptibility, χ^{+-}_{00}, which as we have noted above can be probed by sensitive experimental techniques. This matrix element, plotted as a function of frequency ω, tells us how strongly the system responds to a time-dependent magnetic excitation. In particular, peaks in the frequency-dependent susceptibility reflect the existence of resonant frequencies whereas their inverse widths characterise the lifetimes of the associated spin excitations. In the top (A) panel of Fig. 6.6, the diagonal susceptibility is shown as a function of excitation frequency for a single magnetic impurity (at site 0) and a single peak is identified. The linewidth W_1 of this peak is highlighted. Adding a second impurity at a separation D from the first one will maintain the peaked features of the susceptibility but the linewidths and peak heights should now develop a D dependence. We have seen clearly how the interaction between precessing moments manifests itself in the separation dependence of the off-diagonal term. It is now worth investigating how the diagonal term is affected. We should expect that as the moments are moved further apart they become essentially independent and that their excitation linewidths should approach those found for the single impurity case. We begin by considering the expression for the RPA susceptibility in terms of the

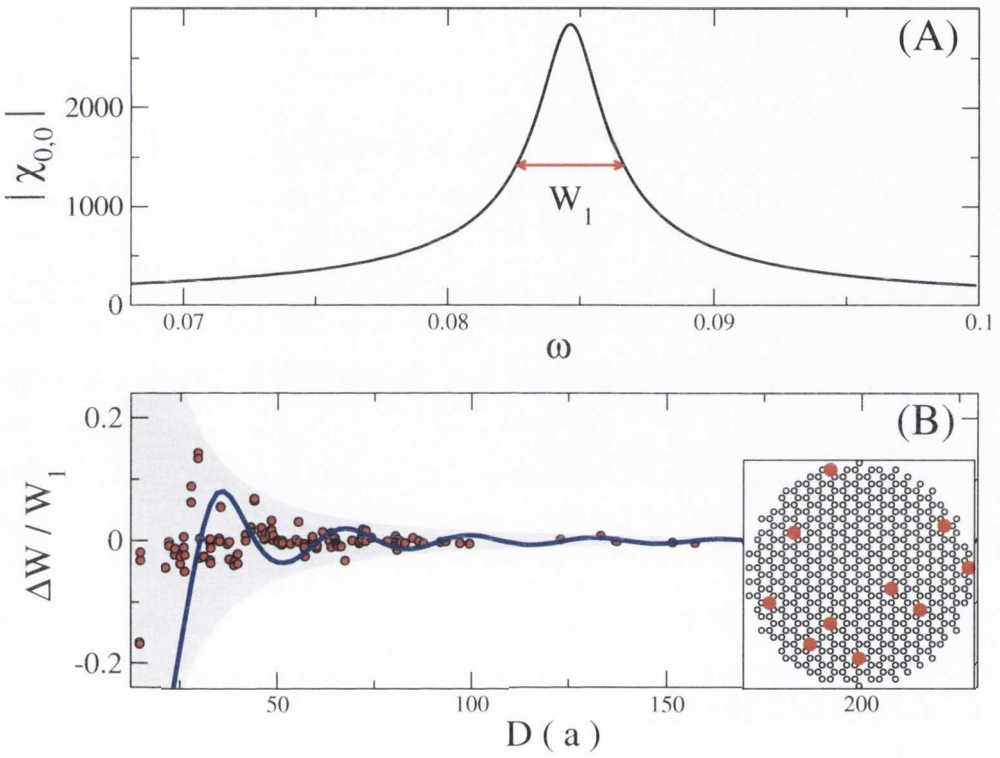

Figure 6.6: (A) Diagonal susceptibility for a single magnetic impurity as a function of excitation frequency. A single peak with linewidth, W_1, is identified. (B) The relative fluctuations of the excitation linewidth, $\frac{W-W_1}{W_1}$, for two magnetic impurities as a function of their separation in the armchair direction is show by the solid blue curve. The shaded area delimits the region spanned by the two impurity result if all possible separation directions are considered. The scattered red dots correspond to the relative linewidth fluctuations of the diagonal susceptibilities $\chi^{+-}_{m,m}$ calculated at different sites m in a disordered array of magnetic impurities embedded in graphene, as illustrated by the schematic example in the inset, plotted against their respective nearest neighbour distances.

non-interacting susceptibility, given by Eq. (6.29), which for two magnetic impurities at sites 0 and m allows us to write

$$\begin{aligned}
\chi_{00}^{+-} &= \chi_{00}^{0} - \chi_{00}^{0}\, U\, \chi_{00}^{+-} - \chi_{0m}^{0}\, U\, \chi_{m0}^{+-} \\
&= \left(1 + \chi_{00}^{0}\, U\right)^{-1} \left(\chi_{00}^{0} - \chi_{0m}^{0}\, U\, \chi_{m0}^{+-}\right) \\
&= \left(1 + \chi_{00}^{0}\, U\right)^{-1} \left(\chi_{00}^{0} - \chi_{0m}^{0}\, U\, \left(1 + \chi_{mm}^{0}\, U\right)^{-1} \left(\chi_{m0}^{0} - \chi_{m0}^{0}\, U\, \chi_{00}^{+-}\right)\right) \\
&\approx \left(1 + \chi_{00}^{0}\, U\right)^{-1} \left(\chi_{00}^{0} - \left(1 + \chi_{mm}^{0}\, U\right)^{-1} \chi_{0m}^{0}\, U\, \chi_{m0}^{0} - \cdots\right) .
\end{aligned} \tag{6.91}$$

The first term on the right hand side of the above equation corresponds to the diagonal susceptibility in the case of a single magnetic impurity. The diagonal susceptibility for two impurities can therefore be written in terms of the one-impurity case as a series expansion in powers of χ_{0m}^{0} and χ_{m0}^{0}. We recall that these terms individually decay as D^{-1} as the separation between the moments is increased. The lowest order correction to the diagonal susceptibility when a second magnetic moment is introduced is given by the second term in the equation above. This term contains a product of off-diagonal susceptibilities, $\chi_{0m}^{0}\chi_{m0}^{0}$, so we should therefore expect that it decays with separation as D^{-2}. The blue, solid curve in Fig. 6.6(B) plots the fluctuation of the excitation linewidth relative to the result for the single impurity case as a function of the moment separation in the armchair direction. We note that the linewidth fluctuates around the one impurity value and its rate of decay is in good agreement with the D^{-2} rate predicted above and indicated in the figure by the shaded area enveloping the two-impurity curve. It is worth noting that a change in direction will lead to only a phase shift or additional oscillatory features in the solid blue curve so that if all possible directions were considered the resultant data points would generate the shaded area.

Rather than just having one or two isolated impurities along a given direction, a more realistic scenario is that depicted in the inset of Fig. 6.6(B), namely several magnetic moments randomly located across a graphene sheet. To model such a setup, we may consider several disordered configurations of multiple moments and obtain the linewidth of each. By plotting these as a

function of their respective nearest neighbour distance we should be able to confirm the predicted decay rate. The scattered red points in Fig. 6.6(B) represent the linewidth fluctuations found from 25 randomly generated configurations of five magnetic impurities as a function of the nearest neighbour distance. The calculated linewidths all fall within the shaded area containing the two-impurity linewidth oscillations, confirming that the dynamic interaction between nearest neighbour impurities tends to dominate and determine the lifetime of the spin excitations in these disordered configurations. The important trend to note is that the amplitude of the fluctuations around the one-impurity linewidth, W_1, decays as D^{-2} with the nearest neighbour separation. Bearing in mind that the average nearest-neighbour distance between two impurities scales as $\frac{1}{\sqrt{\rho}}$, where ρ is the impurity concentration, we can predict that the standard deviation (σ_W) of the experimental measurements of spin-excitation linewidths will scale with the magnetic impurity concentration as $\sigma_W \sim \rho$. Evidence of this scaling would be a clear indication of the RKKY interaction in its dynamic form.

Experimental considerations

The inset of Fig. 6.6(B) matches quite closely the experimental setup of Ref. [144], which measured the spin-excitation lifetimes of Fe atoms randomly dispersed on Cu surfaces using ISTS techniques. In fact, because C atoms have smaller spin-orbit coupling than Cu, these features should be more pronounced in graphene and thus easier to probe. However, there are some further factors that need to be taken into account when considering how our results could be compared to those from an ISTS experiment. In particular, detecting experimental signatures of the dynamic RKKY interaction involves measuring fluctuations in the ISTS magnetic excitation linewidths. From Fig. 6.6(B), we observe that fluctuations in the linewidth of 5% or greater are present up to separations of approximately $80\,a$ (200 Å), whereas the linewidth for the single impurity case is approximately $0.02\,eV$. However, the linewidth and resonance energy depend strongly on the value of the static Zeeman field entering into the Hamiltonian in Eq. (6.1). The

value we have chosen corresponds to a magnetic field of approximately $100\,T$. This is significantly larger than any experimentally realisable static, homogeneous field, but is necessary to allow our numerical study. Since the peak positions and widths scale linearly with the field strength in this frequency regime [207, 211], we can extrapolate our findings to more feasible field values of $\sim 10T$. Here we estimate that the fluctuations in Fig. 6.6(B) in the distance range $70 - 200$ Å are of the order $10^{-3} - 10^{-4}\,eV$. Comparing this with the energy resolution of $1.5 \times 10^{-4}\,eV$ reported in Ref. [144], we see that we are very near the limit of what may be feasible experimentally. However, there is another degree of freedom available to us in controlling the widths of such features, namely the choice of magnetic impurity. In this work, we have considered a very generic parameterisation of the magnetic impurity. When a more complete parameterisation is considered, for example by comparison with *ab initio* results, the choice of magnetic species can play a large role. The width of resonance features is controlled by the local density of states at the impurity sites, and in particular if the impurity spin levels cross the Fermi energy a much broader peak feature is expected [211, 212]. A recent study examining a range of substitutional $3d$ transition metal impurities in graphene suggests that such a property may be present for Cu, Zn and V [195]. Thus careful selection of the type of magnetic impurity considered may enhance the predicted signatures of the dynamic RKKY interaction, and make them more accessible to experimental verification. Another relevant consideration for experiment or device application is the temperature to which such interactions persist. The long-ranged dynamic contribution emerges from the I_3 term, which contains an integral over a short energy interval defined by the resonance frequency of the excitation. At finite temperatures, the introduction of the relevant Fermi functions into Eq. (6.74) will lead to a smearing, or averaging out, of these contributions, especially when the thermal energy approaches that of the resonance. For the moment parameterisation considered in Fig 6.6(A), adjusted for realistic field values, we find that the excitation energy corresponds to $\sim 200K$. This is a very basic approximation and we further note that the resonance energy can be altered by changing the magnetic species considered as discussed earlier for

the peak width. Another point to note is that impurity elements with larger spin-orbit splittings, such as $5d$ transition metal atoms, should tend to increase the excitation energy due to their intrinsic magnetic anisotropy [213]. The study of graphene doped with such impurities may lead to room temperature spintronic devices utilising the dynamic interactions considered here.

6.5 Summary of Chapter

In this chapter we extended the discussion of magnetic interaction between impurities embedded in a graphene sheet to the dynamic case where the moments are set to precess. This work was motivated by the fast decay rates found for the static, or RKKY-like, interaction to date in graphene systems. Such quick decay rates are an obstacle for the implementation of magnetically doped graphene systems in spintronic devices, as it limits the region over which magnetic moments can feel each other's presence. A longer ranged interaction is essential for manipulating the properties of a system or for the transfer of information between different locations in a potential device.

In section 6.2, we introduced the theory necessary to describe the response of the system to a dynamic magnetic excitation. The dynamic spin susceptibility was calculated using the RPA approximation. By connecting this susceptibility to the non-interacting susceptibility, we demonstrated how the full calculation could be written in terms of the single-particle Green function propagators that have been used repeatedly throughout this work. A dynamic analogue to the static RKKY-like interaction was suggested in the form of the off-diagonal matrix element of the dynamic susceptibility, which gives the dynamic response of a magnetic moment to an induced magnetic precession elsewhere in the system. The relationship between the susceptibility and the flow of spin current was revealed.

To fully explore the concept of a dynamic RKKY interaction between magnetic moments in graphene, in section 6.3 we extended the methods developed in Chapters 3 and 5 to examine the separation dependence of the interaction. By splitting the integral used to calculate the susceptibility, we discovered a term not found in the static case that contributes a decay rate of

D^{-1}, a significantly longer-ranged decay than the D^{-3} rate predicted for the static moments. An excellent agreement was found between the analytical treatment and full numerical calculations of the dynamic interaction. The behaviour observed here was connected to the spin current flow from a single precessing moment in graphene.

Finally, in section 6.4 we argued that the difficulty in experimentally probing the RKKY interaction in graphene-related materials may be overcome by simply exciting the magnetisation of the magnetic objects in contact with graphene, something that is currently achievable and has been recently reported using inelastic scanning tunnelling spectroscopy. We demonstrated how deviations in the excitation lifetimes probed by this method were related to the dynamic interaction studied in this chapter. We suggest that the behaviour of these measurements as a function of separation, or of impurity concentration, provides a clear signature of the dynamic magnetic interaction in graphene.

The work presented in this chapter on the dynamic magnetic interaction in graphene has been submitted under the title "Dynamic RKKY interaction in graphene".

CHAPTER

SEVEN

Conclusions and Further Work

7.1 Summary of thesis

This thesis has considered a number of different topics relating to graphene systems, and in particular those doped with impurities. A strong focus was placed on the interactions between magnetic impurities embedded into graphene. Understanding how such impurities interact is a vital step in preparing magnetically-doped graphene systems for use in spintronic applications. The work in this thesis has combined theoretical and numerical approaches to examine several issues that arise in this field. In this section, the principal methods and findings of the thesis will be summarised before suggestions for possible extentions to the work presented here are made.

Chapter 2 reviewed the concept of Green functions and how they can be calculated and manipulated for use in the sort of calculations found throughout the thesis. Simple examples were used to illustrate the various methods. The Green function formalism was shown to be useful for describing perturbed and disordered systems where the Dyson equation could be used. Methods for calculating the Green function for a large system in a recursive fashion were demonstrated. A description of the Lloyd formula method for calculating the change in various properties of the system when a perturbation is applied, and details on performing integrals involving the Green

function were outlined. Finally, a brief introduction to the Hubbard model and its treatment within the mean-field approximation was given. The steps of a self-consistent procedure to include magnetic moments within the formalism developed earlier in the chapter were described.

Chapter 3 focused on the electronic properties of graphene materials and how these could be calculated within the nearest-neighbour tight-binding approximation.The resulting band structure was analysed and a brief discussion of the popular linear approximation often used for small Fermi energies was given. The band structures of one-dimensional graphene systems, namely nanotubes and nanoribbons, were presented and their calculation related to that of graphene sheets. A large part of this chapter was devoted to calculating the Green function matrix elements for graphene sheets. Using the Stationary Phase Approximation we derived an analytical expression for the off-diagonal Green function that was extremely accurate over a wide energy range. A detailed description of this calculation for the two principal high-symmetry directions in graphene and an outline of its implementation in more general cases was given. The existence of an analytical expression for the Green function allows for the behaviour of many physical properties to be explored in a mathematically transparent fashion. It also offers advantages over existing techniques like the linear dispersion approximation which is only accurate in a narrow energy range and numerical methods which can lack transparency. Our expression found repeated use in later chapters. Finally, the recursive methods introduced in the previous chapter were demonstrated explicitly for the case of graphene nanoribbons.

In Chapter 4 we examined some position dependent features in graphene nanoribbons doped with impurity atoms. The effect of impurity location on the conductance through a ribbon was discussed with reference to the literature and a simple model calculation. The presence of a qualitative difference between the transport through ribbons with uniform disorder or disorder localised principally at the ribbon edge was emphasised. We then examined how the binding energy of such impurities depends on their location and how the resulting behaviour may result in a degree of spatial segregation in their distribution across a ribbon. In the case of zigzag-edged nanoribbons a non-

monotonic feature observed was connected to the sublattices of the graphene atomic structure. A simple theoretical model for calculating how the energy variation changes across a ribbon was developed and found to be in agreement with the results of DFT calculations. We postulated that control of the adsorbed impurity segregation within a ribbon is possible by adjusting the Fermi energy and that this may allow tuning of the magnetic profile and electronic properties of a ribbon. For the case of magnetic impurity atoms, we then considered how the magnetic moment depended on the impurity position. A variety of impurity configurations were considered with robust features especially noted for magnetic impurities on zigzag-edged ribbons. For both edge geometries and impurity configurations, edge vacancies were introduced to test the robustness of the features against structural disorder. We showed that an edge vacancy did not have a significant effect on the moment of a magnetic impurity located more than one or two lattice spacings away. Furthermore, we demonstrated that the distinctive moment profile on a zigzag-edged ribbon was robust in the presence of an extended edge disorder. In light of these findings, we argued that magnetically-doped nanoribbons may provide a route to applications previously envisaged for nanoribbons with intrinsic magnetic ordering, which is less stable in the presence of experimentally imposed constraints such as imperfect edge geometry.

Chapter 5 began our investigation of coupling between magnetic impurities in graphene. The concept of an indirect exchange coupling mediated by the conduction electrons of the host was introduced. The Quantum Well method of calculating the coupling was formulated and compared to the more commonly known RKKY method, which was shown to be a second-order perturbative approximation to the coupling. The results in the literature regarding such interactions in graphene systems were discussed before an analytical treatment of the RKKY coupling in graphene was performed using the Stationary Phase Green functions. We were able to calculate the principal features of the interaction without resorting to a 'cutoff function' that is required by previous analytical studies. The distance-dependent properties of the interaction were found to emerge in a mathematically transparent fashion from our results and agree with both our numerical calculations and

the expected results from the literature. In particular we confirmed the very fast D^{-3} decay rate predicted for the interaction in undoped graphene, where D is the distance between the impurities. Numerical methods were used to probe the magnetic interaction beyond the standard RKKY model by varying the parameterisation of the magnetic impurities considered. We found that a preferential anti-ferromagnetic alignment may persist to large separations between magnetic moments located on the same sublattice. Such a finding contradicts the expected RKKY result. We conclude that a richer range of magnetic coupling features is present in graphene than had been previously anticipated. Finally, we demonstrated that the magnetic coupling discussed to date may play a significant role in explaining some unusual *ab initio* results occurring in the literature, including the unexpected absence of a magnetic moment on an iron atom embedded in a graphene sheet. The use of single-impurity-doped unit cells in DFT calculations was shown to be highly inappropriate to describe magnetically doped graphene and may lead to fundamentally erroneous results as a consequence of the magnetic interaction between impurities in neighbouring unit cells. A mathematically transparent criterion for the formation of magnetic moments in graphene was developed and tested in a number of cases. Such a tool is useful for predicting impurity atoms that may play a role in future graphene-based spintronic devices.

In Chapter 6 we extended the discussion to the dynamic case where the impurity moments are set to precess. The fast decay rates noted in the previous chapter for the static interaction may prove an obstacle for the implementation of magnetically-doped graphene systems in spintronics. However, longer range interactions have been predicted for dynamic systems. The theory necessary to describe the response of a magnetically-doped graphene system to a dynamic magnetic excitation was introduced. A dynamic analogue to the static RKKY-like interaction was suggested in the form of the off-diagonal matrix element of the dynamic spin susceptibility, a quantity which gives the response of a magnetic moment to a magnetic precession induced elsewhere in the system. A decay rate of D^{-1}, significantly longer-ranged than the D^{-3} static rate, was predicted using an analytic approach

and an excellent agreement was found with full numerical calculations. The behaviour observed was related to the spin current flow from a single precessing moment in graphene. Furthermore, we argued that the interaction studied can be linked to the lifetimes of magnetic excitations in such systems. Recent experimental progress in measuring such quantities using inelastic scanning tunnelling spectroscopy suggest a method of probing the interaction in graphene. We predict that the behaviour of such measurements as a function of separation, or of impurity concentration, should provide a clear signature of the dynamic magnetic interaction in graphene.

7.2 Further work and possible extensions

The methods used and results obtained in this thesis suggest many possible extensions beyond what has been presented here. Many are natural continuations to the work presented, whereas others avail of some of the methods and techniques used to address currently open questions in graphene science.

In Chapter 4 we addressed position dependent effects in graphene nanoribbons. As part of this topic, we examined magnetic impurities and how their properties were affected by the impurity location and by edge disorder. This work was partly motivated by the prospect of magnetically-doped nanoribbons providing an alternative route to spintronic devices proposed for nanoribbons with intrinsic magnetic ordering. Among the suggestions for such systems are magnetoresistance devices [102, 103]. Given that these devices in general rely on pristine edge geometries that may be difficult to achieve experimentally [51] and that magnetoresistance effects have been previously reported in doped carbon nanotubes [119], we believe it is prudent to investigate the possibility of magnetoresistance in doped nanoribbon systems. Such a study would combine the nanoribbon Green function and transport calculations of Chapters 3 and 4 with the magnetic coupling features discussed in Chapters 5.

The exploration of static and dynamic magnetic interactions in Chapters 5 and 6 focused on simple impurities in graphene sheets. A natural extension of this work is to explore these interactions for more general impurity types

and for other graphene systems like nanoribbons or multilayers. In nanoribbons in particular the presence of edges introduces interesting features that may affect the interaction. Furthermore, one dimensional systems in general tend to have slower decay rates and so may be more suitable for spintronic applications. A range of devices have been suggested with properties that depend on spin current flow in graphene systems [137–139]. Using the formalism developed in Chapter 6 the feasibility of similar devices in nanoribbons in the presence of edge disorder can be easily investigated.

Apart from these natural extensions to the work described in the thesis, a range of other systems and properties can be investigated using similar methods. Within the tight-binding description we employ to describe the electronic structure of graphene, it is quite simple to include, for example, externally applied magnetic fields [14, 214] or the effect of strain [215, 216]. Both these features can be accounted for by corrections to the hopping parameters in the tight-binding Hamiltonian. Inclusion of magnetic fields allows the investigation of the Quantum Hall Effect and other features in graphene systems, whereas strain effects in graphene are currently a popular topic due to the possibility of using strain to tune or alter physical properties of the system. The effect of strain on the transport properties or magnetic interactions found in graphene could have interesting potential applications.

The examples listed here are just a sample of the possible studies that could be undertaken using the methods set out in this thesis. The combination of analytical and numerical methods allows for a mathematically transparent description of the features investigated whilst also permitting, for example, the study of larger systems or configurational averaging over disordered samples. The beauty of graphene physics is that a wide variety of unique and interesting features can be explored using pen-and-paper or relatively lightweight numerical techniques. We hope that the work presented in this thesis has given a flavour of what is possible using such approaches.

BIBLIOGRAPHY

[1] P. Harris. On charcoal. *Interdisciplinary Science Reviews* **24**, 301 (1999).

[2] H. Petroski. *The Pencil: A History of Design and Circumstance.* Knopf, 1st edition, (1990).

[3] P. Delhas. *Graphite and precursors.* Gordon & Breach, (2001).

[4] A. K. Geim and K. S. Novoselov. The rise of graphene. *Nature Materials* **6**, 183 (2007).

[5] A. K. Geim. Graphene: Status and prospects. *Science* **324**, 1530 (2009).

[6] A. H. Castro Neto, F. Guinea, N. M. R. Peres, K. S. Novoselov, and A. K. Geim. The electronic properties of graphene. *Reviews of Modern Physics* **81**, 109 (2009).

[7] K. S. Novoselov. Nobel lecture: Graphene: Materials in the flatland. *Reviews of Modern Physics* **83**, 837 (2011).

[8] J.-C. Charlier, X. Blase, and S. Roche. Electronic and transport properties of nanotubes. *Reviews of Modern Physics* **79**, 677 (2007).

[9] A. H. Castro Neto, F. Guinea, and N. M. R. Peres. Drawing conclusions from graphene. *Physics World* **19**, 33 (2006).

[10] H. W. Kroto, J. R. Heath, S. C. O'Brien, R. F. Curl, and R. E. Smalley. C60: Buckminsterfullerene. *Nature* **318**, 162 (1985).

[11] S. Iijima. Helical microtubules of graphitic carbon. *Nature* **354**, 56 (1991).

[12] M. Monthioux and V. L. Kuznetsov. Who should be given the credit for the discovery of carbon nanotubes? *Carbon* **44**, 1621 (2006).

[13] L. Radushkevich and V. Lukyanovich. O strukture ugleroda, obrazujucegosja pri termiceskom razlozenii okisi ugleroda na zeleznom kontakte. *Zurn Fisic Chim* **26**, 88 (1952).

[14] R. Saito, G. Dresselhaus, and M. S. Dresselhaus. *Physical Properties of Carbon Nanotubes.* Imperial College Press, London, (1998).

[15] R. Saito, M. Fujita, G. Dresselhaus, and M. S. Dresselhaus. Electronic structure of chiral graphene tubules. *Applied Physics Letters* **60**, 2204 (1992).

[16] S. J. Tans, M. H. Devoret, H. Dai, A. Thess, R. E. Smalley, L. J. Geerligs, and C. Dekker. Individual single-wall carbon nanotubes as quantum wires. *Nature* **386**, 474 (1997).

[17] K. S. Novoselov, A. K. Geim, S. V. Morozov, D. Jiang, Y. Zhang, S. V. Dubonos, I. V. Grigorieva, and A. A. Firsov. Electric field effect in atomically thin carbon films. *Science* **11**, 666 (2004).

[18] K. S. Novoselov, A. K. Geim, S. V. Morozov, D. Jiang, M. I. Katsnelson, S. V. Dubonos, I. V. Grigorieva, and A. A. Firsov. Two-dimensional gas of massless Dirac fermions in graphene. *Nature* **438**, 197 (2005).

[19] R. E. Peierls. Quelques proprietes typiques des corpses solides. *Ann. I. H. Poincare* **5**, 177 (1935).

[20] L. D. Landau. Zur theorie der phasenumwandlungen ii. *Phys. Z. Sowjetunion* **11**, 26 (1937).

[21] P. Blake, P. D. Brimicombe, R. R. Nair, T. J. Booth, D. Jiang, F. Schedin, L. A. Ponomarenko, S. V. Morozov, H. F. Gleeson, E. W. Hill, A. K. Geim, and K. S. Novoselov. Graphene-Based liquid crystal device. *Nano Letters* **8**, 1704 (2008).

[22] Y. Hernandez, V. Nicolosi, M. Lotya, F. M. Blighe, Z. Sun, S. De, M. T., B. Holland, M. Byrne, Y. K. Gun'Ko, J. J. Boland, P. Niraj, G. Duesberg, S. Krishnamurthy, R. Goodhue, J. Hutchison, V. Scardaci, A. C. Ferrari, and J. N. Coleman. High-yield production of graphene by liquid-phase exfoliation of graphite. *Nature Nanotechnology* **3**, 563 (2008).

[23] A. K. Geim. Nobel lecture: Random walk to graphene. *Reviews of Modern Physics* **83**, 851 (2011).

[24] C. Lee, X. Wei, J. W. Kysar, and J. Hone. Measurement of the elastic properties and intrinsic strength of monolayer graphene. *Science* **321**, 385 (2008).

[25] I. Meric, M. Y. Han, A. F. Young, B. Ozyilmaz, P. Kim, and K. L. Shepard. Current saturation in zero-bandgap, top-gated graphene field-effect transistors. *Nature Nanotechnology* **3**, 654 (2008).

[26] A. A. Balandin, S. Ghosh, W. Bao, I. Calizo, D. Teweldebrhan, F. Miao, and C. N. Lau. Superior thermal conductivity of Single-Layer graphene. *Nano Letters* **8**, 902 (2008).

[27] J. S. Bunch, S. S. Verbridge, J. S. Alden, A. M. van der Zande, J. M. Parpia, H. G. Craighead, and P. L. McEuen. Impermeable atomic membranes from graphene sheets. *Nano Letters* **8**, 2458 (2008).

[28] P. R. Wallace. The band theory of graphite. *Physical Review* **71**, 622 (1947).

[29] J. W. McClure. Diamagnetism of graphite. *Physical Review* **104**, 666 (1956).

[30] J. C. Slonczewski and P. R. Weiss. Band structure of graphite. *Physical Review* **109**, 272 (1958).

[31] O. Klein. Die reflexion von elektronen an einem potentialsprung nach der relativistischen dynamik von Dirac. *Zeitschrift für Physik* **53**, 157 (1929).

[32] M. I. Katsnelson, K. S. Novoselov, and A. K. Geim. Chiral tunnelling and the Klein paradox in graphene. *Nature Physics* **2**, 620 (2006).

[33] R. V. Gorbachev, A. S. Mayorov, A. K. Savchenko, D. W. Horsell, and F. Guinea. Conductance of p-n-p graphene structures with Air-Bridge top gates. *Nano Letters* **8**, 1995 (2008).

[34] A. F. Young and P. Kim. Quantum interference and Klein tunnelling in graphene heterojunctions. *Nature Physics* **5**, 222 (2009).

[35] Y. Zhang, Y.-W. Tan, H. L. Stormer, and P. Kim. Experimental observation of the quantum Hall effect and Berry's phase in graphene. *Nature* **438**, 201 (2005).

[36] K. S. Novoselov, Z. Jiang, Y. Zhang, S. V. Morozov, H. L. Stormer, U. Zeitler, J. C. Maan, G. S. Boebinger, P. Kim, and A. K. Geim. Room-Temperature quantum hall effect in graphene. *Science* **315**, 1379 (2007).

[37] K. S. Novoselov, E. McCann, S. V. Morozov, V. I. Fal'ko, M. I. Katsnelson, U. Zeitler, D. Jiang, F. Schedin, and A. K. Geim. Unconventional quantum Hall effect and Berry's phase of 2π in bilayer graphene. *Nature Physics* **2**, 177 (2006).

[38] E. McCann, D. S. Abergel, and V. I. Fal'ko. Electrons in bilayer graphene. *Solid State Communications* **143**, 110 (2007).

[39] K. Nakada, M. Fujita, G. Dresselhaus, and M. S. Dresselhaus. Edge state in graphene ribbons: Nanometer size effect and edge shape dependence. *Physical Review B* **54**, 17954 (1996).

[40] M. Fujita, K. Wakabayashi, K. Nakada, and K. Kusakabe. Peculiar localized state at zigzag graphite edge. *Journal of the Physical Society of Japan* **65**, 1920 (1996).

[41] Y.-W. Son, M. L. Cohen, and S. G. Louie. Half-metallic graphene nanoribbons. *Nature* **444**, 347 (2006).

[42] J. Fernández-Rossier. Prediction of hidden multiferroic order in graphene zigzag ribbons. *Physical Review B* **77**, 075430 (2008).

[43] K. Wakabayashi, K.-i. Sasaki, T. Nakanishi, and T. Enoki. Electronic states of graphene nanoribbons and analytical solutions. *Science and Technology of Advanced Materials* **11**, 054504 (2010).

[44] L. Brey and H. A. Fertig. Electronic states of graphene nanoribbons studied with the Dirac equation. *Physical Review B* **73**, 235411 (2006).

[45] L. Tapaszto, G. Dobrik, P. Lambin, and L. P. Biro. Tailoring the atomic structure of graphene nanoribbons by scanning tunnelling microscope lithography. *Nature Nanotechnology* **3**, 397 (2008).

[46] A. Fasoli, A. Colli, A. Lombardo, and A. C. Ferrari. Fabrication of graphene nanoribbons via nanowire lithography. *physica status solidi (b)* **246**, 2514 (2009).

[47] J. Bai, X. Duan, and Y. Huang. Rational fabrication of graphene nanoribbons using a nanowire etch mask. *Nano Letters* **9**, 2083 (2009).

[48] J. Cai, P. Ruffieux, R. Jaafar, M. Bieri, T. Braun, S. Blankenburg, M. Muoth, A. P. Seitsonen, M. Saleh, X. Feng, K. Mullen, and R. Fasel. Atomically precise bottom-up fabrication of graphene nanoribbons. *Nature* **466**, 470 (2010).

[49] D. V. Kosynkin, A. L. Higginbotham, A. Sinitskii, J. R. Lomeda, A. Dimiev, B. K. Price, and J. M. Tour. Longitudinal unzipping of carbon nanotubes to form graphene nanoribbons. *Nature* **458**, 872 (2009).

[50] C. Tao, L. Jiao, O. V. Yazyev, Y. Chen, J. Feng, X. Zhang, R. B. Capaz, J. M. Tour, A. Zettl, S. G. Louie, H. Dai, and M. F. Crommie. Spatially resolving edge states of chiral graphene nanoribbons. *Nature Physics* **7**, 616 (2011).

[51] J. Kunstmann, C. Özdoğan, A. Quandt, and H. Fehske. Stability of edge states and edge magnetism in graphene nanoribbons. *Physical Review B* **83**, 045414 (2011).

[52] Y.-W. Son, M. L. Cohen, and S. G. Louie. Energy gaps in graphene nanoribbons. *Physical Review Letters* **97**, 216803 (2006).

[53] Z. Chen, Y. Lin, M. J. Rooks, and P. Avouris. Graphene nano-ribbon electronics. *Physica E: Low-dimensional Systems and Nanostructures* **40**, 228 (2007).

[54] M. Y. Han, B. Özyilmaz, Y. Zhang, and P. Kim. Energy Band-Gap engineering of graphene nanoribbons. *Physical Review Letters* **98**, 206805 (2007).

[55] X. Li, X. Wang, L. Zhang, S. Lee, and H. Dai. Chemically derived, ultrasmooth graphene nanoribbon semiconductors. *Science* **319**, 1229 (2008).

[56] T. C. Li and S.-P. Lu. Quantum conductance of graphene nanoribbons with edge defects. *Physical Review B* **77**, 085408 (2008).

[57] E. R. Mucciolo, A. H. Castro Neto, and C. H. Lewenkopf. Conductance quantization and transport gaps in disordered graphene nanoribbons. *Physical Review B* **79**, 075407 (2009).

[58] M. Evaldsson, I. V. Zozoulenko, H. Xu, and T. Heinzel. Edge-disorder-induced anderson localization and conduction gap in graphene nanoribbons. *Physical Review B* **78**, 161407 (2008).

[59] A. Cresti and S. Roche. Range and correlation effects in edge disordered graphene nanoribbons. *New Journal of Physics* **11**, 095004 (2009).

[60] S. Ihnatsenka and G. Kirczenow. Conductance quantization in strongly disordered graphene ribbons. *Physical Review B* **80**, 201407 (2009).

[61] S. Ihnatsenka, I. V. Zozoulenko, and G. Kirczenow. Band-gap engineering and ballistic transport in edge-corrugated graphene nanoribbons. *Physical Review B* **80**, 155415 (2009).

[62] D. A. Areshkin, D. Gunlycke, and C. T. White. Ballistic transport in graphene nanostrips in the presence of disorder: importance of edge effects. *Nano Letters* **7**, 204 (2007).

[63] I. Martin and Y. M. Blanter. Transport in disordered graphene nanoribbons. *Physical Review B* **79**, 235132 (2009).

[64] D. Querlioz, Y. Apertet, A. Valentin, K. Huet, A. Bournel, S. Galdin-Retailleau, and P. Dollfus. Suppression of the orientation effects on bandgap in graphene nanoribbons in the presence of edge disorder. *Applied Physics Letters* **92**, 042108 (2008).

[65] P. W. Anderson. Absence of diffusion in certain random lattices. *Physical Review* **109**, 1492 (1958).

[66] P. A. Lee and T. V. Ramakrishnan. Disordered electronic systems. *Reviews of Modern Physics* **57**, 287 (1985).

[67] C. W. J. Beenakker. Random-matrix theory of quantum transport. *Reviews of Modern Physics* **69**, 731 (1997).

[68] V. M. Pereira, J. M. B. Lopes dos Santos, and A. H. Castro Neto. Modeling disorder in graphene. *Physical Review B* **77**, 115109 (2008).

[69] E. R. Mucciolo and C. H. Lewenkopf. Disorder and electronic transport in graphene. *Journal of Physics: Condensed Matter* **22**, 273201 (2010).

[70] V. A. Rigo, T. B. Martins, A. J. R. da Silva, A. Fazzio, and R. H. Miwa. Electronic, structural, and transport properties of Ni-doped graphene nanoribbons. *Physical Review B* **79**, 075435 (2009).

[71] B. Biel, X. Blase, F. Triozon, and S. Roche. Anomalous doping effects on charge transport in graphene nanoribbons. *Physical Review Letters* **102**, 096803 (2009).

[72] E. Cruz-Silva, Z. M. Barnett, B. G. Sumpter, and V. Meunier. Structural, magnetic, and transport properties of substitutionally doped graphene nanoribbons from first principles. *Physical Review B* **83**, 155445 (2011).

[73] O. V. Yazyev and L. Helm. Defect-induced magnetism in graphene. *Physical Review B* **75**, 125408 (2007).

[74] J. J. Palacios, J. Fernández-Rossier, and L. Brey. Vacancy-induced magnetism in graphene and graphene ribbons. *Physical Review B* **77**, 195428 (2008).

[75] J. Haskins, A. Kınacı, C. Sevik, H. Sevinçli, G. Cuniberti, and T. Çağın. Control of thermal and electronic transport in defect-engineered graphene nanoribbons. *ACS Nano* **5**, 3779 (2011).

[76] A. P. Sutton and R. W. Balluffi. *Interfaces in Crystalline Materials.* Clarendon, Oxford, (1995).

[77] J. d'Albuquerque e Castro, A. C. de Castro Barbosa, and M. V. Tovar Costa. Quantum interference effects on the segregation energy in diluted metallic alloys. *Physical Review B* **70**, 165415 (2004).

[78] L. Gong, I. A. Kinloch, R. J. Young, I. Riaz, R. Jalil, and K. S. Novoselov. Interfacial stress transfer in a graphene monolayer nanocomposite. *Advanced Materials* **22**, 2694 (2010).

[79] A. C. Ferrari, J. C. Meyer, V. Scardaci, C. Casiraghi, M. Lazzeri, F. Mauri, S. Piscanec, D. Jiang, K. S. Novoselov, S. Roth, and A. K. Geim. Raman spectrum of graphene and graphene layers. *Physical Review Letters* **97**, 187401 (2006).

[80] A. C. Ferrari. Raman spectroscopy of graphene and graphite: Disorder, electronphonon coupling, doping and nonadiabatic effects. *Solid State Communications* **143**, 47 (2007).

[81] L. Malard, M. Pimenta, G. Dresselhaus, and M. Dresselhaus. Raman spectroscopy in graphene. *Physics Reports* **473**, 51 (2009).

[82] Y. Lin, K. A. Jenkins, A. Valdes-Garcia, J. P. Small, D. B. Farmer, and P. Avouris. Operation of graphene transistors at gigahertz frequencies. *Nano Letters* **9**, 422 (2008).

[83] J. S. Moon, D. Curtis, M. Hu, D. Wong, C. McGuire, P. M. Campbell, G. Jernigan, J. L. Tedesco, B. VanMil, R. Myers-Ward, C. Eddy, and D. K. Gaskill. Epitaxial-Graphene RF Field-Effect transistors on Si-Face 6H-SiC substrates. *IEEE Electron Device Letters* **30**, 650 (2009).

[84] L. A. Ponomarenko, F. Schedin, M. I. Katsnelson, R. Yang, E. W. Hill, K. S. Novoselov, and A. K. Geim. Chaotic Dirac billiard in graphene quantum dots. *Science* **320**, 356 (2008).

[85] N. R. Wilson, P. A. Pandey, R. Beanland, R. J. Young, I. A. Kinloch, L. Gong, Z. Liu, K. Suenaga, J. P. Rourke, S. J. York, and J. Sloan. Graphene oxide: Structural analysis and application as a highly transparent support for electron microscopy. *ACS Nano* **3**, 2547 (2009).

[86] R. R. Nair, P. Blake, J. R. Blake, R. Zan, S. Anissimova, U. Bangert, A. P. Golovanov, S. V. Morozov, A. K. Geim, K. S. Novoselov, and T. Latychevskaia. Graphene as a transparent conductive support for studying biological molecules by transmission electron microscopy. *Applied Physics Letters* **97**, 153102 (2010).

[87] X. Wang, L. Zhi, and K. Mullen. Transparent, conductive graphene electrodes for Dye-Sensitized solar cells. *Nano Letters* **8**, 323 (2007).

[88] A. Reina, X. Jia, J. Ho, D. Nezich, H. Son, V. Bulovic, M. S. Dresselhaus, and J. Kong. Large area, Few-Layer graphene films on arbitrary substrates by chemical vapor deposition. *Nano Letters* **9**, 30 (2008).

[89] K. S. Kim, Y. Zhao, H. Jang, S. Y. Lee, J. M. Kim, K. S. Kim, J. Ahn, P. Kim, J. Choi, and B. H. Hong. Large-scale pattern growth of graphene films for stretchable transparent electrodes. *Nature* **457**, 706 (2009).

[90] O. V. Yazyev. Emergence of magnetism in graphene materials and nanostructures. *Reports on Progress in Physics* **73**, 056501 (2010).

[91] S. A. Wolf, D. D. Awschalom, R. A. Buhrman, J. M. Daughton, S. von Molnr, M. L. Roukes, A. Y. Chtchelkanova, and D. M. Treger. Spintronics: A Spin-Based electronics vision for the future. *Science* **294**, 1488 (2001).

[92] D. D. Awschalom and M. E. Flatte. Challenges for semiconductor spintronics. *Nature Physics* **3**, 153 (2007).

[93] C. Chappert, A. Fert, and F. N. Van Dau. The emergence of spin electronics in data storage. *Nature Materials* **6**, 813 (2007).

[94] A. Fert. Nobel lecture: Origin, development, and future of spintronics. *Reviews of Modern Physics* **80**, 1517 (2008).

[95] C. L. Kane and E. J. Mele. Quantum spin hall effect in graphene. *Physical Review Letters* **95**, 226801 (2005).

[96] D. Huertas-Hernando, F. Guinea, and A. Brataas. Spin-orbit coupling in curved graphene, fullerenes, nanotubes, and nanotube caps. *Physical Review B* **74**, 155426 (2006).

[97] H. Min, J. E. Hill, N. A. Sinitsyn, B. R. Sahu, L. Kleinman, and A. H. MacDonald. Intrinsic and rashba spin-orbit interactions in graphene sheets. *Physical Review B* **74**, 165310 (2006).

[98] D. Huertas-Hernando, F. Guinea, and A. Brataas. Spin-Orbit-Mediated spin relaxation in graphene. *Physical Review Letters* **103**, 146801 (2009).

[99] B. Trauzettel, D. V. Bulaev, D. Loss, and G. Burkard. Spin qubits in graphene quantum dots. *Nature Physics* **3**, 192 (2007).

[100] O. V. Yazyev. Hyperfine interactions in graphene and related carbon nanostructures. *Nano Letters* **8**, 1011 (2008).

[101] J. Fischer, B. Trauzettel, and D. Loss. Hyperfine interaction and electron-spin decoherence in graphene and carbon nanotube quantum dots. *Physical Review B* **80**, 155401 (2009).

[102] M. Wimmer, I. Adagideli, S. Berber, D. Tománek, and K. Richter. Spin currents in rough graphene nanoribbons: Universal fluctuations and spin injection. *Physical Review Letters* **100**, 177207 (2008).

[103] W. Y. Kim and K. S. Kim. Prediction of very large values of magnetoresistance in a graphene nanoribbon device. *Nature Nanotechnology* **3**(7), 408 (2008).

[104] E. H. Lieb. Two theorems on the hubbard model. *Physical Review Letters* **62**, 1201 (1989).

[105] L. Xie, X. Wang, J. Lu, Z. Ni, Z. Luo, H. Mao, R. Wang, Y. Wang, H. Huang, D. Qi, R. Liu, T. Yu, Z. Shen, T. Wu, H. Peng, B. Ozyilmaz, K. Loh, A. T. S. Wee, Ariando, and W. Chen. Room temperature ferromagnetism in partially hydrogenated epitaxial graphene. *Applied Physics Letters* **98**, 193113 (2011).

[106] D. Soriano, N. Leconte, P. Ordejn, J. Charlier, J. Palacios, and S. Roche. Magnetoresistance and magnetic ordering fingerprints in hydrogenated graphene. *Physical Review Letters* **107**, 016602 (2011).

[107] S. S. P. Parkin, N. More, and K. P. Roche. Oscillations in exchange coupling and magnetoresistance in metallic superlattice structures: Co/Ru, Co/Cr, and Fe/Cr. *Physical Review Letters* **64**, 2304 (1990).

[108] S. S. P. Parkin. Systematic variation of the strength and oscillation period of indirect magnetic exchange coupling through the 3d, 4d, and 5d transition metals. *Physical Review Letters* **67**, 3598 (1991).

[109] D. M. Edwards, J. Mathon, R. B. Muniz, and M. S. Phan. Oscillations of the exchange in magnetic multilayers as an analog of de Haas - van Alphen effect. *Physical Review Letters* **67**, 493 (1991).

[110] D. M. Edwards, J. Mathon, R. B. Muniz, and M. S. Phan. Oscillations in the exchange coupling of ferromagnetic layers separated by a nonmagnetic metallic layer. *Journal of Physics: Condensed Matter* **3**, 4941.

[111] M. A. Ruderman and C. Kittel. Indirect exchange coupling of nuclear magnetic moments by conduction electrons. *Physical Review* **96**, 99 (1954).

[112] T. Kasuya. A theory of metallic ferro- and antiferromagnetism on zener's model. *Progress of Theoretical Physics* **16**, 45 (1956).

[113] K. Yosida. Magnetic properties of Cu-Mn alloys. *Physical Review* **106**, 893 (1957).

[114] P. Bruno and C. Chappert. Oscillatory coupling between ferromagnetic layers separated by a nonmagnetic metal spacer. *Physical Review Letters* **67**, 1602 (1991).

[115] P. Bruno and C. Chappert. Ruderman-kittel theory of oscillatory interlayer exchange coupling. *Physical Review B* **46**, 261 (1992).

[116] A. T. Costa, D. F. Kirwan, and M. S. Ferreira. Indirect exchange coupling between magnetic adatoms in carbon nanotubes. *Physical Review B* **72**, 085402 (2005).

[117] D. F. Kirwan, C. G. Rocha, A. T. Costa, and M. S. Ferreira. Sudden decay of indirect exchange coupling between magnetic atoms on carbon nanotubes. *Physical Review B* **77**, 085432 (2008).

[118] D. F. Kirwan. *Theoretical Studies of Carbon Nanotubes Interacting with Magnetic Atoms.* PhD thesis, School of Physics, Trinity College Dublin, Dublin, (2009).

[119] D. F. Kirwan, V. M. de Menezes, C. G. Rocha, A. T. Costa, R. B. Muniz, S. B. Fagan, and M. S. Ferreira. Enhanced spin-valve effect in magnetically doped carbon nanotubes. *Carbon* **47**, 2533 (2009).

[120] V. Krstic, C. P. Ewels, T. Wågberg, M. S. Ferreira, A. M. Janssens, O. Stephan, and M. Glerup. Indirect magnetic coupling in light-element-doped single-walled carbon nanotubes. *ACS Nano* **4**, 5081 (2010).

[121] M. A. H. Vozmediano, M. P. López-Sancho, T. Stauber, and F. Guinea. Local defects and ferromagnetism in graphene layers. *Physical Review B* **72**, 155121 (2005).

[122] V. K. Dugaev, V. I. Litvinov, and J. Barnas. Exchange interaction of magnetic impurities in graphene. *Physical Review B* **74**, 224438 (2006).

[123] S. Saremi. RKKY in half-filled bipartite lattices: Graphene as an example. *Physical Review B* **76**, 184430 (2007).

[124] L. Brey, H. A. Fertig, and S. D. Sarma. Diluted graphene antiferromagnet. *Physical Review Letters* **99**, 116802 (2007).

[125] E. H. Hwang and S. Das Sarma. Screening, kohn anomaly, friedel oscillation, and RKKY interaction in bilayer graphene. *Physical Review Letters* **101**, 156802 (2008).

[126] J. E. Bunder and H. Lin. Ruderman-Kittel-Kasuya-Yosida interactions on a bipartite lattice. *Physical Review B* **80**, 153414 (2009).

[127] A. M. Black-Schaffer. RKKY coupling in graphene. *Physical Review B* **81**, 205416 (2010).

[128] M. Sherafati and S. Satpathy. RKKY interaction in graphene from the lattice green's function. *Physical Review B* **83**, 165425 (2011).

[129] B. Uchoa, T. G. Rappoport, and A. H. Castro Neto. Kondo quantum criticality of magnetic adatoms in graphene. *Physical Review Letters* **106**, 016801 (2011).

[130] A. M. Black-Schaffer. Importance of electron-electron interactions in the RKKY coupling in graphene. *Physical Review B* **82**, 073409 (2010).

[131] S. R. Power and M. S. Ferreira. Electronic structure of graphene beyond the linear dispersion regime. *Physical Review B* **83**, 155432 (2011).

[132] M. Sherafati and S. Satpathy. Analytical expression for the RKKY interaction in doped graphene. *Physical Review B* **84**, 125416 (2011).

[133] E. Kogan. RKKY interaction in graphene. *Physical Review B* **84**, 115119 (2011).

[134] E. Šimánek and B. Heinrich. Gilbert damping in magnetic multilayers. *Physical Review B* **67**, 144418 (2003).

[135] B. Heinrich, Y. Tserkovnyak, G. Woltersdorf, A. Brataas, R. Urban, and G. E. W. Bauer. Dynamic exchange coupling in magnetic bilayers. *Physical Review Letters* **90**, 187601 (2003).

[136] A. T. Costa, R. B. Muniz, and M. S. Ferreira. Dynamic interaction between localized magnetic moments in carbon nanotubes. *New Journal of Physics* (2008).

[137] F. S. M. Guimarães, D. F. Kirwan, A. T. Costa, R. B. Muniz, D. L. Mills, and M. S. Ferreira. Carbon nanotube: A low-loss spin-current waveguide. *Physical Review B* **81**, 153408 (2010).

[138] F. S. M. Guimarães, A. T. Costa, R. B. Muniz, and M. S. Ferreira. Graphene-based spin-pumping transistor. *Physical Review B* **81**, 233402 (2010).

[139] F. S. M. Guimarães, A. T. Costa, R. B. Muniz, and M. S. Ferreira. Graphene as a non-magnetic spin current lens. *Journal of Physics: Condensed Matter* **23**, 175302 (2011).

[140] D. A. Abanin, S. V. Morozov, L. A. Ponomarenko, R. V. Gorbachev, A. S. Mayorov, M. I. Katsnelson, K. Watanabe, T. Taniguchi, K. S.

Novoselov, L. S. Levitov, and A. K. Geim. Giant nonlocality near the Dirac point in graphene. *Science* **332**, 328 (2011).

[141] A. J. Heinrich, J. A. Gupta, C. P. Lutz, and D. M. Eigler. Single-Atom Spin-Flip spectroscopy. *Science* **306**, 466 (2004).

[142] S. Loth, K. von Bergmann, M. Ternes, A. F. Otte, C. P. Lutz, and A. J. Heinrich. Controlling the state of quantum spins with electric currents. *Nature Physics* **6**, 340 (2010).

[143] A. A. Khajetoorians, B. Chilian, J. Wiebe, S. Schuwalow, F. Lechermann, and R. Wiesendanger. Detecting excitation and magnetization of individual dopants in a semiconductor. *Nature* **467**, 1084 (2010).

[144] A. A. Khajetoorians, S. Lounis, B. Chilian, A. T. Costa, L. Zhou, D. L. Mills, J. Wiebe, and R. Wiesendanger. Itinerant nature of Atom-Magnetization excitation by tunneling electrons. *Physical Review Letters* **106**, 037205 (2011).

[145] E. N. Economou. *Green's Functions in Quantum Physics.* Springer, 3rd edition, (2006).

[146] P. Soven. Contribution to the theory of disordered alloys. *Physical Review* **178**, 1136 (1969).

[147] R. J. Elliott, J. A. Krumhansl, and P. L. Leath. The theory and properties of randomly disordered crystals and related physical systems. *Reviews of Modern Physics* **46**, 465 (1974).

[148] M. P. L. Sancho, J. M. L. Sancho, and J. Rubio. Quick iterative scheme for the calculation of transfer matrices: application to mo (100). *Journal of Physics F: Metal Physics* **14**, 1205.

[149] P. Lloyd. Wave propagation through an assembly of spheres: ii. the density of single-particle eigenstates. *Proceedings of the Physical Society* **90**, 207 (1967).

[150] M. Desjonqueres and D. Spanjaard. *Concepts in Surface Physics.* Springer, 2nd edition, (2002).

[151] A. Wall. *Theoretical studies of doped carbon nanotube based materials.* PhD thesis, School of Physics, Trinity College Dublin, Dublin, (2008).

[152] C. G. Rocha, A. Wall, and M. S. Ferreira. Electronic properties of nanotube-based sensors: An inverse modeling approach. *Europhysics Letters* **82**, 27004 (2008).

[153] M. L. Boas. *Mathematical Methods in the Physical Sciences.* Wiley, 3 edition, (2005).

[154] R. M. White. *Quantum Theory of Magnetism: Magnetic Properties of Materials.* Springer, 3rd edition, (2010).

[155] C. T. White and T. N. Todorov. Carbon nanotubes as long ballistic conductors. *Nature* **393**, 240 (1998).

[156] H. Thomann, L. K. Dalton, M. Grabowski, and T. C. Clarke. Direct observation of coulomb correlation effects in polyacetylene. *Physical Review B* **31**, 3141 (1985).

[157] O. V. Yazyev. Magnetism in disordered graphene and irradiated graphite. *Physical Review Letters* **101**, 037203 (2008).

[158] A. Abrikosov. *Fundamentals of the Theory of Metals.* North Holland, (1988).

[159] C. Bena. Effect of a single localized impurity on the local density of states in monolayer and bilayer graphene. *Physical Review Letters* **100**, 076601 (2008).

[160] B. Uchoa, L. Yang, S. Tsai, N. M. R. Peres, and A. H. Castro Neto. Theory of scanning tunneling spectroscopy of magnetic adatoms in graphene. *Physical Review Letters* **103**, 206804 (2009).

[161] V. M. Pereira, J. M. B. Lopes dos Santos, and A. H. Castro Neto. Modeling disorder in graphene. *Physical Review B* **77**, 115109 (2008).

[162] A. Cresti, N. Nemec, B. Biel, G. Niebler, F. Triozon, G. Cuniberti, and S. Roche. Charge transport in disordered graphene-based low dimensional materials. *Nano Research* **1**, 361 (2008).

[163] C. Caroli, R. Combescot, P. Nozieres, and D. Saint-James. Direct calculation of the tunneling current. *Journal of Physics C: Solid State Physics* **4**(8), 916–929 June (1971).

[164] J. Mathon. Large enhancement of the perpendicular giant magnetoresistance in pseudorandom magnetic multilayers. *Physical Review B* **54**, 55 (1996).

[165] N. Gorjizadeh and Y. Kawazoe. Chemical functionalization of graphene nanoribbons. *Journal of Nanomaterials* **2010**, 1 (2010).

[166] S. Latil, S. Roche, and J. Charlier. Electronic transport in carbon nanotubes with random coverage of physisorbed molecules. *Nano Lett.* **5**(11), 2216–2219 (2005).

[167] S. Latil, S. Roche, D. Mayou, and J. Charlier. Mesoscopic transport in chemically doped carbon nanotubes. *Physical Review Letters* **92**(25), 256805 June (2004).

[168] C. G. Rocha, A. Wall, A. R. Rocha, and M. S. Ferreira. Modelling the effect of randomly dispersed adatoms on carbon nanotubes. *Journal of Physics: Condensed Matter* **19**(34), 346201 August (2007).

[169] S. Casolo, R. Martinazzo, and G. F. Tantardini. Band engineering in graphene with superlattices of substitutional defects. *J. Phys. Chem. C* **115**(8), 3250–3256 (2011).

[170] S. Ihnatsenka and G. Kirczenow. Dirac point resonances due to atoms and molecules adsorbed on graphene and transport gaps and conductance quantization in graphene nanoribbons with covalently bonded adsorbates. *Physical Review B* **83**(24), 245442 June (2011).

[171] C. Weeks. Engineering a robust quantum spin hall state in graphene via adatom deposition. *Physical Review X* **1**(2) (2011).

[172] R. E. Cohen, M. J. Mehl, and D. A. Papaconstantopoulos. Tight-binding total-energy method for transition and noble metals. *Physical Review B* **50**, 14694 (1994).

[173] W. M. C. Foulkes and R. Haydock. Tight-binding models and density-functional theory. *Physical Review B* **39**, 12520 (1989).

[174] H. Sevinli, M. Topsakal, E. Durgun, and S. Ciraci. Electronic and magnetic properties of 3d transition-metal atom adsorbed graphene and graphene nanoribbons. *Physical Review B* **77**, 195434 (2008).

[175] J. M. Soler, E. Artacho, J. D. Gale, A. García, J. Junquera, P. Ordejón, and D. Sánchez-Portal. The SIESTA method for ab initio order-N materials simulation. *Journal of Physics: Condensed Matter* **14**, 2745 (2002).

[176] J. P. Perdew, K. Burke, and M. Ernzerhof. Generalized gradient approximation made simple. *Physical Review Letters* **77**, 3865 (1996).

[177] N. Troullier and J. L. Martins. Efficient pseudopotentials for plane-wave calculations. *Physical Review B* **43**, 1993 (1991).

[178] K. Nordlund, J. Keinonen, and T. Mattila. Formation of ion irradiation induced small-scale defects on graphite surfaces. *Physical Review Letters* **77**, 699 (1996).

[179] T. C. M. Chung, Y. Jeong, Q. Chen, A. Kleinhammes, and Y. Wu. Synthesis of microporous boron-substituted carbon (B/C) materials using polymeric precursors for hydrogen physisorption. *J. Am. Chem. Soc.* **130**, 6668 (2008).

[180] A. V. Krasheninnikov and F. Banhart. Engineering of nanostructured carbon materials with electron or ion beams. *Nature Materials* **6**, 723 (2007).

[181] E. J. G. Santos, A. Ayuela, S. B. Fagan, J. M. Filho, D. L. Azevedo, A. G. S. Filho, and D. Sánchez-Portal. Switching on magnetism in ni-doped graphene: Density functional calculations. *Physical Review B* **78**, 195420 (2008).

[182] I. Schnell, G. Czycholl, and R. C. Albers. Unscreened Hartree-Fock calculations for metallic fe, co, ni, and cu from ab initio hamiltonians. *Physical Review B* **68**(24), 245102 December (2003).

[183] S. R. Power, V. M. de Menezes, S. B. Fagan, and M. S. Ferreira. Model of impurity segregation in graphene nanoribbons. *Physical Review B* **80**, 235424 (2009).

[184] P. Venezuela, R. B. Muniz, A. T. Costa, D. M. Edwards, S. R. Power, and M. S. Ferreira. Emergence of local magnetic moments in doped graphene-related materials. *Physical Review B* **80**, 241413 (2009).

[185] A. V. Krasheninnikov, P. O. Lehtinen, A. S. Foster, P. Pyykk, and R. M. Nieminen. Embedding Transition-Metal atoms in graphene: Structure, bonding, and magnetism. *Physical Review Letters* **102**, 126807 (2009).

[186] M. N. Baibich, J. M. Broto, A. Fert, F. N. Van Dau, F. Petroff, P. Etienne, G. Creuzet, A. Friederich, and J. Chazelas. Giant magnetoresistance of (001)fe/(001)cr magnetic superlattices. *Physical Review Letters* **61**, 2472 (1988).

[187] G. Binasch, P. Grünberg, F. Saurenbach, and W. Zinn. Enhanced magnetoresistance in layered magnetic structures with antiferromagnetic interlayer exchange. *Physical Review B* **39**, 4828 (1989).

[188] J. d'Albuquerque e Castro, M. S. Ferreira, and R. B. Muniz. Theory of the exchange coupling in magnetic metallic multilayers. *Physical Review B* **49**, 16062 (1994).

[189] M. S. Ferreira, R. B. Muniz, J. d'Alberquerque e Castro, and D. M. Edwards. The nature and validity of the RKKY limit of exchange

coupling in magnetic trilayers. *Journal of Physics: Condensed Matter* **6**, L619.

[190] M. S. Ferreira, J. d'Albuquerque e Castro, D. M. Edwards, and J. Mathon. Fundamental oscillation periods of the interlayer exchange coupling beyond the rkky approximation. *Journal of Physics: Condensed Matter* **8**, 11259.

[191] J. Charlier and S. Iijima. Growth mechanisms of carbon nanotubes. In *Carbon Nanotubes,* M. S. Dresselhaus, G. Dresselhaus, and P. Avouris, eds., volume 80, 55. Springer Berlin Heidelberg, Berlin, Heidelberg (2001).

[192] P. W. Anderson. Localized magnetic states in metals. *Physical Review* **124**, 41 (1961).

[193] I. C. Gerber, A. V. Krasheninnikov, A. S. Foster, and R. M. Nieminen. A first-principles study on magnetic coupling between carbon adatoms on graphene. *New Journal of Physics* **12**, 113021 (2010).

[194] E. J. G. Santos, D. Snchez-Portal, and A. Ayuela. Magnetism of substitutional co impurities in graphene: Realization of single vacancies. *Physical Review B* **81**, 125433 (2010).

[195] E. J. G. Santos, A. Ayuela, and D. Snchez-Portal. First-principles study of substitutional metal impurities in graphene: structural, electronic and magnetic properties. *New Journal of Physics* **12**, 053012 (2010).

[196] E. Durgun, S. Dag, V. M. K. Bagci, O. Glseren, T. Yildirim, and S. Ciraci. Systematic study of adsorption of single atoms on a carbon nanotube. *Physical Review B* **67**, 201401 (2003).

[197] M. P. López-Sancho, F. de Juan, and M. A. H. Vozmediano. Magnetic moments in the presence of topological defects in graphene. *Physical Review B* **79**, 075413 (2009).

[198] V. Heine, J. H. Samson, and C. M. M. Nex. Theory of local magnetic moments in transition metals. *Journal of Physics F: Metal Physics* **11**, 2645 (1981).

[199] B. Uchoa, V. N. Kotov, N. M. R. Peres, and A. H. Castro Neto. Localized magnetic states in graphene. *Physical Review Letters* **101**, 026805 (2008).

[200] F. J. Himpsel. Correlation between magnetic splitting and magnetic moment for 3d transition metals. *Journal of Magnetism and Magnetic Materials* **102**, 261 (1991).

[201] R. Kubo. Statistical-Mechanical theory of irreversible processes. i. general theory and simple applications to magnetic and conduction problems. *Journal of the Physical Society of Japan* **12**, 570 (1957).

[202] L. H. M. Barbosa, R. B. Muniz, A. T. Costa, and J. Mathon. Spin waves in ultrathin ferromagnetic overlayers. *Physical Review B* **63**, 174401 (2001).

[203] J. F. Cooke. Neutron scattering from Itinerant-Electron ferromagnets. *Physical Review B* **7**, 1108 (1973).

[204] J. F. Cooke, J. W. Lynn, and H. L. Davis. Calculations of the dynamic susceptibility of nickel and iron. *Physical Review B* **21**, 4118 (1980).

[205] H. Tang, M. Plihal, and D. L. Mills. Theory of the spin dynamics of bulk Fe and ultrathin Fe(1 0 0) films. *Journal of Magnetism and Magnetic Materials* **187**, 23 (1998).

[206] R. B. Muniz and D. L. Mills. Theory of spin excitations in Fe(110) monolayers. *Physical Review B* **66**, 174417 (2002).

[207] R. B. Muniz and D. L. Mills. Local spin dynamics of magnetic moments on metal surfaces. *Physical Review B* **68**, 224414 (2003).

[208] D. N. Zubarev. Double-time green function in statistical physics. *Soviet Physics Uspekhi* **3**, 320 (1960).

[209] F. S. M. Guimarães, A. T. Costa, R. B. Muniz, and D. L. Mills. Spin currents in metallic nanostructures: Explicit calculations. *Physical Review B* **84**, 054403 (2011).

[210] R. Sielemann, Y. Kobayashi, Y. Yoshida, H. P. Gunnlaugsson, and G. Weyer. Magnetism at single isolated iron atoms implanted in graphite. *Physical Review Letters* **101**, 137206 (2008).

[211] S. Lounis, A. T. Costa, R. B. Muniz, and D. L. Mills. Dynamical magnetic excitations of nanostructures from first principles. *Physical Review Letters* **105**(18), 187205 (2010).

[212] D. L. Mills and P. Lederer. Dynamical properties of magnetic impurities in transition metals. *Physical Review* **160**(3), 590–599 (1967).

[213] H. Zhang, C. Lazo, S. Blgel, S. Heinze, and Y. Mokrousov. Electrically tunable quantum anomalous hall effect in graphene decorated by 5d Transition-Metal adatoms. *Physical Review Letters* **108**(5), 056802 (2012).

[214] R. Peierls. On the theory of the diamagnetism of conduction electrons. *Z. Physik* **80**, 763.

[215] V. M. Pereira and A. H. Castro Neto. Strain engineering of graphenes electronic structure. *Physical Review Letters* **103**, 046801 (2009).

[216] V. M. Pereira, A. H. Castro Neto, and N. M. R. Peres. Tight-binding approach to uniaxial strain in graphene. *Physical Review B* **80**, 045401 (2009).